+-

Neuromyelitis optica (NMO): identifying imaging markers to improve diagnosis and inform therapeutic innovation

Lise Magnollay

Thesis submitted for the degree of

Doctor of Philosophy

of the University College London

Field of study:

Neuroscience/Magnetic Resonance Imaging

Department of Neuroinflammation,

Institute of Neurology

2017

I, Lise Magnollay confirm that the work presented in this thesis is my own.

Where information has been derived from other sources, I confirm that this has been indicated in the thesis.

Abstract

The main objective of the thesis is to use advanced MRI techniques to look for biomarkers that separate neuromyelitis optica spectrum disorders (NMOSD) from MS to improve diagnosis. NMOSD, a severe inflammatory disease which causes demyelination of the central nervous system, is characterised by optic neuritis (ON) and acute myelitis. Because of similarities with MS, NMOSD is not always correctly diagnosed at onset. As it is both more aggressive and faster progressing than MS, an early accurate diagnosis is crucial. For this thesis, three different MRI techniques were used, together with clinical assessments, to gain a better understanding of the differences between the two diseases. The first was neurite orientation dispersion and density imaging (NODDI), a diffusion MR technique used to analyse the microstructure of dendrites and axons. When applied to a single-shell dataset of RRMS patients, it was shown to detect more regions of diffusion abnormalities than FA maps. The second technique used is phase-sensitive inversion recovery (PSIR), to look for grey matter lesions. This first application to NMOSD patients led to the detection of grey matter lesions in nearly 50% of this group, as well as showing differences in leucocortical and juxtacortical lesions between NMOSD and MS, with juxtacortical lesions emerging as potential markers to differentiate between these diseases. The final part applies magnetisation transfer ratio (MTR) to the optic nerve to assess myelin integrity in both MS and NMOSD patients, together with optic coherence tomography (OCT) for the macula the retinal nerve fibre layer and visual assessments. Significant differences in MTR and OCT values were found in MS and NMOSD patients with ON compared to healthy controls (HC). Significant differences were found between the unaffected nerve of NMOSD patients and HC, but not between groups for either MTR values (after correction for age) and OCT measurements.

In memory of YP, LC, EW and GV

Acknowledgements

I want to thank my supervisors, Professors Olga Ciccarelli and David Miller for their help and support with this thesis, as well as Dr Ferran Prados, who was the unofficial third supervisor and who spent a lot of time developing processing pipelines for both the NODDI and MTR studies.

Thanks are also due to Professor Claudia Gandini Wheeler-Kingshott, who was the *de facto* supervisor for the NODDI study, as well as to Dr Francesco Grussu who assisted me with the NODDI fitting and answered my questions about NODDI both while conducting the study and when writing this thesis. Thanks are also due to Gary Hui Zhang, the creator of NODDI, for his assistance. Finally, I also owe a lot to Dr Arman Eshaghi, for guiding me through the complexities of SPM and assisting me whenever I was encountering problems with VBM, and Dr Matteo Pardini for advising on the selection of cognitive tests.

The NMOSD vs MS study would not have been possible without the help of the two neurologists who did all the clinical assessments, so many thanks to my two dear friends, Dr Floriana De Angelis and Dr Rosanna Cortese. As well as the Walton Centre in Liverpool, in particular Dr Anu Jacob, Dr Khaled Abdel-Aziz and Kerry Much, who recruited NMOSD patients for the study.

As the key parts of this thesis are based on MRI data, warm thanks to the radiographers for their work on what was a very demanding protocol: Dr Marios Yiannakas, who also always answered my questions about MRI with great clarity as well as reading my MR physics chapter; Luke Hoy, who did many late Friday shifts to scan most of the patients who took part in the NMOSD vs. MS study, together with Chichi Ugorji, who also did some of the scanning.

Special thanks are also due to Dr Viktor Wottschel, who helped me with many image processing problems and developed the initial registration used for the MTR of the optic nerve, as well as Dr Ahmed Toosy who helped with both the MTR analysis and the OCT acquisition.

Very warm thanks to Professor Tarek Yousry, for checking all the lesion markings on the PSIR scans. I would not have felt confident about the results if he had not so generously undertaken this very time consuming task.

Many thanks to Dr Carmen Tur and Dr Dan Altmann, the perfect statisticians, who not only did the statistics for both the MTR and PSIR studies, but were also always happy to answer my questions and explain what they did and why.

I also want to thank Dr Wallace Brownlee for training me to do the cognitive tests, Dr Becky Samson for helping me with all things related to MTR, Jon Steel, our IT guru, as well as all the other clinicians from the Queen Square MS group who were always happy to answer my clinical questions. And of course all the other fellows in the group, who make it such a great team to be part of.

Research of the type conducted for this thesis would not be possible without patients generously agreeing to take part, especially when the study is as long as the NMOSD vs. MS was. Especially when, as was the case of for many NMOSD patients, it also involved travelling all the way from the north of England.

Finally, I owe thanks to Drs Hugh Selsick and Gill Hyams, from the Insomnia Clinic at UCLH, without whose help I would never been able to complete this thesis.

Contributors

The work presented in this thesis would not have been possible without contributions from the following people:

For the NODDI study

NODDI fitting: Drs Francesco Grussu, Gary Hui Zhang and Professor Gandini Wheeler-Kingshott.

VBM analysis: Drs Ferran Prados (image processing) and Arman Eshaghi (assistance with SPM and VBM).

For the NMOSD vs MS study

Clinical assessments: Drs Floriana De Angelis and Rosa Cortese.

PSIR: Professor Tarek Yousry (quality control of lesion masks) and Dr Dan Altmann (statistics).

MTR and OCT: Drs Feran Prados and Viktor Wottschel (registration), Ahmed Toosy (assistance with OCT acquisition and MTR analysis), Carmen Tur and Dan Altmann (statistics), Marios Yiannakas (MTR protocol development).

Conference presentations

Some of the results included in this thesis were presented at conferences:

Application of NODDI to single-shell data, ROIs approach:

An investigation of brain neurite density and dispersion in multiple sclerosis using single shell diffusion imaging
Lise Magnollay, Francesco Grussu, Claudia Wheeler-Kingshott, Varun Sethi, Hui Zhang, Declan Chard, David Miller, Olga Ciccarelli
Poster, ISMRM-ESMRMB, 2014

Application of Neurite Orientation Dispersion and Density Imaging (NODDI) to RRMS patients
Lise Magnollay, Francesco Grussu, Claudia Wheeler-Kingshott, Varun Sethi, Hui Zhang, Declan Chard, David Miller, Olga Ciccarelli
Poster, ECTRIMS, 2013

Optic neuritis in MS and NMOSD:

Can optic nerve MTR and OCT distinguish between multiple sclerosis and neuromyelitis optica?
Lise Magnollay, Floriana De Angelis, Ferran Prados, Viktor Wottschel, Ahmed Toosy, Carmen Tur, Daniel Altman, Marios Yiannakas, Rosa Cortese, Sebastient Ourselin, David Miller, Olga Ciccarelli
Shortlisted Poster, ECTRIMS, 2015

Table of Contents

List of Figures

List of Tables

Abbreviations

α	Flipping angle
ART	Automatic retinal tracking
B0	External magnetic field
B1	RF field/pulse applied at Larmor frequency
CI	Confidence interval, Cognitive impairment
COV	Coefficient of variation
CSF	Cerebrospinal fluid
DARTEL	Diffeomorphic anatomical registration through exponentiated Lie algebra
DGM	Deep grey matter
DIR	Double inversion recovery
dMRI	Diffusion magnetic resonance imaging
DOF	Degrees of freedom
ELISA	Enzyme-linked immunosorbent assay
FA	Fractional anisotropy
FID	Free induction decay
GM	Grey matter
HARDI	High angular resolution diffusion imaging
HC	Healthy controls
Hz	Hertz
ICC	Interclass correlation coefficient
IPND	International Panel for NMO Diagnosis
IR	Inversion recovery

LEON	Longitudinally extensive optic neuritis
LETM	Longitudinal extensive transverse myelitis
MD	Mean diffusivity
MRI	Magnetic resonance imaging
M	Magnetisation vector
MD	Mean diffusivity
MS	Multiple sclerosis
NAWM	Normal appearing white matter
NMO-IgG	Neuromyelitis optica immunoglobin G
NODDI	Neurite orientation dispersion and density index
PD	Proton density
PSIR	Phase-sensitive inversion recovery
QSM	Quantitative susceptibility mapping
RF	Radio frequency
RNFL	Retinal nerve fibre layers
SCA	Spinal cord atrophy
SE	Spin echo
SMT	Spherical Mean Technique
STM	Short transverse myelitis
TE	Echo time
TI	Inversion time
TR	Repetition time
TBSS	Tract-based spatial statistics
WM	White matter

Chapter 1

Introduction: the NMOSD vs MS study

The data for this thesis were obtained as part of a larger study aiming to develop and apply novel imaging biomarkers to MS and NMOSD, using advanced MRI techniques combined with other tests. The study was looking for biomarkers that could separate NMOSD from MS, and would therefore improve diagnosis.

1.1 Rationale for the study

Neuromyelitis optica (NMO), like multiple sclerosis (MS), is an inflammatory disease causing demyelination of the central nervous system. Both diseases have similar characteristics, including optic neuritis and myelitis, making an accurate early diagnosis difficult. While the discovery in 2004 of an NMO specific antibody, the auto-antibody neuromyelitis optica immunoglobin G (NMO-IgG) which binds to the antigen aquaporin-4 (AQP4) and the subsequent development of accurate detection tests greatly improved diagnosis accuracy, it did not fully solve the problem of NMOSD patients being initially misdiagnosed with MS: as Jarius and colleagues[1] report, even after the introduction of the NMO-IgG test, 20% of NMOSD patients received an initial diagnosis of MS. The issue of misdiagnosis, especially in the early stages of the disease, remains true today[2] and is particularly problematic as some drugs used for the treatment of MS (interferon-β, natalizumab, and fingolimod) may aggravate NMO[3,4]. Therefore finding new markers which could ensure a correct diagnosis at the earliest possible stage is crucial in order to provide patients with the most efficient treatment.

1.2 Patients recruitment

In order to recruit the required number of NMOSD patients, recruitment was conducted at The Walton Centre in Liverpool besides the National Hospital for

Neurology and Neurosurgery. All MS patients were recruited at the National Hospital for Neurology and Neurosurgery.

1.3 Study protocol

The study is divided in three sections, the first looked at the brain, the second into the effect of optic neuritis, while the last focused on the cervical spinal cord, with each part including both MR scans and various assessments:

Brain:

- Proton density (PD)/T2-weighted imaging.
- Phase Sensitive Inversion Recovery (PSIR).
- Susceptibility-weighted imaging (SWI).
- 3D-T1 weighted imaging.
- Cognitive assessments: National Adult Reading Test (NART), delayed story and figure recalls, Hayling Sentence Completion Test, Brixton Spatial Anticipation Test, Symbol Digit Modalities Test (SDMT) and Paced Auditory Serial Addition Test (PASAT).

Effects of optic neuritis:

- Dynamic T2-weighted imaging of the optic nerves.
- Magnetisation transfer ratio (MTR) of the optic nerves.
- Optic coherence tomography (OCT): measurements of the macular volume and retinal nerve fibre layer (RNFL) thickness.
- Visual acuity assessment (letter charts and 100-hue test).

Cervical spinal cord:

- Proton density/T2-weighted imaging.
- Coronal T2-weighted imaging.
- Magnetic resonance spectroscopy (MRS) optimised for myo-inositol.
- 3D-Fast Field Echo (FFE), commonly known as 3D gradient-echo.
- Diffusion tensor imaging (DTI).
- Posturography to assess balance.
- Assessments of hand grip and sensitivity to vibrations.

Clinical assessment:

A clinical assessment, covering disease history and Expanded Disability Status Scale (EDSS) for all patients, was carried out by two neurologists, Dr Floriana De Angelis and Dr Rosa Cortese, who also did the visual acuity and spinal cord assessments.

1.4 Data analysis

For the purpose of this thesis, the data from the Phase Sensitive Inversion Recovery (PSIR) scans, together with the data collected for the section covering the effects of optic neuritis were analysed and are presented in **Chapter 5** and **Chapter 6** respectively.

For the spinal cord spectoscropy, too few valid spectra were obtained in the patient groups for the full data analysis to be feasible: only 7 out of 20 spectra from MS patients and 4 out of 18 from NMOSD ones were usable.

Dr Rosa Cortese analysed the data for the other spinal cord scans as well as the SWI scans in the brain. The latter was looking for central vein signs in the WM lesions, to assess whether they differed between the two diseases. The results for these three studies were presented as posters at both the American Accademy of Neurology and ECTRIMS[5-7].

1.5 Neurite Orientation Dispersion and Density index (NODDI)

An additional study was conducted in parallel to the acquistion of the NMOSD-MS data: the application of Neurite Orientation Dispersion and Density index (NODDI)[8] to a selection of relapsing-remitting multiple sclerosis (RRMS) patients and matched healthy controls who underwent dMRI scanning as part of a previous study[9]. The aim of this study was to assess the sensitivity of NODDI indices to changes occurring in normal appearing white matter (NAWM) when compared to fractional anisotropy (FA). The prospect of detecting microstructural changes in NAWM at an early stage could prove useful in the quest of new markers to differentiate NMOSD from MS since MS patients generally have a much higher WM lesion load than NMOSD ones

(4.85ml in MS patients vs.0.99 in NMOSD ones in the cohort recruited for this thesis), therefore a higher rate of changes in NAWM is also likely to occur. The results of this study are presented in **Chapter 4**.

Since the focus of this thesis is to investigate new ways to distinguish between NMOSD and MS, it will be useful first to get an overview of the current understading of the similarities and difference between these two diseases, as well as the evolving perception of NMOSD and its diagnosis. Therefore the next chapter will give an overview of NMOSD and MS, from their key characteristics to the usefulness of MR techniques for diagnosis purposes and gaining a better understanding of the underlying disease mechanisms.

Chapter 2

From Devic's disease to neuromyelitis optica spectrum disorders (NMOSD): the evolving face of a complex disease

2.1 Main characteristics of NMOSD and how they compare to MS

Neuromyelitis optica (NMO), like multiple sclerosis (MS), is an inflammatory disease causing demyelination of the central nervous system. It is characterised by optic neuritis (ON) in at least one eye and acute myelitis, happening either simultaneously or more commonly sequentially[1-4]. Unlike MS, it can be both monophasic (optic neuritis and myelitis occurring either simultaneously or within of short period, without any suggestion of recurrence) or relapsing, but seldom secondary progressive. However, the monophasic course is infrequent (<10% to 20% depending on studies findings[1-3]), while the clinical characteristics of the relapsing-remitting course is very similar to MS. It is also extremely rare, with incidence ranging from 0.053 to 0.4 per 100,000 people and prevalence from 0.51 to 4.4 per 100,000 people[5,6], with estimates that NMOSD account for about 0.5% to 1% of patients seen in MS clinics[4]. A good illustration of its rarity is the number of NMOSD patients in the UK in 2013: 400[8]. This scarcity of patients also makes the disease much more difficult to study.

The similarities with MS makes NMOSD difficult to diagnose, but there are also some key differences between these two diseases that make an early accurate diagnosis crucial, including the fact that NMOSD is much more aggressive, with a very small percentage of patients (24%[1]) making a full recovery after the first attack, an average that goes down to 17% when all attacks are taken into account[1]. Optic neuritis in particular is much more severe, leaving a much larger proportion of NMOSD patients with serious visual

impairments: after a median of 7.7 years from disease onset, 60% of NMOSD patients experience either unilateral or bilateral blindness, compared to only 4% of MS patients after 15 years[9]. Furthermore, bilateral ON (either simultaneously or sequentially) is much more prevalent in NMOSD patients. Another difference is that in NMOSD the posterior parts of the optic nerve, including the optic chiasma are also more often affected than in MS[10].

Further dissimilarities are found at the level of disease progression, which is more rapid in NMOSD than MS: if not treated, more than 50% of NMOSD patients will be either suffering from severe visual loss in in one or both eyes or requiring ambulatory help within 5 years from onset, while the survival rate over the same period can be as low as 68%[11]. An accurate diagnosis leading to early treatment can greatly reduce these numbers, as shown in a retrospective study of AQP4- and AQP4+ NMOSD patients who received immunosuppressant therapy at the Mayo Clinic. The following estimates for what would be expected 5 years after onset are given by Jiao and colleagues: 28% of AQP4- and 22% of AQP4+ patients were expected to need a cane to walk, while no AQP4- and only 8% of AQP4+ cases were likely to be restricted to a wheelchair[12].

Furthermore, immunosuppressant therapy also led to a sharp decline in the relapse rate: for AQP4+ patients, the annual average was 2.2 (SD: 2.7) relapses for untreated patients vs 0.7 (SD: 0.9) for those on therapy (p=0.0001). Interestingly, this difference was much lower in the AQP4- group, with an average annual relapse rate of 2.1 (SD: 2.7) while not on therapy vs 1.0 (SD: 1.6) on therapy (p=0.44)[12]. As will become clear below, there appear to be quite a few differences between AQP4- and AQP4+ patients. Independently of serostatus, Jiao and colleagues findings clearly illustrate the importance of an accurate diagnosis, something which remain a pressing issue, since according to Jarius and colleagues[1], 20% of patients are wrongly diagnosed with MS before getting a NMO diagnosis. This not only means potential delays in patient receiving the correct treatment, but also exposes them to the risk of being treated

with interferon-β, natalizumab, or fingolimod, which appear to aggravate NMOSD activity, in particular increasing the recurrence of relpsases[4,13,14].

There are however some obvious differences between the two diseases that should be mentioned. One of them is the age at onset, as NMOSD patients are on average 10 years older than MS ones, with a mean age at onset around 40 for NMO and 30 for MS[1,15]; another is the female to male ratio (2:1 in MS, 9:1 in NMO[16]), but these ratios can vary quite a lot: from 2:1 to 10:1[4]. Wingerchuk also mentions the fact that it had been suggested that NMOSD is proportionally more common in patients of non-white ancestry, such as African American, Afro-Caribbean and Asians, and that a percentage of cases of Asian 'optic-spinal MS' are likely to be NMOSD, but he argues that further population-based data is required to establish this as a fact; particularly since the prevalence and incidence rates reported across various populations worldwide are relatively similar[4]. A view shared by the authors of two reviews looking at the prevalence and incidence of NMOSD[6,17], and certainly backed up by the fact that the prevalence of 4.4 per 100,000 people mentioned above was in Denmark, with the population studied predominately white[6].

There are also some clinical characteristics that differ between MS and NMOSD, such as the extended spinal lesions spanning three or more vertebral segments, known as longitudinally extensive transverse myelitis (LETM) compared to shorter lesions of mostly one vertebral segment in MS[4], which will be discussed in details in the diagnosis section below, but first it would be useful to look at how our understanding of NMOSD changed over time.

2.2 A brief history of NMOSD

The term neuromyelitis optica, initially neuromyelitis optica acuta, is the translation of the Fench term *neuro-myélite aigüe* coined by the French neurologist Eugène Devic (1858-1930), who together with his student, Fernand Gault (1873-1936) described a novel syndrome combining severe transverse myelitis and optic neuritis (Devic presented a paper at the *Congrès Français de Médecine*, while Gault published his doctoral thesis, both in 1894). Devic's

paper was based on the study of 16 cases in whom he found both acute myelitis and optic neuritis, which he felt justified the creation of a new syndrome. Devic's paper will also lead to the disease being renamed after him, as Devic's disease, following a suggestion made by the Turkish physician Peppo Acchioté (1870-1916) in a paper on a case of NMO he presented at the *Société de Neurologie de Paris* in 1907. As Jarius and Wildemann note, Acchioté's choice of the term *maladie* (disease) when proposing the new name departed from Devic's use of *syndrome* or *type clinique* rather than disease[18]. This is not just a detail of historical interest, but one among many variants that are encountered when looking at how NMOSD has been defined over time.

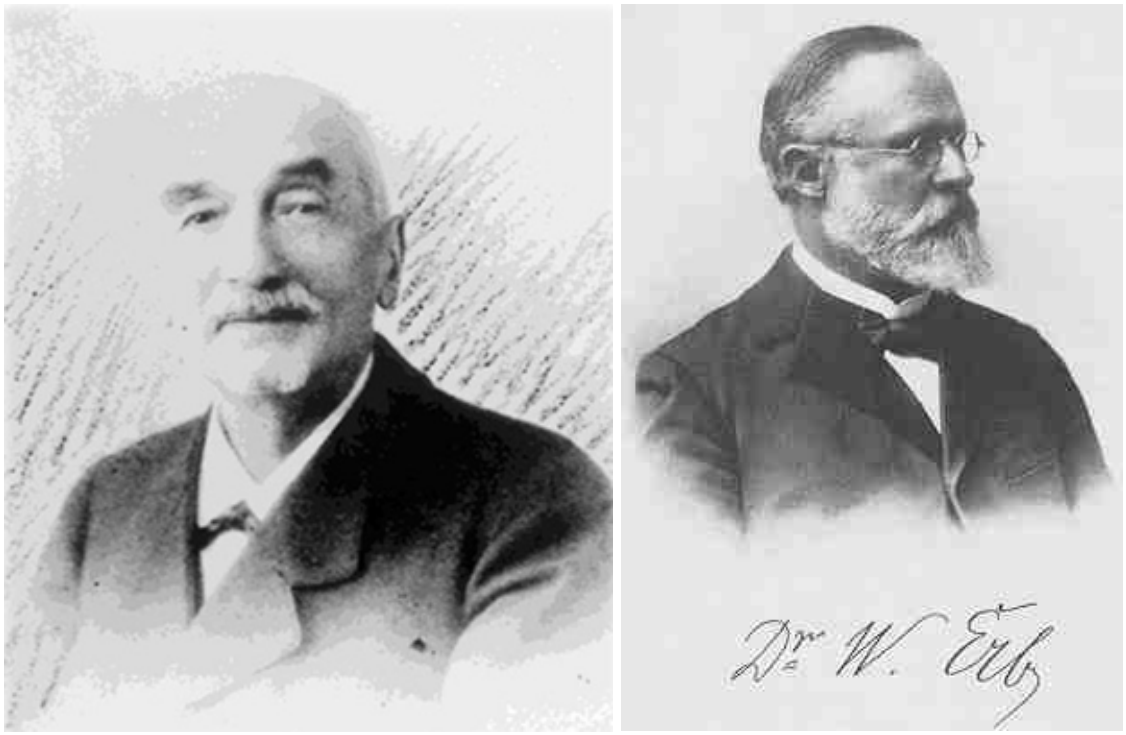

Figure 2-1 Eugène Devic (1858-1930) who named NMO and Wilhelm Heinrich Erb (1840-1921), whose report published in 1880 triggered interest among neurologists and ophthalmologists about the rare syndrome that will become known as neuromyelitis optica (Anonymous photographs, open source).

Interestingly, while Devic may be the first to have given a name to the combination of transverse myelitis and optic neuritis, his paper was not the first description of NMOSD. The first account of a patient with visual loss and spinal cord inflammation was also published by a French anatomist and pathologist, Antoine Portal (1742–1832) in 1804[19], while a potential 'neuroencephalitis optica' (another disease which was thought by Gault to have similarities with NMO) was published in 1829, in the second enlarged edition of John

Abercrombie's (1780–1844) *Pathological and Practical Researches on Diseases of the Brain and Spinal Cord*, in which he describes a case of intractable vomiting, relapsing visual loss, and spinal pain, all of which are key features of NMOSD[4,18]. Jarius and Wildemann list three more reports predating Devic's paper. The first one is by the Genoese physician Giovanni Battista Pescetto (1806–1884), who described a case in 1844, the second by the British physician Christopher Mercer Durrant (1814–1901), appeared in the precursor of the *British Medical Journal* in 1850. The third, published in *The Lancet* in 1862, was by the British neuroanatomist, neuropathologist and neurologist Jacob Augustus Lockhart Clarke (1817–1880). His report is a good illustration of how early recordings of what is likely to be NMO cases used a wide array of designations, as his paper was entitled 'On a case of paralysis', but described a patient with both bilateral optic neuritis and longitudinally extensive transverse myelitis[20]. Another interesting paper was published in 1870, 24 years before Devic coined the term neuromyelitis optica, by Thomas Clifford Allbutt (1836-1925). In it, he reports cases of changes in the optic nerve following spinal injuries (never the other way round), and while he wrote 'I have never seen true optic neuritis with active proliferation as a sequel of spinal disease'[21], one of the patients described had acute myelitis with an eye disorder, which subsequently created an interest for NMO among neurologists and ophtamologists[18]. Jarius and Wildemann also mention some papers published in the early 20th century as the first accounts using the term neuromyelitis optica or acute optic neuromyletis, while a neurological textbook by William Richard Gowers (1845-1915) published in 1904 included a report on the disease, but without using the term neuromyelitis[18].

However, the report which eventually led Devic to coin the term *neuro-myélite aigüe* was published in 1880 by the German neurologist Wilhelm Heinrich Erb (1840-1921): the interest it elicited among neurologists and ophthalmologists, led to the publications of more than a dozen of reports of similar cases. These papers were later collected and summarised by Devic and Gault, and used to corroborate their own cases of the new syndrome as Devic called it[20].

However, even with a name, the concept of NMO, as it was then called, kept changing throughout the 20th century. As Jarius and Wildemann note, certain descriptions excluded some of the criteria which are now known to be typical of the disease, such as a relapsing course, unilateral optic neuritis, symptoms other than optic neuritis and transversal myelitis (even though Devic and Gault described brainstem lesions in some of their patients)[18]. Throughout the 20th century, there was also uncertainty about whether NMO was a distinct disease, as Devic and Gault believed, or a subtype of MS as Russell Brain concluded in 1930[18]. The latter view was also the one adopted by neurological textbooks such as *McAlpine's Multiple Sclerosis* (3rd ed., 1998), *Merrit's Neurology* (10th ed., 2000) and *Adams and Victor's Principles of Neurology* (6th ed., 1997)[22], while a study conducted by O'Riordan and colleagues in 1996 to clarify this issue concluded that NMO is indeed a separate disease[23]. The latter were proven correct in 2004, when Lennon and colleagues discovered an NMO specific antibody, the auto-antibody neuromyelitis optica immunoglobin G (NMO-IgG) which binds to the antigen aquaporin-4 (AQP4)[24].

2.3 Neuromyelitis optica immunoglobin G (NMO-IgG)

The discovery of NMO-IgG and the subsequent development of very accurate tests for its detection, brought a very significant increase in correct diagnosis (according to Jarius[1], 54.2% of patients were misdiagnosed with MS before the test became available in 2005). The early tests using enzyme-linked immunosorbent assay (ELISA) were prone to false positive and had a limited sensitivity, but the cell-based assays which replaced them are more sensitive as well as highly specific (97%). They also increased AQ4-IgG detection rates to nearly 90% compared to 56-68% for non-cell based assays[10,25], subsequently increasing the percentage of seropositive NMOSD patients to 80-90%. However, since testing for NMO-IgG/AQ4-IgG is recommended only in the cases where NMOSD is suspected, other diagnosis tools are necessary[26], including radiological features, making MR techniques crucial for diagnosis as will become clear below.

Furthermore, there has been suggestions that there may be differences between seropositive and seronegative patients. A study by Jarius and colleagues[1] involving 175 patients found that seronegative patients were more likely to be monophasic, while a study by Kiyat-Atamer and colleagues found that seronegative patients had significantly more brain lesions at onset, but that this difference disappeared at follow-up since seropositive were also developing brain lesions as the disease progressed[27]. A recent review of the existing literature by Bernard-Valnet and colleagues concluded that these patients form a distinct subpopulation, with what they describe as the classical Devic syndrome and warn of the danger of such patients being reclassified as MS[28]

2.4 Myelin oligodendrocyte glycoprotein (MOG)

There is another antibody, myelin oligodendrocyte glycoprotein (MOG), which has been detected in approximatively 10-15% of AQ4-IgG negative patients. These patients differ from the AQ4-IgG ones in that bilateral optic neuritis is more common, but they also appear to respond particularly well to steroid treatment[29-31]. Interestingly, a paper by Zamvil and Slavin raises the question whether MOG positive patients with bilateral optic neuritis should really be classified as NMOSD, arguing that the term MOG Ig1 AQP4-seronegative NMOSD is particularly disconnected from our current understanding of NMOSD as an astrocytopathy[32]. Pittock raised a similar issue in a paper discussing the use of clinical and radiological criteria, rather than molecular ones, as the basis of a NMOSD diagnosis. He argues that this approach could potentially lead to the risk of grouping together various disorders with heterogeneous aetiologies, clinical courses, prognoses as well as responses to treatment[33].

The complexity of correctly classifying MOG positive patients is further illustrated in a very thorough study published by Jarius and colleagues in September 2016[14]. They look at the clinical, radiological and serological criteria of 50 MOG positives patients with either both ON and myelitis (44%), only ON (40%) or only myelitis (12%). The remaining 2% had other symptoms, mostly

brainstem involvement (found in nearly 30% of the cohort, so mostly associated with other symptoms). When they look at diagnoses, 33% of the cohort met the 2010 McDonald criteria for MS, 28% Wingerchuk's 2006 revised diagnostic criteria for NMO and 32% the 2015 international consensus criteria for NMOSD, with 16% patients fulfilling the criteria for both diseases. Their conclusion is that since there is a substantial phenotypic overlap with both AQP4-IgG-positive NMOSD and MS, which suggests that all MOG-positive patients belong to the same immunopathogenetically defined disease spectrum, MOG-positive patients should not be included in the AQP4-IgG-negative NMOSD group. They even argued that MOG-IgG seropositivity should be used as an exclusion criteria. The debate on the place of MOG-IgG seropositivity in NMOSD is obviously ongoing, and while it falls beyond the spectrum of this thesis, it is something that needs to be investigated further.

2.5 NMOSD diagnosis criteria: an evolving story

As can be expected with the changing perception of the disease, diagnosis criteria have also been evolving. The latest diagnosis criteria, published in 2015, produced by the International Panel for NMO Diagnosis (IPND)[34] was reviewing the criteria proposed by Wingerchuck and colleagues in 2006[35], which itself was a revision of the 1999 diagnosis criteria also proposed by Wingerchuck and colleagues[11]. While the 2006 revision was needed following the discovery of the NMO-IgG antibody, the latest criteria reflect the current understanding of the disease in all its complexity and heterogeneity. It also abandons the term NMO, replacing it with neuromyelitis optica spectrum disorders (NMOSD), using NMOSD with AQ4-IgG for seropositive patients and NMOSD without AQ4-IgG for seronegative ones. The concept of a broader spectrum named NMOSD, used for patients with atypical clinical presentations, was first described in a 2007 paper by Wingerchuck and colleagues[16]. It follows the suggestion they made in the conclusion of the diagnosis paper that the concept of pure NMO should be abandoned because their data revealed a wide

array of neurological symptoms preceding or accompanying NMO, which were not necessarily associated with a recognisable CNS lesion[35]

Tables 2.1 & 2.2, adapted from Bennet's paper on the evolution of NMO diagnosis[7], give the criteria and methodology used for each classifications. Optic neuritis and transversal myelitis remain crucial clinical features throughout, as do the spinal cord lesion extending over three vertebral segments detected by MRI, while criteria such as bilateral optic neuritis or severe vision loss are no longer deemed to have sufficient diagnostic sensitivity[7]. After the discovery of AQP4-IgG, the revised diagnosis had one absolute requirement, which was the simultaneous or sequential occurrence of optic neuritis and transversal myelitis, together with 2 of 3 supporting criteria (brain MRI inconsistent with MS, MRI spinal cord lesion extending over three or more vertebral segments and AQP4-IgG positivity). These criteria also improved both the sensitivity and specificity of the 1999 diagnosis, with a sensitivity of 94% and a specificity of 96% compared to 85% and 48% for the 1999 criteria[35].

The latest diagnosis criteria were formulated by an International Panel for NMO Diagnosis (IPND), are based on clinical, neuroimaging and neurophysiological data as well as laboratory testing. As mentioned above, the panel also decided to adopt the term NMOSD together with the specification of the patient serostatus. For a diagnosis of NMOSD with AQP4-IgG, at least one of core clinical characteristics, which include syndromes such as such as area postrema syndrome and acute brainstem syndrome, as well as optic neuritis and myelitis (see **Table 2.1** for the full list) is needed, together with the exclusion of any alternative diagnosis. For a diagnosis of NMOSD without AQP4-IgG or in the cases where the AQP4-IgG status is unknown, at least two core clinical characteristics occurring as a result of one or more clinical attacks and meeting a list of specific requirements (also listed in **Table 2.1**), which include data from brain and spinal cord MRI, are needed[34]. In order to avoid the risk of misdiagnosis in the absence of AQP4-IgG seropositivity, the panel also emphasised the importance of a list of so-called 'red flags' detailing findings

atypical for NMOSD incorporating clinical features and laboratory findings as well MRI characteristics for both the brain and the spinal cord[34], one of which is cortical lesions.

Diagnosis criteria		
Wingerchuk 1999 NMO Criteria	**Wingerchuk 2006 NMO Criteria**	**IPND 2015 NMOSD Criteria**
All absolute criteria and 1 major or 2 minor supportive criteria **Absolute criteria** 1 Optic neuritis 2 Acute myelitis 3 No evidence of clinical disease outside optic nerve or spinal cord **Supportive criteria** *Major* 1 Negative brain MRI at onset 2 Spinal cord MRI with lesion extension over 3 vertebral segments 3 CSF pleocytosis of 50 WBC/mm or 5 neutrophils/mm *Minor* 1 Bilateral optic neuritis 2 Severe optic neuritis with fixed visual acuity worse than 20/200 in at least one eye 3 3. Severe, fixed, attack related weakness (MRC grade 2) in one or more limbs	All absolute criteria and 2 supportive criteria **Absolute criteria** 1 Optic neuritis 2 Acute myelitis **Supportive criteria** 1 Contiguous spinal cord MRI lesion extending over 3 vertebral segments 2 Brain MRI not meeting diagnostic criteria for MS 3 AQP4-IgG–seropositive status	**NMOSD with AQP4 IgG** 1 At least 1 core clinical characteristic 2 Positive test for AQP4IgG using best available detection method* 3 Exclusion of alternative diagnoses **NMOSD without AQP4 IgG** 1 At least 2 core clinical characteristics occurring as a result of one or more clinical attacks and meeting all of the following requirements: a) At least 1 core clinical characteristic must be optic neuritis, acute myelitis with LETM, or area postrema syndrome b) Dissemination in space (2 or more different core clinical characteristics) c) Additional MRI requirements, as applicable 2 Negative tests for AQP4IgG using best available detection method* or testing unavailable 3 Exclusion of alternative diagnoses **Core clinical characteristics:** Optic neuritis; acute myelitis; area postrema syndrome (hiccups; nausea and vomiting); acute brainstem syndrome; symptomatic narcolepsy or acute diencephalic clinical syndrome with NMOSD typical diencephalic MRI lesions (Figure 2.2); symptomatic cerebral syndrome with NMOSD typical brain lesions (Figure 2.2) *AQP4IgG serology: Cell-based assay is strongly recommended
AQP4IgG: anti–aquaporin4 immunoglobulin G; CSF: cerebrospinal fluid; IPND: International Panel for NMO Diagnosis; LETM: longitudinally extensive transverse myelitis; MRC: Medical Research Council; MRI, magnetic resonance imaging; MS: multiple sclerosis; NMO: neuromyelitis optica; NMOSD: neuromyelitis optica spectrum disorder; WBC: white blood cell		

Table 2-1 Historical classification of Neuromyelitis Optica and Neuromyelitis Optica Spectrum Disorder (Adapted from Bennett, 2016[7]).

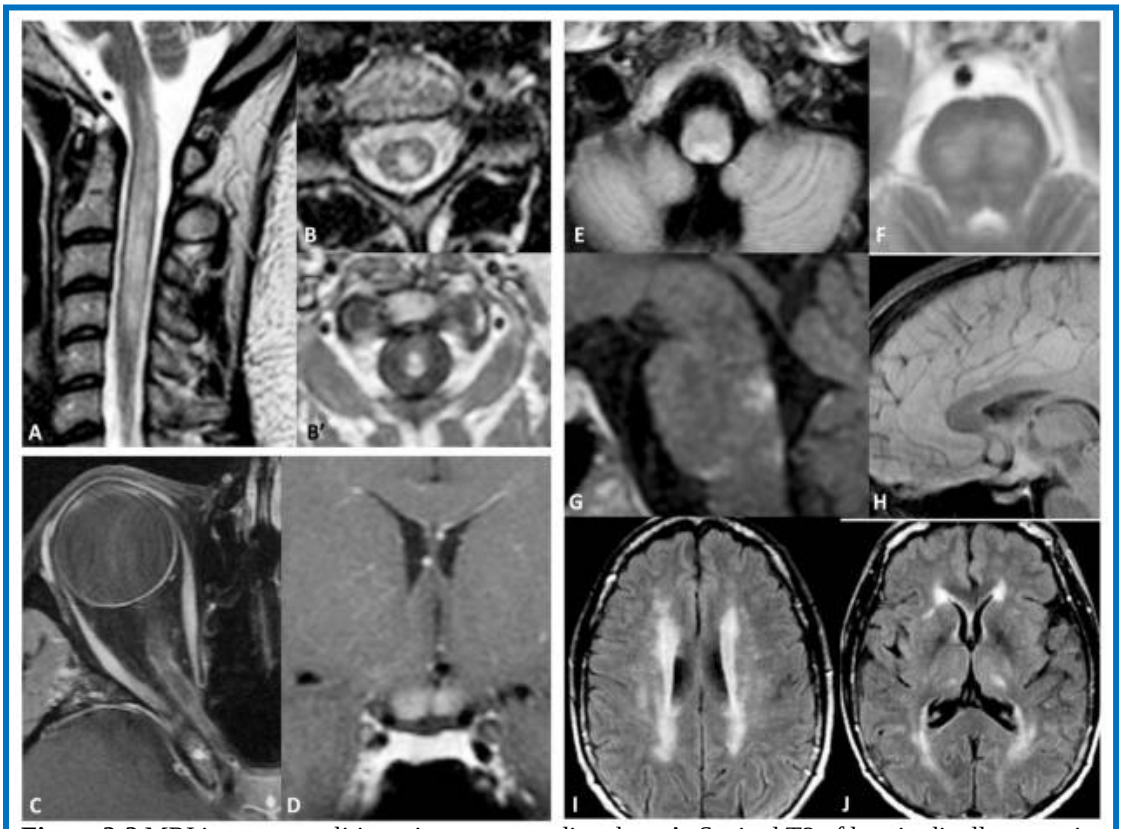

Figure 2-2 MRI in neuromyelitis optica spectrum disorders. A. Sagittal T2 of longitudinally extensive cervical cord lesion extending into dorsal medulla. B. T2 and B′. post-contrast T1 of central spinal cord lesions. C. Post-contrast T1 of an extensive enhancing lesion of the optic nerve. D. Post-contrast T1 of bilateral prechiasmal and chiasmal optic nerve inflammation. E. Bilateral FLAIR lesions involving the dorsal medulla (area postrema). F. Bilateral confluent T2 lesions in mid-pons. G. Sagittal FLAIR of periependymal lesions around the 4th ventricle. H. Sagittal FLAIR image of diffuse hypothalamic inflammation. Axial FLAIR images of bilateral, confluent deep white matter (I, J) and thalamic (J) lesions. (Adapted from Bennett, 2016[7]) Reproduced with permission from Wolters Kluwer Health, Inc.

Methodology		
Wingerchuk 1999 NMO Criteria	**Wingerchuk 2006 NMO Criteria**	**IPND 2015 NMOSD Criteria**
Criteria were defined by chart analysis of the clinical, radiologic, and laboratory data from 71 patients with NMO at the Mayo clinic; there was no independent validation cohort	Criteria were defined by the evaluation of data from 129 patients ascertained through the Mayo Clinic MS Centres in Rochester, MN, and Scottsdale, AZ, and tested for NMO IgG; there was no independent validation cohort	Criteria were developed by an 18 member panel of NMO physicians from 9 countries; working groups in clinical presentation, neuroimaging, laboratory studies/serology, paediatrics, systemic autoimmunity, and opticospinal MS conducted systematic literature reviews, and initial characteristics for NMOSD were rated and further refined by panel members using electronic surveys and clinical vignettes; those characteristics endorsed by a two thirds majority were used to develop criteria for AQP4IgG-seropositive and AQP4IgG-seronegative NMOSD

Table 2-2 Historical classification of Neuromyelitis Optica and Neuromyelitis Optica Spectrum Disorder: methodology used (Adapted from Bennett, 2016[7])

Bennett also notes the greater sensitivity of the new diagnosis criteria, both for identifying AQP4-IgG negative patients and faster detection of AQP4-IgG positive ones, enabling treatment to be started earlier[7].

Clearly, MRI plays an important role in the diagnosis of NMOSD, especially with the new criteria. The next section will be a brief overview of key findings which led to the inclusions of these features.

2.6 Usefulness MRI to distinguish between NMOSD and MS

2.6.1 Spinal cord

Extensive lesions resulting from LETM are one of the most commonly cited radiological difference between MS and NMOSD, but as Wingerchuk notes, such lesions may break into smaller non-consecutive lesions or even disappear completely over time[4], so unless MRI scans acquired during the acute phase are available, this feature may not be an entirely reliable an indicator. Furthermore, the percentage of patients with such lesions varies from 64% to 93% (found in the largest cohort)[1,36-38], while short transverse myelitis (STM) lesions have also been found in some patients[39]. The distribution of lesions is also extremely variable: only two studies found cervical cord spinal lesions in all NMOSD patients[40,41], in the others the percentage of patients with this type of lesions varies from less than 30%[42] to 87%[43], while thoracic spine lesions are less common in NMOSD: Jarius and colleagues found them in 20% patients[1] and Cabrera-Gómez in 26% of NMOSD patients[42]. On the other hand, hypointense lesions appear to be specific to NMOSD patients[40,44].

Wang and colleagues also looked at spinal cord atrophy (SCA) and its impact, and found an interesting association between atrophy and the localisation of lesions in NMOSD patients: of those with SCA, 87% had lesions in the cervical spine but only 13% in the thoracic spine, while in those without SCA, 48% had cervical lesions and 38% thoracic ones. Furthermore, they also found that the presence of SCA was independent of longitudinally extensive transverse myelitis (LTEM)[45].

The application of dMRI techniques to the spinal cord led to the detection of further differences between NMOSD and MS: fractional anisotropy (FA) and axial diffusivity (AD) were found to be significantly reduced in lesions and in upstream/downstream sections in both MS and NMOSD, while mean diffusivity (MD) and radial diffusivity (RD) were significantly increased. These changes were also found to be significantly larger in NMOSD when compared to MS[41,44,46,47]. Looking at 'unaffected' tracts, Klawiter and colleagues also found a decrease in FA and an increase in RD in MS patients, but no changes in NMO patients[47]. Another study, which looked at the different columns in C2 and C7, found highly localised increases in FA and RD wich were also significantly higher in MS than in NMOSD[48]. Looking at specific type of lesions as potential biomarkers is commonly explored, but not always successfully as a recent study looking at ring-enhancing lesions: while it differentiated NMOSD from other causes of LETM, they were not significantly different from MS[49]. There is however a study by Yonezu and colleagues who discovered a type of lesions they describe as "bright spotty lesions" which were nearly exclusively found in NMOSD patients[50].

2.6.2 Brain and visual pathways

The different parts of the visual pathways have been extensively studied as abnormalities have been reported in both diseases from the 19th century onward. However, beyond the fact that the optic chiasm appeared to be affected solely by NMOSD, no further significant differences between the two diseases were found[51,52]. A study looking at patients during the acute phase of optic neuritis found that longitudinally extensive optic neuritis (LEON), defined as an acute gadolinium enhancing lesion extending for at least 17.6 mm, could help differentiate between the diseases as it is much more common in NMOSD than MS (81% vs 23%)[53] while another study also looked at the extent of inflammation on the optic nerve and found that lesions were both more extensive as well as involving the more posterior part of the visual pathway (from the cranial section of the optic nerve to the optic tract)[54]. Finally, dMRI

studies also found increased MD and decreased FA in the optic radiation in NMOSD patients when compared to healthy controls[55-57], further supporting a greater involvement of the posterior section of the visual pathway as a characteristic of NMOSD.

2.6.3 Brain

MRI studies of the brain have been of particularly useful in extending the diagnosis criteria for NMOSD. While the 1999 criteria had 'No evidence of clinical disease outside optic nerve or spinal cord' as an absolute criteria, the 2006 diagnosis had 'Brain MRI not meeting diagnostic criteria for MS' as a supportive criteria. The 2015 criteria include a whole list of neuroimaging characteristics encompassing the brain as well as the spinal cord and optic nerve and including descriptions of the types of brain lesions typical of NMOSD[34]. These characteristics were previously reported in many studies using conventional MR techniques, which detected either brain abnormalities or lesions in 20% to 70% of NMOSD patients. Overall, the majority of lesions detected tend to be non-specific and are mostly found in deep white matter, with the following regions most commonly reported as locations of abnormalities: corticospinal tract (in particular the posterior limb of internal capsule)[55-59], periventricular areas[42,55,57,60,61] and the medulla[55,58,61-63], all of which are now included in the latest NMOSD diagnosis criteria. However these localisations are also common in MS, therefore the appearance of lesions and other signs are necessary to differentiate between the two diseases. Among possible additional markers, Sinnecker and colleagues looked at the position of lesions in relations to veins and found that while MS lesions are nearly exclusively centred on small veins, this rarely happened in NMOSD[64]. These finding were reproduced by Dr Rosa Cortese using the SWI data from the same cohort of patients used for this thesis[65].

Further evidence of the usefulness of combining location and lesions appearance comes from a study by Lu and colleagues, which looked at lesions in the brainstem and found that only those located in the pons and medulla were

significantly different between MS and NMOSD, but that the lesions appearance could be a potential marker, as in MS they had well defined margins while in NMOSD the margins were poorly defined[66]. Variations in appearance and shape of lesions have been suggested as potential markers by other studies, but need to be applied carefully since, as Matsushita and colleagues report, some overlap between the two disease remains common: they found ovoid lesions in more than 80% of MS patients but also in more than 30% of NMO ones[67].

As is made clear by the new diagnosis criteria, NMOSD patients often have lesions located in specific parts of the brain. The medulla is one of this regions where lesions are both more common and more numerous in NMOSD than in MS, as evidence by the large cohort studied by in Jarius and colleagues, in which 26% of NMOSD patients had medullary lesions[1], while a much smaller study Lim and colleagues found some lesions of this type in 1 of the 3 NMO patients who had brain lesions, but none in any of the 36 MS patients they scanned[68]. Interestingly, the hypothalamus is another region where lesions, while rare, appear to be significantly more common in NMOSD than MS[68-70].

It has also been suggested that the absence of cortical lesions or abnormalities in NMOSD patients could be a reliable marker to differentiate the two diseases[36]. However, as it will be explained in **Chapter 5**, which report on the application of phase inversion recovery (PSIR) to look for GM cortical lesions in both MS and NMOSD, this is very much an open issue. Five studies applying a variety of techniques: from VBM to measure atrophy[71], to DIR[36] and MR spectroscopy[72], as well two which used a 7T scanners[64,73], failed to detect either lesions or significant changes in NMOSD patients cortical grey matter. Another study by Popescu and colleagues used histology to look at cortical demyelination in NMOSD and did not find any[74]. On the other hand, two studies by Rocca and colleagues, one using fMRI[75] and the other a combination of MTR and dMRI[75] found changes in NMOSD patients cortex when compared to healthy controls. Similarly, Yu and colleagues also found cortical abnormalities when looking at normal appearing brain tissues using dMRI[62] and a study by

Kim and colleagues looking for cortical lesions in NMOSD found some in a small subset of patients[76]. Finally, a study by Saji and colleagues used histology to look at cortical degeneration in NMOSD and did find it. They also confirmed Popescu and colleagues findings that demyelination does not occur in the cortex of NMOSD patients[77].

MTR, dMRI and MR spectroscopy have also been used to look at either normal appearing white matter (NAWM) or specific areas of the brain, but often comparing NMOSD patients to healthy controls rather than MS patients. Using dMRI, multiple studies found reduced FA and increased MD in the corpus callosum, multiple WM tracts, including the corticospinal tract, as well as higher FA in the thalamus and putamen[40,55-57,62,78,79]. This suggests that dMRI could be a useful approach, particularly with new techniques such as neurite orientation dispersion and density index (NODDI), which was assessed on MS patients as part of this thesis (**Chapter 4**). For MTR, besides the study looking at GM mentioned above, there are only two additional studies, possibly because neither found any significant difference between NMOSD patients and healthy controls when looking changes in normal appearing brain tissues[79,80], while a significant decrease in MTR was found in MS patients brain when compared to healthy controls by Filippi and colleagues[80]. As these studies were done on 1.5T scanners, it would be interesting to do a new study on 3T or even 7T scanner to see if the increased signal yields different results. Last but not least, there had been four studies using MR spectroscopy: two looked at NAA in NMOSD patients and compared them to healthy controls without finding any differences between the two groups[81,82]. The third study, by de Seze and colleagues, looked myo-inositol as well as NAA and choline, but again failed to detect any significant difference between NMOSD and healthy controls[72], while the last study, by Aradi and colleagues, looked at differences for glutamate/glutamine, creatine as well as NAA, choline and myo-inositol in WM lesions compared to healthy controls. They only found significant differences for NAA and myo-inositol[83].

Finally, cognitive decline in NMOSD patients is an aspect of the disease in which there currently is a lot of interest as no less than 18 studies have been published since 2008, which was also the first study looking at this topic. Quite a few are case studies (5) and one is a systematic review, but of the remaining 11, 8 are combining cognitive assessments with MRI. The most interesting paper when looking at the differences between MS and NMOSD is the systematic review and meta-analysis done by Meng and colleagues, which looked specifically at studies comparing cognitive impairment (CI) between NMOSD and MS patients and concluded that none of them found a significant difference between the two groups[84]. As they note, most studies are comparing NMOSD patients to healthy controls. Of the studies combining MRI and cognitive assessments, all found some degree of impairment in NMOSD patients when compared to healthy controls, but not all of them found correlations between the abnormalities detected on the MRI scans and the impairments measured. As mentioned above, Kim and colleagues detected cortical thinning in NMOSD, as well as CI in NMOSD patients, but did not find correlations between the two[76], similarly Liu and colleagues also found both CI and brain abnormalities when using a multimodal MR approach, but they did not find any correlation between cortical thickness and CI. They did however find correlations between specific brain regions and the *z* scores calculated from the cognitive assessments[85]. Other studies that found correlations include one done by Blanc and colleagues which used voxel based morphometry (VBM) to detect focal brain atrophy and found correlations between some areas and specific cognitive assessments[86]. Similar results were obtained by He and colleagues using dMRI[87] as well as by Wang and colleagues when making comparison between CI and grey matter volumes (both cortical and deep grey matter)[88].

This brief overview of the type of studies done using MR techniques to look at various aspects of NMOSD clearly demonstrates both the scope and versatility of MR approaches, which are further enhanced through the development of new

MR acquisition protocols as well as analysis techniques. The next chapter will introduce those techniques which were used for the purpose of this thesis.

Chapter 3

A short introduction to magnetic resonance imaging (MRI) and to the techniques used

3.1 What is Magnetic Resonance Imaging

In order to understand what exactly Magnetic Resonance Imaging (MRI) is, it is worthwhile to look briefly at how it was discovered. In 1945, Felix Bloch and Edward Mills Purcell demonstrated the key properties of the atomic nucleus (using water and paraffin respectively) which are at the heart of MRI. They showed that an oscillating magnetic field influences the orientation of proton spins. This was called nuclear magnetic resonance (NMR).

The next stage occurred in the late 1960s, when Raymond Damadian discovered differences between the NMR parameters of tumours when compared to healthy tissues. The usefulness of this finding was limited by the fact that he could not spatially locate the position of the various tissue types. This problem was solved in 1971, when the chemist Paul Lauterbur realised that NMR signals could be converted into images with spatial information by using gradients for phase and frequency encoding during acquisition. A Fourier transform is then applied to reconstruct the image. Damadian and his group went on to build the first NMR scanner in 1977, and produced the first MR scan of the human body.

As NMR became more widely used for medical purposes, its name was changed. The term ‘nuclear’ was dropped, due to concerns that the public would think that the technique involved harmful radiations, and Magnetic Resonance Imaging or MRI became the new appellation. Since then, MRI has become a very important tool for both diagnosis and research because it offers non-invasive ways to acquire high resolution images, as well as encompassing techniques enabling quantitative measurements of metabolic changes. The fact that it is radiation free means that scans can be repeated when needed in order to follow disease progression, assess recovery or drug effectiveness.

Now we need to look at how MRI actually works, and for this it is necessary to look at physical principles that makes it possible to distinguish between tissue types as well as precisely locate significant changes such as lesions or tumours when looking at the brain (or damage in other parts of the body since MRI is widely used for diagnostic purposes).

3.2 MRI physics: some basic principles

In the brief history of the development of MRI given above, proton spins, magnetic field, gradients, frequency encoding were mentioned. The following sections will explain these terms. A lot of the information used here was taken from Allen D. Elster's Questions and Answers in MRI[1], Chapter 2 of *All You really need to know About MRI Physics* by Moriel NessAiver[2] and 'mri: Physics: For anyone who does not have a degree in physics' by Evert J. Blink[3].

3.2.1 Protons, spins and magnetic field

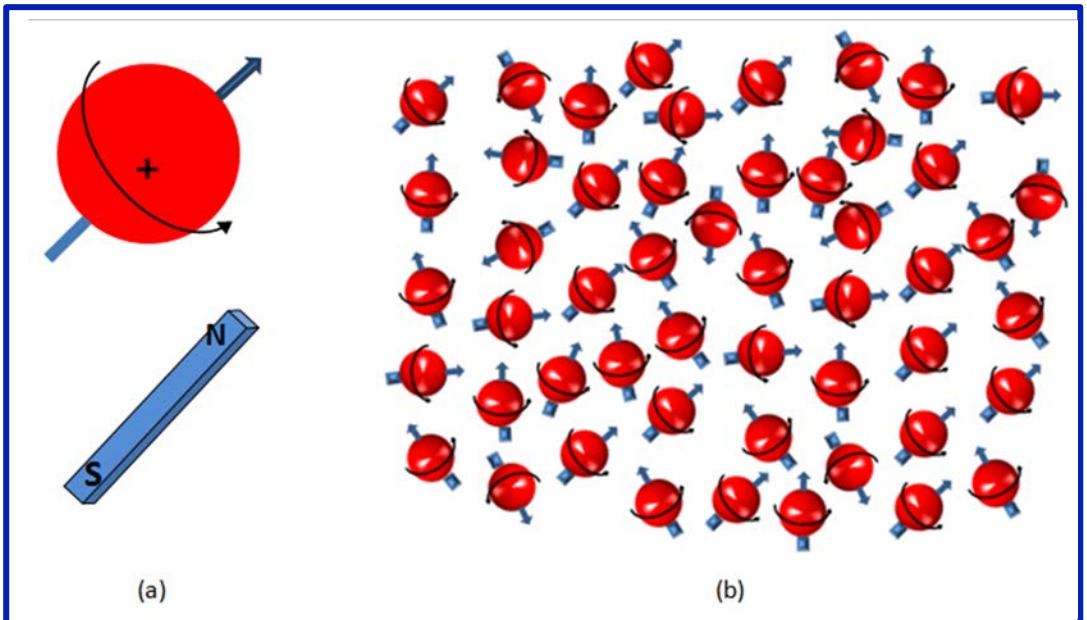

Figure 3-1 (a) Schematic representation of spinning hydrogen atom. (b) Spinning protons with random axes (state of equilibrium) (Fr**o**m Kantzas [et al.][4]). Reproduced with permission from PERM Inc.

Just like the Earth, protons are spinning around an axis (**Figure 3-1a**). Besides, as they have a positive electric charge, the spin, also described as angular momentum, creates its own small magnetic field. As shown in **Figure 3-1b**, when left of their own, the spin axes are randomly aligned. This random

distribution also means that the protons are in an overall state of equilibrium, resulting in a net magnetisation of zero[4]. The protons used for MRI are those from hydrogen atoms in water molecules, ideal as the human body contains on average 60% of water.

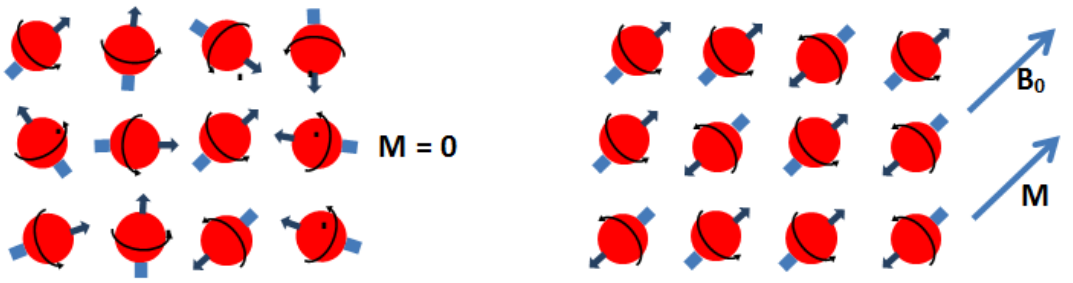

Figure 3-2 Spins lining up in the presence of an external magnetic field (B_0), with the small majority producing the net magnetization vector (M) (From Kantzas [et al.][4]). Reproduced with permission from PERM Inc.

As it can be seen in **Figure 3-2,** when an external magnetic field B_0 is applied, proton spins align either with it (low energy state) or against it (high energy state). The interesting thing is that the two groups are not equal: a small majority of protons, described as the net magnetisation or net magnetisation vector **M** (~$10x10^{-6}$ at 3.0 Tesla), align with the magnetic field. This number may be small, but because of the substantial amount of protons comprised within a single voxel, this small difference means that the actual number of protons aligning with the magnetic field will in fact be very large. This differential amount is directly linked to the external B_0 magnetic field and will therefore be smaller at 1.5 Tesla ($4.5x10^{-6}$) and will become higher with ultra-high-field scanners such as 3T and above. Finally, because such large amounts of protons are involved, quantum mechanics can be mostly ignored when looking into MRI physics, and classical mechanics description applies as what happens at the level of single protons ceases to be relevant in the context of MRI. Similarly, **M** behaves like a regular vector, which is tilted during MRI acquisition as will be explained below.

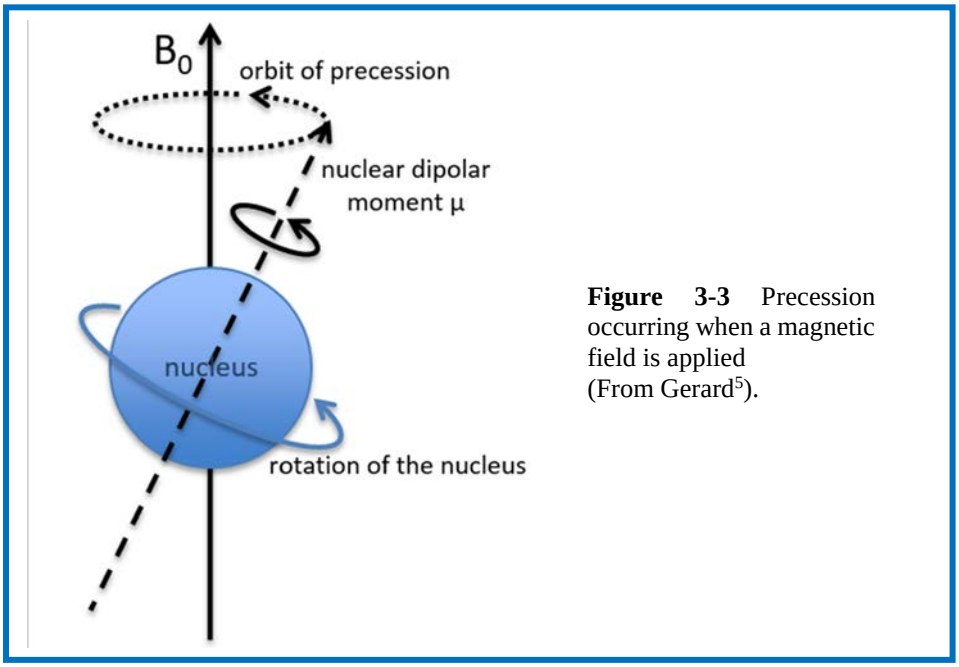

Figure 3-3 Precession occurring when a magnetic field is applied (From Gerard[5]).

The other important thing to know is that this arrangement is not static: the protons also rotate around the axis of the magnetic field while spinning, as shown in **Figure 3-3**. This is called precession and its frequency is directly proportional to the strength of the magnetic field B_0 and the gyromagnetic ratio (a particle-specific constant incorporating size, mass, and spin). It is determined by the Larmor Equation:

$$\omega_0 = \gamma B_0$$

where:

$\boldsymbol{\omega_0}$ is the precessional or resonance frequency, sometimes also called angular frequency, measured in radians per seconds, or cyclic frequency $\mathbf{f_0}$, which is measured in cycles/sec or Hertz [Hz].

$\boldsymbol{\gamma}$ is the gyromagnetic ratio, a constant unique to every atom (42.58 MHz/T for hydrogen).

$\mathbf{B_0}$ is the magnetic field strength (T).

The resonance frequency is proportional to the scanner strength, so for example for a 3.0 Tesla (T) scanner, it will be 42.58 MHz/T x 3.0 T= 127.74 MHz. Conveniently, hydrogen is the atom with the highest gyromagnetic ratio as well as being so widespread in the human body, thus making it particularly suitable as an NMR source[1].

3.2.2 Radio frequency pulse and excitation

In order to acquire images, protons will be first subjected to the external magnetic field until the net magnetisation has reached a steady state of equilibrium, where **M** is aligned with the main magnetic field (B_0), which is always the Z axis in the rotation frame described below.

The next stage is to apply an electromagnetic radio frequency (RF) field at the resonance (Larmor / precession) frequency, which will transfer energy to the protons. As a result, the net magnetisation vector **M** is tilted away from the Z axis, with changes in directions described using a frame of rotation with 3 axes: as mentioned above, the Z-axis is always pointing in the direction of the main magnetic field, while the two other axes, X and Y, are pointing at right angles from Z, as shown in **Figure 3-4.**

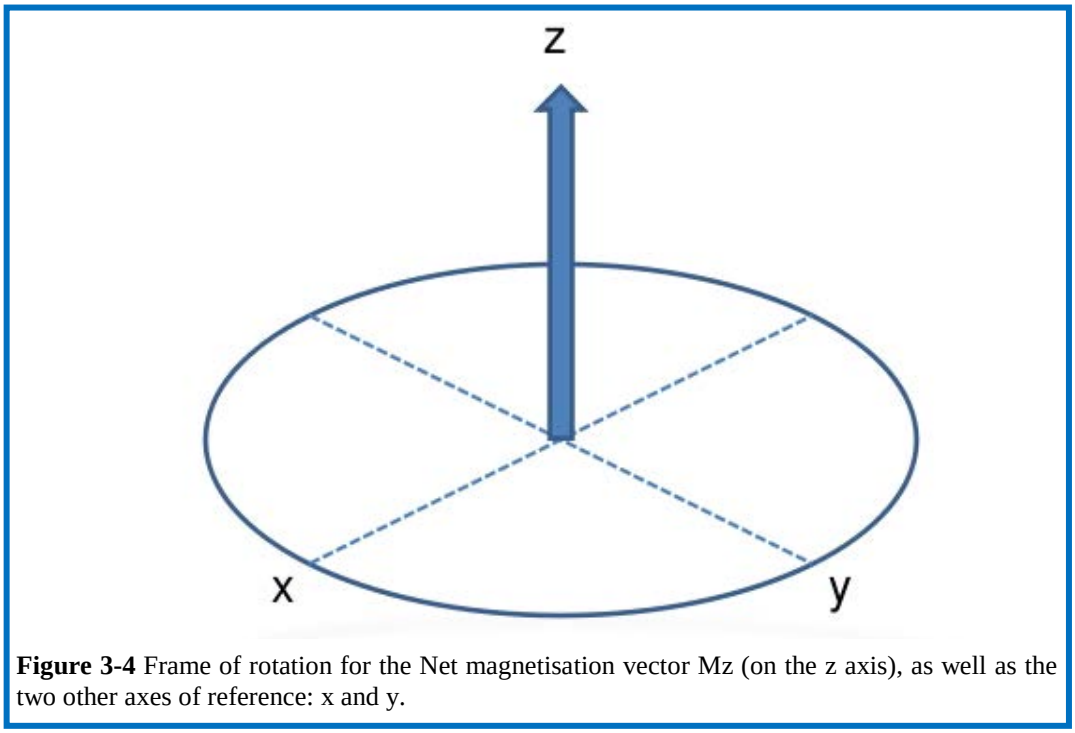

Figure 3-4 Frame of rotation for the Net magnetisation vector Mz (on the z axis), as well as the two other axes of reference: x and y.

The reason why M is tilted after the application of RF field at or near the Lamor frequency is that the effects of B_0 disappear and the precession of M is now locked to B_1, and consequently tipped within the X-Y plane. As **Figure 3-5** shows, the flip or tip angle experienced by M can go all the way to 180º. The flip angle, often represented by the Greek letter alpha α, is determined by both the strength and duration of the RF field/pulse.

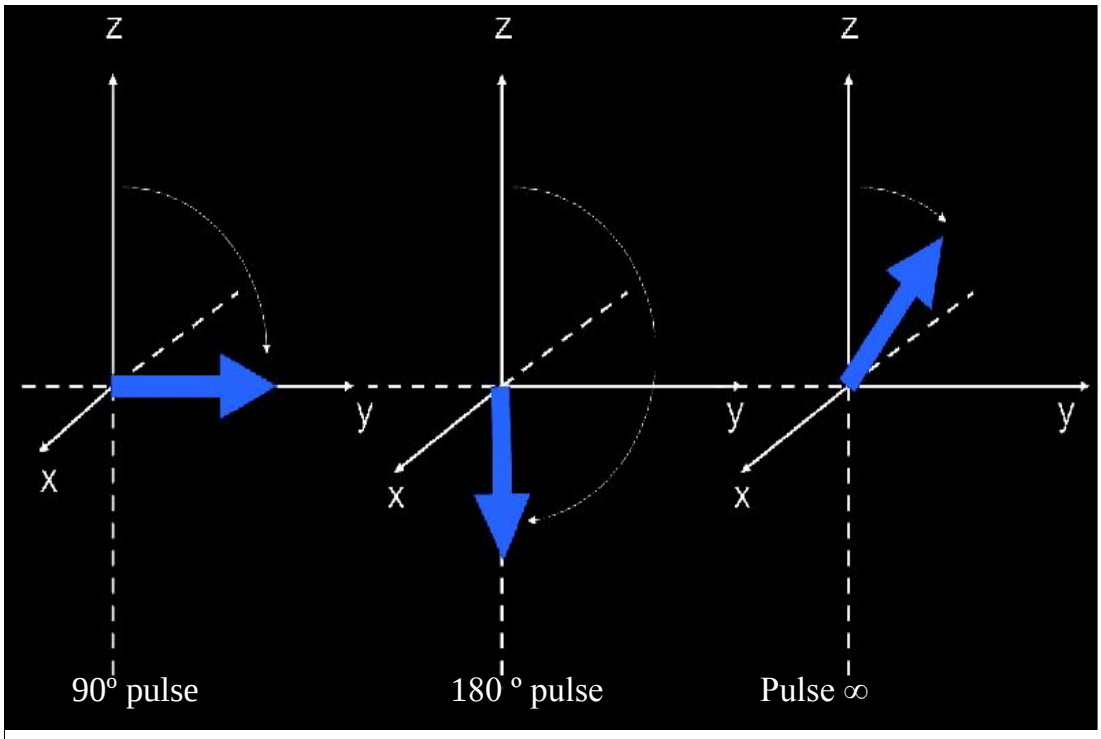

Figure 3-5 Tipping angles with different RF pulse: 90º, 180º and illustrating the fact that M position will be anywhere from 1º to 180º (Adapted from Fonseca[6]). © 2013 Gonçalves Fonseca M .

There are two different frames of reference when descibing what is happening to M. The *laboratory frame* of reference, which can also be described as the one of the external observer and the *rotating frame*, where the observer is inside the frame just like we are on our rotating planet. However, as we cannot leave the earth to experience the laboratory frame, a better analogy is the merry-go-round. Observing things from the laboratory frame is like being on the ground looking at the merry-go-round revolving, while if you are sitting on the merry-go-round watching the world spinning around you, you are inside the rotating frame. For this frame, the coordinate system x', y', z' are used.

The rotating frame is the one used to describe the effects of B_1, since, as can be seen in **Figure 3-6**, you need to be in this frame in order to determine the position of M. This means that when describing the tipping angle or T2 relaxation for example, the axes should be x'-y'-z'. However, to keep things simple, I followed the example of the many authors who use the regular x, y, z at all times.

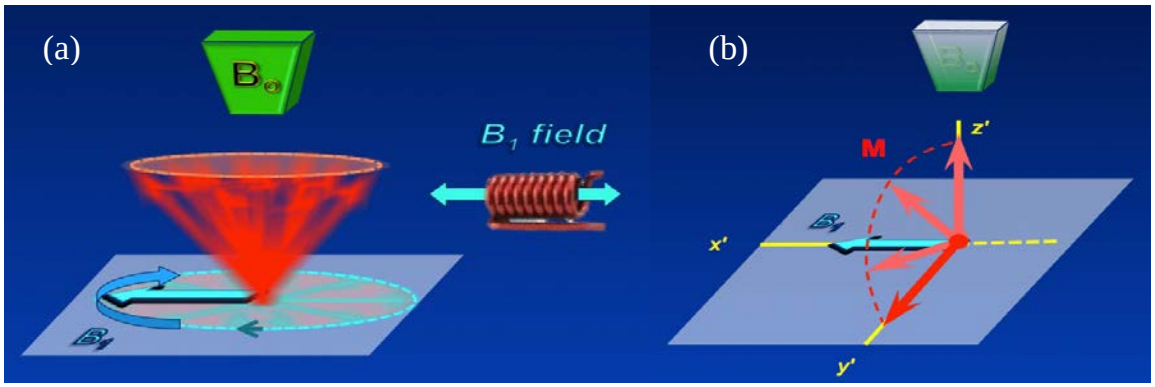

Figure 3-6 The laboratory frame (a) and the rotating frame (b). Viewed from the laboratory frame, the B1 field and spins are all rotating very quickly. The B1 arrow is shown in a fixed position for clarity purposes, but it is actually rotating just as fast as the spins and thus should also be blurred. In the rotating frame, the frame is rotating at the Larmor frequency just as B_1 is. Consequently, this creates a strobe-like, "stop action" image that allows us to model the position of M (Adapted from Elster[1]). Courtesy Allen Elster, MRIquestions.com

3.2.2.1 From excitation to relaxation

The phase during which the magnetisation vector M absorbs energy is described as the excitation phase. The initial position, when M is aligned to B_0, is described as the *longitudinal* magnetisation, while the post-tipping position is called the *transverse* magnetisation. This absorption of energy state caused by B_1 generate the nuclear magnetic resonance (NMR).

When the RF puslse is turned off, the energy absorbed by protons is released in the form of RF waves and M progressively returns to equilibrium, where it is once again aligned to B_0. This process is called relaxation. The RF waves released are the actual source of the MR signal. The process, from the application of the RF pulse to the relaxation is show in **Figure 3-7**.

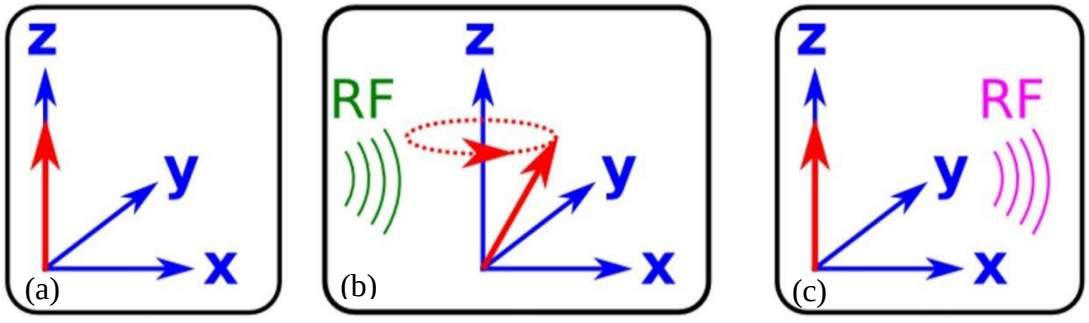

Figure 3-7 Changes from equilibrium to relaxation (a) State of equilibrium with M aligned with Z, (b) tipping following the RF field applcation, (c) relaxation phase, with return to equlibrum and emission of RF wave (From The science of medical imaging: magnetic resonance imaging (MRI)[7]).

3.2.3 Relaxation

There are two types of relaxation, occurring simultaneously but independently of each other: T1 and T2. Both are time constants, with T1 describing the return to equilibrium as M realigns with z, whereas T2 characterises the decay of the signal as the excited protons begin to dephase, with changes occurring on the x and y planes that will be explained below. The two forms of relaxation are illustrated in **Figure 3-8**.

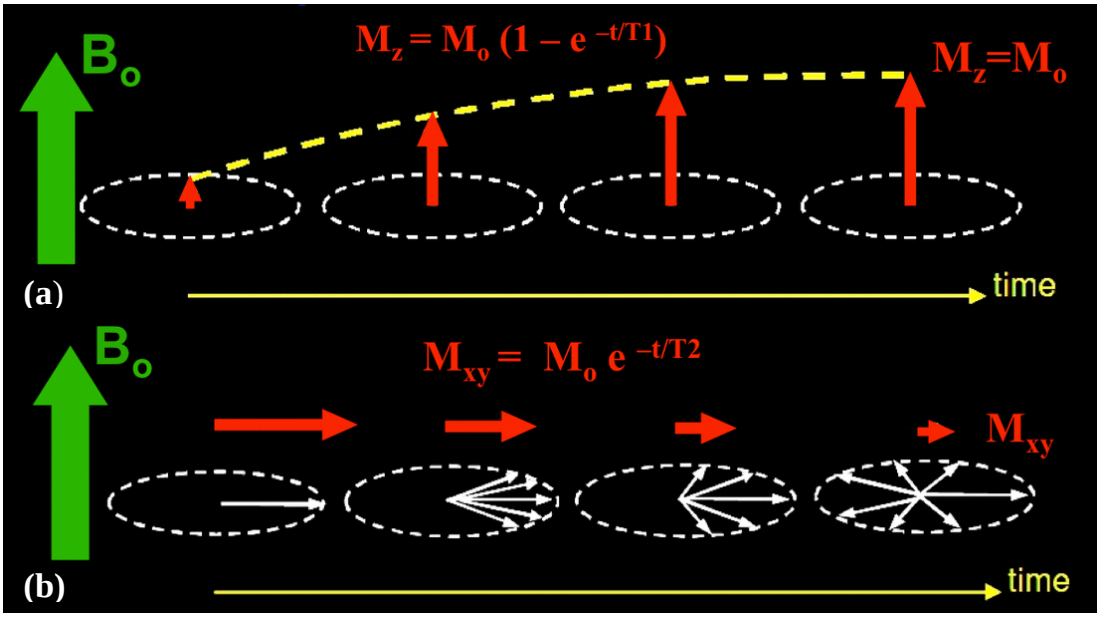

Figure 3-8 (a) T1 relaxation, showing the recovery of Mz along the B_0 axis (b) T2 relaxation, with signal decay and dephasing (Adapted from Elster[1]). Courtesy Allen Elster, MRIquestions.com

T1 relaxation is also known as the *longitudinal* or spin-lattice relaxation because in the early NMR experiments a crystalline lattice of atoms was used. Today, the surrounding tissue in which energy is released is described as the lattice. It is also sometimes described as thermal relaxation because the energy dissipates as heat. T2 relaxation, on the other hand, is also called *transverse* or spin-spin relaxation, because it is the transient and random interaction occurring between two excited spins that causes the loss of phase, which in turn leads to the loss of signal.

3.2.3.1 T1 relaxation

T1-relaxation time, which is unique to each tissue, is determined by the way in which protons are bound and is generally longer at higher field strengths. In

adipose tissues for example, the protons are tightly bound and will therefore release the energy in their surroundings much faster than loosely bound protons, like those in cerebrospinal fluid (CSF). In other words, the speed at which tissues release the energy/relax will determine the value of T1.

The time constant T1, modelled as an exponential growth curve (**Figure 3-9**), corresponds to the time needed after the excitation pulse for M to reach 63% of its initial value. Finally, the fact that T1 values vary with tissue types is also the rationale behind the good contrast resolution in MRI scans.

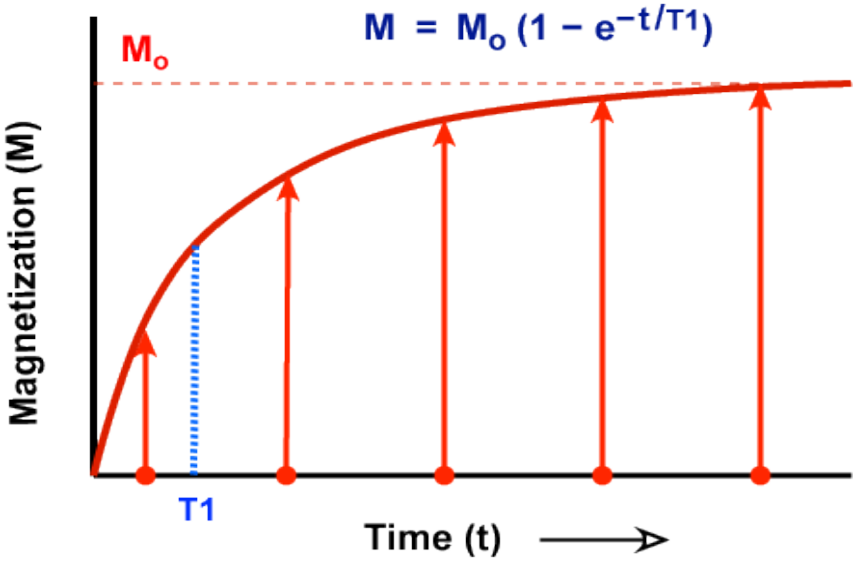

Figure 3-9 T1 relaxation curve. M reaches 63% of its maximum value (M0) at t = T1 and is very close to maximal at t = 5 x T1 (From Ester[1]). Courtesy Allen Elster, MRIquestions.com

3.2.3.2 T2 relaxation

The first thing to remember when looking at T2 relaxation is that after the RF pulse has been applied, the spins have been tilted in the xy plane (Mxy), and all

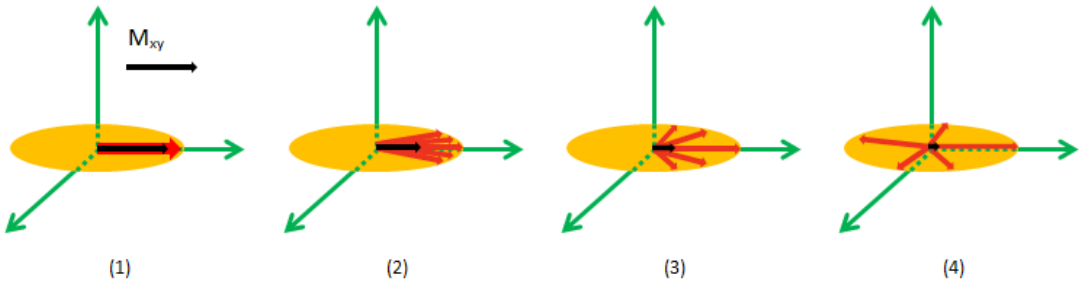

Figure 3-10 T2 relaxation, showing the progressive dephasing, with all spins aligned on the Mxy plane in (1) and their progressive dispersion or dephasing (2-4) (From Kantzas [et al.][8]). Reproduced with permission from PERM Inc

proton spins are both synchronized and precessing at the same frequency. This is the stage where protons are in phase. As mentioned above, it is the loss of this synchronisation, or dephasing, which causes the T2 relaxation. The process is illustrated in **Figure 3-10.**

So why this dephasing does occur? As stated earlier, the T2 relaxation is also called spin-spin relaxation, and the reason for this is because the dephasing is caused by interactions between spins. There will be transfer of energy from excited protons to nearby non-excited ones. This affects the speed at which each proton spins, and causes progressive inhomogeneity that leads to signal decay.

Just like T1 relaxation, the signal decay occurring during T2 relaxation can be modelled as an exponential curve, similar to the concept of radioactive decay, with a half-life measured in tens of ms, as shown in **Figure 3-11.**

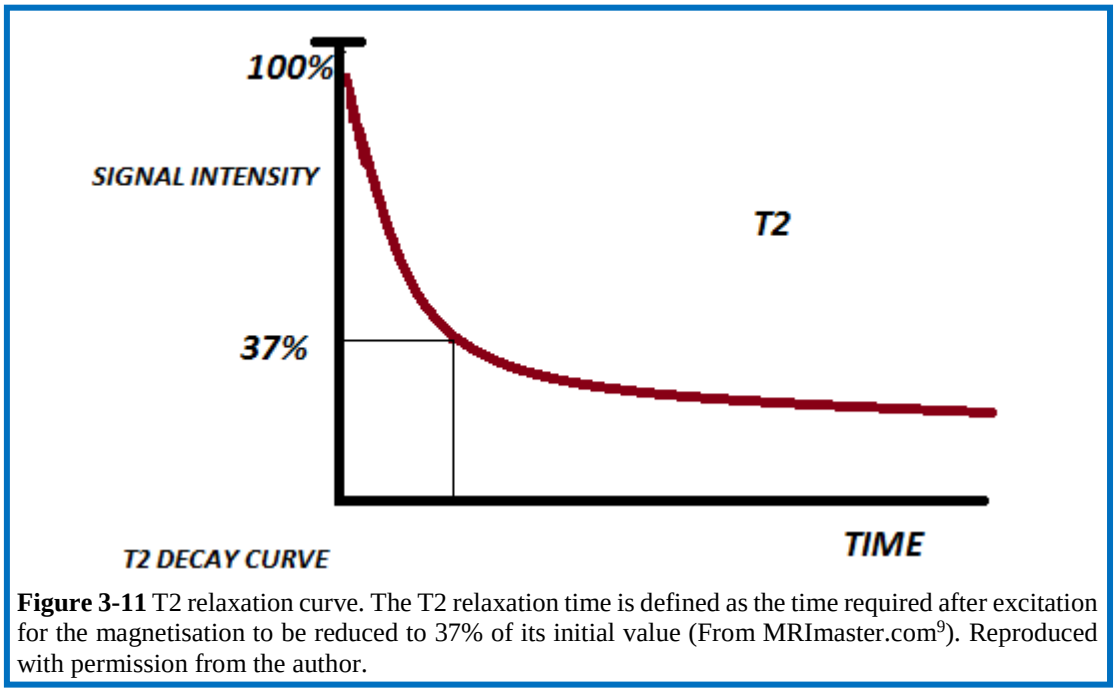

Figure 3-11 T2 relaxation curve. The T2 relaxation time is defined as the time required after excitation for the magnetisation to be reduced to 37% of its initial value (From MRImaster.com[9]). Reproduced with permission from the author.

The time constant T2 corresponds to the length of time elapsing between the excitation and the point at which the signal has been reduced to 36.8% of its original value (or has lost 63.2% of its amplitude). In other words, it is the opposite of T1 where 63.2% of Mz recovery is the benchmark for the T1 constant.

Moreover, just as is the case for T1, the value of T2 is unique for every kind of tissue and is determined primarily by the chemical environment. So taking the examples used for T1, adipose tissue will de-phase quickly, while the process will be much slower for CSF. T2 values are also much less affected by field strength than T1.

Finally, it should be noted that T2 relaxation happens much faster than T1 relaxation: it only takes tens of milliseconds compared to up to seconds for T1.

3.2.3.3 Free Induction Decay (FID)

It was mentioned above that the MR signal is linked to T2 relaxation. This signal is called Free Induction Decay (FID). Its initial amplitude is determined by the degree to which M has been flipped on the xy plane, with the highest signal obtained when the vector has been flipped to 90º. The signal is modelled with a decay curve (**Figure 3-12**), which contains the actual signal. The signal itself is oscillating at the resonance frequency in the MHz range. A curve as the

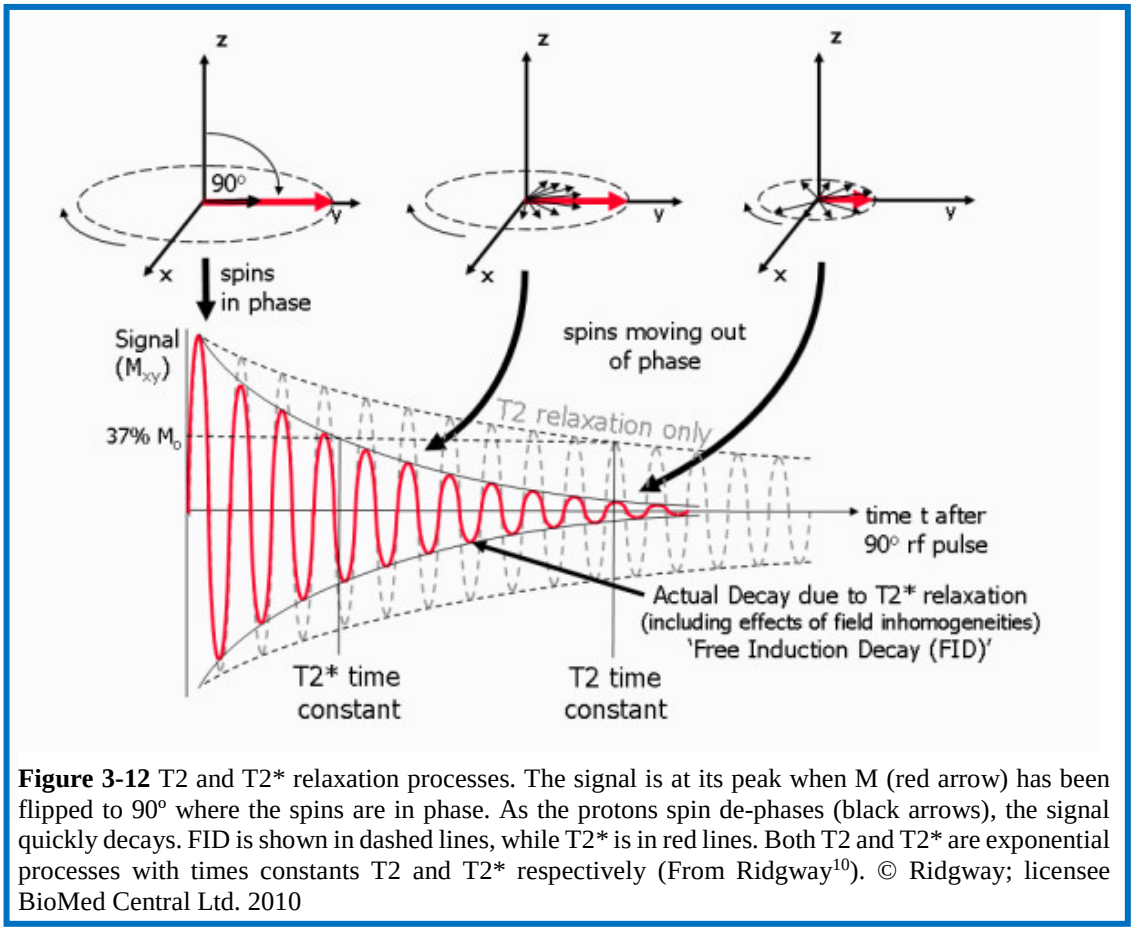

Figure 3-12 T2 and T2* relaxation processes. The signal is at its peak when M (red arrow) has been flipped to 90º where the spins are in phase. As the protons spin de-phases (black arrows), the signal quickly decays. FID is shown in dashed lines, while T2* is in red lines. Both T2 and T2* are exponential processes with times constants T2 and T2* respectively (From Ridgway[10]). © Ridgway; licensee BioMed Central Ltd. 2010

one shown in **Figure 3-12** would occur if nothing is affecting the homogeneity of the magnetic field. Obviously, such homogeneity does not happen in the real world, as the magnet is likely to have some flaws in its manufacture, and tissues variability means that each tissue has a different magnetic susceptibility, which causes field distortions at tissue borders. As a consequence of all this, the signal decays faster than the T2 relaxation would predict and the actual signal is called T2*, as can be seen in **Figure 3-12**.

MR signals can also be produced using spin echo and gradient echo, as will be explained in the next two sections.

3.2.4 Spin Echo (SE) and Echo Time (TE)

A Spin Echo (SE) is generated when a second 180º RF-pulse applied a short time after the 90º one. The effect of this pulse is to rotate the entire system upside-down (an analogy used is "flipping a pancake"), causing the spins to rephase, and thus producing a large signal: the Spin Echo. In order to have the optimal effect, the 180º pulse has to be applied at a specific time in the sequence. Corresponding to the middle time point between the first RF pulse and the peak of the spin echo. This time interval is called Echo Time (TE), and can be

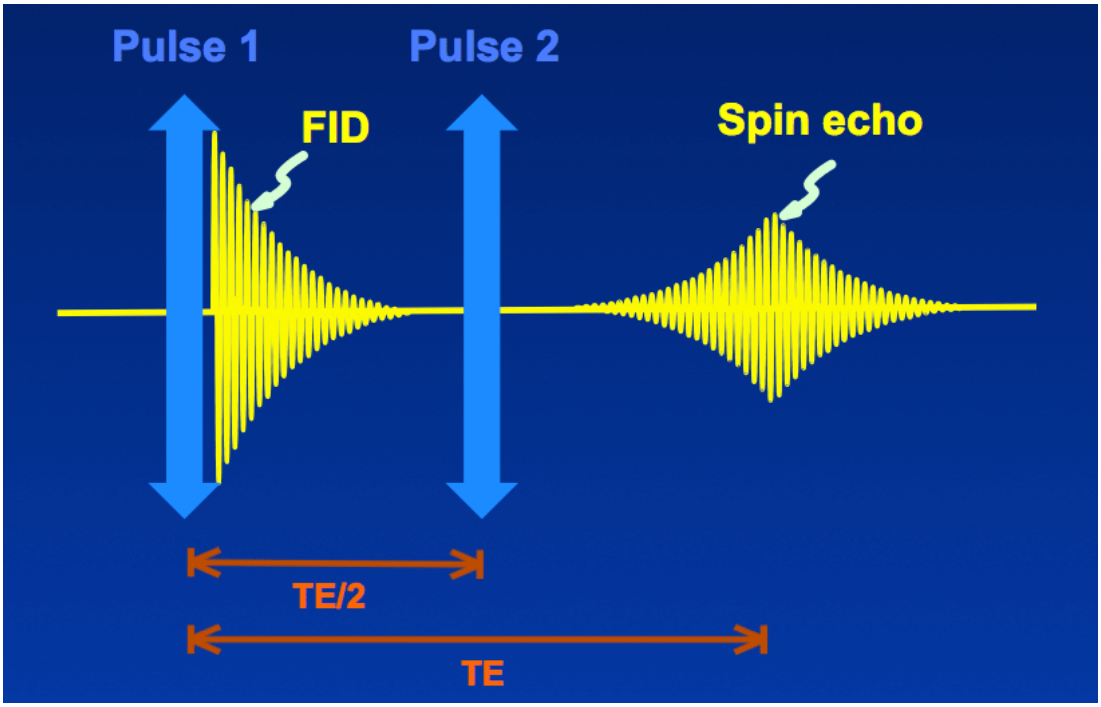

Figure 3-13 Creation of a spin echo by two RF pulses. The first RF pulse generates an FID, while the 2nd pulse generates the Spin Echo. The echo time (TE) is twice the inter-pulse interval (From Elster[1]). Courtesy Allen Elster, MRIquestions.com

anything in the range of 5 to 250 ms. The time at which the 180º pulse must be applied is defined as TE/2. The whole sequence is shown in **Figure 3-13.**

What happens to the protons when the system has been turned on its head is that the faster precessing spins are now at the back of the pack. A good analogy that is often used is one of a race in which participants have a great variety of speeds. At the start of the race, they are all aligned or in MRI terms, in phase. Once the race starts (at t = 0), the contestants all start moving at their fastest pace, and soon find themselves at different spots. At a given point (TE/2 in the MRI sequence), they are told to turn around without losing speed, which means that the starting line is now the finish. As the fastest contestants will be furthest away from the starting/finishing line and the slowest ones the closer, if they all keep going at the same speed as they did before, they should all reach the finishing line at the same time. For the protons, this will be another TE/2, after which they will be in phase once more.

Once all the spins are back into phase, they immediately start to dephase again. However, a second 180° pulse can be applied, using the same TE, to generate a second echo. The process can be repeated until the time at which T2 relaxation has caused the signal to decay completely as illustrated in **Figure 3-14**. It should

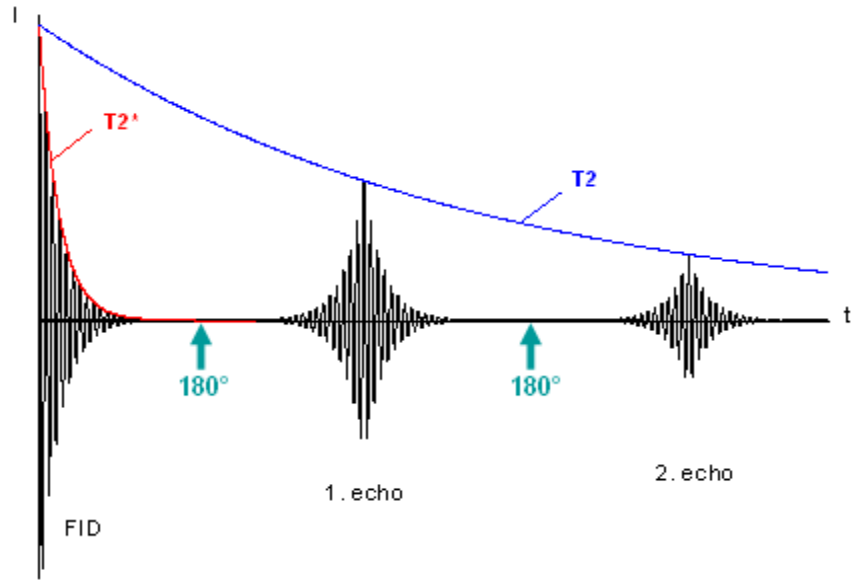

Figure 3-14 Exponential decrease of spin echoes maxima caused by T2 decay (From: Flögel][11]) Reproduced with permission from Uli Flögel.

be noted here that while the 90°-180° sequence gives the strongest signal, spin echoes can be generated with others flip angles.

3.2.5 Gradient Echo (GRE)

Gradient echo, sometimes also called gradient-recalled echo, differs from spin echo in two important ways: first, the flip angle is usually less than 90° (from of about 10° to 80°) and second, the 180° RF rephasing pulse is not needed. So how is the echo generated and how does the signal differ from the spin echo one?

The signal is generated through the application of a bipolar gradient, which consists of a pulse with a positive polarity followed by one with a negative one, which dephase and rephase the spins respectively. First the positive gradient leads to rapid dephasing of the transverse magnetisation, and brings the FID signal to zero, then the second gradient with a negative magnetic field is applied to reverse the dephasing caused by the first gradient. This gradient will generally be twice as long as the first one, and will have an effect similar to the one of the second pulse in the spin echo, with the rephasing and recovery of the FID signal generating a gradient echo. The double length of the second gradient is necessary to produce a full cycle of first rephasing/FID, followed by dephasing to zero. The process is illustrated in **Figure 3-15.**

What happens at the protons level is that the dephasing speed of the spins is reversed, with the fastest one slowed down, and the slower ones sped up until they are in phase again. Another important fact with this sequence is that the use of lower flip angles means a lower amount of magnetisation tipping in transverse plane, and consequently a shorter longitudinal/T1 recovery. Practically, this means that the sequence is faster than spin echo ones. The flip side is that the recovery is equivalent to the T2* decay rather than the T2 one, as is the case with the spin echo sequence. This is because GRE cannot correct for magnetic field inhomogeneity, and therefore leads to lower signal intensities and higher amounts of artefacts.

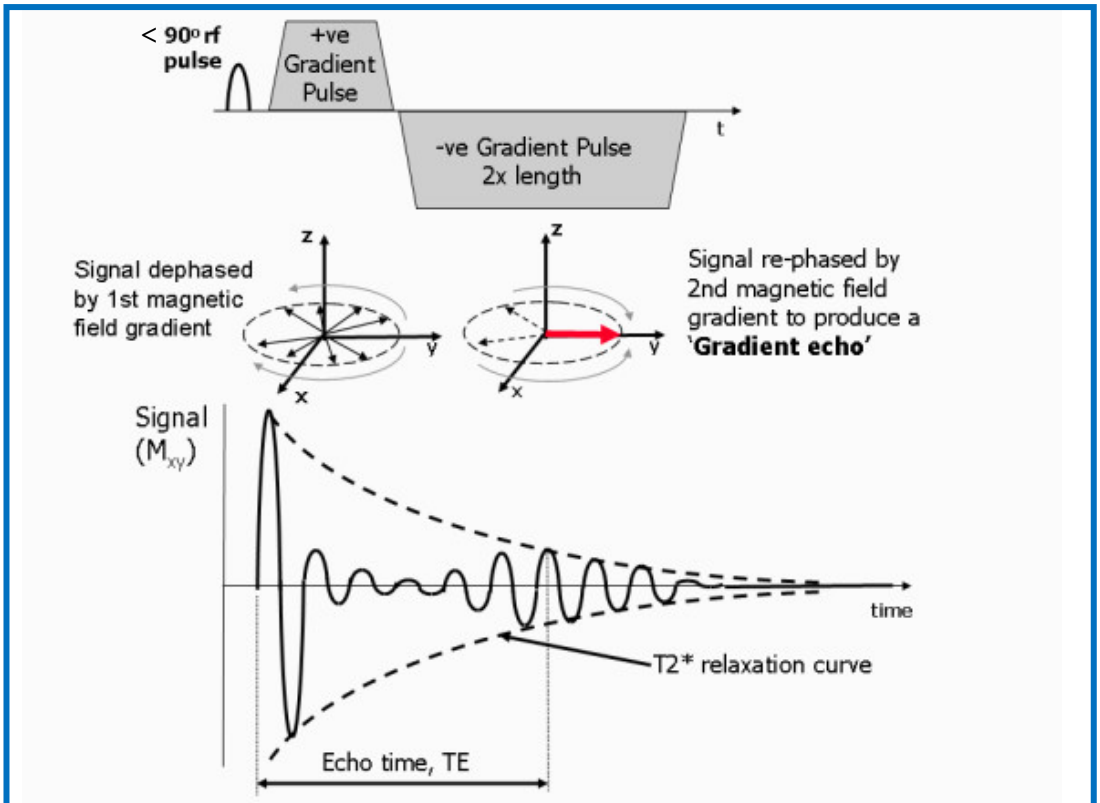

Figure 3-15 Gradient echo sequence. The magnetic field gradients applied, their effect on protons and FID with the T2* relaxation curve (From Ridgway[10]). © Ridgway; licensee BioMed Central Ltd. 2010

Nevertheless, the GRE sequence can be repeated, leading to several dephasing and rephasing, as long as the T2* relaxation is not complete. Each new echo will be smaller, as since T2* relaxation is faster than T2, only 3-4 usable echoes can be produced.

There is one more sequence that can be used to produce MR signals that needs to be introduced: Inversion Recovery

3.2.6 Inversion Recovery (IR) and Inversion Time (TI)

As can be seen from **Figure 3-16**, Inversion Recovery (IR) is a standard spin echo (SE) sequence that is preceded by a 180° inverting pulse. The 180° excitation pulse is called inverting because it flips the direction of the longitudinal magnetisation, so that it points in the opposite direction of the main magnetic field (B_0). After the initial 180° pulse, the T1 relaxation of the magnetisation starts from a negative or inverted value, rather than from zero as would be the case when the 90° pulse is applied in the SE sequence, and therefore will also be twice the length of what it would be in SE. The time

between the 180° inverting pulse and the 90° one, known as the inversion time (TI), can be varied in order to adjust the contrast.

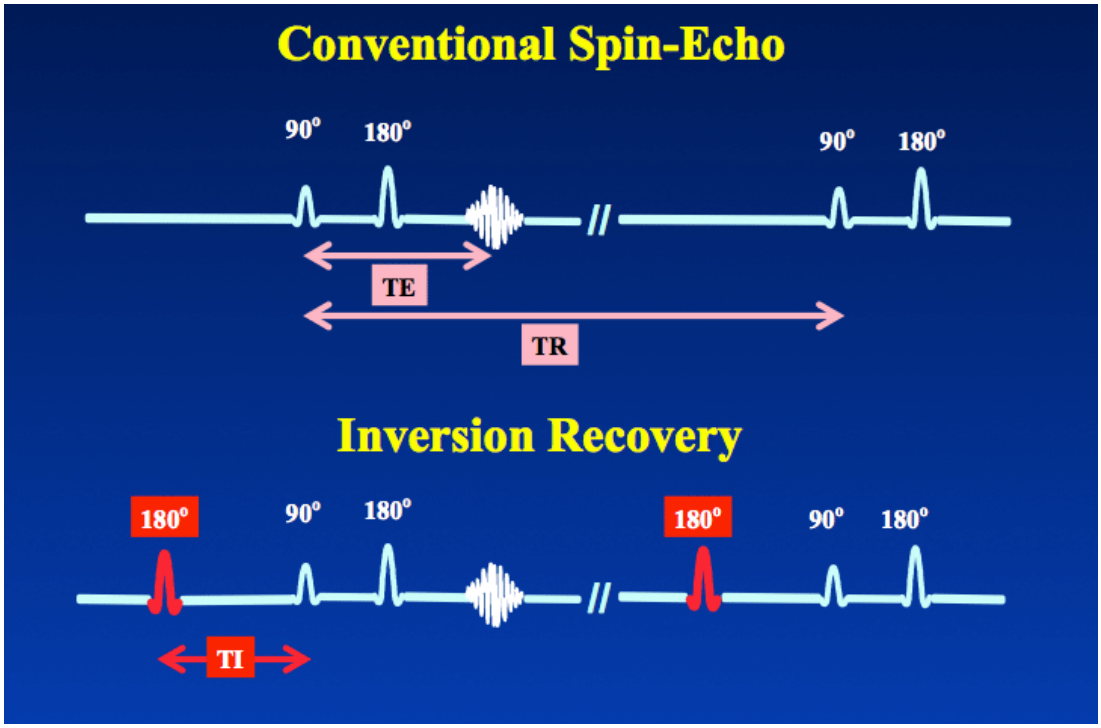

Figure 3-16 Spin Echo (SE) and Inversion Recovery (IR) sequences. The IR sequence is basically a SE sequence preceded by a 180° inverting pulse at time TI (From Elster[1]). Courtesy Allen Elster, MRIquestions.com

The increase in T1 relaxation times when compared to SE, combined with the fact that different tissues will have different T1 recovery time means that IR provides a better discrimination between tissues than SE. The degree of separation between different tissues in both SE and IR is illustrated in **Figure 3-17**. IR can also be used to suppress the signal of a specific tissue, like fat or CSF for example. To achieve this, the selected TI duration will match the T1 relaxation time of the targeted tissue. The sequence used to suppress the signal from fat is called Short Tau Inverse Recovery (STIR), while the one suppressing CSF signal is the Fluid Attenuation Inverse Recovery (FLAIR) sequence. In the context of this thesis, the application of IR with a different type of reconstruction, phase-sensitive inversion recovery (PSIR), is used to look at grey matter lesions. This technique will be the topic of section 3.4.

There is another sequence that had been used in the context of this thesis, echo planar imaging (EPI). As it specifically used for diffusion MRI, it will be explained in that section. For now, there is one more generic feature of MR

acquisition that needs to be discussed: the repetition time briefly mentioned when discussing the spin echo.

3.2.7 Repetition Time (TR)

The repetition time (TR) is the time elapsing between the repetitions of the sequence. So for the SE sequence, it will between the 90º pulses (as shown in **Figure 3-17**). For the gradient echo one, it will the time between the flipping angle pulses and for IR sequence between the 180º pulses. The combination of different TR and TE is also used to determine the contrast, as will be explained in the next section.

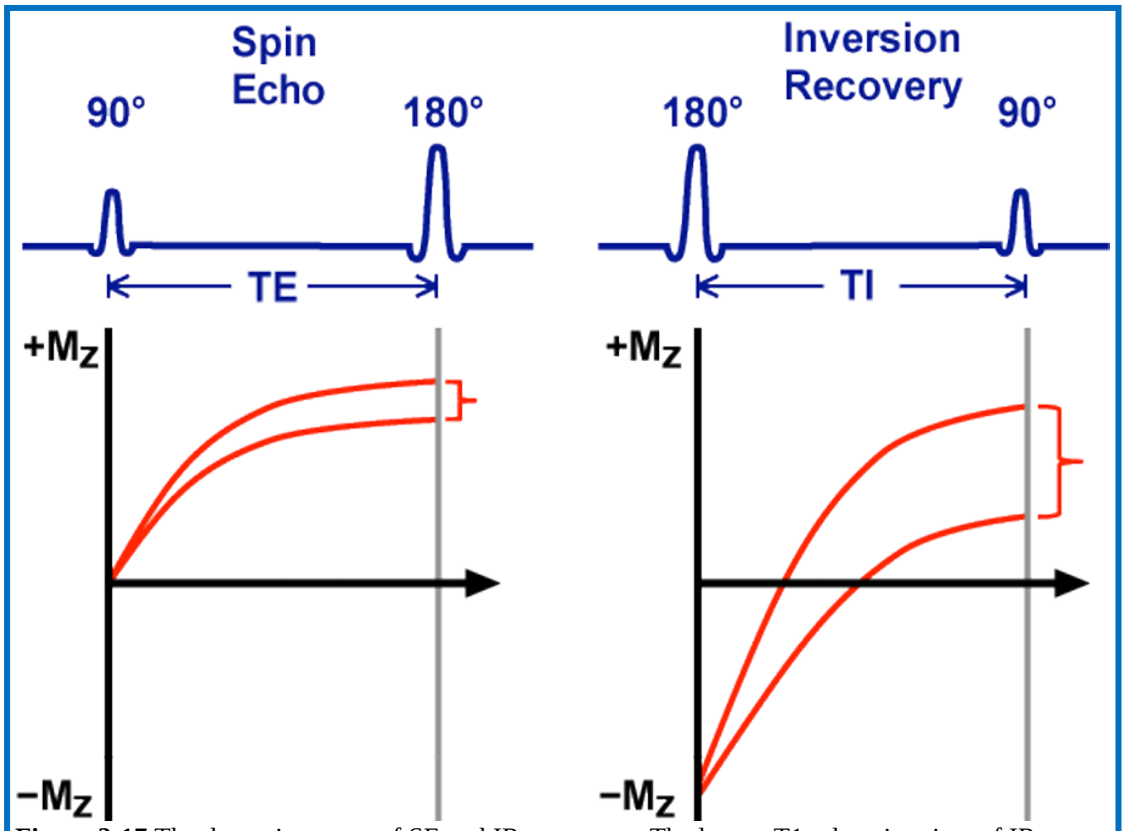

Figure 3-17 The dynamic ranges of SE and IR sequences. The longer T1 relaxation time of IR means that IR can potentially discriminate tissues on more subtle variations than SE (From Elster[1]) Courtesy Allen Elster, MRIquestions.com

3.2.8 Image contrasts: T1, T2 and proton density (PD)

In SE sequences, the image contrast depends on the combination of TE and TR values, with three combinations used:

- ❖ Short TR/Short TE → T1-weighted
- ❖ Long TR/Short TE → PD-weighted
- ❖ Long TR/Long TE → T2-weighted

The short TR/long TE combination is not used because as shown in **Figure 3-17** it produces a poor contrast.

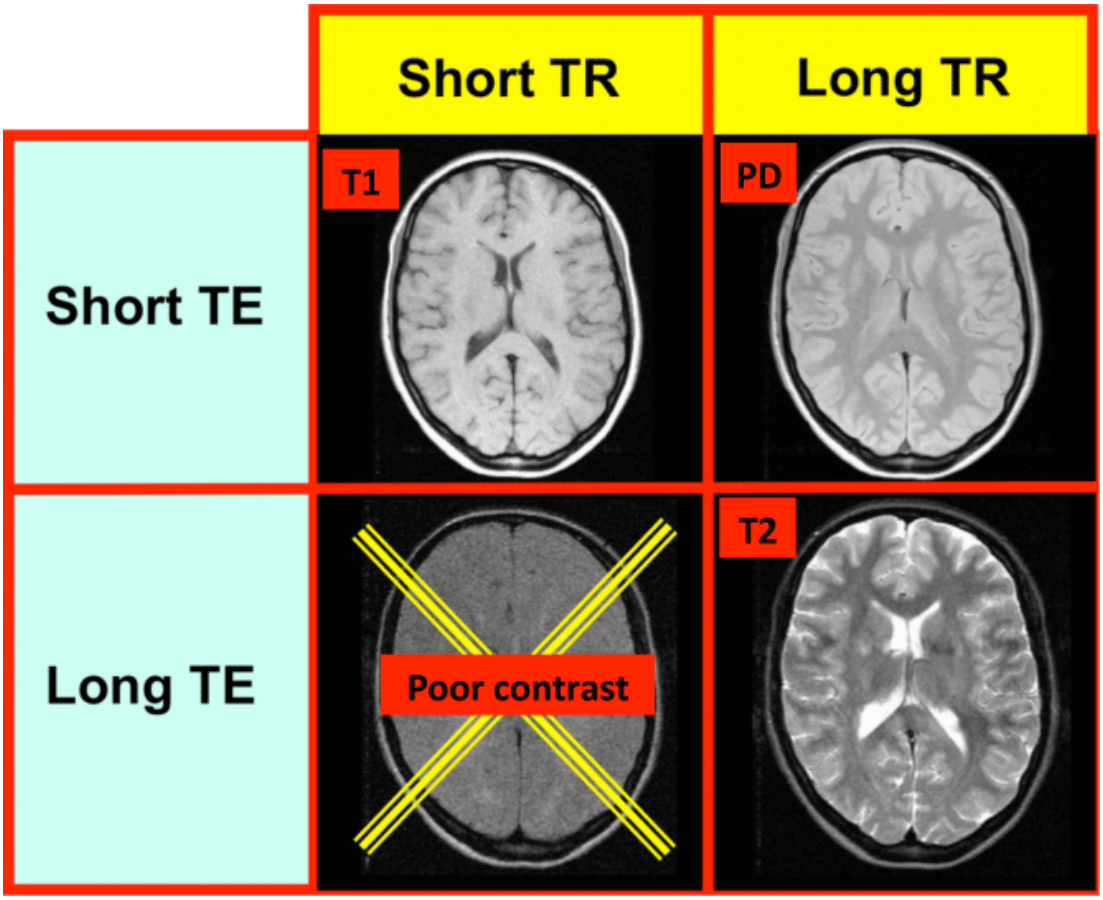

Figure 3-18 TE and TR combinations in SE sequences and the image contrasts obtained (From Elster[1]). Courtesy Allen Elster, MRIquestions.com

T1, T2 and PD can also be obtained when using GRE sequences, except that here the contrast is determined by different combination of the flipping angle (α) and TE.

- High α/Short TE → T1-weighted
- Medium α/Short TE → PD-weighted
- Low α/Long TE → T2-weighted

Standard IR sequences will give T1 images, however sequences such as FLAIR can be used to produce both T1- and T2-weighted images.

For the purpose of this thesis, T1-weighted images were used for image co-registration, while PD/T2-weighted ones are used to mark lesions in MS and NMOSD patients. An example of T1, T2, PD contrast in the same patient is shown in **Figure 3-19.**

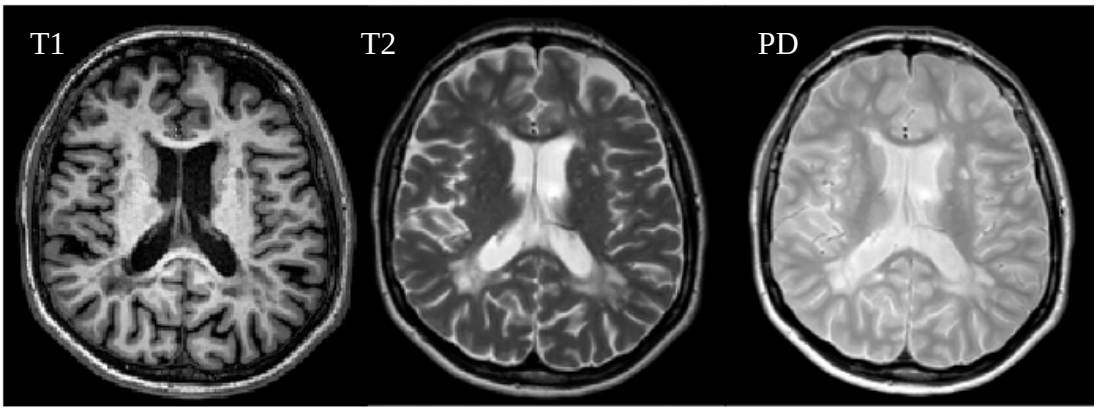

Figure 3-19 T1-, T2- and PD-weighted images in a patient with MS showing large periventricular lesions.

Having discussed how images are produced, the next step is to understand how the localisation of the signal can be detected.

3.2.9 Spatial localisation

When the sequences mentioned above are used, they do not provide any information about the location of the signal. So in order to include spatial localisation of the signal, its x, y and z coordinates need to be specified. As mentioned in the introductory section, Lauterbur showed that this can be done using gradients. So what are those gradients and how are they produced? The term gradients (G) is used to describe fields with a magnetic gradient: that is they vary in magnitude or direction between two points in space. They are defined as the change in field (ΔB) divided by the change in distance (Δs)[1].

$$\text{So: } G = \Delta B / \Delta s$$

Gradients are generated by spatial encoding coils, known as gradient coils, which can produce secondary magnetic fields in the x, y, and z directions. These fields, which are much weaker than the main magnetic field B_0, slightly distort it in a predictable manner (their effect can be seen in **Figure 3-20)**, causing spatial variations in the resonance frequency of protons which can then be used for spatial encoding.

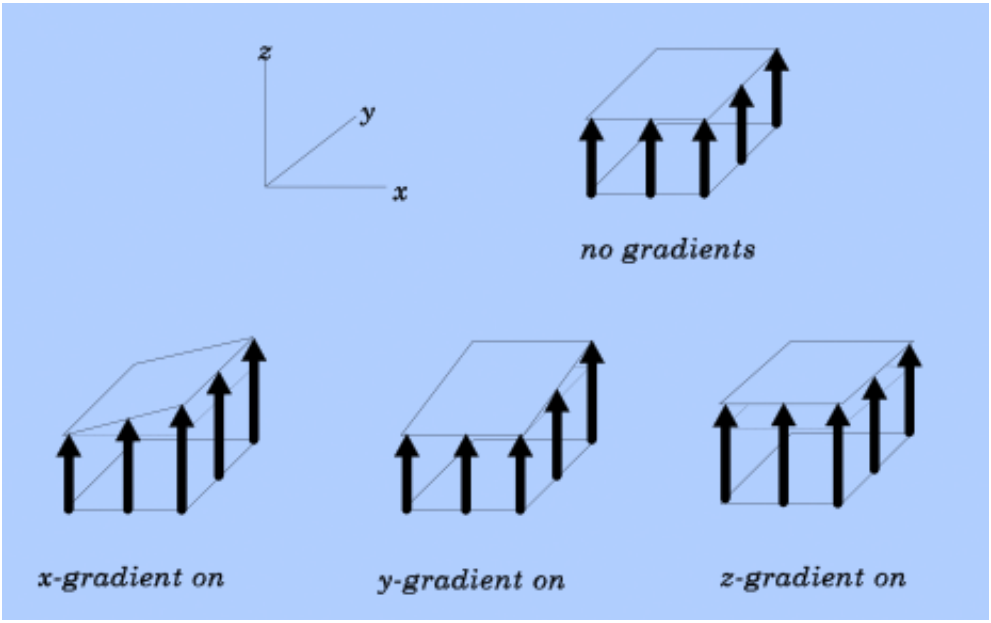

Figure 3-20 The effects of the application of x, y and z gradients on B_0 (From Elster[1]). Courtesy Allen Elster, MRIquestions.com

Spatial encoding has three stages: slice selection, frequency-encoding, and phase-encoding.

3.2.9.1 Slice selection

This is done using a slice encoding or slice selection gradient, GS, together with a simultaneous RF pulse at the Lamor frequency determined by the selected slice. Consequently, only the protons in the chosen slice will be excited. Since each slice contains a range of frequencies or bandwidth, the RF pulse transmitted needs to comprise the whole range. The thickness of the slice itself is determined by a combination of the strength/steepness of the gradient together with the range of frequencies/bandwidth in the RF pulse. The process is illustrated in **Figure 3-21.**

Now that the source of the signal has been located in a specific area, further encoding is necessary to know its position within the slice, which is the reason why a phase encoding gradient is applied next.

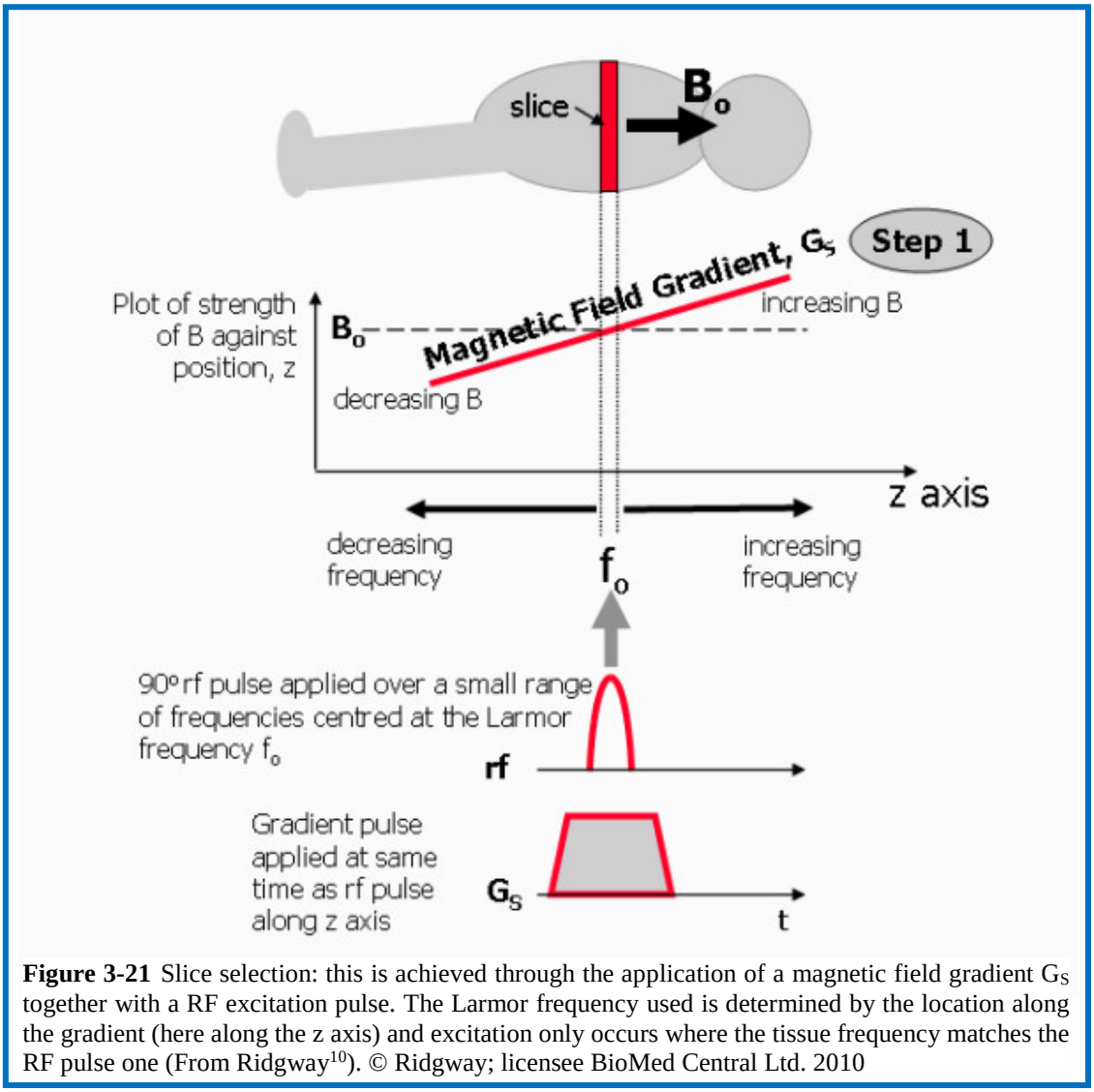

Figure 3-21 Slice selection: this is achieved through the application of a magnetic field gradient G_S together with a RF excitation pulse. The Larmor frequency used is determined by the location along the gradient (here along the z axis) and excitation only occurs where the tissue frequency matches the RF pulse one (From Ridgway[10]). © Ridgway; licensee BioMed Central Ltd. 2010

3.2.9.2 Phase encoding

The phase encoding gradient (G_P) is applied for a specific period in the vertical direction, causing the protons to rotate at different frequencies depending on their position along the gradient. Precession will increase where the gradient increases, and similarly decrease in the part of the slice where the gradient causes a decrease in the magnetic field. In other words, the protons will have different phases depending on their position, and this persists after the gradient is switched off. So now all the protons are precessing with the same frequency but have different phases. To obtain an image, multiple repetitions with different encoding gradients, which are progressively incremented is necessary, as can be seen in **Figure 3-22**.

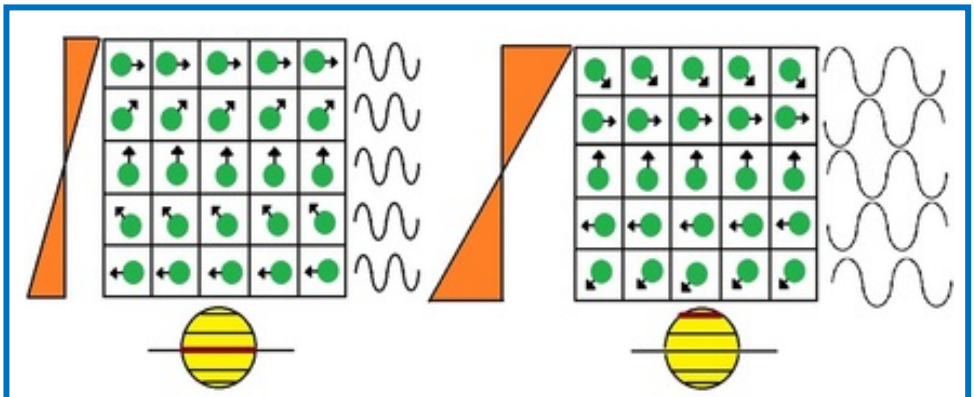

Figure 3-22 Two phase encoding gradients and their effects on protons phases (From MRI shark[12]). Reproduced with permission from the author.

So now there is just one more direction that needs encoding, and for this frequency encoding is used.

3.2.9.3 Frequency encoding

Last, the frequency encoding gradient (G_F) is applied at right angle from the previous gradient. It affects protons frequencies according to their positions along the gradient direction and therefore modifies the Larmor frequencies in the remaining direction for the duration of its application, while the phase changes from G_P remain after the pulse is turned off. **Figure 3-23** summarises what happens to the protons through the spatial location sequence, while **Figure 3-24** illustrate the whole sequence.

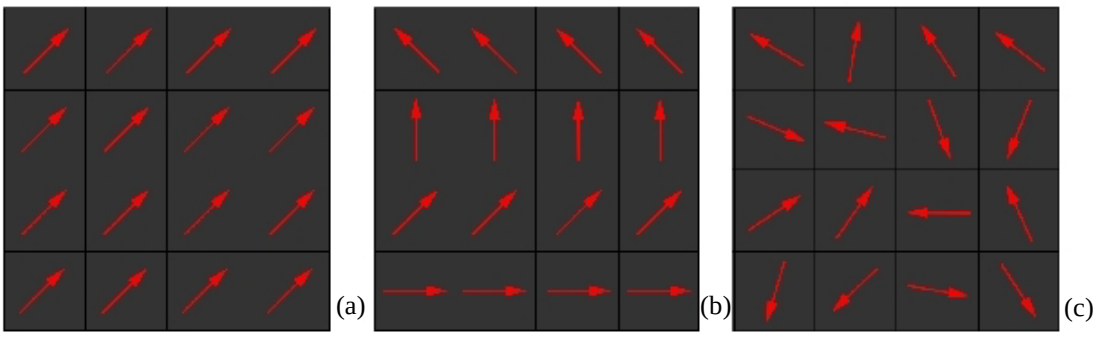

Figure 3-23 Changes in precession phases of protons through spatial location stages (a) After slice selection (b) After phase encoding (c) After frequency encoding, with the signal of each voxel uniquely encoded (Adapted from Adair [et al.][13]).

Having looked through the different aspects of image acquisition, the next stage is to see how the image is reconstructed.

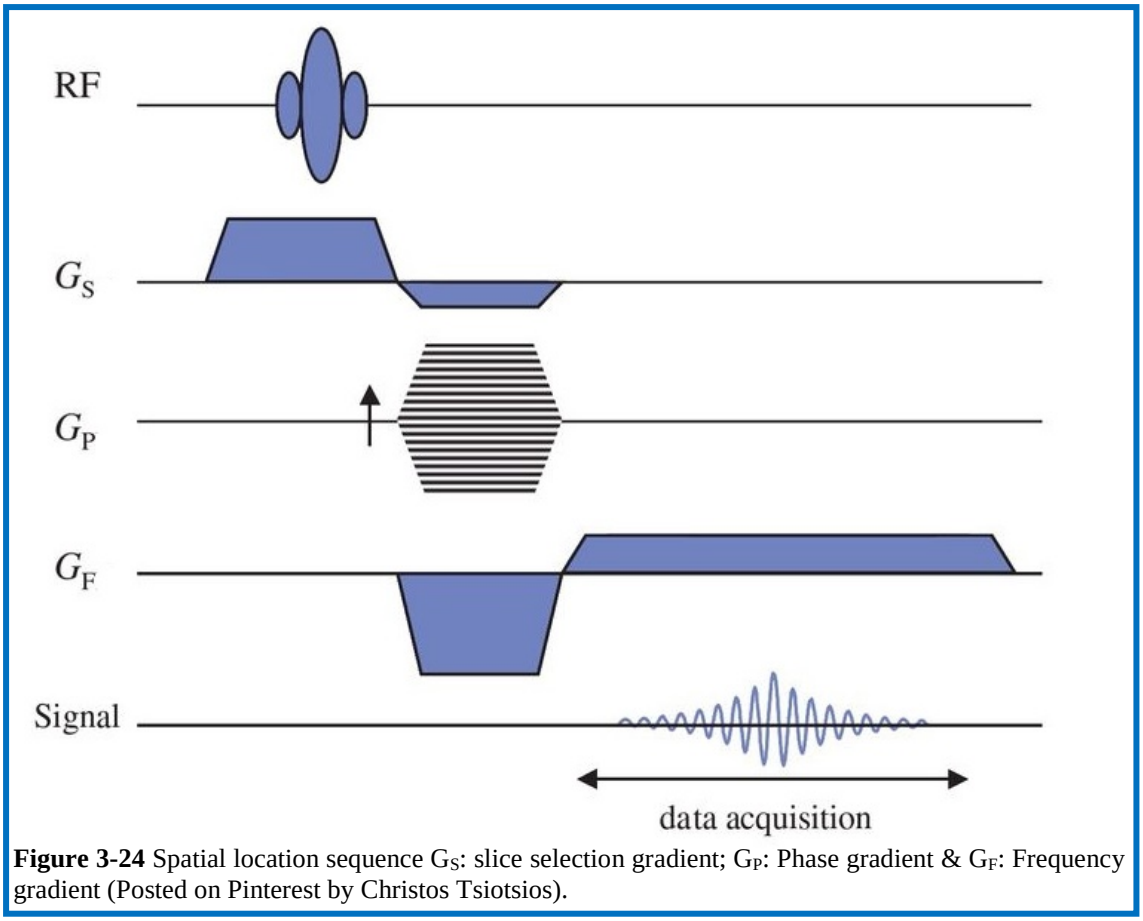

Figure 3-24 Spatial location sequence G_S: slice selection gradient; G_P: Phase gradient & G_F: Frequency gradient (Posted on Pinterest by Christos Tsiotsios).

3.2.10 Fourier transform and k-space

There are two important concepts that need to be explained in order to understand how MR images are reconstructed: *k*-space and Fourier transform. Since the reconstruction process involves the Fourier transformation of *k*-space in order to get an image, I will start with this.

A very straightforward definition of *k*-space was quoted by NessAiver: "The MRI data prior to becoming an image (raw or unprocessed data) is what makes up k-space"[2]. This definition has the advantage of being a clear and simple, and is therefore a useful starting point, but in order to understand how the Fourier transformation works, the one given by Allen D. Elster, describing "k-space as an array of numbers representing spatial frequencies in the MR image"[1] introduces one key notion, that *k*-space is about spatial frequencies and it is these frequencies that will be transformed in order to produce an image, as can be seen in **Figure 3-25.**

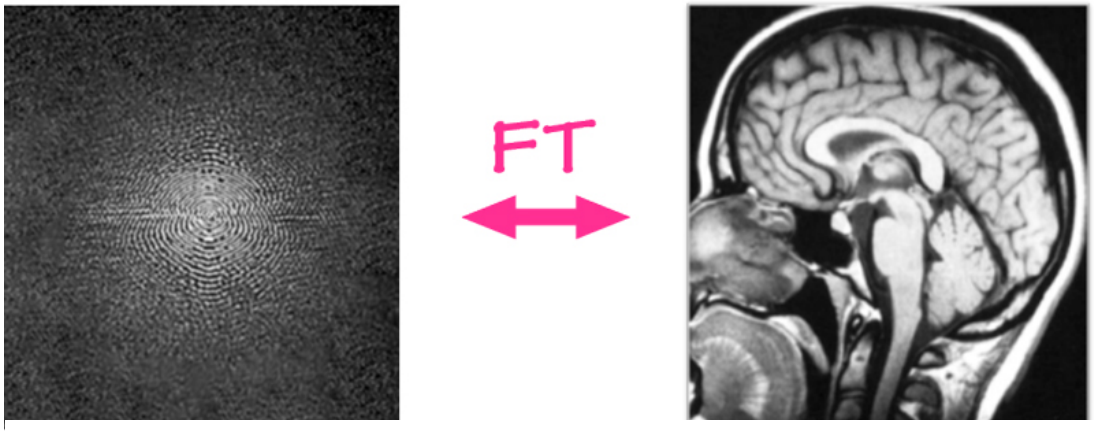

Figure 3-26 *k*-space and Fourier transformed image. As the double arrow indicates, the transformation works in both directions (From Elster[1]). Courtesy Allen Elster, MRIquestions.com

k-space is represented by a square, with *k*x and *k*y axes corresponding to x (horizontal) and y (vertical) axes in the actual image. However, as already mentioned, the axes in *k*-space represent spatial frequencies rather than positions, with each *k*-space point containing both phase and spatial frequency information about each pixel in the final image, as illustrated in **Figure 3-26**. So the centre of *k*-space comprises signals with low spatial frequencies (converting into general shapes and contours), while the high-spatial frequencies signals (holding information about edges, details, giving the image its sharpness) are located in the periphery.

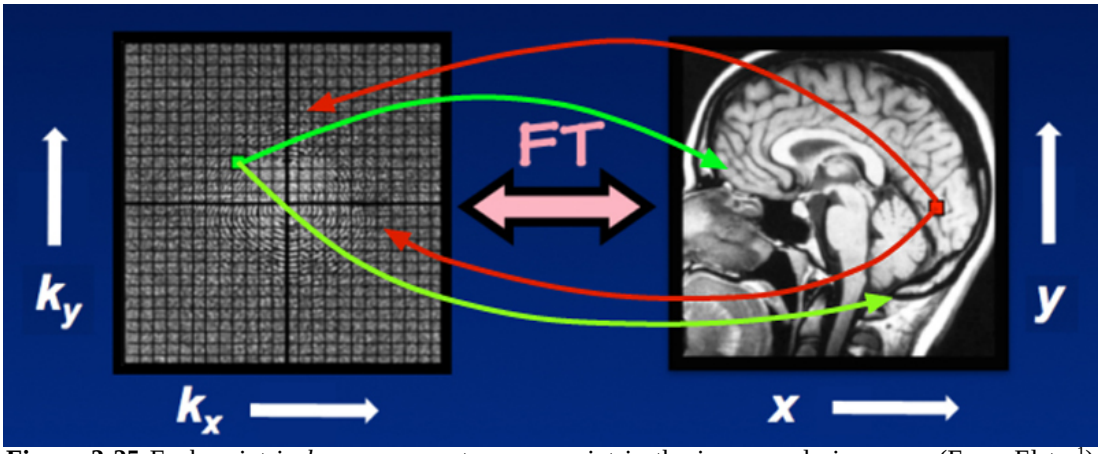

Figure 3-25 Each point in *k*-space maps to every point in the image and vice-versa (From Elster[1]). Courtesy Allen Elster, MRIquestions.com

It is beyond the scope of this thesis to explain in details how the Fourier transformation works, but a brief explanation will be useful to understand image reconstruction. Joseph Fourier (1768–1830), a French mathematician and physicist, uncovered the fact that a complicated signal can be rewritten as the

sum of a series of simple waves. In term of MRI signals, that means decomposing it into a sum of sine waves of different frequencies, phases, and amplitudes, which as shown above are all components of the signals.

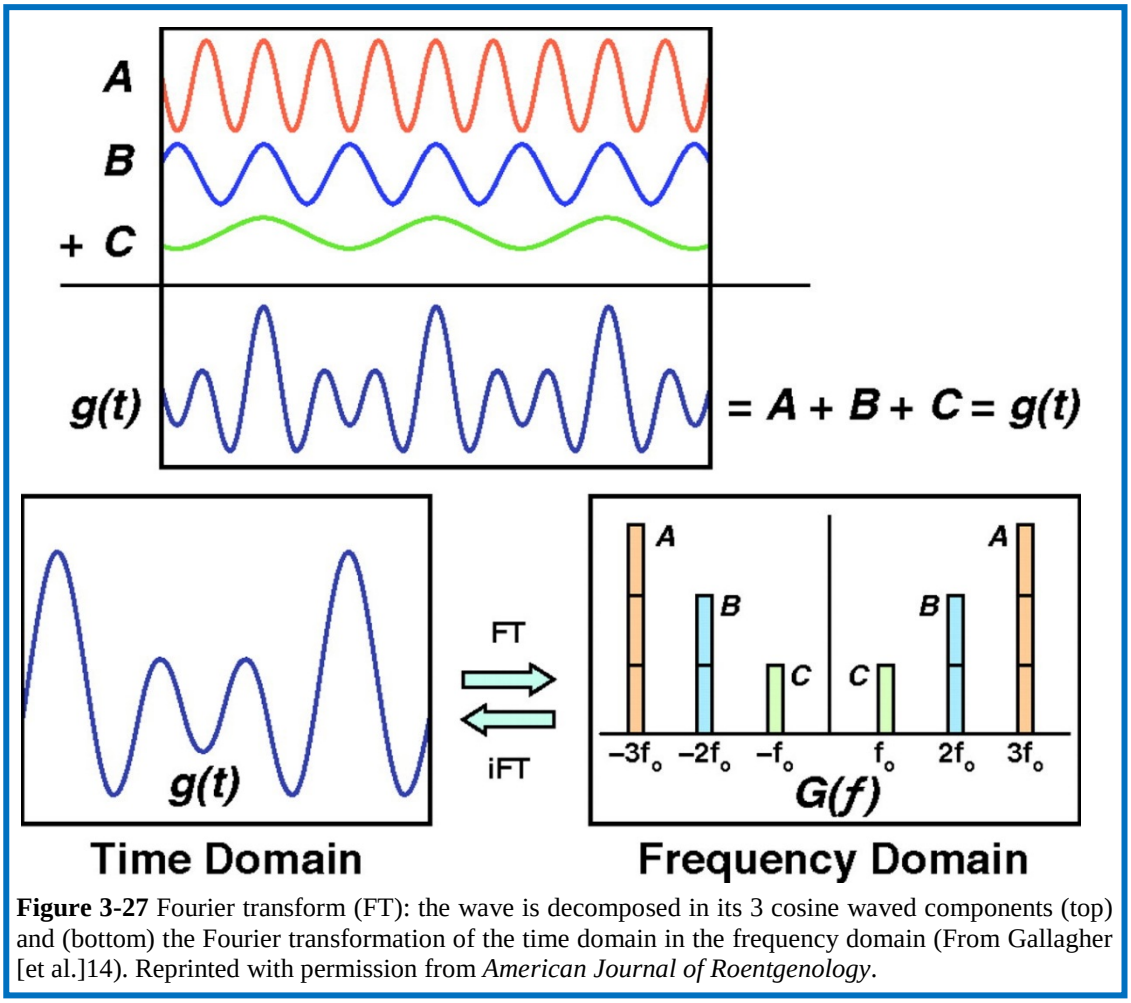

Figure 3-27 Fourier transform (FT): the wave is decomposed in its 3 cosine waved components (top) and (bottom) the Fourier transformation of the time domain in the frequency domain (From Gallagher [et al.]14). Reprinted with permission from *American Journal of Roentgenology*.

Concretely, **Figure 3-27** shows how a complex wave is decomposed into its 3 cosine waves before its time domain is transformed into a frequency domain.

Having looked into *k*-space and Fourier transformation, it is worth having a quick peek at the whole process from acquisition. **Figure 3-28** shows how the different spatial frequencies of a coronal slice of a brain are acquired by successively altering magnetic field gradients (open arrows in top three images) during frequency- and phase-encoding stages. The diagram only shows three gradients, but it is important to remember that a much larger number of gradients are necessary to fill *k*-space sufficiently to make image reconstruction possible.

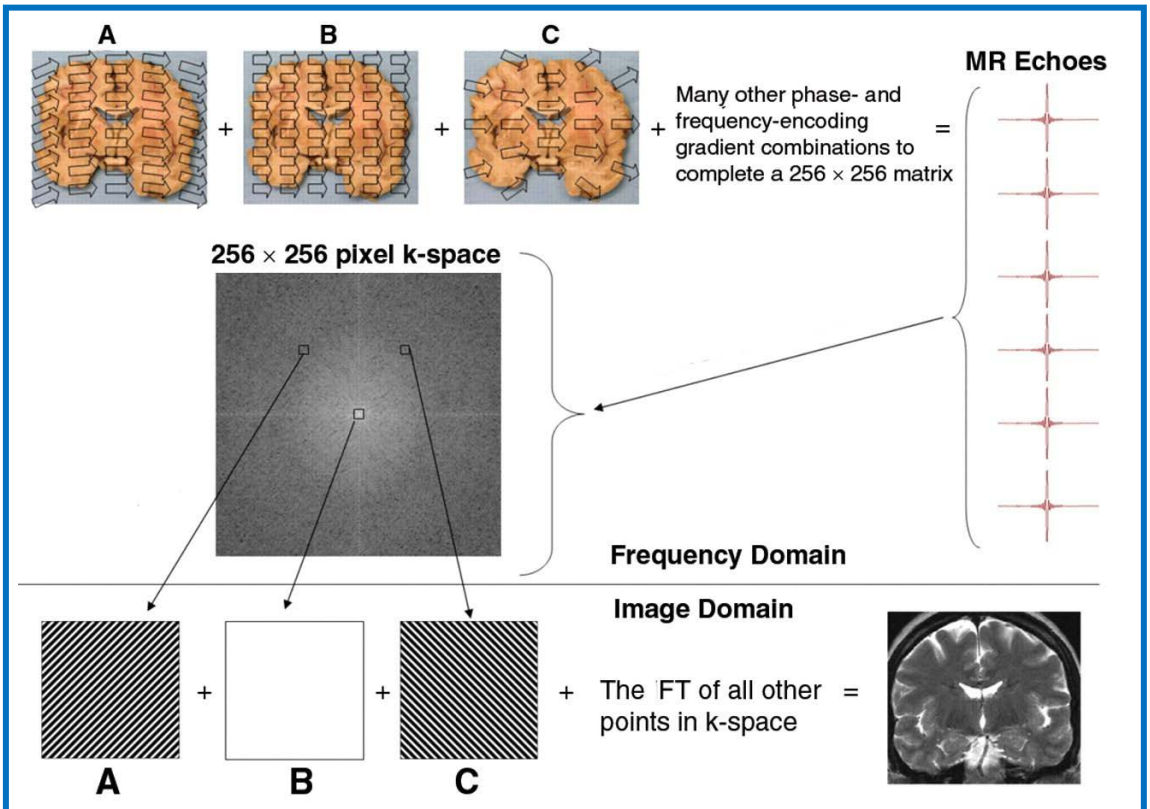

Figure 3-28 Sequence from acquisition to MR image. A, B & C at the top represent different gradients, used during acquisition, while the corresponding images at the bottom show how they appear in *k*-space, before going through the Fourier transformation (FT) to produce the image of a coronal slice of the brain (Adapted from Gallagher [et al.][14]) Reprinted with permission from *American Journal of Roentgenology*.

Now that we have seen how MR images are acquired and reconstructed, the next sections will introduced the different MRI techniques used for this thesis: diffusion-weighted magnetic resonance imaging (dMRI), phase-sensitive inversion recovery (PSIR) and magnetisation transfer ratio (MTR).

3.3 Diffusion-weighted magnetic resonance imaging

Specific techniques are used to look at different aspects of the brain. In the case of diffusion-weighted magnetic resonance imaging (dMRI), it is a non-invasive method allowing *in-vivo* studies that can provide information on both white matter integrity and structural changes in the human brain. This is particularly relevant in the context of progressive or degenerative diseases, as it enables researchers and clinicians to assess changes occurring in patient's brains at different time points, and thus to assess parameters such as disease progression or drugs efficiency. The fact that this technique is highly relevant for both

clinical and research applications explains why it is not just widely used, but also gives rise to ever more complex innovations, from Tract-Based Spatial Statistics (TBSS), q-ball imaging or Neurite Orientation Dispersion and Density Imaging (NODDI), which is the technique used in **Chapter 4**.

3.3.1 The physics and representation of dMRI:

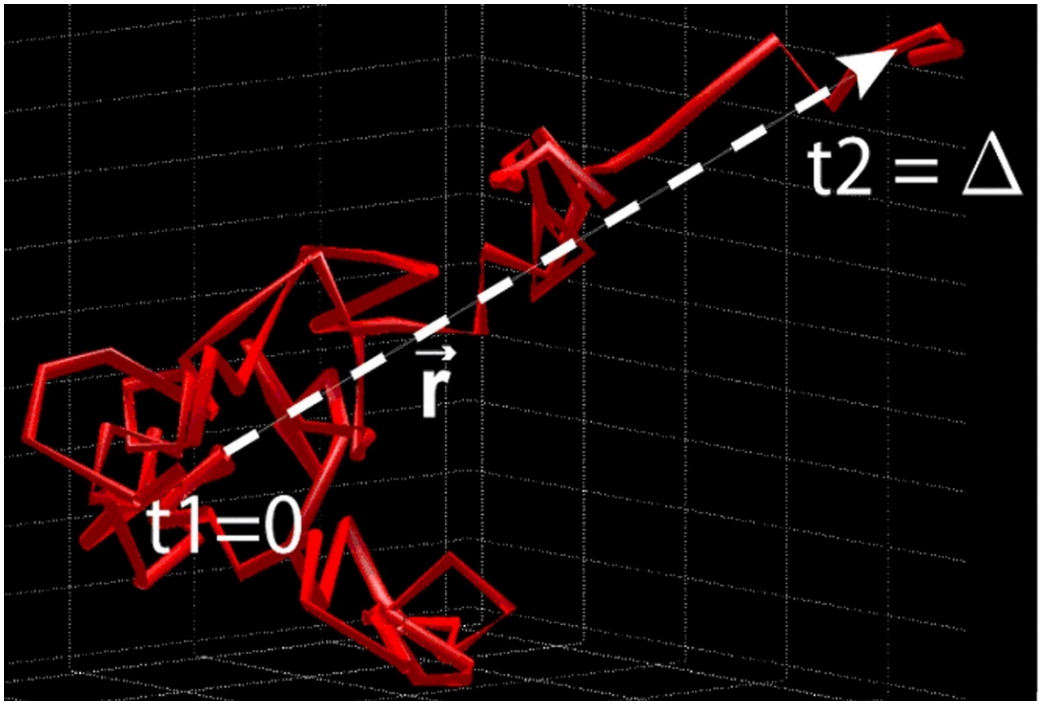

Figure 3-29 The red line shows the random trajectory of a diffusion-driven single water molecule. The molecular displacement during the diffusion time interval between t1 = 0 and t2 = Δ is represented by dotted white line (vector r) (From Hagmann [et al][15], ©RSNA, 2006). Reproduced with permission from RSNA

dMRI is based on the fact that water molecules diffuse differentially in different tissue types, but also do so in a random and erratic way as illustrated in **Figure 3-29**. This erratic motion is defined as a displacement distribution. In statistical terms, this displacement distribution describes the proportion of molecules shifted in a specific direction and to a specific distance[15]. Where there is pure liquid, such as in cerebrospinal fluid-filled regions, the absence of narrow barriers means that diffusion is the same in all directions and will have a Gaussian (bell shaped) distribution. A similar diffusion pattern is also found in spherical cell and in voxels covering randomly orientated axons. In all these cases, the 3D displacement distribution will have a spherical shape and is called isotropic.

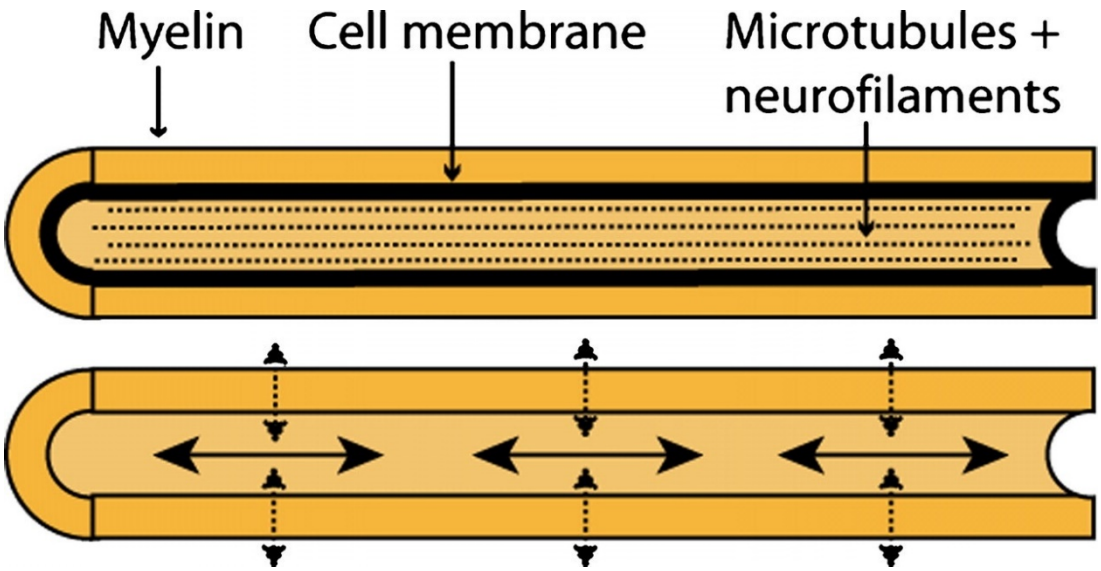

Figure 3-30 A schematic longitudinal view of a myelinated axon, showing the different structures which could support diffusion along the axon direction and hinder perpendicular diffusion, thus resulting in anisotropic diffusion (From Hagmann [et al.][15], ©RSNA, 2006). Reproduced with permission from RSNA

However, most neuronal tissues are formed of tightly packed fibres such as axons, and are frequently organised in bundles. When looking at diffusion that means that the movement of water molecules is highly constrained, largely by the cell membrane (**Figure 3-30).** This type of diffusion is described as anisotropic and will occur primarily along the tract length, as perpendicular diffusion is extremely restricted. Accordingly, the displacement distribution will have an ellipsoidal shape and no longer be Gaussian[15-17]. Practically this means that in brain tissues, diffusion is isotropic in cerebrospinal fluid as well as grey matter (GM), where the lack of precise orientation in the fibres results in random diffusion, but anisotropic along white matter tracts[18,19]. As for the source of diffusion within axons, myelin only play a small part in anisotropic diffusion, since it occurs mostly in the cell membrane, and primarily in the direction of the axon fibre. Microtubules and neurofilaments too seem to play only a minor role, while the function of cellular density and amount of myelination appears to be purely regulatory[15,18]. Obviously diffusion within cells occurs in three dimensions, and therefore a three-dimensional (3D) model is required to represent the probability of displacement or displacement distribution within three intersecting planes.

As shown in **Figure 3-31**, this can be done using colour coding, and is applied to the different types of diffusion, which in this figure is the probability density function in a voxel containing either spherical cells or randomly oriented intersecting tubular structures (like axons). This is a good example of isotropic diffusion, similar to the unrestricted diffusion found in the CSF (but in this case is restricted by biological barriers) as it has a roughly Gaussian distribution with no preferential direction of diffusion. The vector **r** indicating the displacement distance[15].

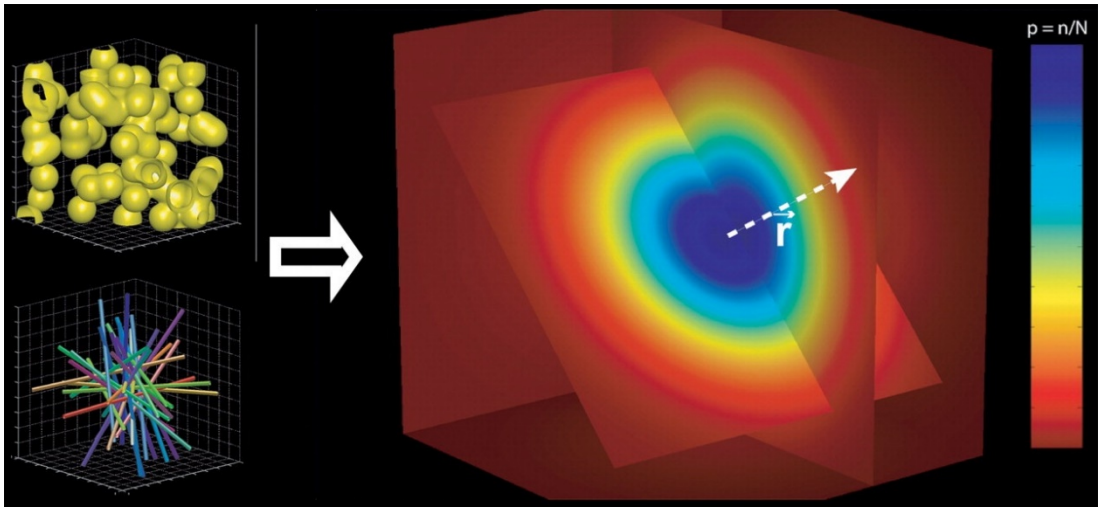

Figure 3-31 The colour coding used to indicate the probability diffusion level within a single voxel, from the highest in blue to lowest in red, with the full spectrum shown in the colour bar on the side. A 3D diffusion probability density function in a voxel containing either spherical cells (top left) or randomly oriented tubular structures that intersect, such as axons (bottom left). The roughly bell shaped 3D displacement distribution results in a symmetric image, as there is no preferential direction of diffusion. The distribution is similar to that in unrestricted diffusion, but narrower since biological barriers hinder molecular displacement. The centre of the image (origin of the r vector) indicates the proportion of molecules (n/N) not displaced during the diffusion time interval (From Hagmann [et al.][15], ©RSNA, 2006). Reproduced with permission from RSNA

Before looking at how diffusion in the type of complex environment found in biological tissue is modelled, it is useful to look at the model of diffusion in a homogeneous medium. There the Gaussian distribution will depend on the type of molecule, temperature and time allowed for diffusion. The parameter which controls the spread of Gaussian distribution, variance (σ^2) depends on two variables: the diffusion time interval (Δ) and the diffusion coefficient *D*. The latter characterises either how easily molecules are displaced or the viscosity of the medium. This can be sum as:

$$\sigma^2 = 2 \times D \times \Delta$$

For water at 37º, the approximate value of *D* is 3 x10^{-3} mm^2s^{-1}, while for biological tissues these values are only about 10-50% as long, possibly around 1.0 x 10^{-3} mm^2s^{-1} [1].

A key feature of biological tissues is their heterogeneity, with multiple compartments with varying diffusivities. As mentioned above, neuronal tissues, which are the ones of interest in this thesis, have a fibrillar structure. In white matter, axons, along with the adjacent glial cells, are tightly packed bundles, with mostly coherently distributed fibres. **Figure 3-32** clearly shows the ellipsoidal shape of the diffusion resulting from the hindrance enforced by the tissue microstructure (highly hindered in the perpendicular direction to the axon orientation). This is a good example of the anisotropic diffusion mentioned above, which is directionally aligned with the fibres bundle.

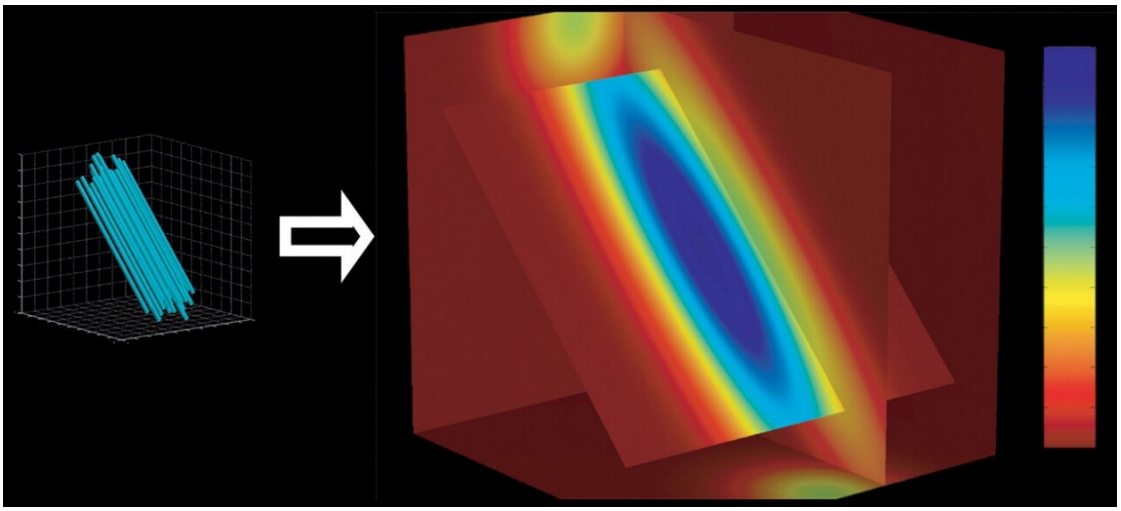

Figure 3-32 3D diffusion probability density function within a voxel in which all the axons are directionally aligned, resulting in a cigar shaped displacement distribution that is aligned with the axons (From Hagmann [et al.][15], ©RSNA, 2006). Reproduced with permission from RSNA

This particular representation works well in voxels covering large tracts with the same orientation, but becomes much less straightforward as soon as there are crossing fibres. **Figure 3-33** shows what happens to the diffusion probability density function when two bundles of fibres cross at a 90º angle[15], resulting in a cross-shaped diffusion model. Even this, as we will see below, is a rather simple model since voxels often includes bundles of fibres with multiple orientations rather than just two.

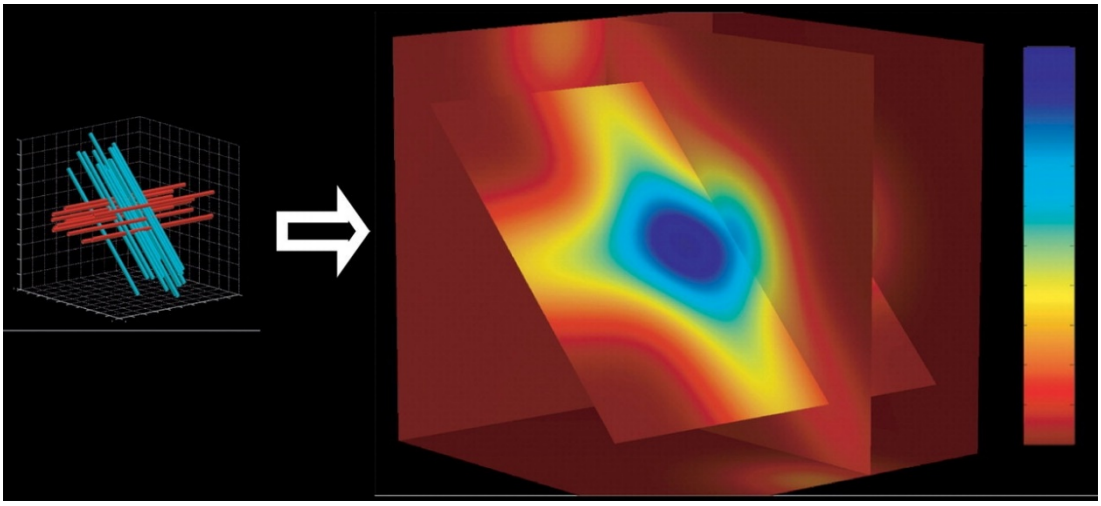

Figure 3-34 3D diffusion probability density function within a voxel containing two populations of fibres crossing at a 90° angle, producing a cross shaped molecular displacement distribution (From Hagmann [et al.][15], ©RSNA, 2006). Reproduced with permission from RSNA

The final level that needs to be included in the analysis is the position of the voxel, this is another 3D vector designated as **p**. So for the full description of what is happening in each voxel, the position **p** is assigned a diffusion probability density function (*f*), with ***f*(p,r)** describing the proportions of molecules in a voxel at position **p** that have been displaced a distance **r**. These additional three dimensions pose another challenge for representation. As the most relevant information comes from determining the direction of the most rapid diffusion, which is likely to correspond with the axons orientation, an orientation distribution function (ODF) is computed. Here too colours are used, this time it is to code the diffusion direction along the x, y, z axes: [x,y,z] = [r,b,g,], where r = red, b=blue and g=green[15]. An example of what an orientation distribution function for a single voxel would look like is given in **Figure 3-34,** with a map of coronal section shown in **Figure 3-35.**

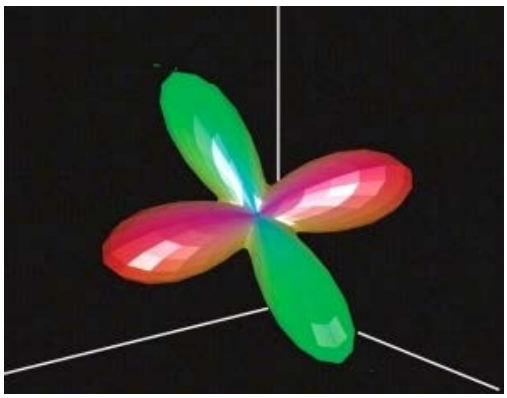

Figure 3-33 An example of the computation of the orientation distribution function (ODF). distribution.

(Adapted from Hagmann [et al.][15], ©RSNA, 2006). Reproduced with permission from RSNA

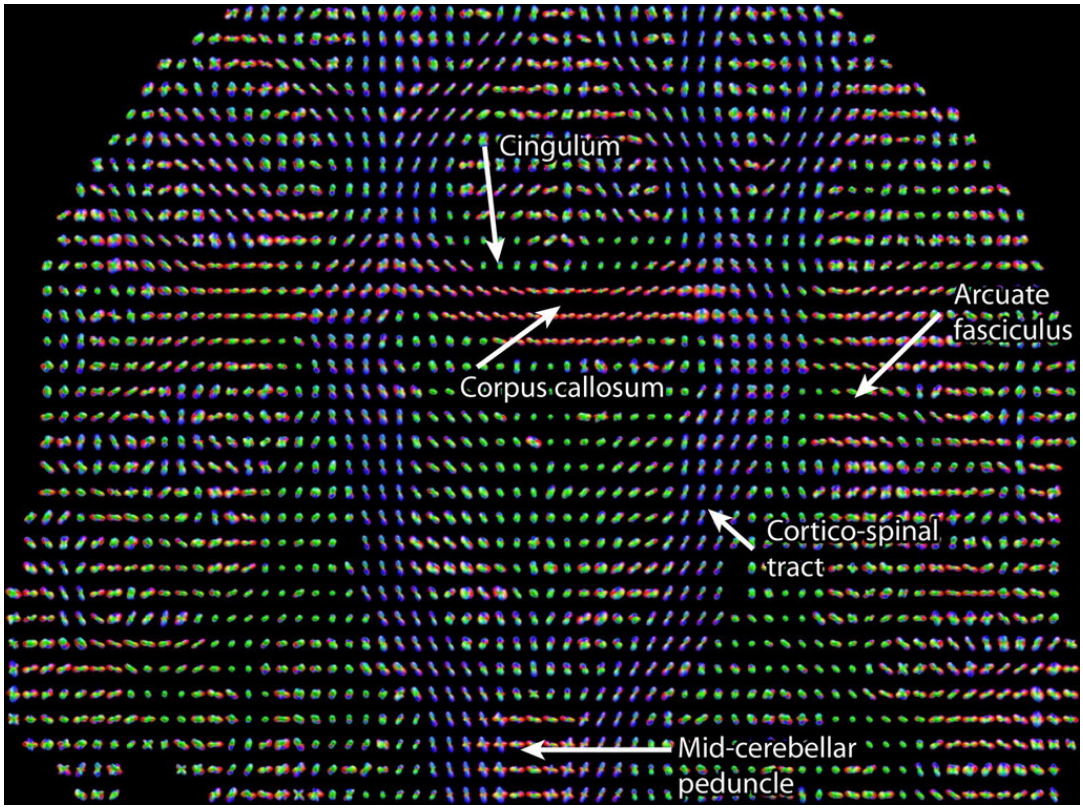

Figure 3-35 ODF map of a coronal brain section, with some easily identifiable tracts: corticospinal tract (mostly blue) and corpus callosum (predominantly red). Other tracts, such as the cingulum, the arcuate fasciculus (primarily green), and the middle cerebellar peduncle (chiefly red) are more difficult to see (From Hagmann [et al.][15], ©RSNA, 2006). Reproduced with permission from RSNA

3.3.2 dMRI acquisition

dMRI measures are based on the dephasing of protons spins following the application of diffusion-weighting gradients in varying directions. Scans are usually acquired using echo-planar imaging (EPI) involving a single 90º-180º pair of RF pulses, as well the diffusion gradients. **Figure 3-36** illustrates a 3D dMRI spin echo sequence, with the diffusion-weighted (DW) gradients applied in all three directions. The DW gradients induce spatially-dependent phase shift and then reverse it. Consequently, static/non-diffusing spins return to their initial state, while spin that have moved because of diffusion will undergo a total phase shift leading to a decreased intensity of the measured MR signal[16,20]. The TE used is normally greater than 100ms. The protocol also needs to incorporates a varying number of sampled orientations, with values between 20 and 60 gradient directions being among the most commonly used.

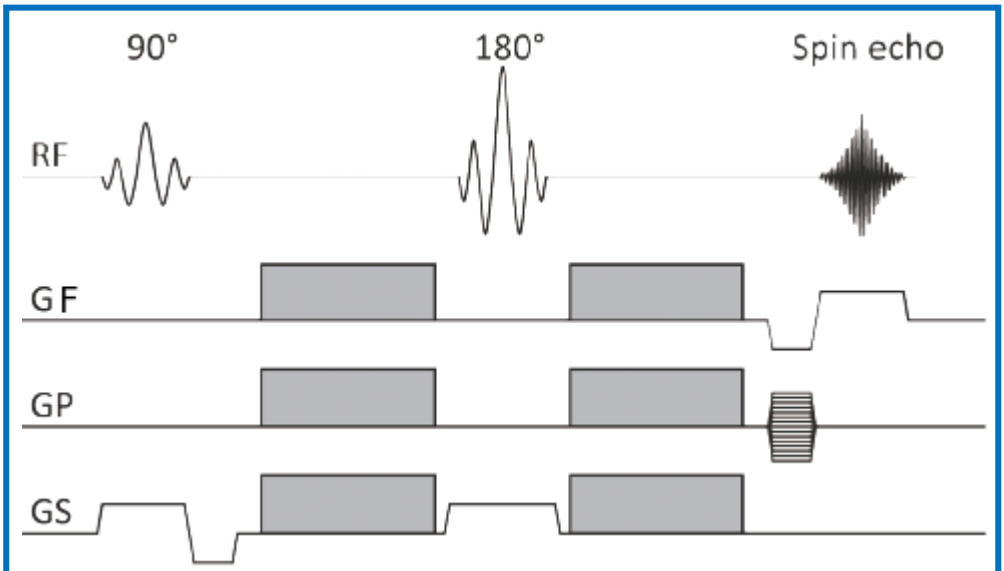

Figure 3-36 A 3D dMRI spin echo acquisition sequence, with the diffusion-weighted gradients represented as grey blocks included in each spatial encoding gradient (Adapted from Winston, 2012[16]). Adapted with permission from AME Publishing Company

In order to measure the actual diffusion, at least two sets of images are necessary, beginning with one with no diffusion, known as *b*0. For the brain, the second one, which will used to determine the diffusion coefficient *D* in each voxel, consists of *b*-values varying between 700 and 1300 s/mm^2, with 1000 s/mm^2 being the most commonly used one[20]. However, when it comes to measuring the actual diffusion from MRI scans, because diffusion in tissues is anisotropic, *D* is replaced by the apparent diffusion coefficient (ADC).

3.3.3 Apparent diffusion coefficient (ADC) and diffusion tensors

ADC reflects the diffusion as it occurs in tissues, incorporating facts such as the hindrance caused by biological barriers, as well as other aspects also affecting the signal, such as cytoplasmic streaming, blood flow in the microcirculation or phase dispersion due to susceptibility effects. In anisotropic tissues such as white matter (WM), the ADC will vary with the direction in which it is measured (determined by the direction of the diffusion gradients used): fast along the axon, as it is the main direction of diffusion, and slower perpendicularly because it is highly restricted. In GM however, as diffusion is mainly isotropic, the direction of the diffusion gradients will hardly have any influence[1,16]. Besides while ADC can be used to map the mean diffusivity

(MD), diffusion measurements are mostly done using a tensor model, commonly called diffusion tensor imaging (DTI).

Tensors are based on measurements along 6 spatial directions: three eigenvalues (λ1, λ2, and λ3) and three eigenvectors (ε1, ε2, and ε3) which define the shape and orientation of the tensor (see **Figure 3-37**) and reflect the various diffusion properties of each voxel.

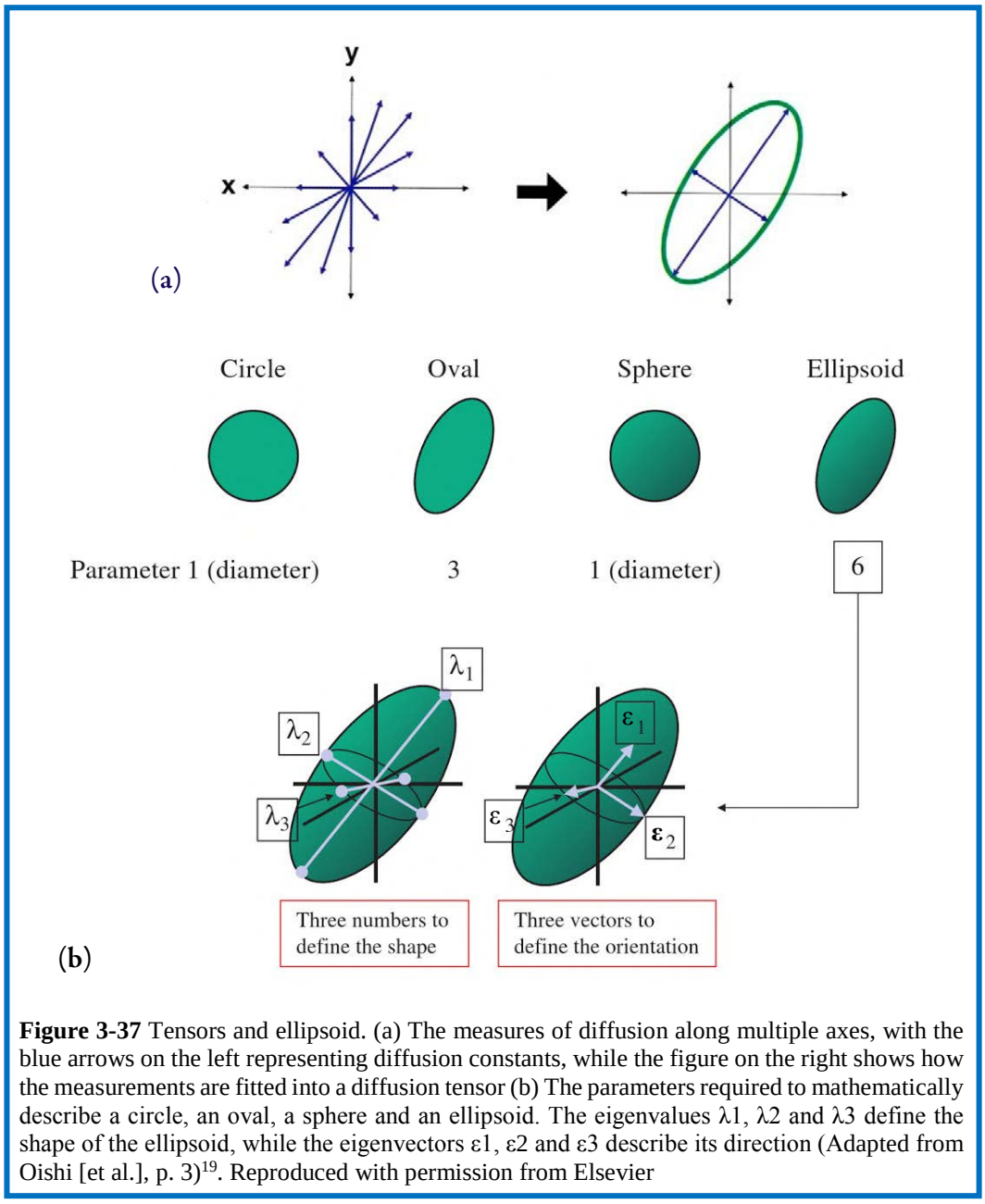

Figure 3-37 Tensors and ellipsoid. (a) The measures of diffusion along multiple axes, with the blue arrows on the left representing diffusion constants, while the figure on the right shows how the measurements are fitted into a diffusion tensor (b) The parameters required to mathematically describe a circle, an oval, a sphere and an ellipsoid. The eigenvalues λ1, λ2 and λ3 define the shape of the ellipsoid, while the eigenvectors ε1, ε2 and ε3 describe its direction (Adapted from Oishi [et al.], p. 3)[19]. Reproduced with permission from Elsevier

Tensors are calculated using both eigenvalues (λ1, λ2, and λ3) and eigenvectors (ε1, ε2, and ε3) using a 3x3 covariance matrix (the whole process is shown in **Figure 3-38**), while ADC is the average of the eigenvalues (λ1,λ2,λ3).

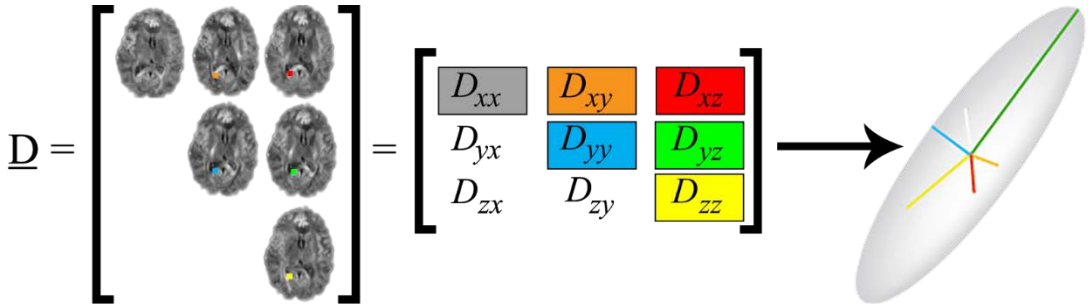

Figure 3-38 From gradients to tensors: how the different gradients are combined to calculate the tensor (From Tromp [et al.][21]). Reproduced with permission from the authors.

Eigenvalues are also used to calculate multiple diffusion measurements besides MD: longitudinal/axial diffusivity (AD), radial diffusivity (RD) and the most commonly used, fractional anisotropy (FA), which is one of the techniques applied in the next chapter.

3.3.4 Fractional anisotropy (FA)

Fractional anisotropy measures the amount of diffusion asymmetry within a voxel, based on the relative difference between the largest eigenvalue when compared to the others:

$$FA = \sqrt{\frac{3}{2}}\sqrt{\frac{(\lambda_1 - (\lambda))^2 + (\lambda_2 - (\lambda))^2 + (\lambda_3 - (\lambda))^2}{\lambda_1^2 + \lambda_2^2 + \lambda_3^2}}$$

The value of FA varies between 0 and 1, with 0 representing perfect isotropic diffusion where all the eigenvalues are equal, while 1 will be an elongated ellipsoid where λ_1 will be much larger than the other two eigenvalues. It is used to generate a map in which a grey-scale display of FA values represent the diffusion across the brain, with more anisotropic areas appearing brighter[1,22] as can be seen in **Figure 3-39**.

However, because tensors can only show the dominant fibre orientation, they only work well in those voxels where fibres mostly have a single orientation. They cannot be used to map voxels covering tracts with multiple orientations

or crossing fibres. Moreover, DTI models also proves inadequate for grey matter since diffusion there is mostly isotropic[1,16]. This the reason why new models, such as Neurite Orientation Dispersion Imaging (NODDI), the technique applied in the next chapter, have been developed.

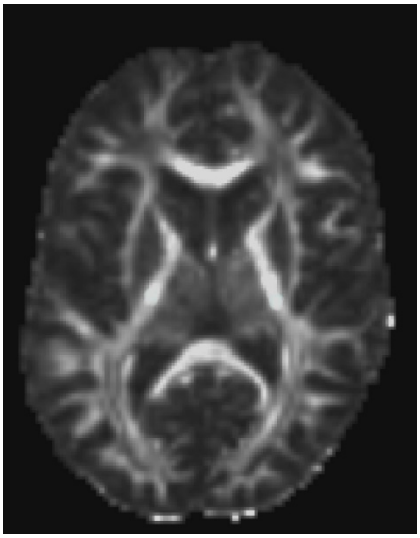

Figure 3-39 FA map, with the internal capsules and corpus callosum appearing particularly bright as highly organised tracts have high FA values.

3.3.5 Neurite Orientation Dispersion and Density Imaging (NODDI)

NODDI was introduced and validated by Zhang and colleagues in 2012[23], offering a new way to model the microstructure of dendrites and axons, with the aim to offer more specific markers than standard indices from diffusion tensor imaging, such as fractional anisotropy or mean diffusivity.

In order to achieve this, the NODDI tissue model uses three compartments representing the three main components of microstructural environment: intra-cellular, extra-cellular and CSF. To obtain a good representation of the orientation dispersion in both grey and white matter, the model uses the concept of a zero radius cylinders or sticks to represent the intracellular space, followed by the application a Watson distribution to determine the orientation distribution[23]. The extra-cellular compartment and the CSF one are represented by Gaussian distribution, anisotropic for the first and isotropic for the second[16]. An illustration of the NODDI tissue model is shown in **Figure 3-40**.

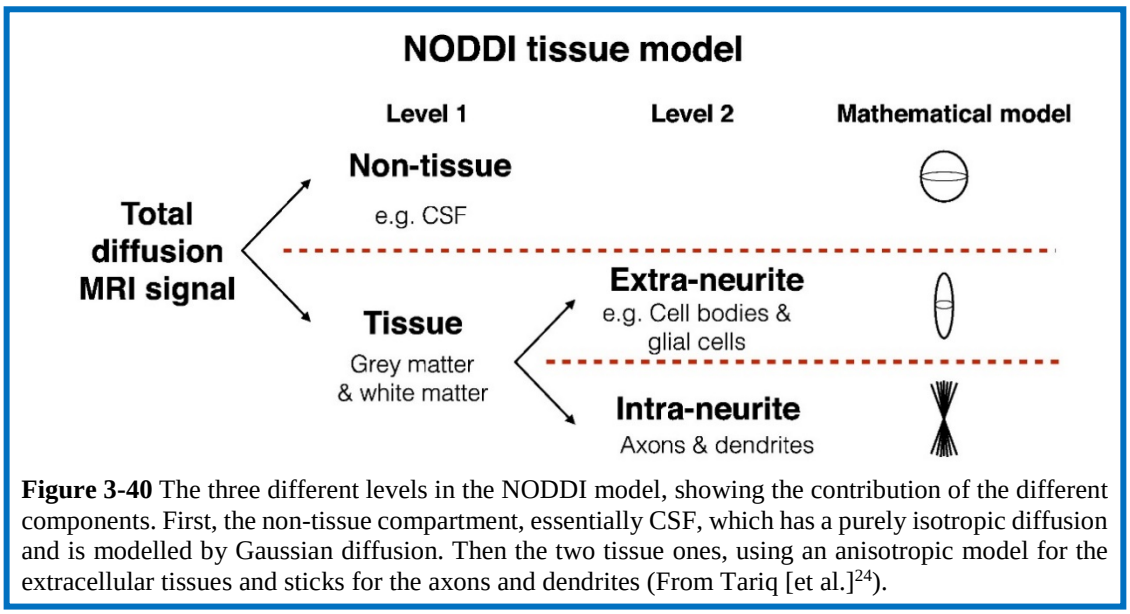

Figure 3-40 The three different levels in the NODDI model, showing the contribution of the different components. First, the non-tissue compartment, essentially CSF, which has a purely isotropic diffusion and is modelled by Gaussian diffusion. Then the two tissue ones, using an anisotropic model for the extracellular tissues and sticks for the axons and dendrites (From Tariq [et al.][24]).

3.3.5.1 NODDI maps

Three parameters maps can be generated with the NODDI tissue model: orientation dispersion index (ODI), neurite dispersion index (NDI) and isotropic volume fraction (v_{iso}), which are shown in **Figure 3-41**. The estimates of tissue microstructure provided by the ODI and NDI maps make it possible to disentangle two key variables contributing to FA, therefore providing additional information about the nature of the changes observed[25]. The reason why this new information is particularly relevant is because of the lack of specificity in FA when it comes to identifying the causes underlying the observed changes[22,26,27].

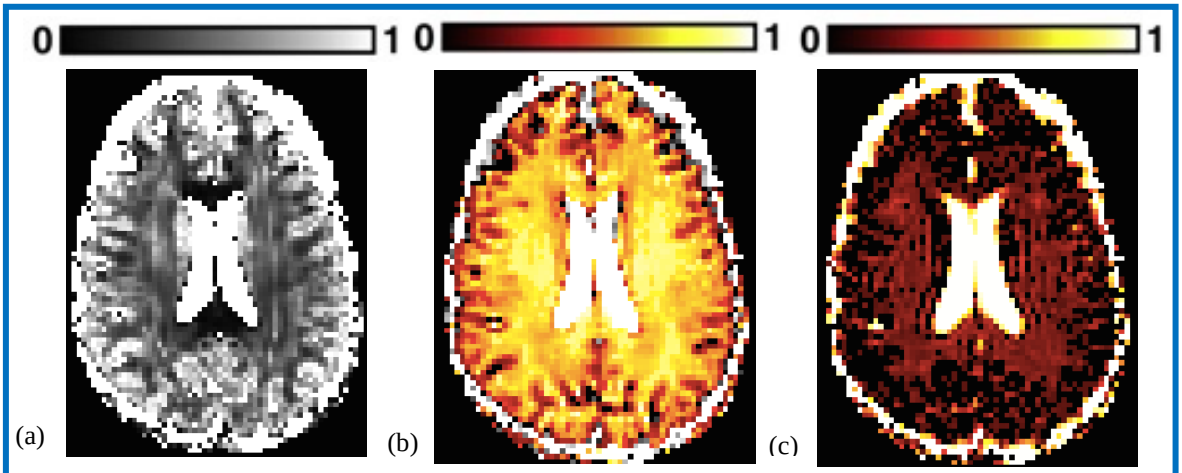

Figure 3-41 NODDI maps: (a) ODI, (b) NDI, (c) v_{iso} (From Zhang [et al.][23]). Reproduced with permission from Elsevier

3.3.5.2 NODDI acquisition

The acquisition of images for NODDI requires at least two high angular resolution diffusion imaging (HARDI) shells for the optimal fitting to be obtained. For the purpose of this thesis, the technique was applied to single-shell data to assess feasibility, as will be explained in the next chapter.

3.4 Phase-Sensitive Inversion Recovery (PSIR)

As mentioned in section 3.2.5 on inversion recovery, PSIR is a reconstruction technique. The images are acquired using an inversion recovery sequence, with two separate interleaved acquisitions (**Figure 3-42**) and can have a high resolution. For example, for the study a voxel size of 0.5x0.5 mm in-plane and 2 mm slice thickness was used. The interleaving is necessary when thin slices are required: as the RF has a Gaussian shape, while slices have a rectangular one, parts of the adjacent slices will get excited, thus causing partial excitation of adjacent slices ('cross-talk' effect). The two separate acquisitions mean that the cross-talk effect is prevented and also that slices are back to equilibrium by the time the second series of images are acquired.

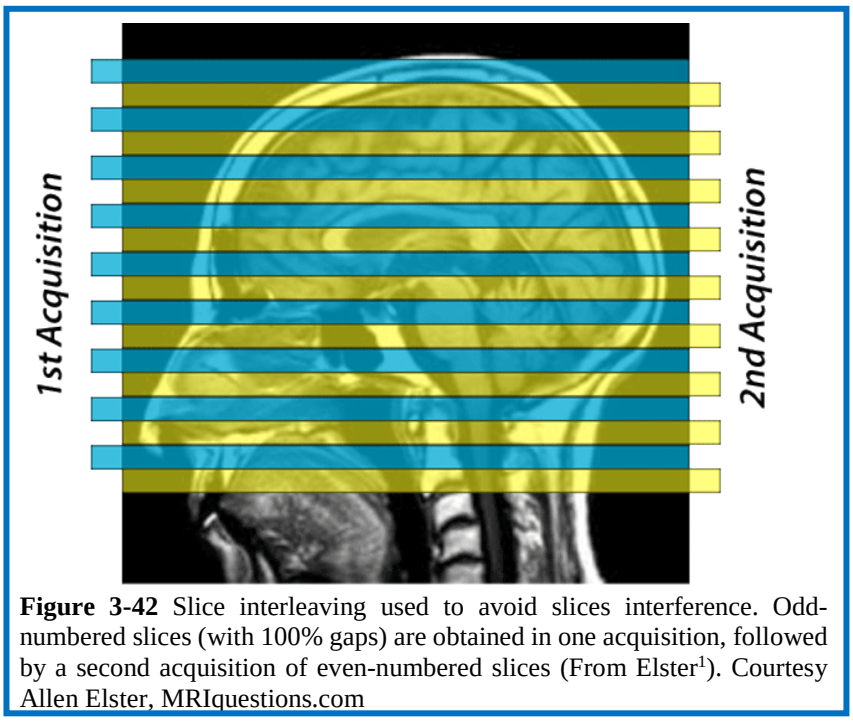

Figure 3-42 Slice interleaving used to avoid slices interference. Odd-numbered slices (with 100% gaps) are obtained in one acquisition, followed by a second acquisition of even-numbered slices (From Elster[1]). Courtesy Allen Elster, MRIquestions.com

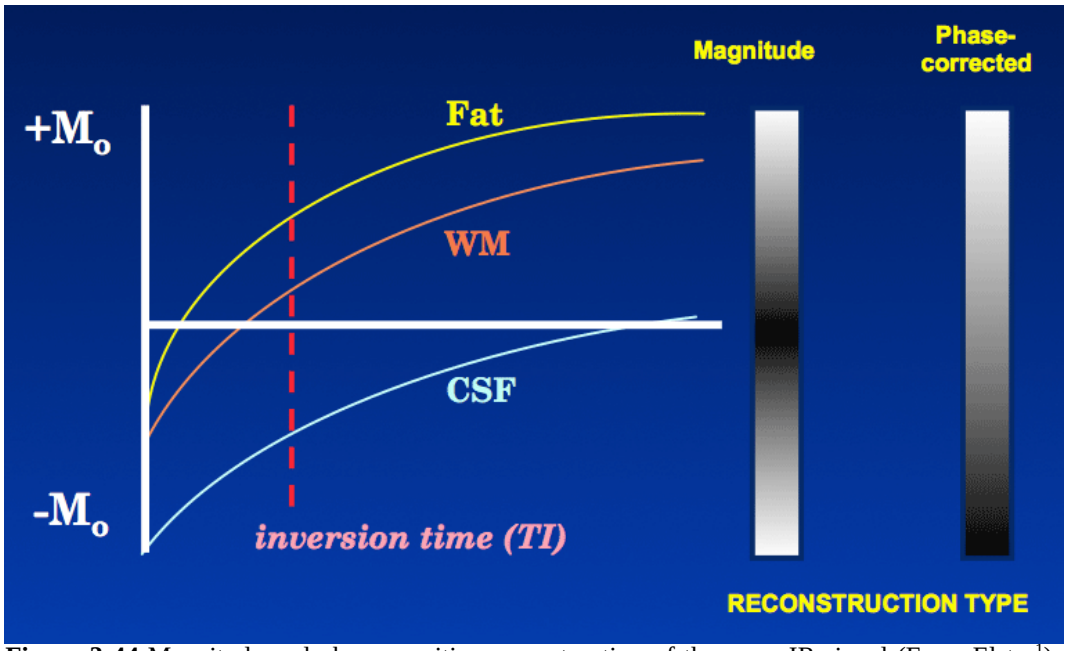

Figure 3-44 Magnitude and phase-sensitive reconstruction of the same IR signal (From Elster[1]). Courtesy Allen Elster, MRIquestions.com

The other advantage of this technique is the high contrast resulting from the phase-sensitive reconstruction. The reason for this is that this reconstruction retains the positive and negative polarities of tissues. In other words, the magnetisation measured will go from negative to positive, differentiating between tissues with similar magnetisation but opposite polarities. This differs from the more traditional magnitude reconstruction used for IR, which does not take the polarity of the signal into account. So after the selective nulling, all the tissues will have positive signal intensities and therefore two tissues whose magnetisation at inversion time is equal but with opposite polarities will be represented in the same shade of grey and thus be indistinguishable[1]. The reconstructions and the contrasting results obtained can be seen in **Figures 3-43** and **3-44**.

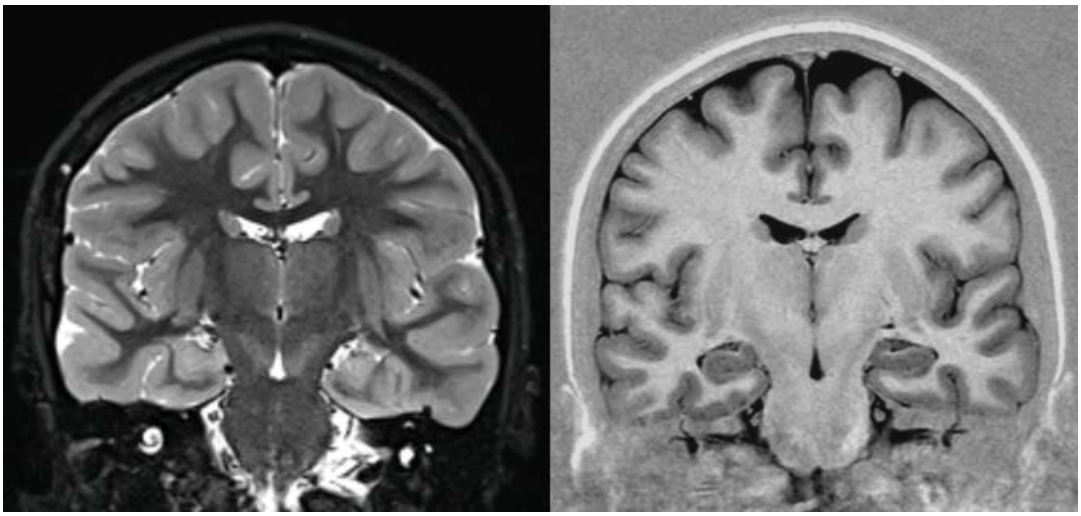

Figure 3-43 Magnitude (left) and phase-sensitive (right) reconstructions (From Elster[1]). Courtesy Allen Elster, MRIquestions.com

3.5 Magnetisation transfer ratio

The last MRI technique used in the context of this thesis is magnetisation transfer ratio. In order to explain how this technique works, it is necessary first to look at the different sources of MRI signal.

3.5.1 Sources of MRI signal

There are five main sources with enough ^{1}H protons to be used for MR signals[1], and four them are shown in **Figure 3-45**. They are as follows:

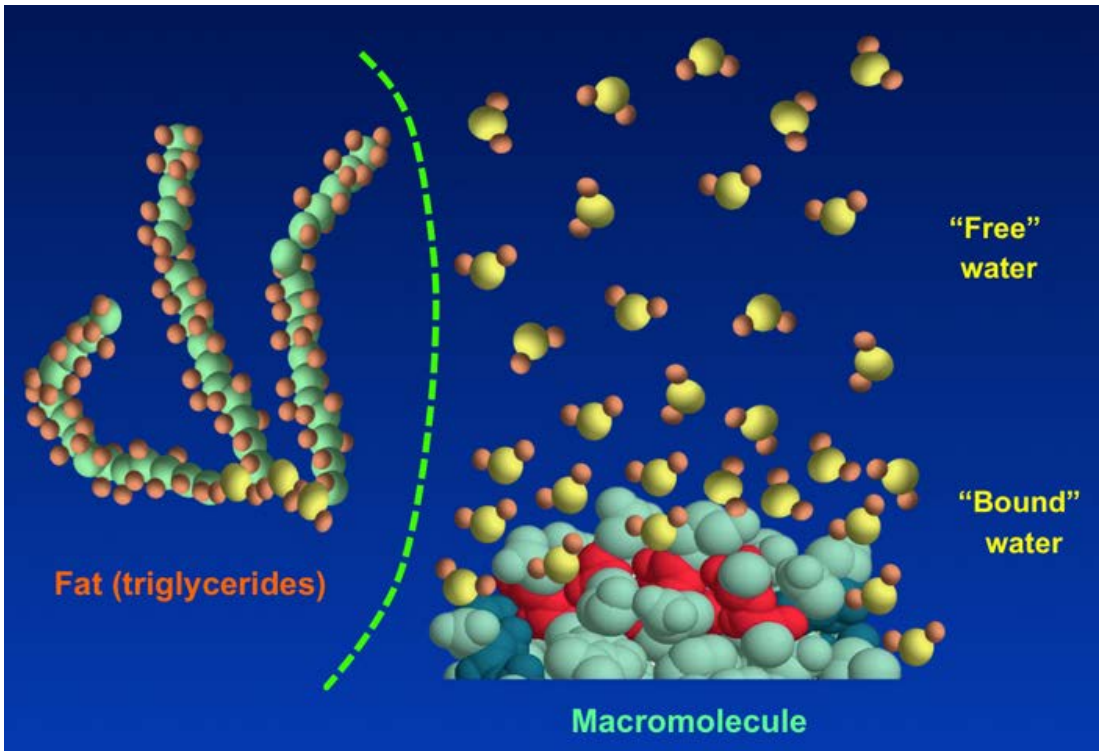

Figure 3-45 The major sources of protons at the origin of the MR signal or its modulation: free water, bound water, macromolecules, and fats. As lipid stores are usually in isolated compartments, they are separated by the dotted line (From Eslter[1]). Courtesy Allen Elster, MRIquestions.com

- **Free Water:** In the brain, it is mostly the CSF, but it is also found in the cytosol. Just as in the rest of the body, this is largest and most important source of NMR signal. Moreover, because water molecules in this pool only bind transiently (which is why they are described as 'free'), ^{1}H protons will rotate very quickly and over a wide range of frequencies. Consequently, this pool has long T1 and T2 relaxation times.
- **Fat:** The long chains of fatty acids found in tissues comprising large amounts of lipids (including triglycerides) are an important source of ^{1}H protons, thus

making a substantial direct contribution to the MR signal. As would be expected, motion of protons from this pool is relatively restricted, resulting in short T1 and T2 values (a few hundreds of ms and a few dozens of ms respectively). Tissues contributing to this pool include adipose and skeletal tissues, as well as bone marrow, but not cell membrane phospholipids or myelin (both have very short T2 values, so cannot be directly observed).

- **Macromolecules:** This category includes molecules such as proteins, phospholipids or polysaccharides. Most ^{1}H protons they contain will have highly restricted motion, resulting in very short T2 (μs or less) and signal decay so rapid that it is undetectable by conventional MRI techniques. They do however affect the speed at which protons within water molecules rotate, therefore increasing the signal produced.
- **'Bound' water**: This pool consists of water molecules bound to the surface of macromolecules (for example around the hydrophilic heads of phospholipids). Because hydrogen atoms binds at specific sites of the macromolecules, water motion becomes restricted, and thus the normally rapid rotation of water molecules is slowed down, shortening both T1 and T2 values when compared to free water. The degree to which this occurs will depend on both the concentration and size of the macromolecules, as well as on the number of hydrophilic groups available to bind water molecules. Finally, and a key aspect for magnetisation transfer, 'bound' water hinders free water on its outer surface, thus creating a pathway for transfer of magnetisation between the macromolecular and free pools.
- **Small organic molecules:** A wide range of small molecules such as amino acids, sugars, sodium and various metabolites such as N-Acetylaspartate (NAA), choline, creatine, etc. also emit MR signals which can be used in MR spectroscopy. It is important to note however that because their concentrations are so small when compared to water, the water signal has to be totally suppressed in order to measure them. A process that can be quite difficult to achieve, in particular in the spinal cord.

3.5.2 Magnetisation Transfer

As the discussion about the sources above suggests, there are two pools involved in magnetisation transfer: the bound pool consisting of bound water and the free pool, containing the free water. As can be seen in **Figure 3-46**, both are centred on the same Larmor frequency, but the bound pool has a broad range of resonance frequencies (<10-50 kHz) and a very short T2 (10-20 μs), while the frequencies range for the free water is extremely narrow (<0-100 Hz) and the T2 relatively long (>10-100 ms)[1,28].

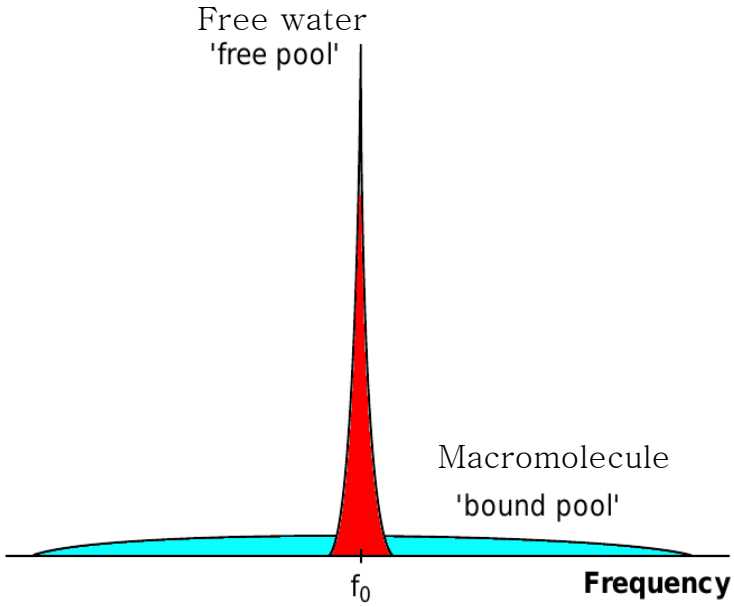

Figure 3-46 The frequencies range of the bound and free pools (Adapted from de Boer[28]). Reproduced with permission from the author.

Under normal MR conditions, magnetisation is exchanged between both pools so that they are in a state of equilibrium, with changes occurring in both pools when a RF pulse is applied. In order to use magnetisation transfer, this situation needs to be altered. This is done by selectively saturating the bound pool with an off-resonance RF pulse, known as the MT pulse. This can be achieved because of the broad frequencies range of the bound pool and will not affect the free water pool. The next stage consists of following the magnetisation transfer from the free pool to the bound one as the two pools return to equilibrium[1,28].

De Boer[28] offers an excellent explanation of the magnetisation transfer (MT) phenomenon by using a simplified model of a biological tissue containing a free pool made of four water molecules with four proton spins and a macromolecule with three proton spins as a bound pool. **Figure 3-47** illustrates the different stages of MT from the pre-saturation equilibrium with a signal to noise ratio (S/N) of 4 to the new equilibrium post MT where it has decreased to 2. This is due to the partial saturation of protons in the free pool reducing the net magnetization of the free water pool when a RF pulse at the Larmor frequency is applied. This process is known as cross-relaxation and reduces the longitudinal magnetisation available for imaging. The new shorter longitudinal relaxation time is described as the apparent longitudinal relaxation time ($T1_{sat}$).

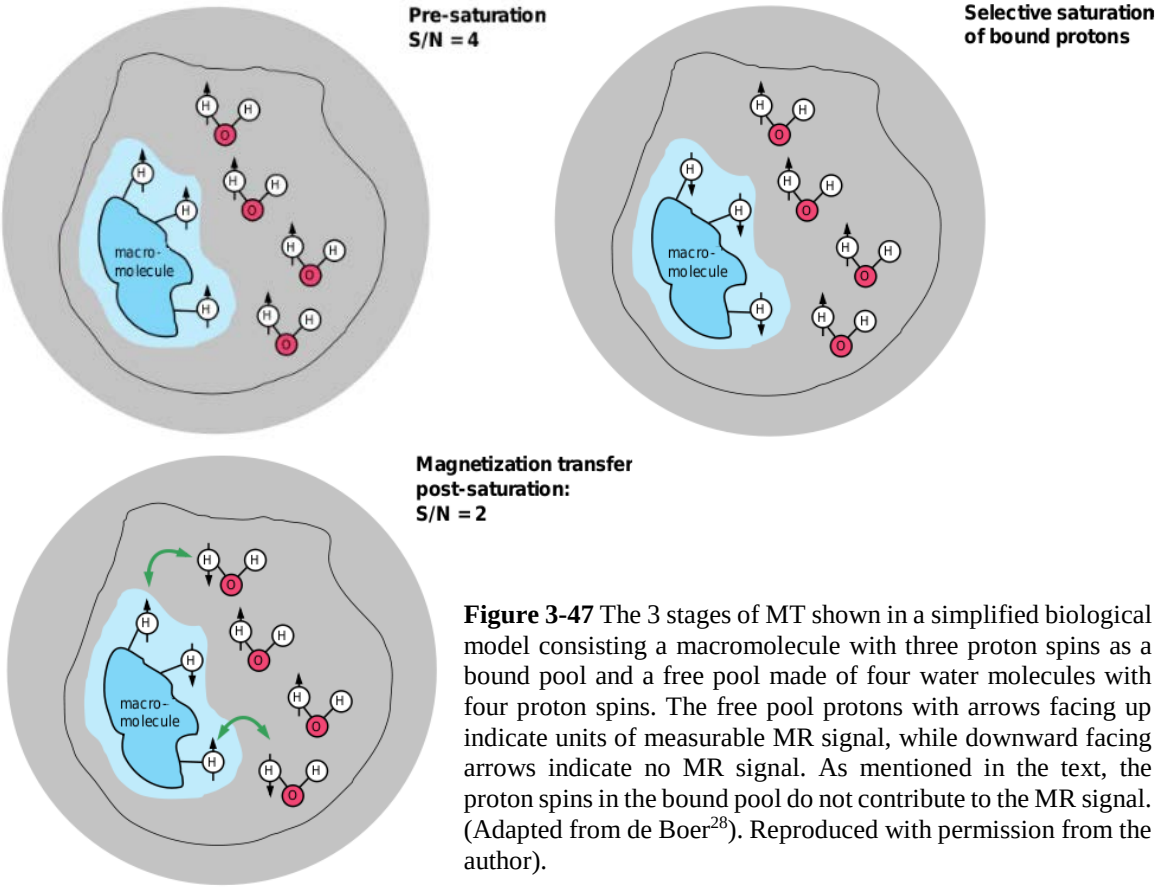

Figure 3-47 The 3 stages of MT shown in a simplified biological model consisting a macromolecule with three proton spins as a bound pool and a free pool made of four water molecules with four proton spins. The free pool protons with arrows facing up indicate units of measurable MR signal, while downward facing arrows indicate no MR signal. As mentioned in the text, the proton spins in the bound pool do not contribute to the MR signal. (Adapted from de Boer[28]). Reproduced with permission from the author).

Having seen how MT works, how can it be used to improve MRI contrast? Once again, de Boer simplified models are very useful. In this case, two hypothetical tissues are used. As can be seen in **Figure 3-48**, the central tissue has the same structure as the previously used model, while the peripheral tissue consists of

four free water molecules with four spins. As both tissues have the same number of detectable spins, both will have a S/N of 4 and therefore be indistinguishable on an MR image. However, after selective saturation has been applied to the bound pool and MT exchange has occurred, the central tissue now has a S/N of 2 while the peripheral tissue has not been affected. So now there is a new equilibrium situation in which there is a large contrast between the two tissues.

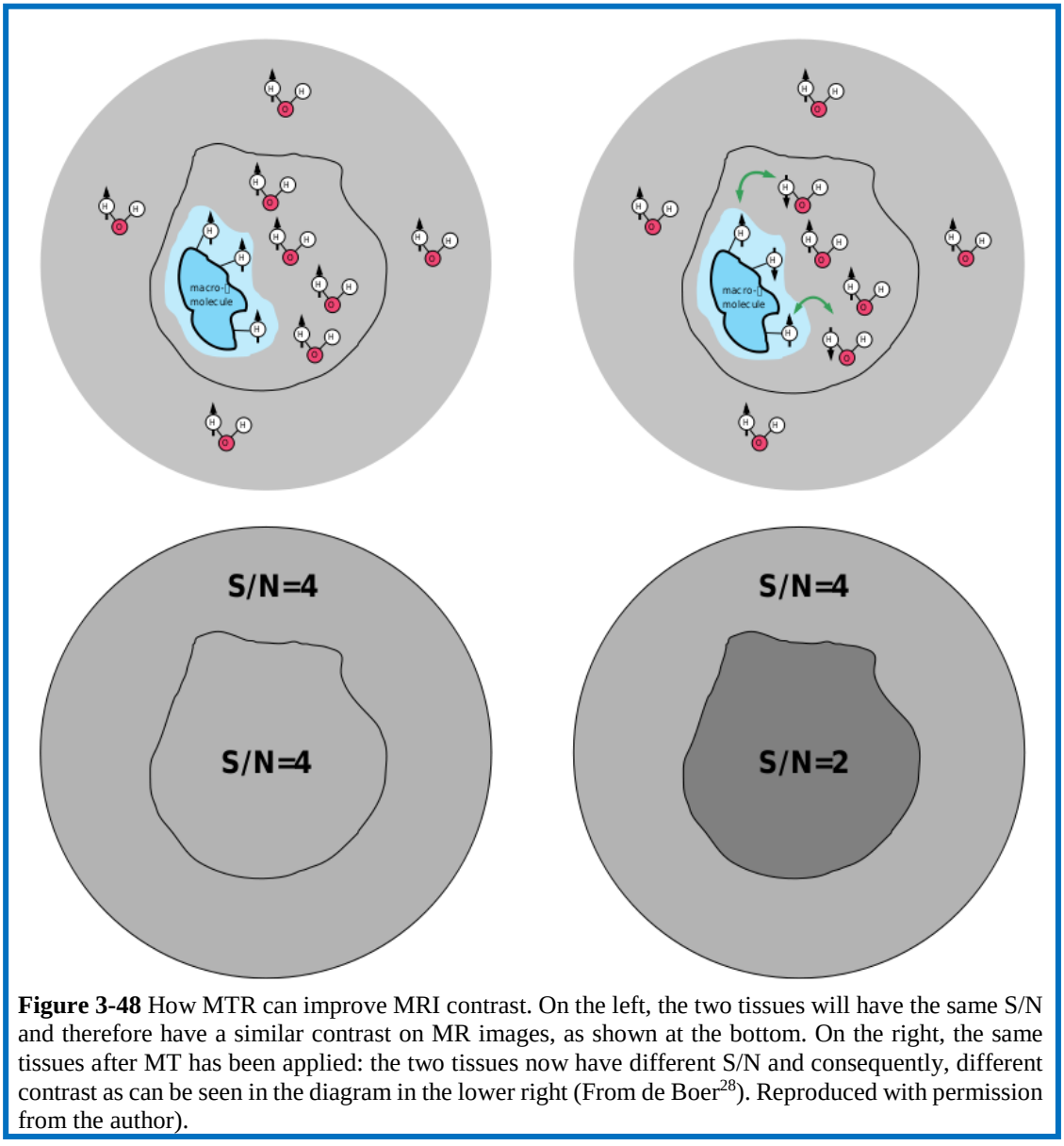

Figure 3-48 How MTR can improve MRI contrast. On the left, the two tissues will have the same S/N and therefore have a similar contrast on MR images, as shown at the bottom. On the right, the same tissues after MT has been applied: the two tissues now have different S/N and consequently, different contrast as can be seen in the diagram in the lower right (From de Boer[28]). Reproduced with permission from the author).

3.5.3 Cross-relaxation

Cross-relaxation is the term used to describe the energy exchange between the bound and free pools occurring during MT, but what is the mechanism behind it? In the model above, the interactions have been described between a simple

two pools representation, however as often the case when looking at biological tissues, things are slightly more complicated. The so-called free pool is in fact composed of two different 'strata': the largest part is made of fully mobile water molecules, but the water molecules closest to the macromolecule actually form an intermediate layer (see **Figure 4-49**), also known as hydration layer, and are less free than the fully free water, but nowhere as restricted as the water molecules in the bound pool. The initial transfer will occur between the bound water molecules and the transiently bound ones in the intermediate layer. The two layers from the free water exchange protons by diffusion, which is also how the magnetisation is transferred to the free water pool molecules, leading to the signal reduction mentioned above[1,28,29].

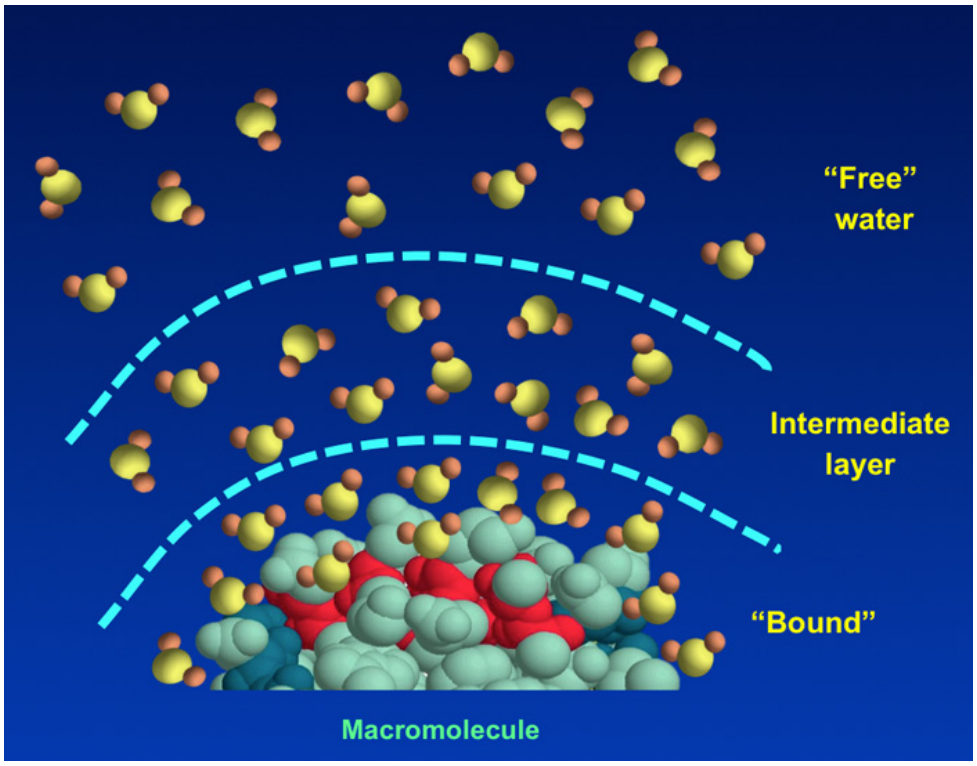

Figure 3-49 The two layers found in the free water pool. The water molecules closest to the macromolecules are less mobile and play a central role in the magnetization transfer from the macromolecule to the free water molecules (Form Ester[1]). Courtesy Allen Elster, MRIquestions.com

3.5.4 Saturating pulses, on- and off-resonance pulses

The last thing that needs to be looked into is the two key elements of the MT acquisition protocol: a saturating off resonance MT pulse is applied prior to the pulse sequence used to create the MT contrast. As mentioned above, the saturation pulses consist of RF pulses which are shifted 1000 to 25,000 Hz from

the centre of the Larmor frequency, which will saturate protons in the bound pools through diffusion, before transferring to the free water pool and leading to the signal reduction (**Figure 3-50**). Following saturation, a standard acquisition pulse is applied. This sequence needs to be repeated in order to achieve a steady state of relaxation[1,28-30].

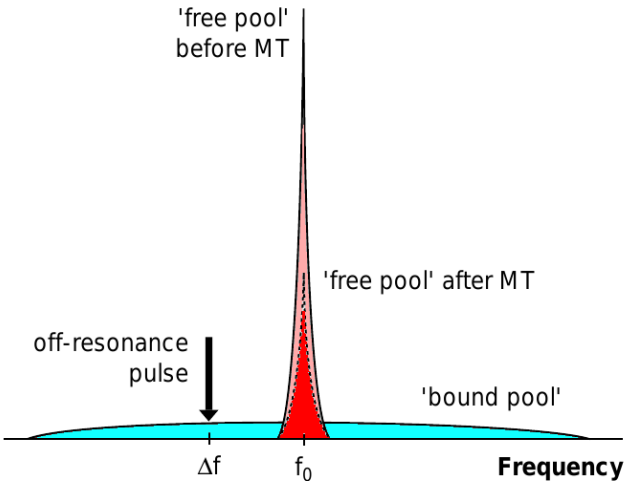

Figure 3-50 Effect of off-resonance pulse and MT on free pool (Adapted from de Boer[28]). Reproduced with permission from the author).

Finally, for the images themselves, the magnetisation transfer ratio (MTR) is based on the difference in intensity between the off-resonance and on-resonance images[29]. It is calculated as follows:

$$100\times(M_0-M_s)/M_0$$

where M_s and M_0 represent signal intensities from images with and without pre-saturation pulses. The three different images can be seen in **Figure 3-51.**

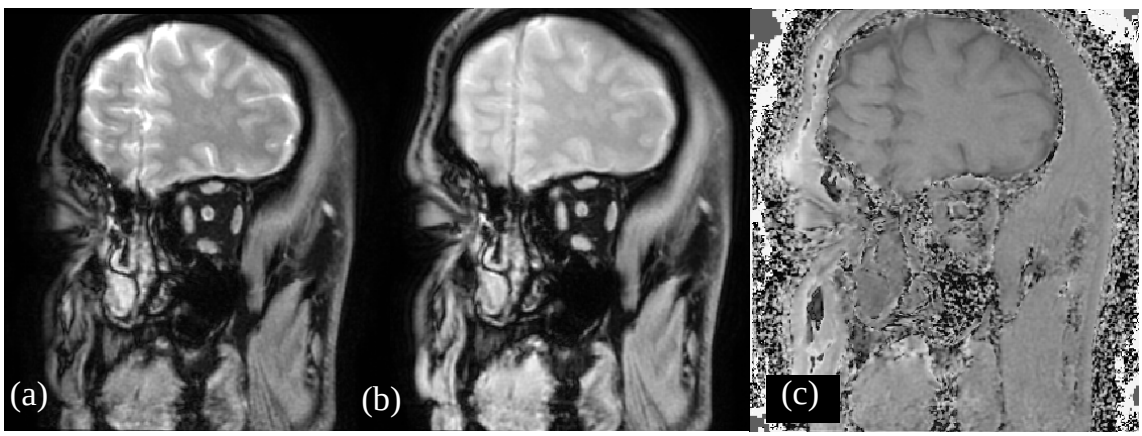

Figure 3-51 MT images: (a) MT off, (b) MT on, (c) MTR map acquired to look at the optic nerve.

One of the key reasons why this technique is particularly valuable, and the reasons it was used in this thesis, is that it provides information about myelin integrity[31]. This is something that cannot be achieved with other MRI techniques and thus gives MTR its distinctive significance among the wide array of MR procedures available. However, it should also be noted that MTR is only 'semi-quantitative' as it is dependent on the parameters of the pulse sequence, which means that data will also vary with the sequence used, making comparison between studies difficult.

3.6 Conclusion

Now that all the different MR techniques used in this thesis have been introduced, the next stage is to look at their application. The first one, which will be the topic of the next chapter, is diffusion MRI and NODDI.

Chapter 4

Application of single-shell Neurite Orientation Dispersion and Density Imaging (NODDI) to MS

4.1 NODDI

As described in Chapter 3, diffusion magnetic resonance imaging (dMRI) provides a mean to probe microstructures of the human brain in a non-invasive way. It can be used to assess the condition of the brain microstructures in both healthy subjects and patients suffering from neurological conditions, including multiple sclerosis (MS)[1]. The most common application in the first group is to evaluate changes associated with ageing[2,3], while in patients it is used to track the effects the disease and identify the areas most affected. Among disease related changes, those affecting neurites (the term use to cover both dendrites and axons) have proven particularly relevant. Thus a technique that can quantify morphological alterations in these structures could deliver new crucial data, in particular when it comes to detecting microstructural changes at an early stage (i.e. before they translate into visible damage such as lesions or plaques for example[1]). This would not only be useful for early diagnosis, but also open new prospects to understand disease mechanisms.

The previous chapter described the numerous limitations of traditional dMRI techniques based on tensors, which techniques such as NODDI attempt to address. Therefore, in the context of a study looking at new imaging techniques, we thought it would be interesting to test whether NODDI could provide valid data when applied to images obtained with a single-shell acquisition rather than the optimised two-shells NODDI protocol described in Zhang's paper[4]. For this purpose, we used a selection of relapsing-remitting multiple sclerosis (RRMS)

patients and matched healthy controls who underwent dMRI scanning as part of a previous study[5]. The key idea behind this study was to compare the performance of NODDI indices to FA in the context of MS in order to see whether NODDI could detect both additional differences between patients and controls, and correlations with clinical changes that were not detected with FA.

The notion that applying NODDI to single shell data may provide useful information is based on Zhang's paper, in which he demonstrated that single shell acquisition with $b \geq 1000$ s/mm^2 can produce a good estimate of the orientation dispersion index (ODI)[4]. This was the first application of the technique in the context of MS, and among the first applications to clinical data. Since then, NODDI has been used to look various diseases and conditions, including Alzheimer's disease[6], epilepsy[7-9], Parkinson's disease[10,11], stroke[12] and glioma[13]. It has also been applied to MS using a multiple shells acquisition protocols by Dr Wallace Brownlee[14], who is also attached to the Queen Square MS Centre.

In order to assess NODDI performance when looking at changes occurring in normal-appearing white matter (NAWM) and grey matter (GM) of RRMS patients, we used both ODI and the neurite density index (NDI), employing two different approaches. The first one was region-specific and consisted of 9 regions of interest (ROIs) in both NAWM and grey matter. The second approach aimed to look at the whole brain, using voxel-based morphometry (VBM), building up on the results obtained with the ROIs. The aim was to find how much the two NODDI indices used would differ from FA, and whether these differences would furnish us with additional information on the underlying structural damage occurring in the NAWM and grey matter of RRMS patients, when compared to the more conventional DTI measures such as FA.

4.2 Methods

4.2.1 Subjects

26 RRMS patients and 26 age and gender matched healthy controls taken from a cohort study conducted between 2010 and 2012[5]. Patients were diagnosed using the revised 2010 McDonald criteria, their mean age was 44.96 years (range 25-64), 18 were females and 8 males, the mean disease duration was 12.6 years (range: 1-33), and the median EDSS 1.5 (range 1-6.5). A group 26 age and gender matched healthy controls with a mean age of 43.08 years (range: 27-65), consisting of 14 females and 12 males, with no known neurological or psychiatric conditions, was also included. Patients also underwent cognitive tests, of which the following were used for this study: the symbol digit modalities test (SDMT)[15], a story recall and the Paced Auditory Serial Addition Test (PASAT)[16] as they were considered the most relevant in this context[17]. Clinical, cognitive and demographic data for the two groups are given in **Table 4-1**.

	RRMS patients	Healthy controls
Age (years)	44.96±10.03	43.08±8.92
Gender (F/M)	18/8	14/12
Median EDSS (range)	1.5 (1-6.5)	N/A
Disease duration (years)	12.6±9.58	N/A
WM PD/T2 LL (ml)	13.64 ±18.148	N/A
SDMT	49.28±14.44	N/A
PASAT	33.69±18.71	N/A
Story recall	30.88±11.90	N/A

Abbreviations: EDSS: Expanded Disability Status Scale; WM PD/T2 LL: white matter PD/T2 lesion load. Values are means unless otherwise indicated

Table 4-1 Demographic and clinical data

All subjects were scanned on a clinical 3T TX Philips Achieva scanner with a 32-channel head-coil and a dMRI imaging protocol that consisted of 61 b = 1200 s/mm2 dMRI volumes and 7 non- dMRI (b=0) volumes (voxel resolution of 2x2x2 mm^3). The number of sampled orientations for the dataset used was

61 while the optimised protocol has 30 in the first (low *b*-value) shell and 60 in the second (high *b*-value) shell. The images were eddy current corrected using FSL (FMRIB, Oxford, UK).

4.2.2 NODDI fitting

The optimised NODDI acquisition protocol[4] requires two high angular resolution diffusion imaging (HARDI) shells with *b*-values of 711 and 2855 s/mm^2, while the data used was acquired with a single shell (*b*-value: 1200 s/mm^2). To compensate for the absence of a second *b*-shell, the volume fraction of the isotropic compartment was set at 0; this means that that the CSF was not fitted in the model used, thus reducing degree of variance in the NDI maps (CSF voxels have the default value of 0.70482 in ODI maps and 0 in NDI ones).

To reduce the time taken for the fitting (6-7 hours), a brain mask based on the mean *b*0 (produced by averaging the seven b = 0 volumes) was created, using the BET tool in FSL with the -f value set at 0.3 (and in some cases 0.2) in order to ensure that the frontal lobes were fully included. This mask was then manually corrected in order to remove the superfluous areas included before using it for the fitting, which was thus limited to the brain.

Two maps, the Orientation dispersion index (ODI) and the Neurite density index (NDI), which was called intra-cellular volume fraction (Ficvf) in Zhang's paper[4], were used for the analysis.

4.2.3 ROIs approach

White matter	**Grey matter** (each region in both hemispheres)
Genu of corpus callosum	Frontal lobes (middle or superior frontal gyrus)
Body of corpus callosum	Occipital lobes (superior occipital gyrus)
Splenium of corpus callosum	Hippocampus
Posterior limb of the internal capsule	Thalamus (next to trigone of lateral ventricle)

Table 4-2 Regions of interest used.

15 regions of interest (ROI) of 9 voxels commonly affected by MS were selected (see **Table 4-2**) and manually positioned on the mean *b*0 map using Jim v. 6.0 (Xinapse systems, Aldwincle, UK, http://www.xinapse.com). Great

care was taken to avoid partial volumes in the genu and splenium, and whenever possible, the body of the corpus callosum. The broadest part of the posterior limb of the internal capsule was chosen for the same reason. Further checks were then conducted on both FA and ODI map to ensure that the whole mask was within the area of interest. The position of the white matter ROIs can be seen in **Figure 4-1**.

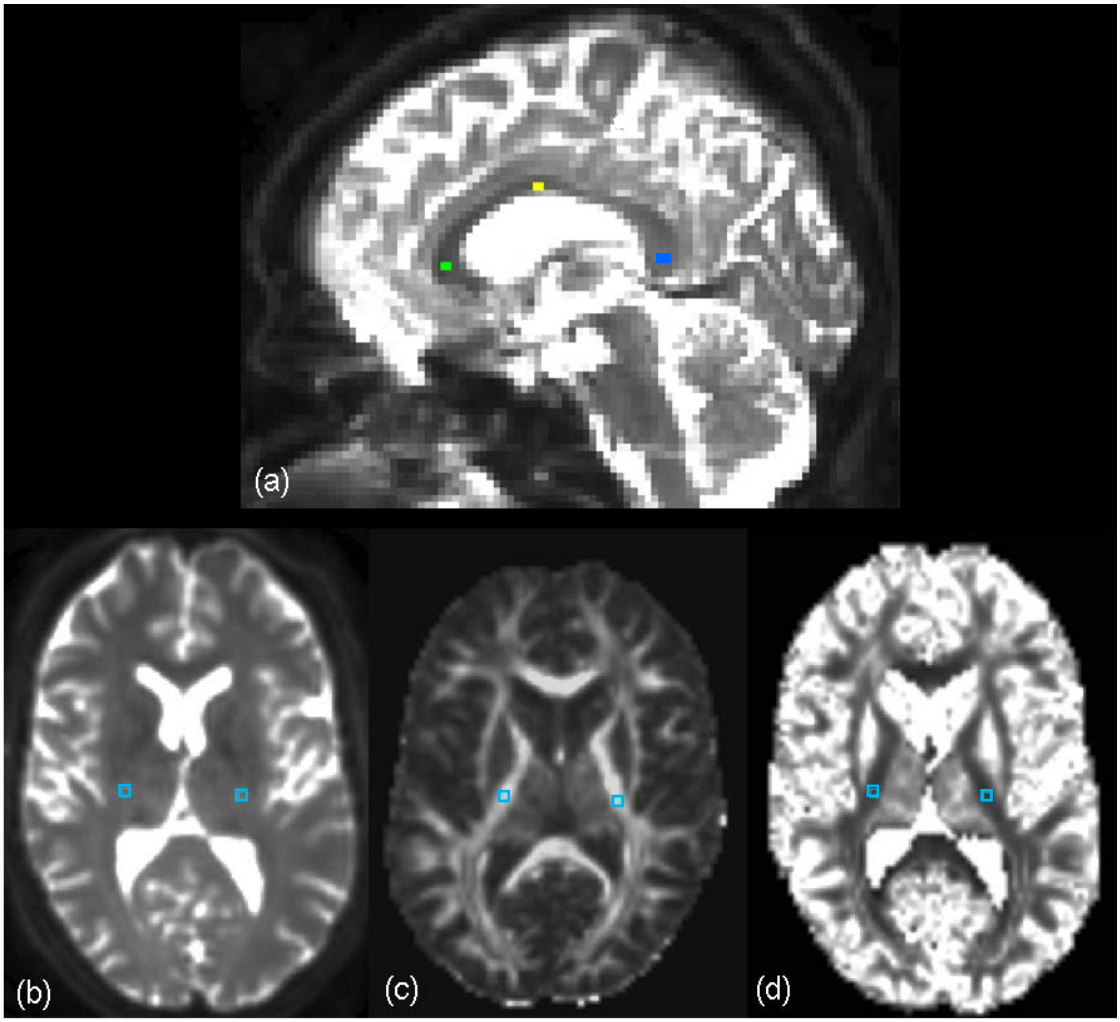

Figure 4-1 White matter ROIs: (a) in corpus callosum: genu (green), body (yellow) & splenium (blue); (b)-(d): internal capsules in mean B0, FA and ODI maps.

For the patients, hyperintense lesions had been manually outlined by an experienced neurologist on proton density (PD) images using the semi-automated edge finding tool from Jim v6.0. The lesion masks were then registered to the dMRI space and used to ensure that no ROI mask was positioned within a lesion. When that happened or when the lesion was sufficiently close to incur the risk of contamination, the position of the ROI was

changed. There were 6 patients with lesions in the left internal capsules (two requiring mask repositioning, together with a patient who had a lesion just below the internal capsule), but only two patients with lesions on the right, including one who had bilateral lesions.

Other ROIs repositioning was required in the WM of two patients: one had lesions both in the left internal capsule and the genu of the CC, while the other one had a lesion close to the body of the corpus callosum. One patient also had a highly atrophied corpus callosum, making the positioning of the ROIs in both the body and splenium quite difficult, and resulting in the possibility of some partial voxels.

Thalamic ROIs had to be repositioned in one patient, the one with bilateral lesions in the internal capsules, who also had enlarged ventricles due to atrophy leading to a narrowing of the thalamus. Two other patients had lesions in the thalamus, but not in the mask area.

For the cortical regions, the NDI maps (where CSF values was fixed at 0) were also used to ensure there was no CSF contamination of the ROIs (**Figure 4-2**). The thalamus was positioned next to the trigone of the lateral ventricle (**Figure 4-2**). Finally, T1 images were used to locate the hippocampus as this cannot be done on the mean *b*0 map due to the low spatial resolution. The following procedure was used to ensure correct positioning of the ROI: the shape of the

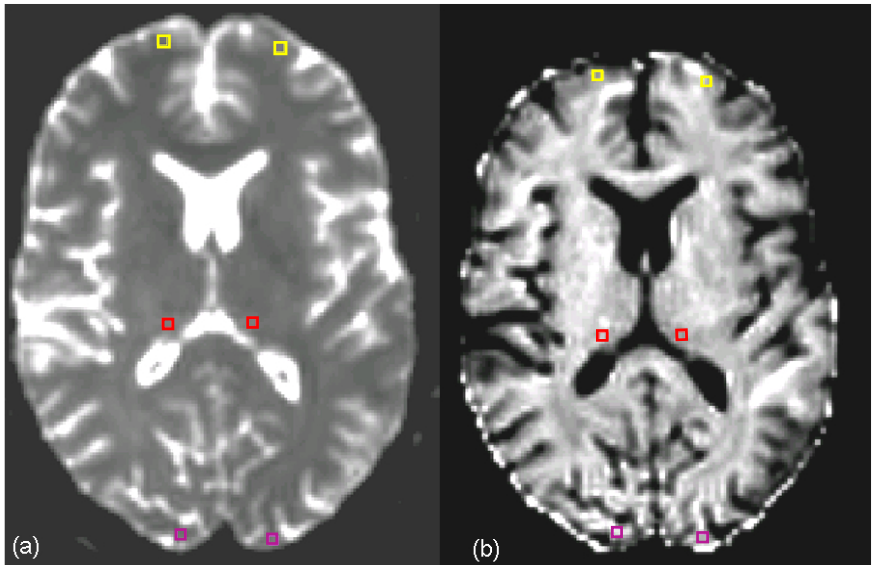

Figure 4-2 Grey matter ROIs: frontal lobes (yellow), occipital lobes (purple) and thalamus (red) in: (a) mean B0 & (b) NDI maps.

peduncles and position in relation to the cerebellum were used as landmarks to select the slice in the mean *b*0 map; the inferior (temporal) horn of the lateral ventricle was then compared between the T1 and mean *b*0 maps in order to locate the hippocampus (**Figure 4-3**).

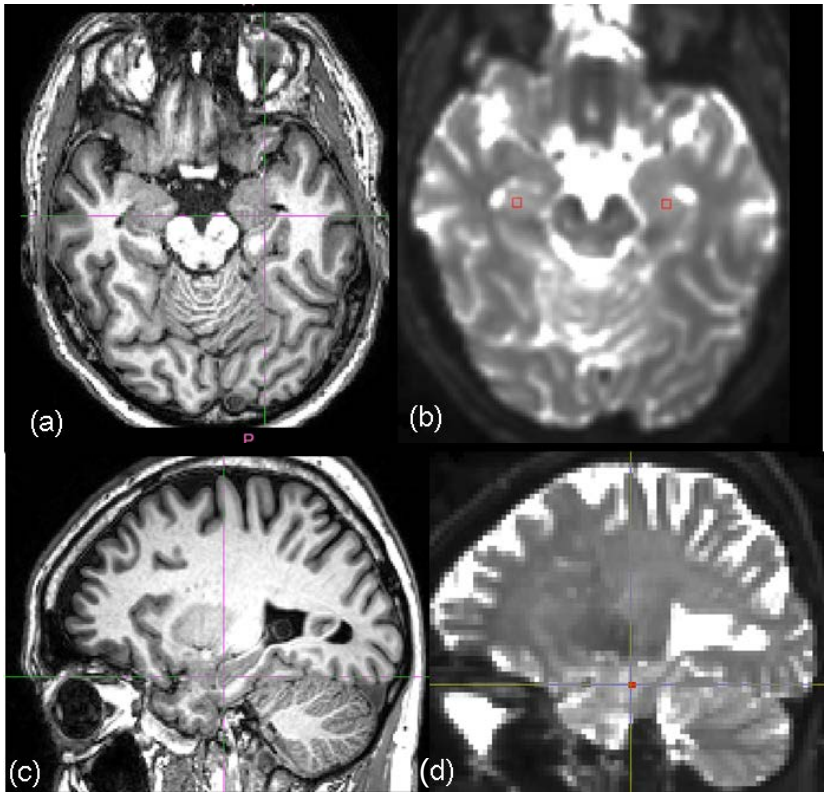

Figure 4-3 Positioning of hippocampal ROI with T1 images: (a) & (c) axial and sagittal T1, (b) & (d) corresponding mean B0 slides. The cerebellum and the shape of the peduncles were two key landmarks used to identify the hippocampus.

Two patients had lesions in the hippocampal region (one on the left and one on the right) necessitating some adjustment of the ROIs. Three patients had a lot of atrophy in the frontal lobes, one with some in the occipital lobes too.

Each side of specific structures were analysed separately in order to assess lateral differences. Finally, the mean FA, ODI and NDI values for each region were calculated using Jim v. 6.0.

4.2.3.1 Statistics for ROIs approach

The Mann-Whitney U test was used to compare ODI, NDI and FA between patients and controls. The correlations between FA, ODI, NDI and clinical scores were tested using Spearman's rho correlation coefficient. Results associated with $p<0.05$ were considered significant.

4.2.4 Voxel based morphometry (VBM) approach

Two important preparatory stages were necessary in order to apply VBM to the dataset. The first one was to fill the lesions to ensure they were not affecting the analysis since the aim was to detect changes in NAWM. For this purpose, the PD-weighted lesion masks underwent a symmetric and full affine co-registration to the 3D-T1 images, using a pseudo-T1 image generated by subtracting the PD from the T2-weighted image[18]. The affine transformation is used to remove size differences between brains, thus making it possible to align the different brain maps.

The lesion masks were then transformed from native space to 3D-T1 space using a nearest neighbour interpolation threshold, after which the 3D-T1 images were filled using a non-local patch match lesion filling technique[19]. Next comes the most crucial step: the registration.

4.2.4.1. Registration and normalisation

This stage was necessary because VBM is based on group comparisons, in the case of this study, the patients group versus the healthy controls one. This type of comparison also meant that it was imperative to get this stage right as any distortion or aberration caused by either the registration or the normalisation would produce unsound results. As it will become clear below, this phase involved much complex processing and finding the right pipeline proved highly challenging as can be seen in some of the results shown in **Figure 4-4.**

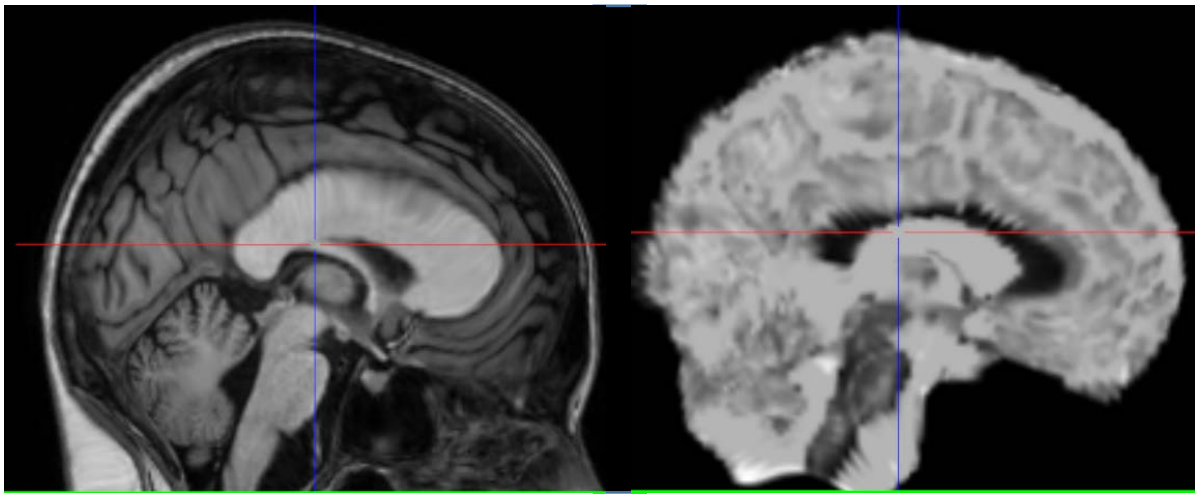

Figure 4-4 Distorted CC ODI too blurred to be used

In some cases, problems only became apparent at the final stage, when the clusters generated by VBM appeared in the ventricles, outside the brain or as shown in **Figure 4-5**, slightly displaced.

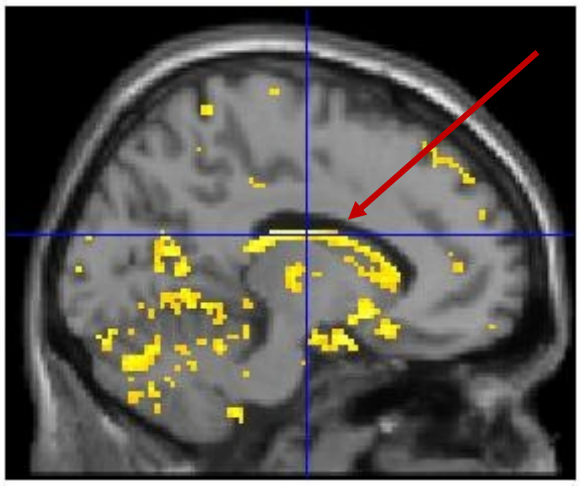

The arrow points towards a cluster that is very likely to be the corpus callosum (CC).

Figure 4-5 Displaced clusters.

The final version of the pipeline used was as follow: for the patients, the lesion filled maps were used for the registration and each of the 61 diffusion-weighted images were registered to the non-diffusion-weighted *b*0. Each subject's 3D-T1-weighted images and dMRI data were registered following the protocol described in Muhlert et al.[5]. Pseudo-T1 images computed from the PD/T2-weighted scans were used as an intermediate step, providing a contrast similar to the 3DT1-weighted image.

Next, the MNI152 template (Montreal Neurological Institute) was registered nonlinearly to each subject's lesion-filled 3DT1-weighted image. Thereafter, the 3D-T1-weighted images went through a symmetric and full affine registration to the pseudo-T1 image, while the T2-weighted images were nonlinearly registered to the dMRI maps. In order to transform the data from dMRI-space to MNI space, all the registration were concatenated.

All the registrations were done using NiftyReg (http://niftyreg.sf.net), a software that implements symmetric and inverse-consistent registration, thus ensuring that the results are not biased towards the directionality of the registration process. The symmetric full affine approach[20], with 12 degrees of freedom (DOF), which was used is based on the asymmetric block-matching

approach initially described by Ourselin and colleagues[21]. It concurrently optimised the forward and backward transformations in an inverse-consistent manner. Thus, the 12 DOF transformation were parameterise as 3 translations, 3 rotations in Euler angles, 3 scaling factors and 3 skew factors, and the full matrix was optimized directly. The non-rigid registrations were based on the fast free-form deformation (FFD) algorithm[22]

An illustration of what that means concretely can be seen in **Figure 4-6.** This shows the key stages of the registration and transformations that were necessary in order to apply VBM.

4.2.4.2 Tissue segmentation

In order to apply VBM, tissue segmentation resulting in the creation of distinct grey and white matter maps was necessary. This was done using Geodesic Information Flows (GIF)[23]. For the segmentation, GIF uses a template database as sources of information. The data is coded as local graph patches from which information propagates in voxel-wise annotations, such as tissue segmentation or parcellation, between morphologically dissimilar images. This is achieved by diffusing and mapping the available examples through intermediate steps, using a spatially-variant graph structure to assess connections first between morphologically similar areas and then between subjects from the database of images. This process allows the gradual diffusion of information to all the subjects, even in the presence of large-scale morphological variability such as greatly increased ventricles or brain atrophy, which could be due either to age or neurological diseases, and therefore creates more accurate maps. An illustration of the process can be seen in **Figure 4-7**.

The template database used for this study has 95 MRI brain scans neuroanatomically labelled according to the Neuromorphometrics protocol. GIF is part of the NiftySeg (http://niftyseg.sf.net) software package and is available as online tool at http://cmictig.cs.ucl.ac.uk/niftyweb[24].

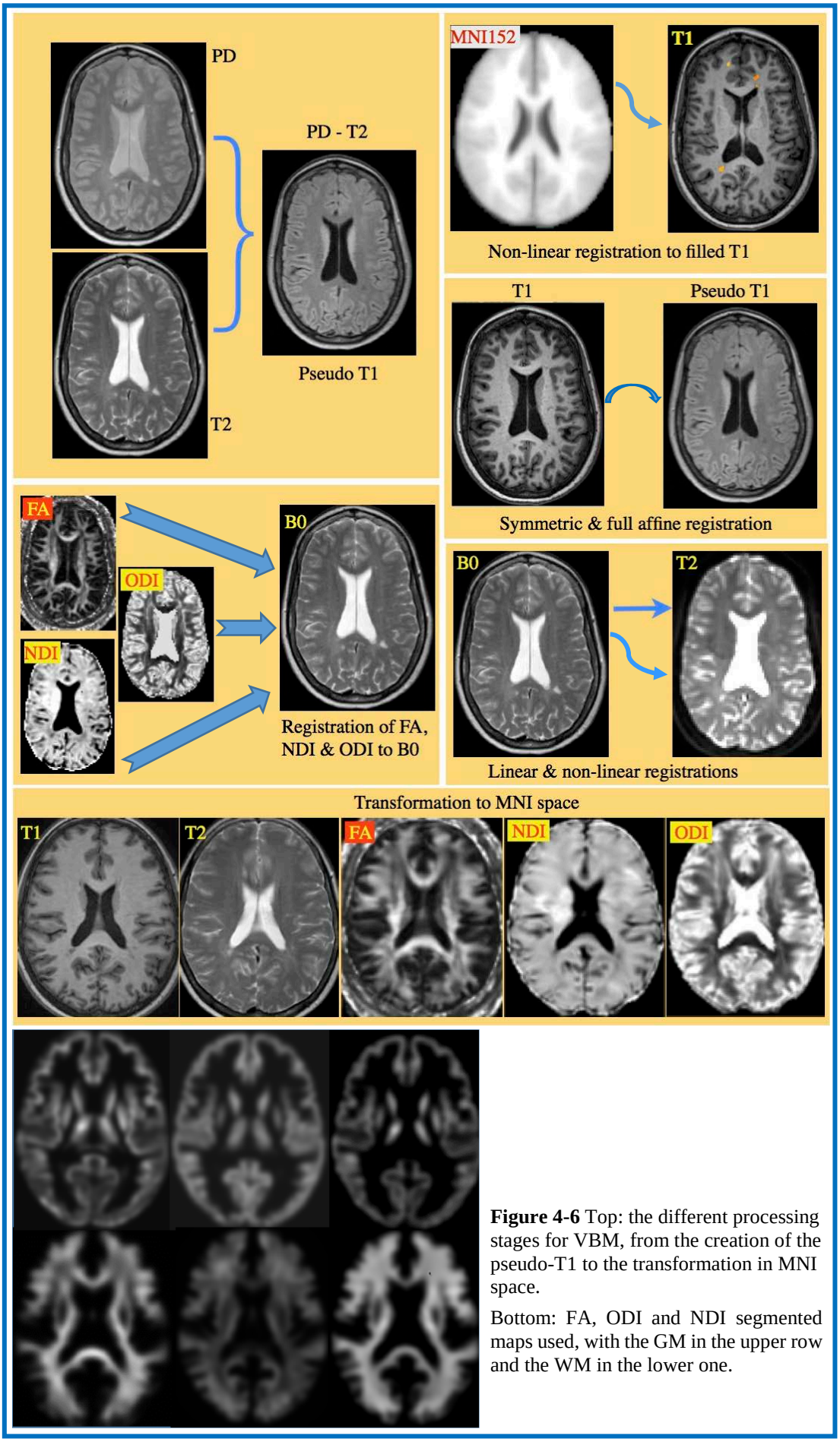

Figure 4-6 Top: the different processing stages for VBM, from the creation of the pseudo-T1 to the transformation in MNI space.

Bottom: FA, ODI and NDI segmented maps used, with the GM in the upper row and the WM in the lower one.

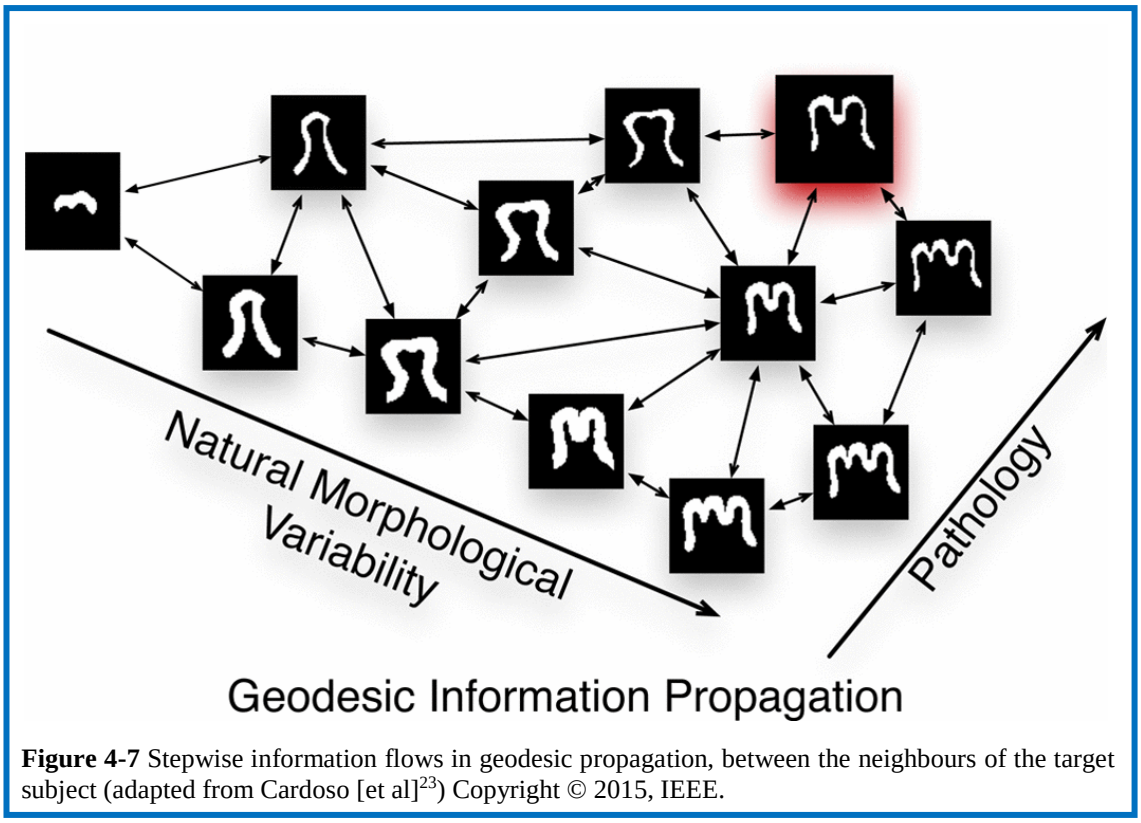

Figure 4-7 Stepwise information flows in geodesic propagation, between the neighbours of the target subject (adapted from Cardoso [et al][23]) Copyright © 2015, IEEE.

4.2.4.3 Smoothing to parametric maps

Once the registration and segmentation were completed, the subsequent steps followed the normal VBM pre-processing protocol, that is the creation of DARTEL (diffeomorphic anatomical registration through exponentiated Lie algebra)[25] templates and normalisation to MNI space within SPM12 (statistical parametric mapping software; www.fil.ion.ucl.ac.uk/spm/software/spm12/, London, UK), with age and gender as covariates. Smoothing was done with a Gaussian FWMH (full width at half maximum) of 6x6x6 mm[26]. Both procedures were necessary in order to be able to obtain the parametric maps.

The factorial design used for the statistics involved a two samples *t*-test, with age and gender entered as covariates and an explicit mask used to limit the analysis to the average grey or white matter tissue maps (based on the averaged SW segmented maps, thresholded at 0.15 and binarised).

The contrasts used to generate the clusters were *Patient values lower than Controls values* and *Patients values higher than Controls values* in the GM and NAWM of FA, ODI and NDI maps. In each case, the family wise error (FWE)

correction was applied, with *p* set at 0.005 and only clusters with more than 15 voxels used. The peak voxel of each of these clusters was spherically expanded to 8 voxels in diameter and the new masks were checked and manually corrected when they expanded beyond WM or GM. **Figure 4-8** illustrate the process from the original clusters to the spherical masks.

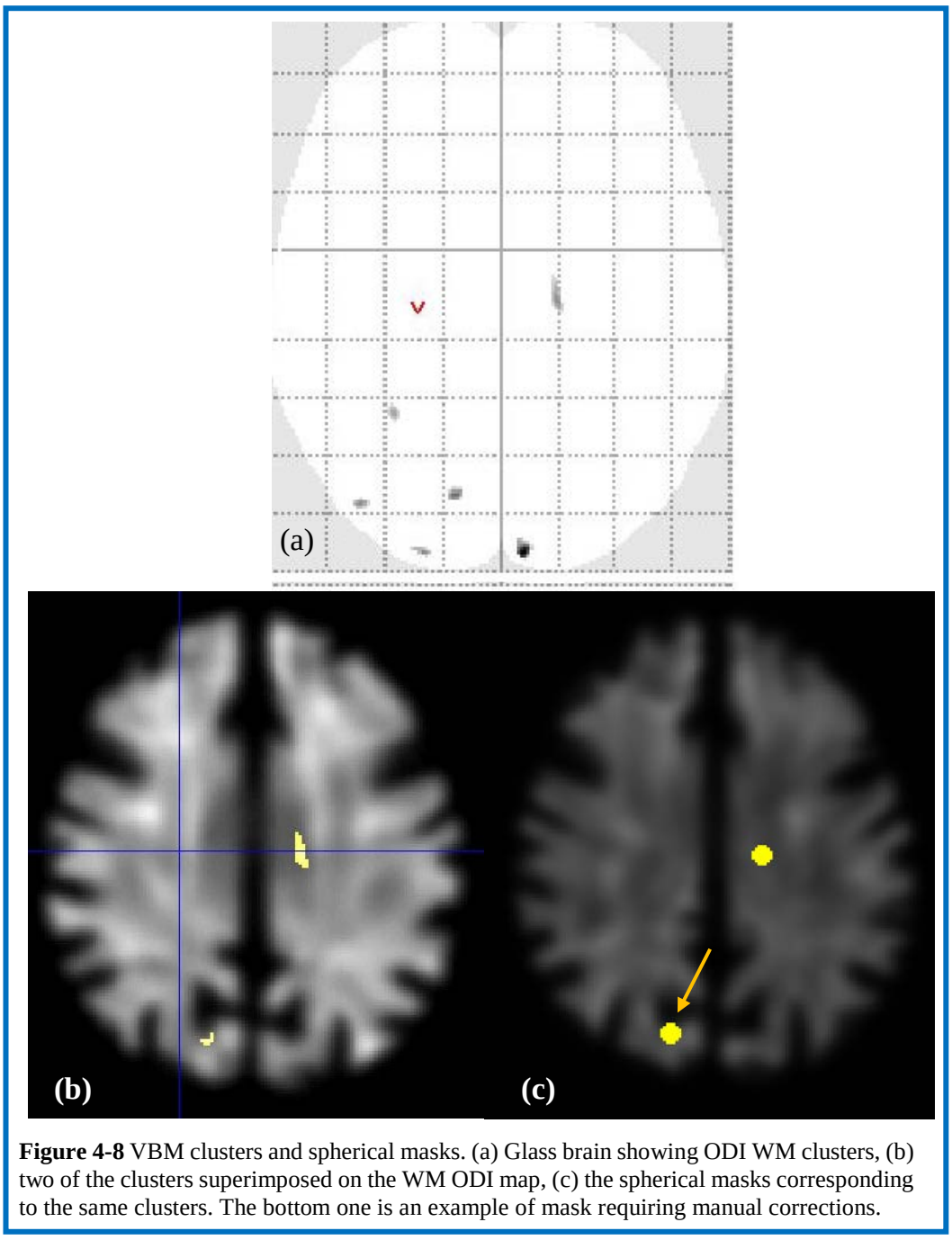

Figure 4-8 VBM clusters and spherical masks. (a) Glass brain showing ODI WM clusters, (b) two of the clusters superimposed on the WM ODI map, (c) the spherical masks corresponding to the same clusters. The bottom one is an example of mask requiring manual corrections.

The correlations between FA, ODI, NDI and both clinical and cognitive assessments were tested using Spearman's rho correlation coefficient. Results associated with $p<0.05$ were considered significant.

The regions in which the clusters/masks were localised were identified using the following atlases:

- JHU ICBM-DTI-81 white-matter labels atlas.
- JHU white-matter tractography atlas.
- Jülich histological (cyto- and myelo-architectonic) atlas.
- Harvard-Oxford Subcortical Structural Atlas (for deep GM).

4.3 Results

4.3.1 ROIs results

The full results for all the ROIs used are shown in **Table 4-3**. In FA maps, values for patients were higher than controls in the right internal capsule (0.7 vs 0.65, p=0.03). In ODI maps, values for patients were lower not only in the right internal capsule (0.13 vs. 0.16. p=0.0001), but also in the left internal capsule (0.13 vs 0.15, p=0.018) and the genu of the corpus callosum (0.08 vs 0.10, p=0.023). Finally, in the NDI maps, patients values were lower in the genu of the corpus callosum (0.64 vs. 0.71 p=0.024) and in the right and left occipital cortex (0.54 vs. 0.60, p=0.023 and 0.52 vs. 0.58, p=0.041).

For NDI, data from the left occipital lobe of 4 controls had to be excluded: the values were abnormally low when compared to the right occipital lobe. When the ROIs were checked, it became clear that their position were significantly different from the $b0$ maps, as can be seen in **Figure 4-9**. If all the ROIs are used, the average value for the left occipital lobe ROI in healthy controls is 0.54, while it is 0.60 on the right. To ensure that the problem was specific to the subjects with low values, the ROIs were also checked in the other controls NDI maps. The position of the ROIs in the NDI maps was very similar to those in the $b0$ ones.

Correction for multiple comparisons was not deemed necessary as the ROIs used for comparisons between patients and controls were specifically placed in areas known to be affected by MS. This method, unlike a generic exploratory approach involving the whole brain, has a low likelihood of false positives.

	FA		ODI		NDI	
	Patients	Controls	Patients	Controls	Patients	Controls
	Mean (SD)	Mean (SD)	Mean (SD)	Mean (SD)	Mean (SD)	Mean (SD)
CC body	0.68 (0.11)	0.70 (0.049)	0.12 (0.031)	0.13 (0.020)	0.63 (0.17)	0.68 (0.097)
CC genu	0.75 (0.081)	0.77 (0.050)	0.086 (0.033)	0.10 (0.021)*	0.64 (0.11)	0.71 (0.10)*
CC splenium	0.74 (0.077)	0.77 (0.055)	0.062 (0.039)	0.071 (0.026)	0.56 (0.094)	0.61 (0.057)
Left internal capsule	0.67 (0.066)	0.64 (0.051)	0.13 (0.025)	0.15 (0.024)*	0.64 (0.11)	0.62 (0.068)
Right internal capsule	0.71 (0.057)	0.65 (0.054)*	0.13 (0.023)	0.16 (0.01)**	0.70 (0.071)	0.69 (0.069)
Left frontal lobe left	0.14 (0.039)	0.14 (0.039)	0.55 (0.080)	0.54 (0.090)	0.53 (0.090)	0.54 (0.164)
Right frontal lobe	0.13 (0.034)	0.14 (0.049)	0.55 (0.065)	0.53 (0.082)	0.50 (0.15)	0.49 (0.11)
Left occipital lobe	0.14 (0.041)	0.16 (0.039)	0.58 (0.069)	0.41 (0.053)	0.52 (0.091)	0.58 (0.065)*
Right occipital lobe	0.16 (0.042)	0.18 (0.049)	0.56 (0.065)	0.43 (0.046)	0.54 (0.11)	0.60 (0.072)*
Left thalamus	0.26 (0.051)	0.23 (0.038)	0.37 (0.087)	0.57 (0.069)	0.55 (0.042)	0.54 (0.046)
Right thalamus	0.26 (0.051)	0.24 (0.036)	0.41 (0.085)	0.55 (0.072)	0.58 (0.040)	0.59 (0.058)
Left hippocampus	0.15 (0.065)	0.13 (0.041)	0.53 (0.087)	0.56 (0.097)	0.48 (0.096)	0.48 (0.061)
Right hippocampus	0.15 (0.064)	0.13 (0.030)	0.55 (0.12)	0.58 (0.081)	0.48 (0.067)	0.49 (0.062)

*p <0.05, **p<0.01, Mann Whitney test.

Table 4-3 Results for the different ROIs in FA, ODI and NDI

Possible correlations between FA and ODI were also explored. In both patients and controls, lower FA values were associated with higher ODI ones for the majority of the ROIs (see **Figure 4.10**). NDI does not relate to FA in the way ODI does, so no correlation analysis was necessary there. In both patients and controls, negative correlations between FA and ODI were found in all GM regions (p=0.0001) and right internal capsule (for patients: Spearman's rho:=-0.54, p=0.004; for controls: r=-0.50, p=0.01). In controls, the left internal capsule ODI (r=-0.48, p=0.01) also correlated with FA.

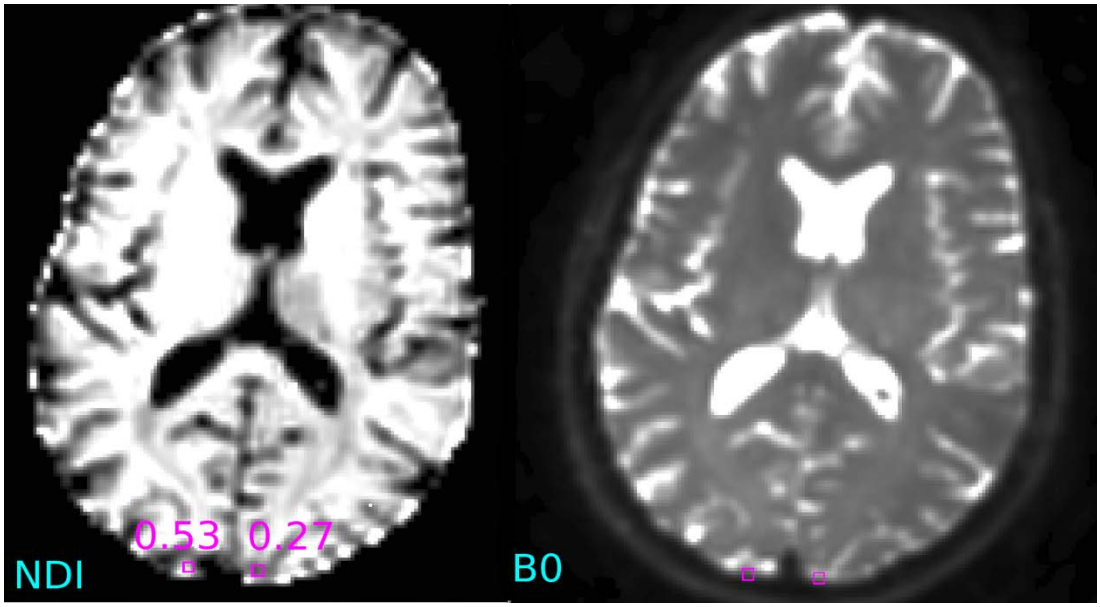

Figure 4-10 Occipital lobe ROIs in NDI and B0 maps, with average values for NDI showing differences between left and right hemisphere.

For the correlations with clinical data in patients, no correlation were found between any of the MRI parameter and EDSS score in the ROIs data from FA and ODI maps. However, lower NDI values in the right occipital cortex correlated with longer disease duration (Spearman's rho: -0.448, *p*=0.022).

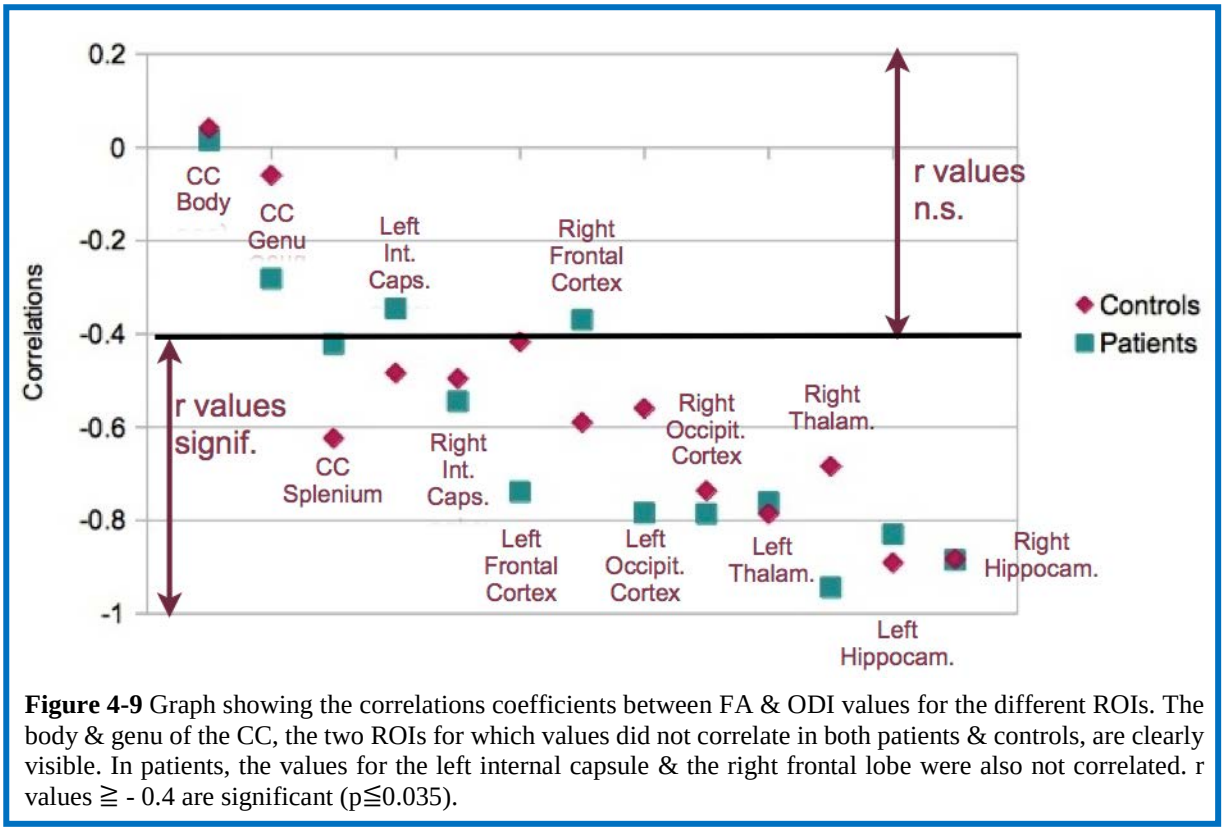

Figure 4-9 Graph showing the correlations coefficients between FA & ODI values for the different ROIs. The body & genu of the CC, the two ROIs for which values did not correlate in both patients & controls, are clearly visible. In patients, the values for the left internal capsule & the right frontal lobe were also not correlated. r values ≧ - 0.4 are significant (p≦0.035).

4.3.2 Voxel-based morphometry results

	FA (Patients>Controls)	
	Localisation	Correlations
Cluster 1	Body of the corpus callosum (towards the splenium)[1].	Delayed story recall (r= 0.548, p=0.006) and the Symbol Digit Modalities Test (SDMT) (r= 0.469, p= 0.021).
Cluster 2	Left anterior corona radiata[1] and left inferior fronto-occipital fasciculus[2].	SDMT (r= 0.484, p= 0.017)
Cluster 3	Right posterior thalamic radiation, including optic radiation[1] and right fronto-occipital fasciculus[2].	SDMT again (r= 0.741, p>0.001) and disease duration (r= -0.527, p= 0.007)
	ODI (Patients<Controls)	
	Localisation	Correlations
Cluster 1	Left optic radiation, connecting to primary (V1) and secondary (V2) visual cortex[3] and left forceps major, left inferior longitudinal fasciculus and left inferior fronto-occipital fasciculus[2].	Delayed story recall (r= -0.548, *p*=0.006) and EDSS score (r= 0.428, *p*= 0.033)
Cluster 2	Right forceps major, right inferior longitudinal fasciculus and right inferior fronto-occipital fasciculus[2], possibly connecting to secondary visual cortex[3].	Paced Auditory Serial Addition Test (PASAT) (r= 0.434, *p*=0.030) and SDMT (r= -0.526, *p*= 0.028)
Cluster 3	Body of the corpus callosum (very central when looking at length of CC)[1, 3].	SDMT (r= -0.483, *p*= 0.017) and disease duration (r= 0.625, *p*= 0.001)
Cluster 4	Right inferior longitudinal fasciculus[2], possibly connecting to V4[3].	Delayed story recall (r= -0.428, *p*=0.037) and SDMT (r= -0.467, *p*= 0.021) as well as EDSS score (r= 0.516, *p*= 0.008).
Cluster 5	Right posterior thalamic radiation, including optic radiation[1], right inferior fronto-occipital fasciculus, right inferior longitudinal fasciculus, right superior longitudinal fasciculus and right forceps major[2], possibly connecting to V2[3]	Age (r= -0.470, *p*= 0.018)
	NDI (Patients<Controls)	
	Localisation	Correlations
NAWM	Splenium (left, but very close to midline)[1], left forceps major[2], body of the corpus callosum[3]	No correlation found
GM	Left hippocampus[4]	Delayed story recall (r= -0.429, p=0.032 and SDMT (r= -0.551, p=0.004).

Table 4-4 Localisation of the clusters and correlations in FA, ODI, and NDI maps. The clusters are listed by decreasing size. Comparison between each clusters and all cognitive tests were made. Only those for which a significant correlation with the cluster was found are reported here.

Clusters showing areas of differences between patients and healthy controls were found in all three maps, however the exclusion of clusters of less than 15 voxels only apply to the ODI maps, which were also the maps in which the largest number of clusters were generated. The full results are given in **Table 4-3**. Clusters were found in all maps for the NAWM, and one cluster was found in the GM in NDI maps. In FA maps, the values were lower for patients than controls, while the opposite occurred in the ODI and NDI maps, were values were higher for patients than controls.

As the family wise error (FWE) correction incorporated in SPM was applied when using VBM to identify clusters where values differed between patients and controls, further corrections for multiple comparisons was not necessary. However, without FWE, such corrections would have been necessary due the high level of false positives produced by VBM when generating uncorrected clusters map.

Correlations with clinical and cognitive data were found for all the clusters with the exception of the one found in the corpus callosum in NDI maps. EDSS and disease duration were the two clinical measurements that most commonly correlated with the areas where differences between patients and controls were found, while for the cognitive assessments, the most common correlations were with SDMT and the delayed story recall. The full results for both the clinical and cognitive data correlations are shown in the right column of **Table 4-3.**

4.4 Discussion

Both NODDI and DTI (on which FA is based) can be used to highlight changes in brain microstructure, particularly areas of damage not visible with conventional sequences. To understand the import of the results from both approaches, and whether or not NODDI provides convincing results and how it compares to more traditional approach such as FA, it is worthwhile to briefly revisit what the different maps are measuring.

Fractional anisotropy, or FA, reveals the incidence of diffusivity along one direction and will therefore be higher in areas with large tracts and few crossing fibres. Subsequently, areas with a large amount of crossing fibres or fanning axons will have lower FA values, which is why results from FA maps require cautious interpretation. Nevertheless, overall, a decrease in FA has been found in NAWM of MS patients[27,28]: it has been suggested that these decreases are associated with demyelination and changes in axonal integrity, including Wallerian degeneration, as well as other types of NAWM damage, such as a diffuse axonopathy[29-31]. However, there also appears to be a general agreement about a lack of specificity when it comes to the type of changes underlying a decrease in FA values[32-34]. A further point of discussion is whether changes detected in NAWM using FA maps are linked to the occurrence of lesions or develop separately[30,31].

This leads to the question of whether the indices provided by NODDI could be more specific as well as more sensitive than FA measurements. Clearly from the results of this study, ODI in particular appears to have a greater sensitivity to subtle changes in NAWM. ODI indicates the degree of dispersion of axons and dendrites and NDI the density of axons and dendrites, both based on an intracellular compartment model. The fact that ODI is inversely correlated to FA[4,35], thus suggesting that an increase in axonal dispersion underlie a decrease in FA, is a further illustration of the lack of specificity of FA metrics mentioned above. However, while ODI may offer further information on fibres orientation, and therefore resolved one of the issues linked to FA (i.e. the link between increased neurite dispersion and decreased FA), it does not appear to be affected by the degree of myelination. In a study looking at myelin density in a mouse model, as well as comparing imaging results with histological data from human brains, Sepehrband and colleagues show that their evaluation of myelin density only had a weak correlation with ODI metrics[35]. In other words, ODI maps provide additional information on tissue microstructure, but only about the degree of axonal dispersion found within a specific voxel rather than on the condition of myelin. This does not make the information obtained from ODI

maps of less interest, but should be kept in mind when interpreting the meaning of the results. Nevertheless, the increase in axonal dispersion that underlies not only ODI, but is also likely to be an important factor in FA[36], may well be due to axonal or dendritic loss (the latter would potentially explain the greater sensitivity of ODI maps when compared to FA observed in this study). Moreover, such changes in tissue microstructure are clinically relevant in their own rights.

The decrease in ODI values, together with the decrease in NDI, found in the genu of the corpus callosum with the ROIs approach is the most unexpected one. In a study looking at different parts of the corpus callosum, Lin and colleagues found reduced FA in the genu[37], which is what would be expected and would likely correlate with an increase in ODI. Clearly, the decrease in axonal dispersion detected is likely to be due to changes in the degree of fanning that characterise this area of the CC. Such changes may well be caused by axonal loss, which in turn would explain the decrease in density detected by the NDI metrics.

On the other hand, the increased ODI found in the body corpus callosum detected with VBM, which was also found in a study applying NODDI to Alzheimer's disease (AD)[6], is likely to reflect the increased disorganisation of fibres, possibly due to a reduction of axonal volumes as there was also a decrease in NDI values. It is worth noting that the changes in the body of the corpus callosum were also detected in the FA maps when VBM was used, but the two NODDI metrics give a more precise indication of the likely cause underlying such changes.

The reason why there were so few areas of differences detected by NDI metrics is likely to be due to the fact that NDI estimates of the neurite density is based on the intracellular volume as a fraction of the non-CSF compartment[4] and the proper fitting of this compartment was severely limited by the impossibility to fit the CSF when using single-shell data. Consequently, it is very likely that this partial fitting significantly reduced the sensitivity of the NDI maps, and

therefore reduced the amount of data that could be extracted from these maps. Nevertheless, since the clusters are located in areas known to be affected by MS, they can be regarded as valid, but are likely to be an underestimation.

Additionally, as noted above, the axonal dispersion underlying ODI is an important component of FA. Zhang and colleagues clearly showed that this fact led to an inverse correlation between FA values[4], something that was found in this study too, showing that single-shell ODI metrics closely match those obtained from an optimised multiple-shells protocol.

A final result from the ROIs approach that requires some comments is the increased FA found in the right internal capsule. As already mentioned, the most common change detected in FA of MS patients NAWM is a decrease, as was the case with the VBM results, therefore this result may seem surprising. Still, a similar asymmetrical difference was found by Roosendaal and colleagues[38] using TBSS. They suggest that the increased FA may be due to brain atrophy and subsequent impaction of WM fibres. Another possible explanation may be a loss of crossing fibres, as there is a clear reduction in the fibres dispersion since the ODI values for the internal capsules were lower in patients than controls in both hemispheres.

The only results found in grey matter were from the NDI maps, which is not surprising as a change in neurite density is easier to measure in the intricate GM than a decrease or increase in dispersion. Moreover, both results are in areas that are known to be affected by MS. The ROIs in the occipital lobe were in the area of the primary visual cortex (V1), in which abnormalities such as degeneration and atrophy have been detected by previous studies[39,40]. Similarly, the hippocampus has likewise been shown to be affected by demyelination[41-43]. Interestingly, while most studies find bilateral changes, Audoin and colleagues[40] also found MTR changes solely in the left hippocampus of MS patients.

Overall, it is also interesting to note that the results obtained with VBM in both the FA and ODI maps are very similar to those obtained using TBSS on FA

maps by Roosendaal and colleagues[38], thus offering further evidence of the validity of single-shell NODDI results. Interestingly they also looked at correlations with cognitive assessments, if different ones from those used in this study, and found correlations between a letter-digit substitution test and a decrease in FA in the left side of the body of the CC.

Numerous correlations were found between the results obtained using VBM and cognitive assessments. How do they compare with other studies? And can it be said that they offer further evidence that single-shell NODDI can provide useful information? Of particular interest is the large number of areas found to correlate with SDMT: the three areas of changes detected by FA, three of the five ones detected by ODI and the left hippocampus with NDI. This fits well with the fact that SDMT has been shown to be particularly sensitive when applied to MS patients, which is one of the reasons why it was chosen for the Brief International Cognitive Assessment for MS (BICAMS)[44]. One of the areas with which it correlates is the corpus callosum, in which changes have been repeatedly correlated with multiple cognitive assessments[28], but also specifically with SDMT[45-48]. Similar NAWM areas have been found by studies looking at cognitive deficit in MS, using SDMT and other tests[49,50], including one also showing a correlation with the hippocampus[51]. So for this part too, the results obtained from the single-shell NODDI metrics can be considered reliable, which is particularly encouraging since all areas of change detected with ODI also correlated with cognitive or clinical measurements.

Altogether, NODDI metrics in general, and ODI in particular, were more sensitive than FA, something which was also found in a study of microstructural changes related to ageing that used a multiple HARDI shells protocols, offering further evidence that the results obtained from single shell data mirror those ensuing from an optimised acquisition protocol[52].

ROIs vs VBM: The ROIs approach was part of the initial exploratory section of the study, used to find out whether the application of NODDI to single HARDI shell data was feasible, and the results from this stage led to the decision to

apply VBM in order to gain further understanding of what could be achieved with NODDI. The fact that in this case the VBM approach was the most sensitive and also detected more areas in NAWM where changes occurred in patients makes the use of this approach especially worthwhile.

It should be noted that while, just as was the case with the ROIs approach, more areas of change were detected by ODI metrics than FA, there is one area, the corona radiata, which was detected in FA maps only. This suggests that there may even be a degree of complementarity between FA and the NODDI metrics, as in this case the decrease in FA was not caused by an increase in neurite dispersion.

As for the reason why the results differ between ROIs approach and VBM, it is likely to be connected to the transformations, smoothing and statistical significance thresholds linked to FWE correction necessary for the application of VBM, which would make changes occurring in small regions less detectable. Billet and colleagues made a similar observation when they compared their ROIs and voxel-based analyses[36]. It is however surprising that VBM detected changes in the body and splenium of the corpus callosum that were not detected by the ROIs approach. However, the latter was potentially limited by the small size of the ROIs used, and it is quite possible that if an ROI incorporating the whole splenium had been used, the same differences could have been found. As far the body of the corpus callosum is concerned, the large amount of atrophy observed in some patients may also have contributed to the VBM results.

4.5 Conclusion

The results from both the ROIs and VBM approaches demonstrated that NODDI can be applied to single HARDI shell data and that ODI and NDI may detect regions of diffusion abnormalities in RRMS patients that are not visible in FA maps. Furthermore, the areas detected in NODDI maps with VBM revealed correlations with both cognitive and clinical measurements, showing

that they are clinically relevant. This means that NODDI can be retrospectively applied to existing dataset for new analyses.

Future studies, with either single or multiple HARDI shells protocols could use NODDI for differentiation between MS and NMO, in particular to look for subtle changes in normal appearing WM, especially in the early stages of both diseases. Multiple-shells protocols may also detect more changes in normal appearing GM, as the fitting of the CSF compartment will provide more sensitive NDI maps. Besides, as suggested by Grussu and colleagues, there may well be some limitations in the ODI maps that needs to be kept in mind while applying NODDI to single-shell data, in particular if the *b*-value is low[53]. Even so, this study shows that while keeping limitations in mind is important, applying NODDI to single-shell provides new and relevant data when compared to FA.

NODDI is only the first MRI techniques used in this thesis. The next chapter will look at the application of phase-sensitive inversion recovery (PSIR) in MS and NMO patients with the aim to investigate cortical and leucocortical lesions in both groups.

Chapter 5

Can phase-inversion recovery (PSIR) detect cortical lesions in NMOSD patients or are they specific to MS?

5.1 Introduction

As explained in Chapter 3, phase-sensitive inversion recovery (PSIR) is a reconstruction technique which allows a very high resolution: for the purpose of this study, the voxel size is 0.5x0.5 mm in-plane, with 2 mm slice thickness. The other advantage of this technique is that it has a high contrast, making it possible to detect lesions not visible with other MR techniques, especially in the cortical grey matter. Cortical lesions are particularly difficult to detect as they do not enhance after gadolinium administration and have been shown by post-mortem studies to be highly underestimated on MRI[1]. Even with 7T scanner, as a recent study using double-inversion recovery (DIR) to look for cortical lesions in MS patients and comparing the results with histology found, only about 60% of lesions were detected[2].

While a 2007 study by Nelson and colleagues did not find a significant difference in cortical lesions detection when comparing PSIR with DIR in MS patients[3], a study published in 2012 by Sethi and colleagues showed a threefold increase in intracortical (IC) and leucocortical (LC) lesions detection with PSIR when compared to DIR[4]. Similar results were obtained by Favaretto and colleagues who found a fourfold detection increase in detection of IC, LC and juxtacortical (JC) lesions when comparing PSIR with DIR[5]. Based on these studies, it seemed interesting to look at IC, LC and JC lesions in NMOSD patients to see whether any IC or LC lesions would be detected.

A further point of interest is the ongoing debate on whether or not cortical lesions do occur in NMOSD patients: a study by Calabrese and colleagues using DIR, published in 2012, did not find any cortical lesion in a group of 30

NMOSD patients[6]. Previous studies which looked at cortical atrophy[7], or applied spectroscopy to normal appearing grey matter did not find changes in cortical grey matter[8] either, nor did two studies conducted on 7T scanners detect any cortical lesions (but they used solely conventional protocols such as T1, T2, T2* and FLAIR for one study[9], and just T2 for the other[10]). Only one study, by Kim and colleagues[11], did detect cortical lesions in NMOSD patients with FLAIR, but those Korean patients were much younger than patients in Europe or the Americas, ranging from 15 to 36 years, compared to a mean age varying from mid-forties to early fifties in most NMOSD studies, thus may have a slightly different pathology. Popescu and colleagues provide further evidence of the absence of cortical lesions in a study in which histology was performed on post-mortem tissues of NMOSD patients and failed to find any intracortical or leucocortical lesions, or to detect cortical demyelination[12].

On the other side, a study using diffusion metrics found significantly increased mean diffusivity (MD) in the parietal and temporal areas of the cortex[13], while two studies by Rocca and colleagues also detected changes in GM: one using fMRI found significant functional alterations in cortical areas when comparing NMOSD patients to healthy controls[14], while the other, using magnetisation transfer ratio (MTR) combined with MD, also found increased MD as well as decreased MTR in normal appearing GM (NAGM)[15]. Finally, a study by Saji and colleagues[16], which used histology, confirmed Popescu[12] findings that cortical demyelination does not occur in NMOSD patients, nor was there any oligodendrocyte loss, but they found other changes. Specifically, when comparing NMOSD patients to healthy controls, they uncovered an increase meningeal inflammation, a loss of AQP4-negative immunoreactivity in astrocyte processes of layer I, a decrease in cortical neurons density in layers II-IV, as well as a large increase of microglial activation in layer II.

So can PSIR detect any abnormalities in NMOSD patients cortex or will it confirm the 7T studies that there is no detectable cortical lesions?

5.2 Methods

5.2.1 Subjects

Written, informed consent was obtained from all participant, and this study was approved by the NRES Committee London Bloomsbury (Formally London REC 2 Ethics Committee). RRMS patients were diagnosed using the revised McDonald criteria[17], while the NMOSD diagnosis was based on the criteria proposed by Wingerchuk and colleagues in 2006[18]. 19 NMOSD patients, aged between 21 and 70 years, and 19 MS patients, aged between 26 and 55 years, with a similar gender ratio and disease duration, as well as 23 healthy controls, aged between 23 and 68 years, were consecutively recruited. 17 of the NMOSD patients were AQP4 positive, while one of the two AQP4 negative was MOG positive. The full details for each group are given in **Table 5-1**.

	RRMS patients *n*=19	NMOSD patients *n*=19	Healthy controls *n*=23
Age (years)	41.28 ±9.86	52.72±11.69	36.87±8.92
Gender (F/M)	15/4	16/3	12/9
Median EDSS (range)	2.5 (1-7.5)	4.25 (2-6.5)	N/A
Disease duration	8.83±6.20	7.89±6.92	N/A
AQP4+	N/A	17	N/A

Table 5-1 Demographic and clinical data.

5.2.1.1 Exclusions

Three NMOSD patients and one MS patient had to be excluded as the amount motion artefacts rendered the scans uninterpretable. In one case, the patient kept her head still for half of the scan, but because of the two separate interleaved acquisitions, there was a succession of one good quality slice followed by a blurred one (**Figure 5-1**), making it impossible to assess whether a lesion was going over more than one slice or checking whether it could be an artefact, an important issue in some regions as will become clear below. Therefore the whole scan was excluded.

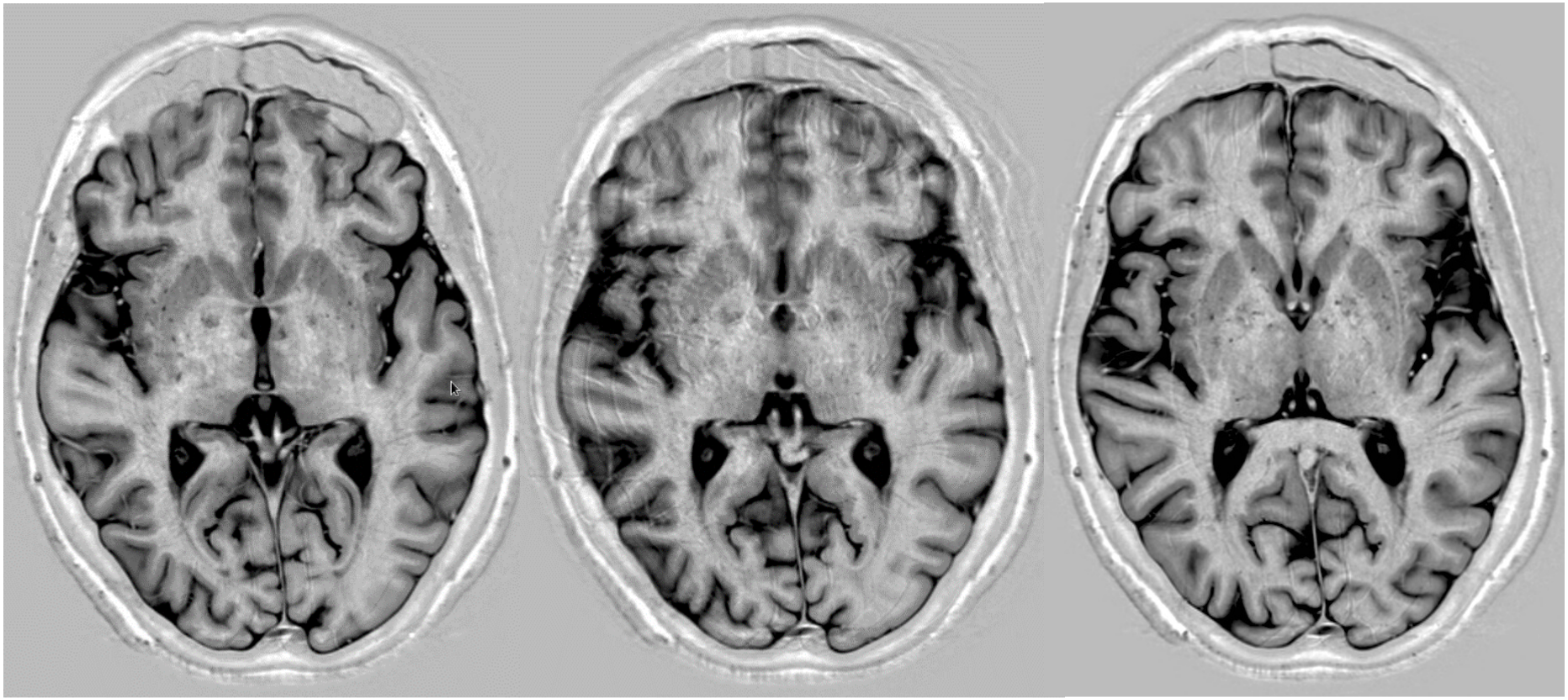

Figure 5-1 Three consecutive sagittal slices showing the effect of the separate interleaved PSIR acquisitions: the first and third slices are clear while the middle is very blurred, in particular in the frontal part of the brain. These three slices are representative of the images obtained for the whole brain.

5.2.2 *Image acquisition*

The brain MRI scans were acquired on a 3T Achieva system with dual-transmit technology (Philips Healthcare, Best, The Netherlands) using a 32-channel coil. For the purpose of this study, both a T2-weighted turbo spin echo and PSIR scans were acquired, using the following sequences:

(i) axial 2D turbo-spin-echo (TSE) PD/T2-weighted sequence, with TR = 3500 ms; TE1/TE2 = 15/85 ms; echo train length = 10 echoes; FOV = 240×180 mm^2; voxel size = 1×1×3 ml; number of excitations (NEX) = 1; 50 contiguous slices, and

(ii) axial 2D turbo-spin-echo (TSE) IR sequence with phase-sensitive reconstruction, with TR = 7304 ms; TE = 13 ms; TI = 400 ms; echo train length = 8 echoes; FOV = 240×180 mm^2; voxel size = 0.5×0.5×2 ml; number of excitations (NEX) = 1; 75 contiguous slices.

5.2.3 *Lesions marking*

The lesions in the PD/T2 scans were marked by two neurologists, Dr Floriana de Angelis and Dr Rosa Cortese, using JIM version 6.0 (Xinapse systems, http://www.xinapse.com). The lesion load from these scans was used for comparative purposes and to calculate the percentage of juxtacortical lesions.

Five types of lesions were marked on the PSIR scans and are defined as follow: intracortical (IC), leucocortical (LC), juxtacortical (JC), deep grey matter (DGM) and cerebellar (CB). Intracortical lesions were entirely located in the cortex, while leucocortical ones either involved both cortex and juxtacortical white matter or the lesion border appeared to break the GM-WM boundary. Finally, juxtacortical lesions involved white matter only, directly abutting the cortex but without any cortical involvement. For the last two categories, deep grey matter ones were those found in any DGM structures, while those found in the cerebellum were not separated in GM and WM categories due to their rarity.

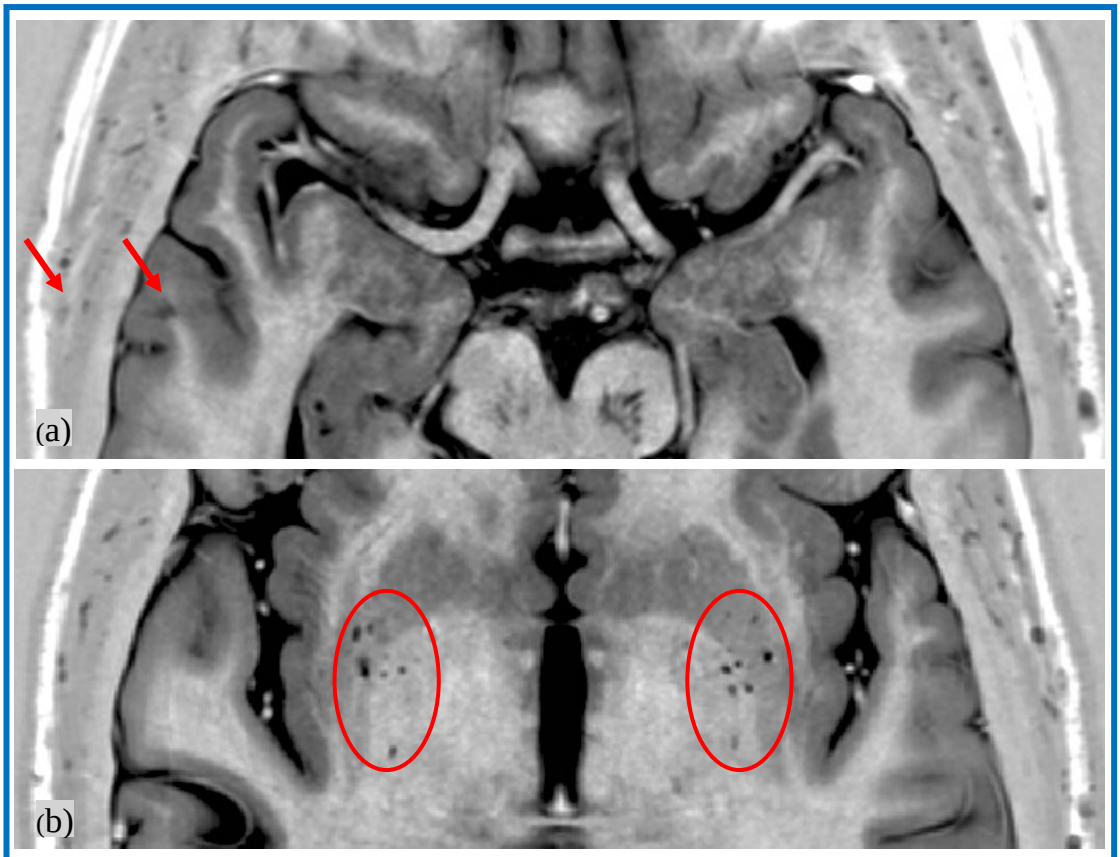

Figure 5-2 (a) Easily identifiable artefact due to the presence of other artefacts in the skull, but also a good illustration of how similar to lesions they can appear; (b) Iron deposits & PVS in deep grey matter.

The lesions marking was done blindly to disease type, using JIM version 6.0 (Xinapse systems, http://www.xinapse.com), and was checked throughout for quality assurance by an experienced neuroradiologist, Professor Tarek Yousry. Careful attention was paid to avoid marking artefacts (**Figure 5-2a**), which were often observed in regions such as the insula, anterior temporal lobes and medial frontal lobes. For this purpose, the slices adjacent to suspected lesions were crucial, and one of the key reasons why interleaved blurred slices made whole scans unusable. A further potential source of error was the iron deposits in the basal ganglia, which look like lesions as can be seen in **Figure 5-2b**. Another common occurrence that initially caused confusion was the high visibility of perivascular or Virchow-Robin spaces, which appear in increased numbers in MS patients[19] and can easily be mistaken for lesions[20], as can be seen in **Figure 5-3**.

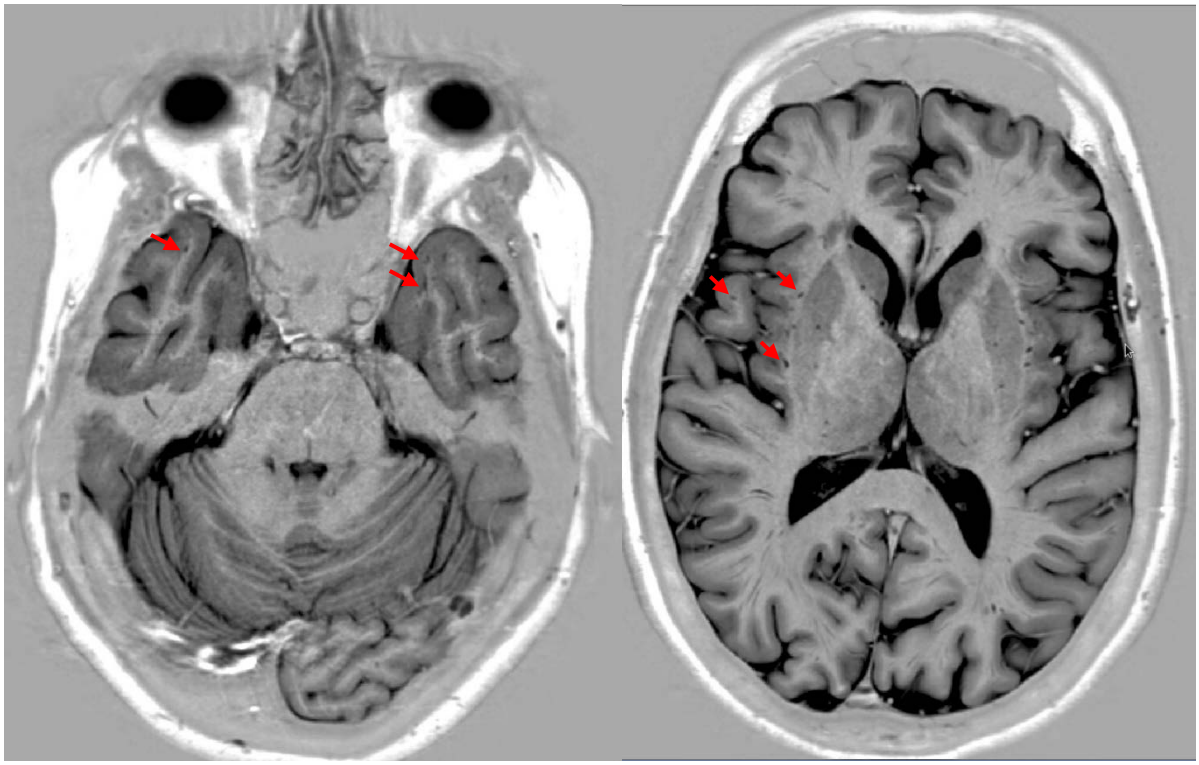

Figure 5-3 Examples Virchow-Robin spaces (VRS) (arrows). In the second images, only 3 VRS have an arrow, but more can be seen, in particular in similar places in the other hemisphere.

There had been very few previous studies using PSIR to look at MS patients lesions, and none to look at NMOSD patients. Therefore the guidelines applied to identify cortical lesions independently on PSIR were those proposed by Dr Varun Sethi and Professor Tarek Yousry in 2012[21], which for the cortical and leucocortical lesions, were as follow:

- Lesions are hypointense relative to the surrounding normal cortex.
- They must involve the cortex in part or whole, and have the following characteristics:
  a) Be confined to the cortex to be classified as intracortical (IC).
  b) If it involves both cortex and juxtacortical WM, it is classified as leucocortical (LC)
- If it is small or ill-defined on a single slice, it must be visible on at least one other contiguous slice.
- Equivocal lesions must be confirmed through retrospective detection of signal abnormality compatible with a lesion found at the same location on the corresponding T2-weighted images.

They also proposed the following exclusion criteria:

- Partial volume effects caused by adjacent cerebrospinal fluid, verified by reviewing adjacent PSIR slices and corresponding T2-weighted scans. This issue is particularly common in sulcal regions, as well as at the temporal poles and near the vertex.
- Artefacts, which can at times be recognised by their symmetrical appearance.
- Vessels, visible as very thin linear hypo-intensities, especially when they do not follow the direction of the cortical ribbon. Cortical lesions can also have a curvilinear or linear appearance, but are less thin and always follow the direction of the cortical ribbon.
- Virchow-Robin spaces, which are particularly common in regions such as the insula and temporal poles. This is particularly true when linear and numerous, giving them a mesh-like or bundle-like appearances (seen in both patients and controls).

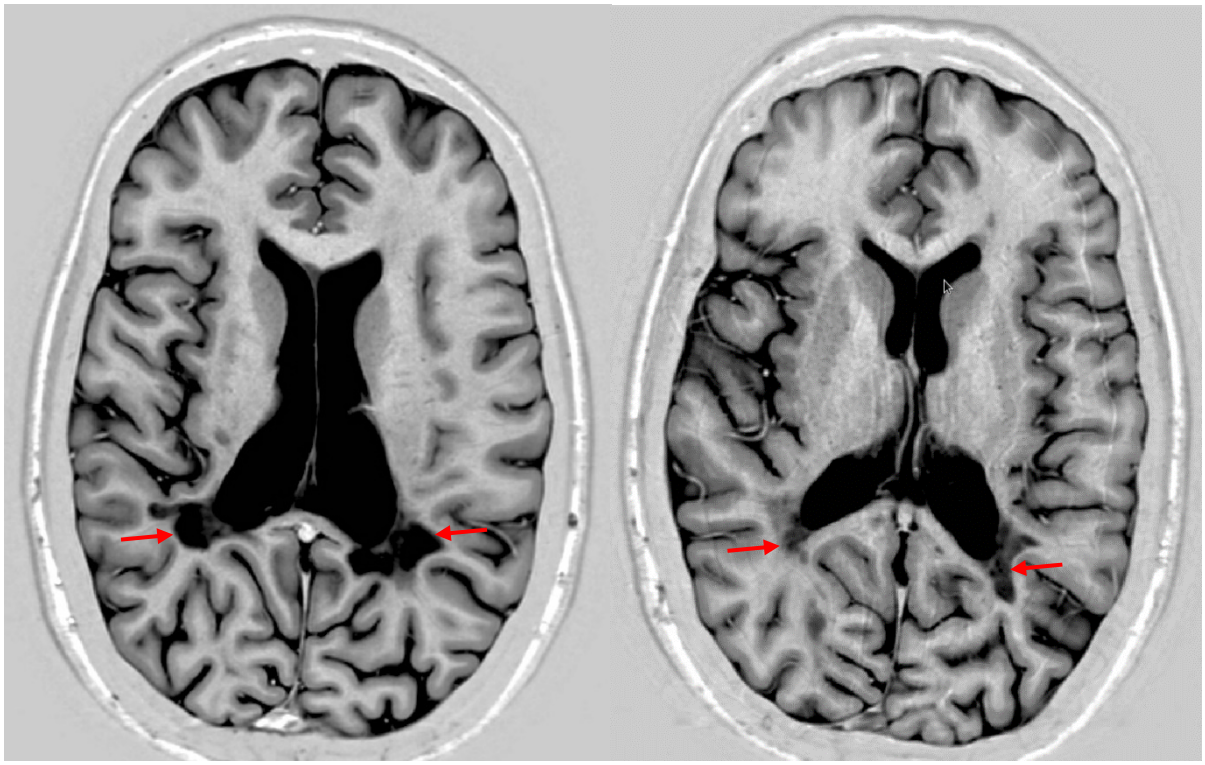

Figure 5-4 Two slices in the same MS patient showing the large confluent lesions that were excluded from the analysis. These lesions extended over multiples slices and had a total volume of 0.2871 ml.

An additional exclusion criterion specific for this study was used in the case of one MS patient who had very large confluent lesions, which were juxtacortical in some slices (**Figure 5-4**). Since this type of lesions does not occur in NMOSD patients, their inclusion as JC lesions would have greatly increased the difference between the two groups and therefore biased the analysis. For this reason, these lesions were excluded from the analysis.

In order to assess how the different types of lesions may differ between MS and NMOSD patients, we looked at the following criteria:

- Numbers of lesions of each types (IC, LC, JC, DGM and CB) in each patient. Since the number of lesions given by JIM is dependant on the number of slices on which lesion masks have been inserted (a lesion going over 3 slices for example will be counted as 3 lesions), the number of lesions were manually counted so that lesions running over multiple slices were considered as a single lesion. This also make it possible to calculate an average lesion volume for each type of lesion.
- The total lesion load for each specific type of lesions.

5.2.4 Statistics

Multiple linear regressions adjusted for age and gender were used to compare the different types of lesion between MS and NMOSD patients. The following comparison were made:

- T2 lesion load in MS and NMOSD.
- Lesion load for each type of lesions (IC, LC, JC, DGM and CB) in MS and NMOSD.

Results associated with $p<0.05$ and 95%CI were considered significant.

For the comparison of the numbers of lesions found at each location (IC, LC, JC, DGM and CB) in MS and NMOSD patients, negative binomial regression was used. Negative binomial regression is similar to Poisson regression, used for counts and rate, with the advantage that negative binomial regression can

allow for between-subject differences in probability of having a lesion. These negative binomial models report ratios of lesions counts.

The last part of the statistics did investigate the lesion types as potential markers of NMOSD vs MS for diagnosis. For this purpose, logistic regression with the following markers was used: T2 lesion loads and for each type of lesions marked in the PSIR images, the lesion loads and lesion numbers. Odds ratios of patients being MS rather than NMOSD were then calculated from the fitted model coefficients. Finally, the classification performance of the model used was assessed with a probability cut off of 0.5.

5.3 Results

As can be seen from **Table 5-2**, each type of lesions was found in both groups, including intracortical ones, but all were much more common in MS patients than in NMOSD ones. Examples of each types of lesions from both groups of patients can be seen in the figures below: intracortical in **Figure 5-5,** leucocortical and juxtacortical in **Figure 5-6,** cerebellar in **Figure 5-7** and deep grey matter in **Figure 5-8**. Both deep grey matter and cerebellar lesions were rare, and in the case of the latter, two patients had what appear to be atypically large lesions (**Figure 5-7, (d) & (e)**), but due to the small number of patients affected, it is not possible to assess how unusual such lesions are.

	RRMS patients	NMOSD patients
WM PD/T2	19/19	17/19
PSIR IC	16/18	6/16
PSIR LC	12/18	4/16
PSIR JC	14/18	6/16
PSIR DGM	4/18	1/16
PSIR CB	6/18	3/16

Table 5-2 Number of MS and NMOSD patients in whom lesions were detected on the PD/T2 and PSIR scans. WM: white matter; IC: intracortical; LC: leucocortical; JC: juxtacortical; DGM: deep grey matter; CB: cerebellum.

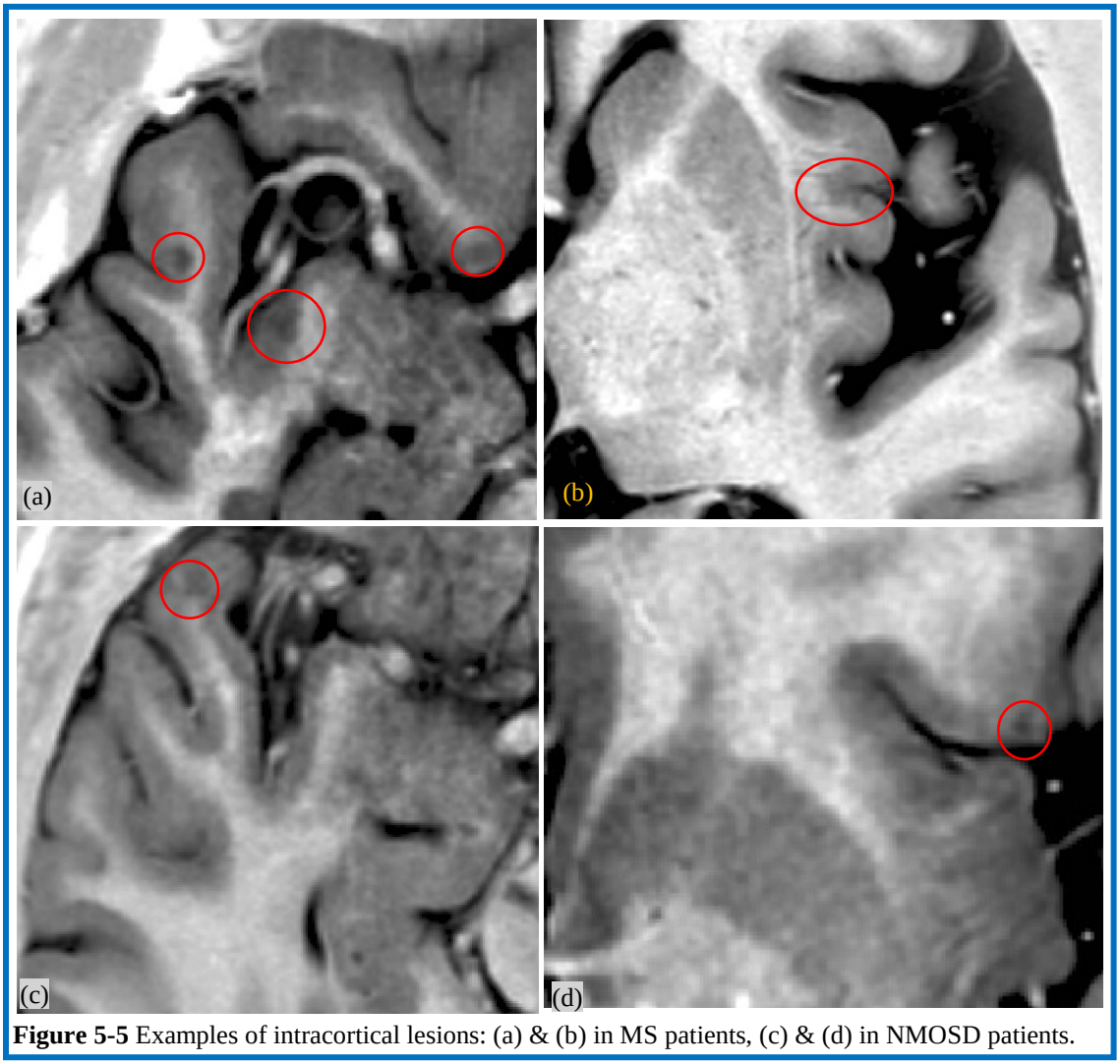

Figure 5-5 Examples of intracortical lesions: (a) & (b) in MS patients, (c) & (d) in NMOSD patients.

The full data for the lesion load, lesion numbers for each type of lesions are given in **Table 5-3**.The average PD/T2 lesion load was much higher in MS patients than NMOSD ones, as was to be expected: 5.080±4.841 ml vs 1.049±1.550 ml respectively, a highly significant difference of 4.030 ml (95% CI 1.596, 6.465), p=0.002. This value is the unadjusted difference as it was not significantly affected by adjustments for age, gender and duration, the same apply to the subsequent results.

As can be seen from the data in **Table 5-3**, the standard deviations for both group were high, particularly so for the NMOSD group. From individual patients data given in **Table 5-4** and **Table 5-5**, it is very clear that there was a lot of variation between patients PD/T2 lesion load. In MS patients it was 0.125 ml to 14.774 ml, while in NMOSD patients with PD/T2 lesions it ranged from 0.00350 ml to 5.234 ml.

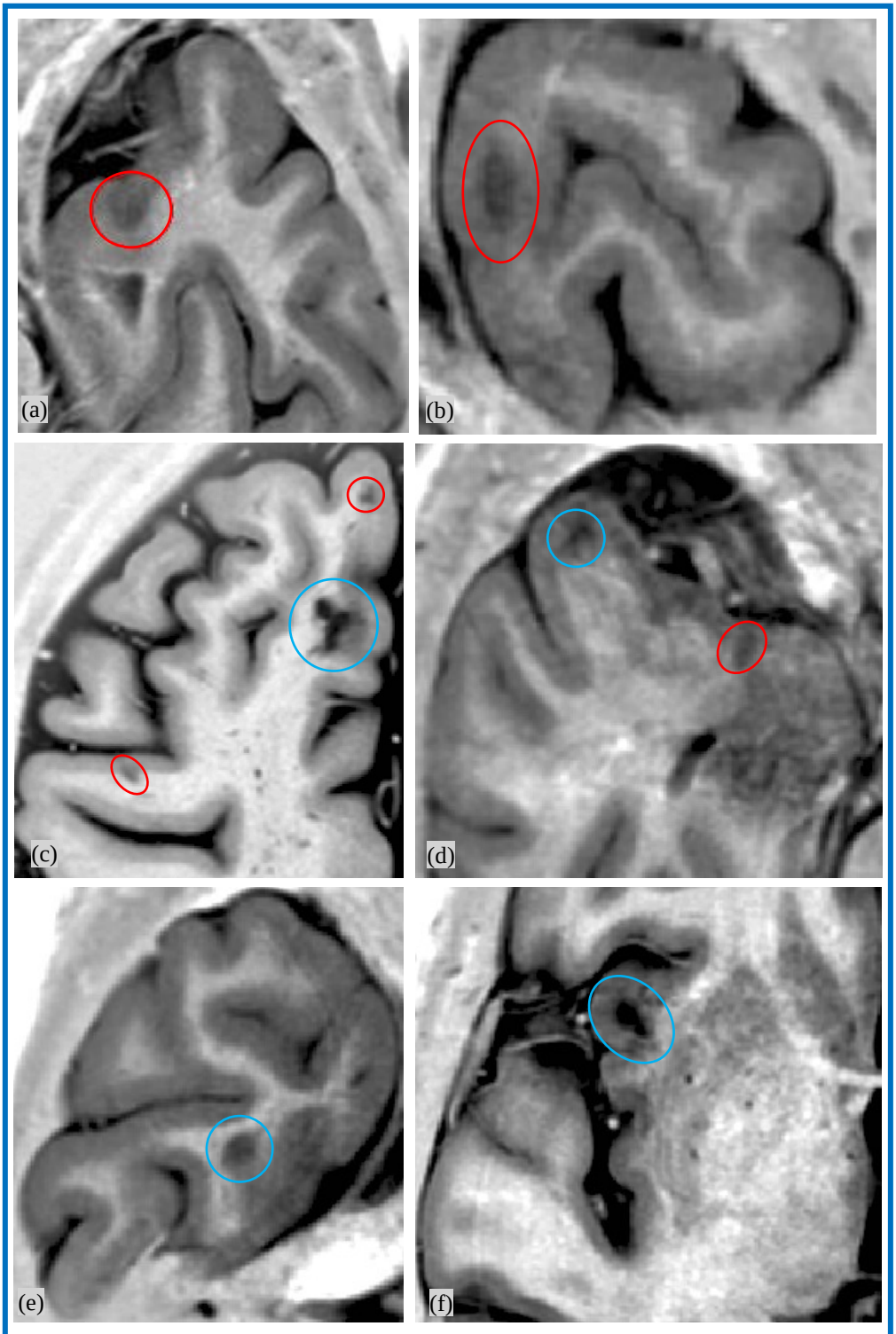

Figure 5-6 Examples of leucocortical (red) and juxtacortical (blue) lesions. As can be seen from (c) & (d), finding both types of lesions together was not unusual. (a), (c) & (e) are from MS patients, (b), (d) & (f) from NMOSD patients.

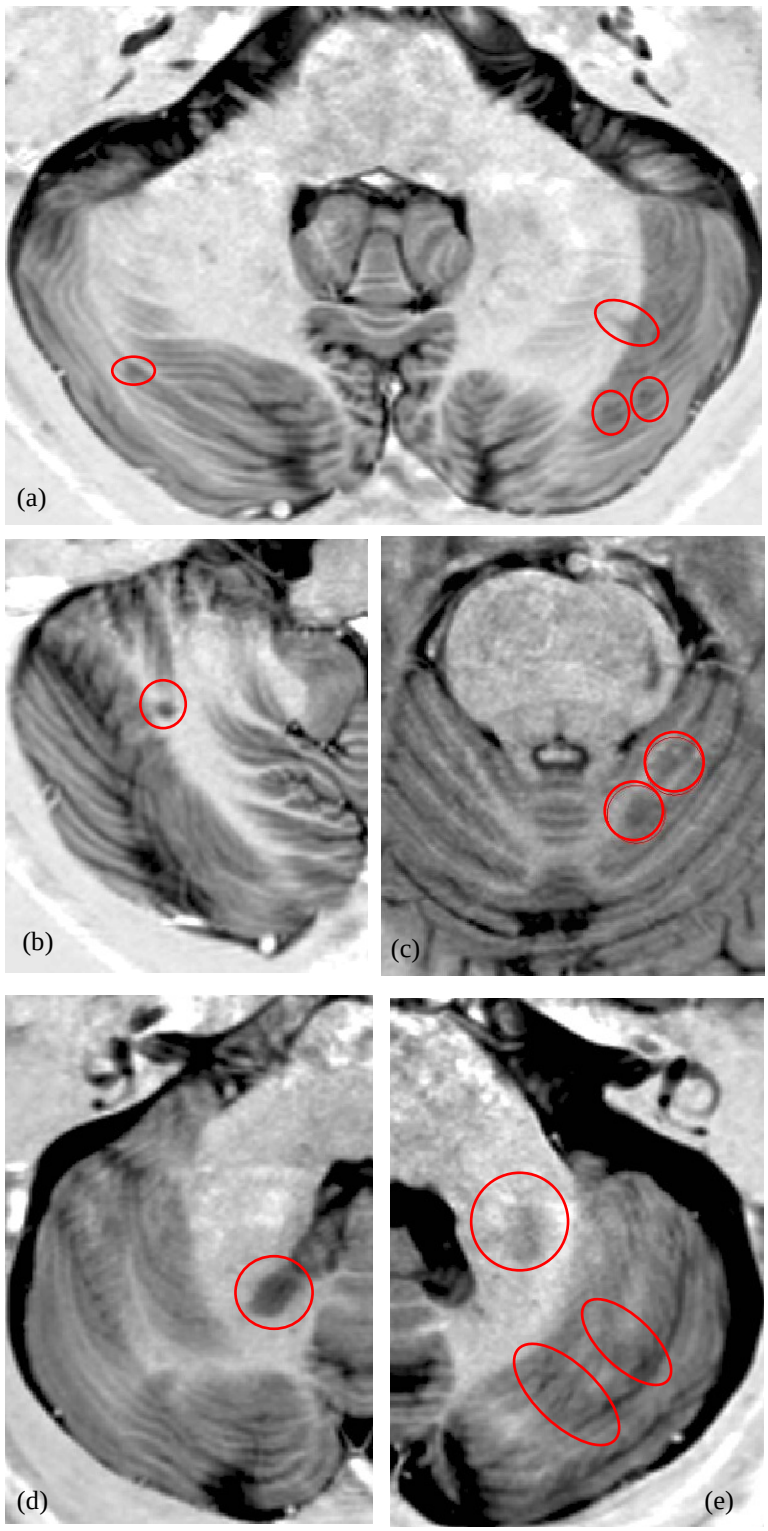

Figure 5-7 Examples of cerebellar lesions: (a) & (b) in MS patients, (c) in a NMOSD patient; (d) &(e) show what could be atypical lesions due to their size in MS & NMOSD patients respectively.

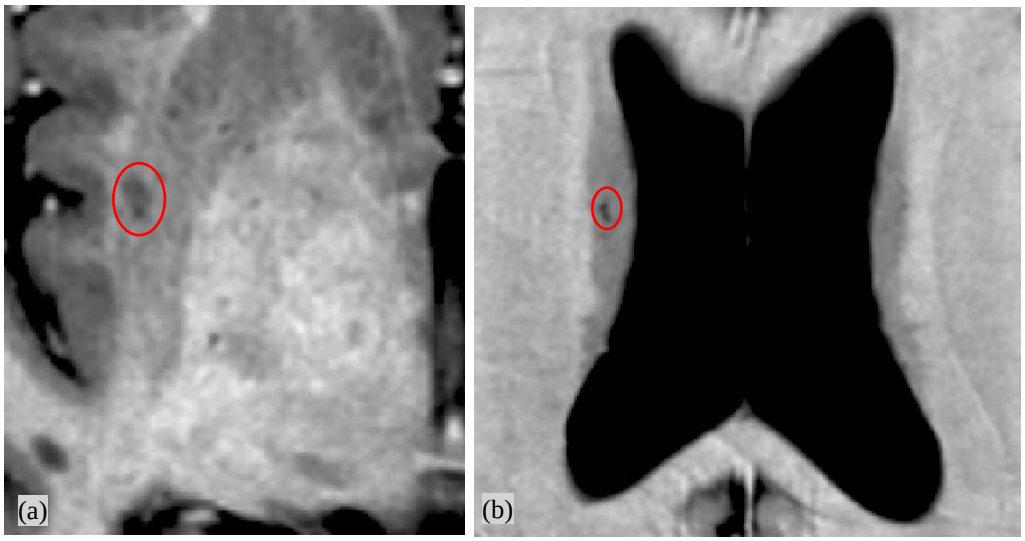

Figure 5-8 Examples of lesions in the deep grey matter: (a) in an MS patient, (b) in an NMOSD patient.

	RRMS patients	NMOSD patients	*p* values
WM PD/T2 LL (ml)	5.080±4.841	1.049±1.550	0.002
PSIR IC LL (ml)	0.118±0.116	0.0353±0.0846	0.025
PSIR IC, average no of lesions (range)	5.611±4.937 (0-18)	2.063±4.3123 (0-17)	0.033
PSIR LC LL (ml)	0.164±0.184	0.0290±0.0651	0.009
PSIR LC, average no of lesions (range)	4.333±4.4985 (0-13)	0.938±1.982 (0-7)	0.05
PSIR JC LL (ml)	0.560±0.663	0.0616±0.103	0.006
PSIR JC, average no of lesions (range)	9.222±9.915 (0-35)	1.813±3.619 (0-13)	0.002
PSIR DGM LL (ml)	0.0265±0.0935	0.00108±0.0043*	n.s.
PSIR DGM, average no of lesions (range)	0.333±767 (0-3)	0.125± 0.500* (0-2)	n.s.
PSIR CB LL (ml)	0.0447±0.105	0.0225±0.0830	n.s.
PSIR CB, average no of lesions (range)	1.056±2.014 (0-6)	0.5±1.317 (0-5)	n.s.

Table 5-3 Results for the different types of lesions.
WM: white matter; LL: lesion load; IC: intracortical; LC: leucocortical; JC: juxtacortical; DGM: deep grey matter; CB: cerebellum; Ave.: average. * indicates data coming from a single patient

The average IC lesion load was also much higher in MS patients than NMOSD ones: 0.118±0.116 ml vs 0.0353±0.0846 ml respectively, a highly significant difference of 0.0830 ml (95% CI 0.0112, 0.155), p=0.025.

Age	Gender	EDSS	Dis. Dur. (y)	PD/T2 LL (ml)	% JC	IC lesions no	IC LL (ml)	LC lesions no	LC LL (ml)	JC lesions no	JC LL (ml)	DGM lesions no	DGM LL (ml)	CB lesions no	CB LL (ml)
21	F	2.5	2.5	5.234	2.43	4	0.070	4	0.0597	7	0.128	0	0	0	0
50	M	3	10	0.556	33.72	4	0.043	*2*	*0.210*	2	0.188	2	0.0172	2	0.0206
53	F	6	3	0.158	40.50	4	0.059	2	0.0246	5	0.0640	0	0	0	0
69	F	6.5	2	2.810	Excluded due to motion artefacts										
53	F	6	3	0.0714	0	0	0	0	0	0	0	0	0	0	0
52	F	4	6	0.00350	0	0	0	0	0	0	0	0	0	0	0
37	F	4	3	0	0	0	0	0	0	0	0	0	0	1	0.00643
56	F	6	2	0.610	0	0	0	0	0	0	0	0	0	0	0
63	F	6.5	14	4.351	3.22	0	0	0	0	**1**	**0.140**	0	0	0	0
41	F	3	4.5	0.398	0	0	0	0	0	0	0	0	0	0	0
66	M	3.5	15	1.343	27.31	3	0.044	*7*	0.170	13	0.367	0	0	**5**	**0.333**
51	F	6	6	0.191	0	0	0	0	0	0	0	0	0	0	0
52	F	2	17	0.385	34.52	0	0	0	0	1	0.0989	0	0	0	0
48	M	2	7.5	0.0291	0	*17*	0.340	0	0	0	0	0	0	0	0
57	F	5.5	4	0.0716	0	0	0	0	0	0	0	0	0	0	0
54	F	2	4.5	0.287	0	0	0	0	0	0	0	0	0	0	0
70	F	4.5	10.5	1.613	Excluded due to motion artefacts										
57	F	5.5	29	0.750	0	1	0.00984	0	0	0	0	0	0	0	0
48	F	6.5	14	0	Excluded due to motion artefacts										

Table 5-4 Full results for NMOSD patients.
WM: white matter; LL: lesion load; % JC: percentage of LL that is juxtacortical; IC: intracortical; LC: leucocortical; JC: juxtacortical; DGM: deep grey matter; CB: cerebellum. The two highlighted patients are AQP4-, the excluded one is MOG+. Results in italics indicate patients with atypical results and in bold patients where the average load for that type of lesions was particularly large but the group is too small to say whether the values are atypical.

Age	Gender	EDSS	Dis. Dur. (y)	T2L (ml)	% JC	IC lesions no	IC LL (ml)	LC lesions no	LC load (ml)	JC lesions no	JC LL (ml)	DGM lesions no	DGM LL (ml)	CB lesions no	CB LL (ml)
36	F	4	13	3.132	13.51	6	0.103	8	0.145	13	0.423	1	0.0350	**5**	**0.406**
24	M	4.5	4	6.562	4.46	18	0.354	13	0.537	8	0.292	1	0.0252	0	0
50	F	2.5	26	7.222	16.52	11	0.212	13	0.322	*35*	1.193	0	0	6	0.217
30	F	1.5	6	0.287	0	1	0.0318	0	0	0	0	0	0	0	0
55	M	7	15	3.378	5.33	2	0.0493	4	0.137	7	0.180	0	0	0	0
35	F	1	5	2.399	4.99	11	0.187	0	0	1	0.120	0	0	0	0
48	F	1.5	10	6.465	9.56	4	0.0651	7	0.222	8	0.618	0	0	0	0
43	F	3	15	14.774	11.77	8	0.115	9	0.465	19	1.738	0	0	0	0
54	M	7.5	9	0.602	58.49	12	0.380	0	0	7	0.485	0	0	0	0
54	F	1.5	5	3.868	15.32	*5*	*0.114*	2	0.0512	16	0.592	0	0	5	0.0570
34	M	4	14	1.488	0	6	0.255	1	0.0951	0	0	1	0.0177	0	0
38	F	1.5	6	0.368	72.97	2	0.0437	2	0.0660	3	0.269	0	0	0	0
31	F	3.5	2	0.214	0	4	0.0829	0	0	0	0	0	0	0	0
42	F	1	5	7.814	2.06	1	0.00614	5	0.321	3	0.161	0	0	1	0.0148
48	F	1.5	5	14.275	9.77	2	0.01378	6	0.110	19	1.394	0	0	1	0.01600
48	F	2.5	13	*0.125*	*0*	*0*	*0*	*0*	*0*	*0*	*0*	*0*	*0*	*0*	*0*
47	F	4	5	12.943	17.71	8	0.118	8	0.483	24	2.292	**3**	**0.399**	**1**	**0.0945**
26	F	1.5	1	5.524	5.82	0	0	0	0	3	0.321	0	0	0	0
46	F	2	14	0.734	Excluded due to motion artefacts										

Table 5-5 Full results for MS patients.
WM: white matter; LL: lesion load; % JC: percentage of LL that is juxtacortical; IC: intracortical; LC: leucocortical; JC: juxtacortical; DGM: deep grey matter; CB: cerebellum. Results in italics indicate patients with atypical results and in bold patients where the average load for that type of lesions was particularly large but the group is too small to say whether the values are atypical.

Just as it was the case for the PD/T2 lesion load, there was a very large variability between patients: from 0.00614 ml to 0.380 ml in the 16 MS patients with IC lesions and 0.00984 ml to 0.340 ml in the 6 NMOSD patients in this category (the highest load is in a patient who also has an unusually high number of lesions). The average number of IC lesions was also 2.72 times higher in MS patients than in NMOSD ones (95% CI 1.09, 6.82; p=0.033), with a large range for each groups too, as the numbers in patient who had lesions ranged from 1 to 18 in MS patients and 1 to 17 in NMO ones.

A larger lesion load average in MS patients was also found when looking at LC lesions: 0.164±0.184 ml vs 0.0290±0.0651 ml, that is a difference of 0.134 (95% CI 0.0360, 0.234), *p*=0.009. Here too, there was an extensive variability in load between patients in both groups, ranging from 0.0512 ml to 0.537 ml in the MS patients, and from 0.0246 ml to 0.170 ml in the NMOSD patients with LC lesions.

The difference in average lesion numbers too was significant, with 5.79 times more LC lesions in MS patients than in NMOSD ones (95% CI 1.70, 19.69; *p*=0.05), again with a large span in MS patients with lesions ranging from 1 to 17, while numbers were more similar in 4 NMOSD patients who had such lesions: 2-7 (three of the patients had between 2-4 lesions).

The last type of lesions where large numbers were found in MS patients is unsurprisingly the juxtacortical ones, where the average lesion load in MS patients was 0.560±0.663 ml compared to 0.0616±0.103 ml in NMOSD ones, a difference of 0.498 ml (95% CI 0.156, 0.840), *p*=0.006. Here too, as the standard deviations suggest, the variation between patients was very large: ranging from 0.120 ml to 2.292 ml in MS patients and 0.0640 ml to 0.367 ml in NMOSD patients.

The difference between the average number of lesions was even larger, as in MS patients it was 9.222±9.915 compared to 1.813±3.619 in NMOSD patients, that is 5.98 times more JC lesions in MS patients when compared to NMOSD ones (95% CI 1.94, 18.38; p=0.002). These numbers also varied a lot between

patients, with the patient with the highest number of lesions in both group being potential outliers. The range was particularly large in MS patients, from 1 to 35 lesions, and even if the patient with 35 lesions was considered as an outlier, the range still goes to 24. In NMOSD patients, the range was from 1 to 13 lesions, or from 1 to 7 if the patient with 13 lesions was considered as an outlier.

As an exploratory analysis, the percentage of WM lesion load that is juxtacortical was calculated for each patient. The results for both groups were once again extremely wide ranging, from 2.6% to 72.97% in MS and 2.43% to 40.50 % in NMO.

Deep grey matter lesions were extremely rare: they were found in only 4 of the 18 MS patients and in 1 NMOSD. The average lesion load for the MS patients was 0.0265±0.0935 ml, compared to 0.00108±0.0043 ml for the two lesions found in the NMO patient. The difference did not reach significance, very likely due to a lack of statistical power. The same applies unavoidably to the lesion numbers, but even with a larger number of patients, it may not become statistically different as three of the MS patients who had this type of lesions had only one lesion and the last one had 3, suggesting that the numbers would remain very low. The load range was also large, varying from 0.0177 ml to 0.0350 ml in the patients with a single lesion, while the load for the NMOSD patient was 0.0172 ml, and for the MS patient with particularly large lesions 0.399 ml.

The last group of lesions, which were rare too, consisted of those found in the cerebellum, which were only slightly more common than the deep grey matter ones, as they were found in 6 MS patients and 2 NMOSD ones. The average lesion load for the MS patients was 0.0447±0.105 ml, compared to 0.0225±0.0830 ml for the NMO patients. Again, the difference was not statistically different. The same unsurprisingly applies to the lesion numbers, for which the average for each group were as follow: 0.333±767 in MS patients and 0.500±1.317 ml in NMO ones. As for the ranges, 3 MS patients had a single lesion, which had a volume between 0.0148 ml to 0.0945 ml, while for the

others, two had 5 lesions with a load ranging between 0.0570 ml and 0.406 ml, and the remaining one had 6 lesions with a load of 0.217. For the three NMOSD patients, one had a single lesion with a volume of 0.00643 ml, one had 2 lesions with a lesion load of 0.0206 ml, while the last one had 5 lesions with a lesion load of 0.333 ml.

Some patients appear to have what could potentially be unusually large lesions, examples of which are shown in **Figure 5-7 (d) & (e)**, like the MS patient with a single lesion that has a volume of 0.0945 ml and the NMOSD patient with the 5 lesions. The two lesions affecting the cerebellar GM visible in **Figure 5-7 (e)** are particularly good examples as their volumes are 0.163 ml and 0.120 ml. The third lesion was only found on this slice and is therefore much smaller (0.0350 ml).

The average sizes for each type of lesions was also calculated and are shown in **Table 5-6**. None were significantly different between NMOSD patients and MS ones, but here too this may be linked to a lack of statistical power due to the small numbers involved. It should also be noted that the average LC lesion size in NMOSD is markedly influenced by one patient who has only two lesions, but very large ones, and is potentially atypical. If he is excluded, the average lesion size decreases to 0.0172±0.00631 ml, and like the other types of lesion becomes smaller than the average size in MS patients.

	RRMS patients	NMOSD patients
Average lesion size for IC (ml)	0.0205±0.00918	0.0146±0.00385
Average lesion size for LC (ml)	0.0330±0.0155	0.0391±0.0441
Average lesion size for JC (ml)	0.0673±0.0309	0.0653±0.0527
Average lesion size for DGM (ml)	0.0527±0.0539	0.00861*
Average lesion size for CB (ml)	0.0423±0.0365	0.0278±0.0337

Table 5-6 Average size for the types of lesions.
WM: white matter; LL: lesion load; IC: intracortical; LC: leucocortical; JC: juxtacortical; DGM: deep grey matter; CB: cerebellum; Ave.: average.
* indicates data coming from a single patient.

The last stage of the analysis was looking at which types of lesion was the best indicator of patients being MS rather than NMOSD. Unsurprisingly, based on the lesion loads and lesion numbers results above, it was the juxtacortical lesions which came out as the most reliable marker. When looking at the JC lesion load, the odd ratio of a patient being MS rather than NMOSD was 2.06 (p=0.019) per additional 0.1 ml of lesion load, while each additional lesion generates an increase in the odd ratio of 1.22, p=0.030. Both set of values were then tested to find their sensitivity and specificity, as well as how good they would be at classifying the patients. The JC lesion load had a very high specificity: 88%, a quite good sensitivity at 72%, and incorrectly classified only 5 patients out of 34, a 79% correct score. The number of JC lesions proved less useful as a marker, since the specificity was down to 81% and the sensitivity to 56%, with only 68% of patients correctly classified. The effect of age, gender and duration was also tested, and while gender and duration did not influence the outcomes, adjusting for age substantially improved all results, with specificity now reaching 94%, sensitivity at 89%, and the rate of correctly classified patients 91%.

5.4 Discussion

The difference in the WM lesion load is what is expected[22] since these lesions need to be nonspecific (i.e. not fulfilling of MS diagnosis criteria) to fulfil the criteria for an NMO diagnosis[18,23], something which continues to be true for the revised criteria published in 2015[24], with some qualifications since it is now accepted that some NMOSD patients will have MS-like lesions.

Undeniably, the most interesting findings are the detection of both intracortical and leucocortical lesions in NMOSD patients. The number of NMOSD patients with IC lesions was much smaller than it was for MS: 37.5% compared to 89% in MS, and these lesions were also less numerous and of smaller size. This also true for the leucocortical lesions, which were found in only 25% of NMOSD patients compared to 67% of MS ones, and again were much less numerous.

So while the fact that a patient has this type of lesions may not be as good a criterion as previously thought to exclude a diagnosis of NMOSD, the lesions were clearly different between the groups, with the greater lesion load found in MS patients not only linked to the higher number of lesions but also potentially to the IC lesions being on average larger in MS patients than in NMOSD ones. As mentioned above, the average lesion volume for LC lesions in NMOSD patients is markedly affected by a single patient who has two very large lesions. Also more data is needed to get enough statistical power to find whether this difference is significant or not. These are nevertheless new and interesting findings which would warrant further investigations.

Another interesting difference between groups is in the numbers of LC vs IC lesions. Most MS patients with LC lesions have at least as many of them as they have IC ones; whereas there is more variations among NMOSD patients. Two patients have twice as many IC lesions than they LC ones, while for the remaining two, one has the same number for both types and the other is the only one with more LC than IC lesions.

In both groups, a few patients have IC but not LC lesions. The two NMOSD ones falling in this category do not have any JC lesions either, even though both have deep WM lesions visible on the PD/T2 scans. In the MS group, 4 patients fall in this category, two of which also have JC lesions. Again, for all of them deep WM lesions were visible on the PD/T2 scans. These differences in lesions distribution are interesting as two pathways leading to the formation of cortical lesions in MS have been described, only one of which appear to apply to NMOSD. The first and most common one is perivenular, with the myelin-scavenging inflammatory cells proliferating along an inflamed central vein, resulting in IC, LC and JC lesions[1] as illustrated in **Figure 5-9**. The second comes from leptomeningeal inflammation which, in MS patients, triggers plaque-like demyelination in the subpial layer of the cortex. Saji and colleagues suggest that the second process is also occurring in NMOSD patients, but without causing demyelination[16].

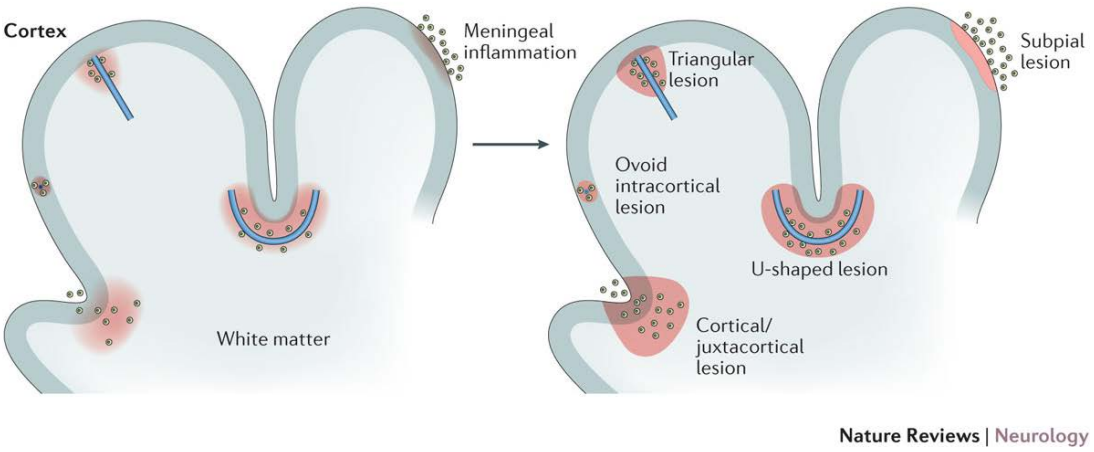

Figure 5-9 Formation of IC, LC and JC demyelinating lesions in MS. The meningeal inflammation is also thought to be involved in NMOSD cortical lesions, however without causing demyelination. (Adapted from Absinta [et al.][1]). Reproduced with permission from Nature Publishing Group

The distribution patterns of the lesions detected in MS patients may suggest that patients with IC lesions but no LC and JC ones have exclusively subpial lesions, while in NMOSD the meningeal inflammation may be at the origin of the purely IC lesions. However, it appear unlikely to be at the origin of the LC ones as Saji and colleagues only found the changes in layers II-IV[16]. Further histology would be required to gain a fuller understanding of potential mechanisms behind this type of lesions.

Since it appears that cortical lesions do indeed occur in NMOSD patients, why did previous studies using either MRI or histology failed to find them? To begin with the histology study by Popescu and colleagues, they only looked for cortical demyelination and did not think that the astrogliosis and neuronal pathology they observed in NMOSD patients were particularly relevant, though admitting they may underly the imaging abnormalities found in previous studies[12]. So while their findings about the absence of demyelination were confirmed, the lack of examination of other cortical changes identified may explain why they did not detect the cortical alterations reported by Saji and colleagues[16].

What about the two studies using 7T scanners and the one using DIR? And why did Kim and colleagues find cortical lesions on a 3T scanner when none were found on 7T? To begin with the study Kim and colleagues[11], besides the fact

that the patients were much younger than in most studies, it is also important to note the really small number of patient in whom lesions were detected (only 6 out of 194 or just 3.1%), as well as the fact that these patients were scanned during the acute phase of the disease, with only one being treated at that time. Furthermore, when four of them had a follow-up scan, they found that the lesions had either disappeared or were markedly attenuated, suggesting that cortical lesions can only be detected on FLAIR scans during the acute phase. This is in agreement with the results of Huh and colleagues, who also found some cortical lesions in NMOSD at onset in a cohort of patients with a median age of 43.87±12.31 years[22]. Besides, insofar as 7T scanners are concerned, it is important to note that while a higher SNR is achieved, generating images with enhanced spatial resolution, it does not necessarily yield higher contrasts between lesional and normal appearing tissue[25]. Consequently, lesions such as those found in the cortex may not be visible on either T2, T2* or FLAIR scans, even at 7T. As for the last MRI study looking for cortical lesions, it used DIR and FLAIR[6]. Since cortical lesions are likely to be visible on FLAIR scans only during the acute phase and, besides the fact that DIR only detects a particularly low percentage of cortical lesions[4], the absence of demyelination in NMOSD cortical lesions is likely to make them be even more elusive on this type of scans[26]. It therefore seems unsurprising that Calabrese and colleagues did not find any, as even if they were there, they would not have been detectable.

The remaining two, much rarer, types of lesions, the deep grey matter and the cerebellar ones, are at least non-controversial as they have been previously found in both MS and NMOSD patients[22,27,28]. Moreover, it is not just their infrequency that makes them less relevant as potential markers to differentiate between the two diseases: two studies made comparisons between MS and NMOSD, one looking at lesion frequencies in both DGM and the cerebellum[22], the other at lesions size in DGM[29], and both failed to find any significant difference.

5.5 Conclusion

Based on the results of this study, the use of PSIR to look for markers to differentiate between MS and NMOSD appears promising. However these results need to be validated on a larger cohort. A combination of post-mortem scanning and histology would also be particularly interesting in order to gain a better understanding of the pathological changes underlying the intracortical and leucocortical lesions in NMOSD patients. An analysis of the lesion distribution could also be useful, in particular if a post-mortem study is envisioned, in order to find out if lesions in NMOSD patients occur more frequently in some areas than in others. This information could then be used for histology, which could then potentially be performed on existing brain bank tissues.

Furthermore, it would be interesting to use the enhanced contrast offered by the PSIR images (and therefore the possibility of a more accurate segmentation) to calculate the cortical volume in both group of patients, as well as in healthy controls, in order to find out whether a more accurate measure of cortical volumes could detect further thinning in the NMOSD group when compared to healthy controls, since some was found by Calabrese and colleagues[6].

All these suggestions are for future studies. As for this thesis, the next chapter will look at the optic nerve, using magnetisation transfer ratio (MTR) to assess changes occurring in patients with and without optic neuritis, and see whether they differ sufficiently between NMOSD and MS to become potential markers.

Chapter 6

Optic neuritis in MS and NMOSD: looking for differences between diseases using MTR of the optic nerve and optic coherence tomography (OCT)

6.1 Introduction

As described in Chapter 2, optic neuritis (ON) is common in both MS and NMOSD patients and includes primary inflammation, demyelination as well as axonal damage of the optic nerve[1]. It also tends to be more aggressive in NMOSD, with a much smaller proportion of patients making a full recovery: 60% of NMOSD patients suffer from either unilateral or bilateral blindness after a median of 7.7 years from disease onset, compared to only 4% of MS patients after 15 years[2].

6.1.1 Why use magnetisation transfer ratio (MTR) of the optic nerve?

As discussed in Chapter 3, section 5, MTR can be used to assess myelin integrity by measuring the exchange of proton between the two 'pools' existing in biological tissues (free water and macromolecules such as proteins or membrane lipids). Maps, based on the signal intensities and showing the estimated MT ratio, are then produced. In the context of optic neuritis, the fact that both the optic nerve myelin (through demyelination followed by remyelination) and axonal density are affected by the disease makes MTR a particularly promising approach to assess changes in myelin and axonal integrity[4,5].

As Klistorner and colleagues observe, previous studies using MTR to look into the optic nerve inflammation have produced inconclusive results when it comes to determine whether a decrease in average MTR is correlated to demyelination or axonal loss. Their own study suggests that MTR is associated with axonal degeneration rather than demyelination[5]. If their conclusions are correct, then

MTR should be a particularly appropriate technique to detect differences between NMOSD and RRMS, as studies looking at the retinal nerve fibre layer (RNFL) thickness found a significantly higher reduction in NMOSD patients when compared to MS ones[7-11]. This finding is of direct relevance when looking into the application of MTR to the optic nerve, as a reduction in RNFL thickness is also a measure of axonal loss[12]. Therefore it would be expected that a larger MTR decrease would be found in NMOSD patients with ON when compared to MS-ON patients.

6.1.2 Optic nerve anatomy

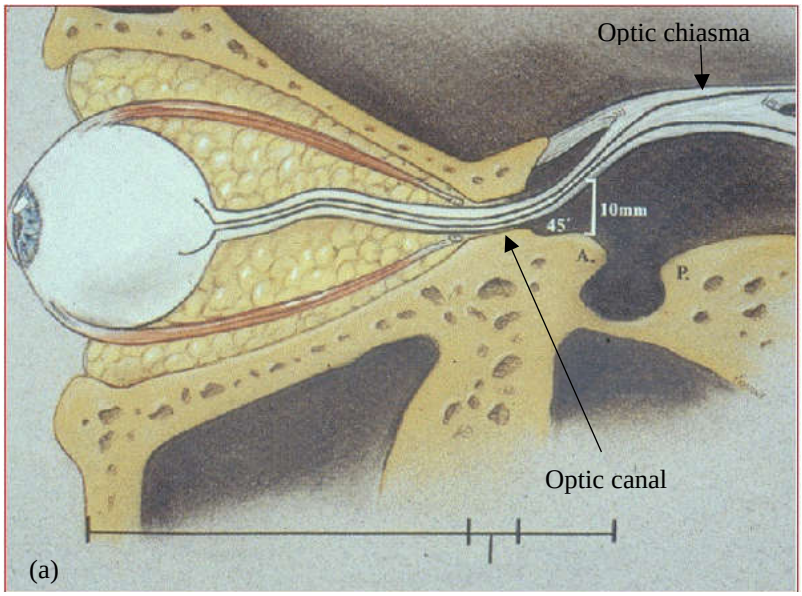

Permission for reproduction not granted.

(b)

Figure 6-1 (a) Optic nerve (Adapted from Schimming [et al.][3]); (b) Schematic cross-sectional view of the optic nerve head. Central retinal artery in red, retinal nerve fibre layer (N) and bundles (A) within the optic nerve, separated by glia (G). The sclera (S) and dura (D) surround the eye and optic nerve respectively (Adapted from Levin[6]).

In order to understand how the MTR measurements were made, as well as some of the problems encountered with the registration in particular, it is worth having a brief look at the anatomy of the optic nerve. As can be seen in **Figure 6-1a**, the optic nerve starts at the back of the eye, enters the skull through the optic canal and ends at the optic chiasma. The optic nerve itself is composed of bundles surrounded by the dura (**Figure 6-1b).** As the images acquired were coronal, they show 'slices' of the optic nerve from the back of the eye to theoretically the optic canal part, but in practice the optic nerve becomes more difficult to differentiate from the surrounding tissues when it reaches the optic

canal, due to a decrease in contrast as the meningeal layers get thinner, as can be seen in **Figure 6-2**.

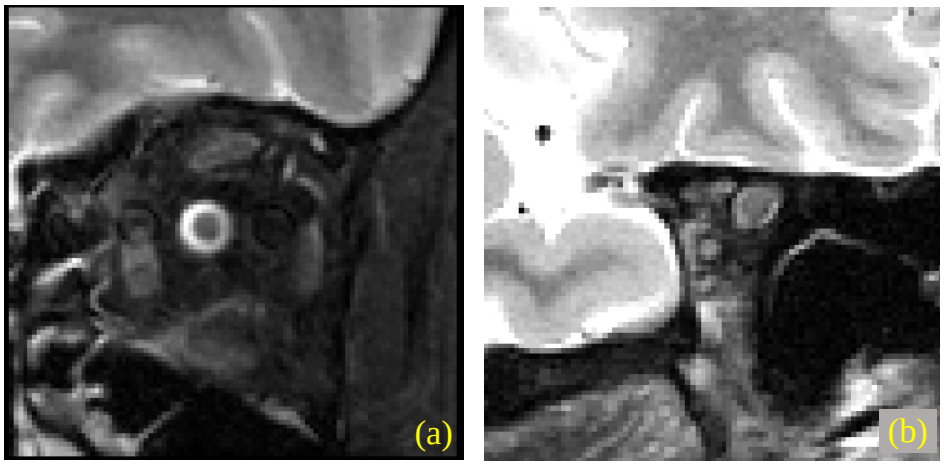

Figure 6-2 T2 images of the optic nerve (a) intra orbital, with the dura and CSF clearly visible as a white ring around the optic nerve; (b) inside the optic canal: even with a subject who kept her eye very still as is the case here, the boundary between the optic nerve and the dura becomes blurred.

A further difficulty, at the level of both image acquisition and registration, is that any eye movement during the scan will lead to motion in the optic nerve, as can easily be imagined from **Figure 6-1**. This causes two different types of problems: from the acquisition point of view, too much motion will result in blurred images that will be useless as the boundary between the dura/CSF and optic nerve is no longer visible; for registration, as a collection of fixed points within the images are used for repositioning, the fact that the exact position of the optic nerve will vary means than an accurate registration is very difficult to achieve, as will be illustrated below.

6.1.3 Optical coherence tomography (OCT)

Optical coherence tomography (OCT) is a non-invasive technique providing high resolution *in vivo* images of the retina, either cross-sectional or 3D. It is similar to ultrasound, but uses light reflections instead of acoustic echoes to acquire scans and can generate images of the microstructure of posterior ocular structures such as the RNFL, optic disc and macula.

It had been used to look at NMOSD and MS patients with a history of optic neuritis and significant differences in both macular and RNFL thickness were found when the two groups were compared[7-11,13]. Thus it appeared that in the

context of this study, it would interesting to assess whether these measurements would correlate with changes in the MTR of the optic nerve.

6.2 Methods

6.2.1 Subjects

Written, informed consent was obtained from all participant, and this study was approved by the NRES Committee London Bloomsbury (Formally London REC 2 Ethics Committee). RRMS patients were diagnosed using the revised McDonald criteria[14], while the NMOSD diagnosis was based on the criteria proposed by Wingerchuk and colleagues in 2006[15]. 19 NMOSD patients, aged between 21 and 70 years, and 19 MS patients, aged between 26 and 55 years, with a similar gender ratio and disease duration, as well as 23 healthy controls, aged between 23 and 68 years, were consecutively recruited. 17 of the NMOSD patients were AQP4 positive, while one of the two AQP4 negative was MOG positive. Not all patients had a history of optic neuritis and none of those who had did suffer from a recent attack (past 12 months). The full details for each group are given in **Table 6-1.**

	RRMS patients *n*=19	NMOSD patients *n*=19	Healthy controls *n*=23
Age (years)	41.28 ±9.86	52.72±11.69	36.87±8.92
Gender (F/M)	15/4	16/3	12/9
Median EDSS (range)	2.5 (1-7.5)	4.25 (2-6.5)	N/A
Disease duration	8.83±6.20	7.89±6.92	N/A
WM PD/T2 LL (ml)	5.08±4.84	1.05±1.55	N/A
AQP4+	N/A	17	N/A
ON (bilateral)	10(1)	12(6)	N/A

Table 6-1 Demographic and clinical data

6.2.1.1 Exclusions

Two controls and one NMOSD patient had to be excluded due to the amount motion artefacts, which either made the scans unusable or the MTR maps were deemed unreliable. Additionally, the scans for one eye in a control and in an

MS patient had to be excluded due to acquisition problems (control) and quality issues with the MT_{off}/MT_{on} registration (patient). In these two cases, only data from one eye was used instead of an average of both eyes.

6.2.2 Image acquisition

Using a 3 T Philips Achieva MRI system with dual-transmit technology (Philips Healthcare, Best, Netherlands) and the manufacturer's 32-channel head coil, the optic nerves were imaged in the coronal-oblique plane (i.e. slices perpendicular to the nerve) from the back of the globe to the optic chiasm. The following sequences were acquired: for use with positioning, (i) an axial 2D turbo-spin-echo (TSE) PD/T2-weighted sequence, with TR = 3500 ms; TE1/TE2 = 15/85 ms; echo train length = 10 echoes; FOV = 240×180 mm^2; voxel size = 1×1×3 mm^3; number of excitations (NEX) = 1; 50 contiguous slices, and (ii) a sagittal 3D-turbo field echo T1-weighted with TR = 7 ms; TE = 3.1 ms; TFE=230; TI: 834 ms; FOV = 256×256 mm^2; voxel size = 1×1×1 mm^3; number of excitations (NEX) = 1; 180 contiguous slices (iii) for cross-sectional area, and for each optic nerve separately, a coronal-oblique fat-suppressed TSE T2-weighted, with slice 1 within the globe and slice 2 at the beginning of the anterior portion of the optic nerve, TR = 3000 ms; TE = 80 ms; echo train length = 15 echoes; FOV = 160×160 mm^2; voxel size = 0.5×0.5×3 mm^3; number of excitations (NEX) = 3; 20 contiguous coronal slices (iv) for MTR imaging, again for each optic nerve separately, using the same positioning than for the TSE-T2w (achieved by copying the geometry between the two scans), consisting of a 3D slab-selective FFE sequence with two echoes (TR = 49 ms, TE1/TE2 = 3.6/6 ms, flip angle α = 9°), performed with and without Sinc-Gaussian shaped MT saturating pulses of nominal α = 360°, offset frequency 1 kHz, duration 16 ms. Twenty slices were acquired in the coronal-oblique plane, with FOV = 160 × 180 mm and acquisition matrix 212× 212 (voxel size 0.75 × 0.75 × 3 mm^3 reconstructed to 0.5 × 0.5 × 3 mm^3), NEX = 2, SENSE acceleration factor = 2, scanning time = 7 min. An example of the field-of-view box used is shown in **Figure 6.3**. The total scan time for the protocol, (iii) and (iv), was ~ 14 minutes per optic nerve.

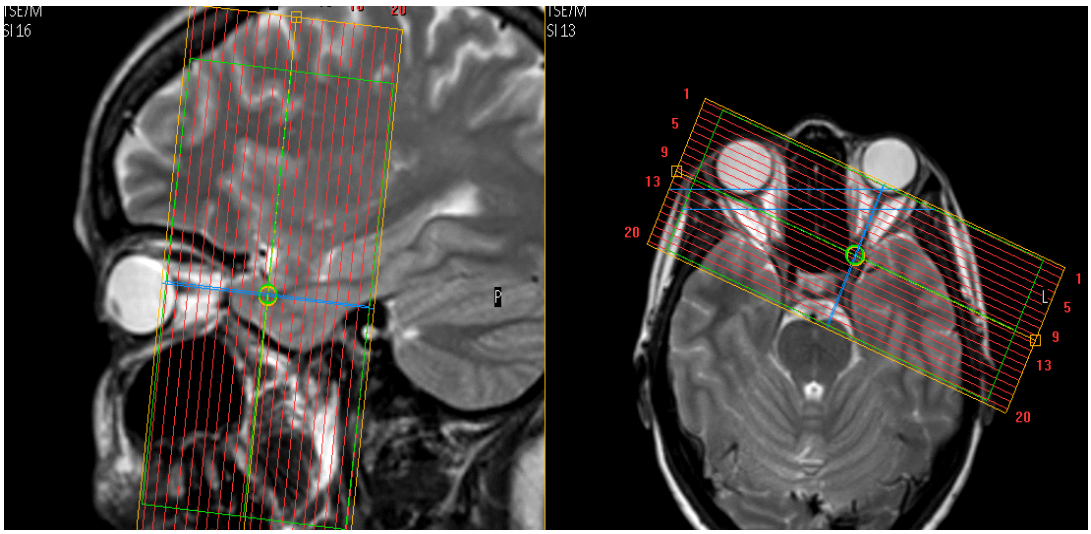

Figure 6-3 Positioning of the field of view box for the left optic nerve**.**

The scans were performed asking the subjects to keep their eyes closed. The MTR protocol was originally developed for the spinal cord[16].

Two sets of MT images were acquired for each eye to obtain a better SNR.

6.2.3 Registration

As explained in the anatomy section, the optic nerve is a mobile structure, which makes achieving a good registration extremely challenging. One of the key problems was that the position of the optic nerve could differ quite substantially between the MT_{off} and MT_{on} maps. Consequently, three different registration pipelines were applied in the context of this study. The first one, which was developed for a previous study, proved unsatisfactory. When looking at the different stages, two problems were detected that could easily be addressed: the images were cropped before the registration was done, thus significantly reducing that amount of information available for this procedure. The second was that the MT_{off} and MT_{on} images were registered to the T2 ones. Since the T2 images were used purely to enhance the accuracy of the positioning of the ROIs in the optic nerve, this process introduced further distortions in the final MTR maps without bringing any advantage. Registering the T2 images to the MT ones caused a small loss in quality, but too small to affect their usefulness for the required purpose. Besides these changes, the number of degrees of freedom used was also increased from 6 to 12.

The full revised pipeline was as follows: the two MT_{off}, the second MT_{on} and the T2 images were affine registered to the first MT_{on} image. The two MT_{off} and two MT_{on} images were then averaged in order to create a single MT_{off} and MT_{on} set of images (needed to produce the MTR map). The next stage consisted of cropping these three sets of images and then creating the MTR maps using the following calculation:

$$100\times(MT_{off} - MT_{on})/ MT_{off}$$

The maps obtained with this registration pipeline were used to delineate the ROIs and for the initial analysis.

The third registration pipeline was introduced at a late stage, in a further attempt to reduce the effect of motion. Just as in the NODDI study, this was done using the NiftyReg software package (http://niftyreg.sf.net), which implements a symmetric and inverse-consistent registration that ensures the results are not biased towards the directionality of the registration process. The new pipeline was as follow: the first stage consisted of rigidly aligning the MT_{off} and MT_{on} maps from the two acquisitions. Then, the transformation to the half-way space between first and second MT acquisition was computed, before moving the four set of images (two MT_{on} and two MT_{off}) to this space. Next, the means of MT_{on} and MT_{off} images were computed. These averaged MT_{off} and MT_{on} images were used to compute the MTR maps with the calculation shown above. Finally, the T2 images were registered to the mean MT_{on} using a rigid transformation.

The ROI masks also underwent a rigid registration similar to the one for the T2 images so that they could be automatically applied to the MTR maps (this was necessary as the software JIM 6.0 allows partial voxels but not NiftyReg). The final stage was the computation of the means and standard deviations for the masked areas in the MTR maps, removing the 2% of outliers.

For both pipelines, the same process was performed for both the left and right eye.

6.2.4 ROIs positioning

Initially, the ROIs were manually delineated, however this was changed in order to increase reproducibility, and the automated contour detecting function in JIM 6.0 (Xinapse systems, http://www.xinapse.com) was used instead. In most subjects, the T2 maps were used to position the ROI (for 6 patients, 3 MS and 3 NMOSD, the quality of the T2 images was too poor), with the Contour ROIs centred in the optic nerve. As at least part of the dura was often included in the ROI due to insufficient contrast for automatic boundary detection, the erosion function was used to reduce the ROI size until only the optic nerve was included. Further repositioning using the averaged MT_{off} and MT_{on} was often

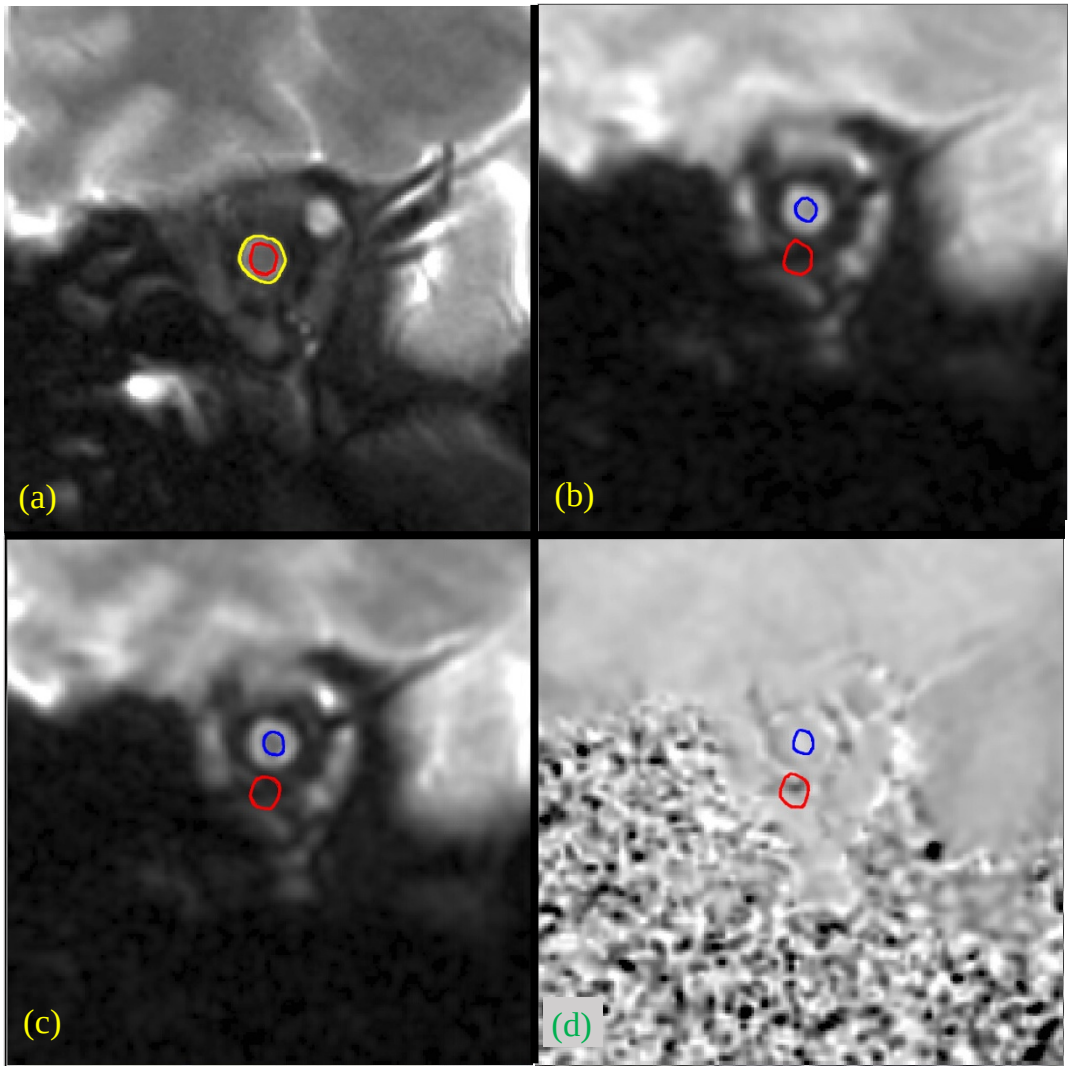

Figure 6-4 ROI positioning (a) T2 map, with the original ROI using the automatic contour detection (yellow) and the eroded one (red) (b)-(d) MT_{off}, MT_{on} and MTR maps showing the position of the original ROI from the T2 map (red) and the repositioned one (blue). As can be seen, the ROI has been eroded further to ensure that only optic nerve tissue is included.

required due to the imperfect registration between the T2 and averaged MT images (**Figure 6-4)**. In some cases, ROIs had to be discarded because of the poor quality of either the MT_{off} or MT_{on}. Further checks were made using a coloured version of the MTR maps as this allowed detection of contrast irregularities that are not easily visible on a greyscale map (**Figure 6-5**).

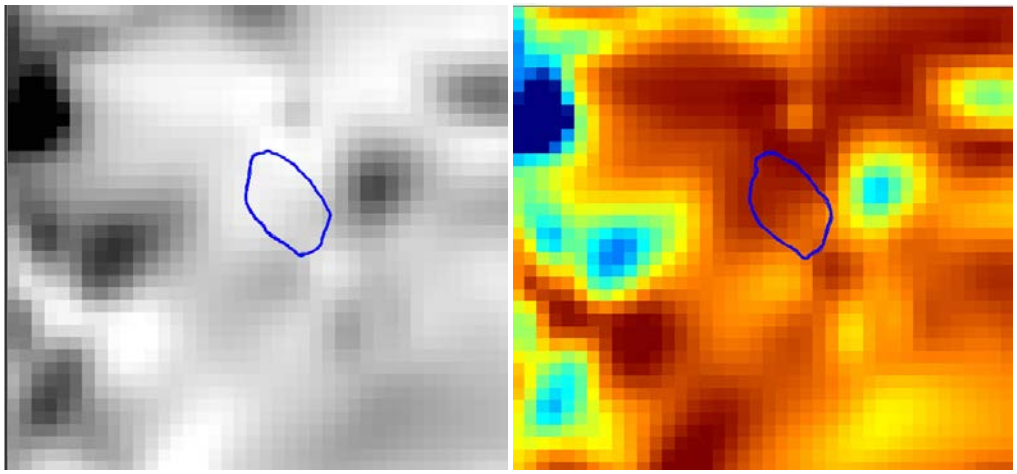

Figure 6-5 Details of grey scale and colour MTR maps. Subtle changes in the contrast are more visible in the colour map. This was used to assess the quality of the MTR maps when there were uncertainties due either motion artefacts or registration issues in the MT_{off} and MT_{on} maps.

An additional advantage of the use of the automated detection was that more ROIs could be incorporated, including in the optic canal and in some cases even in the intra-cranial part of the optic nerve. Nevertheless, the number of ROIs inserted in each eye varied between subjects, in part because motion artefacts often limited the amount of ROIs that could be placed in the anterior portion of the optic nerve, but also because the length of the nerve varies across subjects. The number of ROIs per subject ranged from 3 (in only three nerves) to 12 (in only two nerves), with an average and a median of 7 on both sides. Most ROIs were placed in the orbital section of the optic nerve, but some were in the optic canal. In two controls and one MS patient, one ROI was placed in the intra-cranial section of the optic nerve in at least one eye. The positioning was done while being blinded about the ON status of each nerves.

The average data from all ROIs was used for the analysis, but the values for each individual ROI were checked and, in the cases where inconstancies were found (like sudden large increases or decreases in values), the position of the ROI was checked again and corrections made where necessary.

6.2.5 Protocol validation

In order to assess intra-subject variability related to scan-rescan reliability, 5 healthy controls (HC), 3 females, 2 males, were scanned 3 times with a minimum interval of two weeks between scans. The full data can be seen in **Table 6-2**, while **Figure 6-6** show how the values compared across scans between subjects for both left and right eyes.

Age	Gender	Left eye, scan 1 (SD)	Left eye, scan 2 (SD)	Left eye, scan 3 (SD)	Right eye, scan 1 (SD)	Right eye, scan 2 (SD)	Right eye, scan 3 (SD)
27	M	31.98 (4.63)	34.45 (5.90)	32.67 (6.66)	32.89 (6.76)	34.71 (5.05)	32.32 (4.60)
27	F	33.20 (5.20)	32.17 (3.82)	35.10 (3.46)	33.82 (5.71)	34.47 (7.28)	34.95 (4.60)
50	F	34.09 (7.66)	33.02 (4.28)	36.61 (6.27)	31.10 (6.10)	30.14 (4.38)	30.18 (4.65)
32	F	32.10 (6.37)	33.78 (4.02)	35.10 (5.34)	35.04 (8.06)	33.71 (4.83)	34.03 (4.61)
27	M	37.65 (6.26)	37.16 (8.18)	35.58 (6.64)	33.52 (4.68)	35.50 (6.55)	35.13 (6.80)

Table 6-2 Demographics and data for repeats of healthy controls

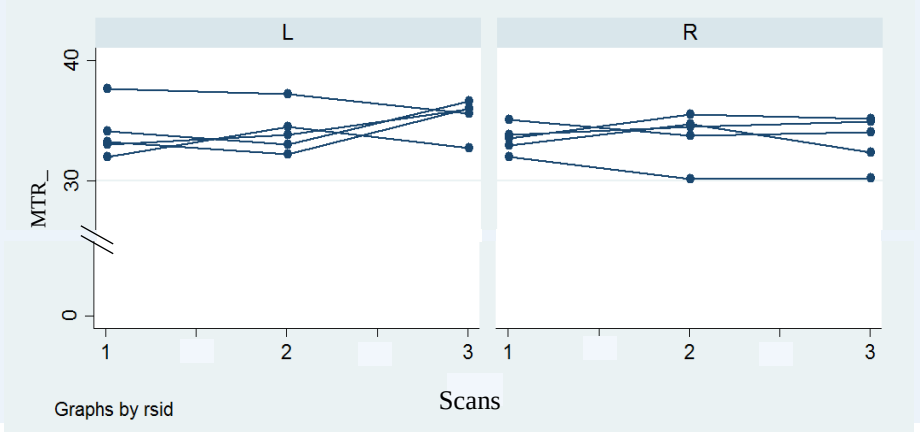

Figure 6-6 MTR values across scans in the left and right eyes. L=left; R=right

Statistical analysis to assess the amplitude of the measurement error was done using interclass correlation coefficient (ICC) and coefficient of variation (COV). Statistics were based on the standard deviation (SD), which characterises biological variability in between-subject comparisons, as some degree of variations is to be expected, but corresponds to a measurement error when looking at variability within subjects across repeats, as such measurements should not fluctuate. The two approaches make different

assessments. 1-ICC gives the within-subject variance (the square of the within-subject SD) as a proportion of the total variance, which consists of the biological variability between subjects together with the measurement of variability within subjects. The reason why two types of statistical tests were used is because 1-ICC can be misleading when applied to small samples of healthy subjects with very little biological variability, as is the case here. The ICC is 0.31, and since the proportion of variability due to measurement error is equal to 1-ICC, it is 0.69. This means that 69% of the total variance is attributed to measurement error.

For the coefficient of variation (COV), the within-subject SD, as a proportion of the mean value of the measure, is averaged across subjects. Its calibration in this context is much broader as it corresponds to the scale of what is measured. So as the mean value for all repeats in both eyes is 34.5, a within-subject SD of around 1 will be calibrated as 1/34.5. As it is very small, it implies that there is very little measurement error. An additional advantage of COV is, that unlike ICC, it is not as affected by sample size. The measurement error found using this approach was indeed much smaller as the COV was 0.044. In other words, the measurement error, which here is represented by the within subject SD, is just 4.4% of the mean.

This means that MTR measurements can reliably detect differences that are of a larger order of magnitude than the within-subject SD, but would not be effective at detecting more subtle changes. For the measurements made here, the average within-subject SD is 1.52, so much smaller than the average differences detected between affected nerves in patients and those of healthy controls, which are -4.92 for MS and -7.77 for NMOSD.

6.2.6 Visual assessment

Visual acuity for each patient eye was tested, using ECTRS letter charts, both with and without pinhole correction (the best result was used), the low contrast Sloan letter charts (1.25% and 2.5% contrasts) and the Farnsworth-Munsell 100-hue test. Visual assessments were not made on healthy controls as these

tests are routinely used in clinical contexts, have a standardised format with the accuracy of their scoring well established.

6.2.7 Optical coherence tomography (OCT)

In order to measure the retinal nerve fibre layers (RNFL) and macular thickness, high resolution spectral domain optical coherence tomography (OCT) images were acquired with a Spectralis OCT device (Heidelberg Engineering, Heidelberg, Germany) equipped with an image alignment eye tracking-software (TruTrack, Heidelberg Engineering, Heidelberg, Germany). Furthermore, the automatic real time (ART) enable the acquisition of a specific number of frames per scans as will be explained below. For the purpose of this study, both patients and controls underwent OCT scanning using the following protocol:

- For the RNFL, the scan is circular with a diameter of approximately 3.5 mm, centred on the middle of the optic disc (**Figure 6.7a**), with 100 frames.
- For the macular thickness, the scan is centred on the fovea (20 x 20° field) and the images acquired in a series of 25 sections comprising 9 frames each (**Figure 6.7b**).

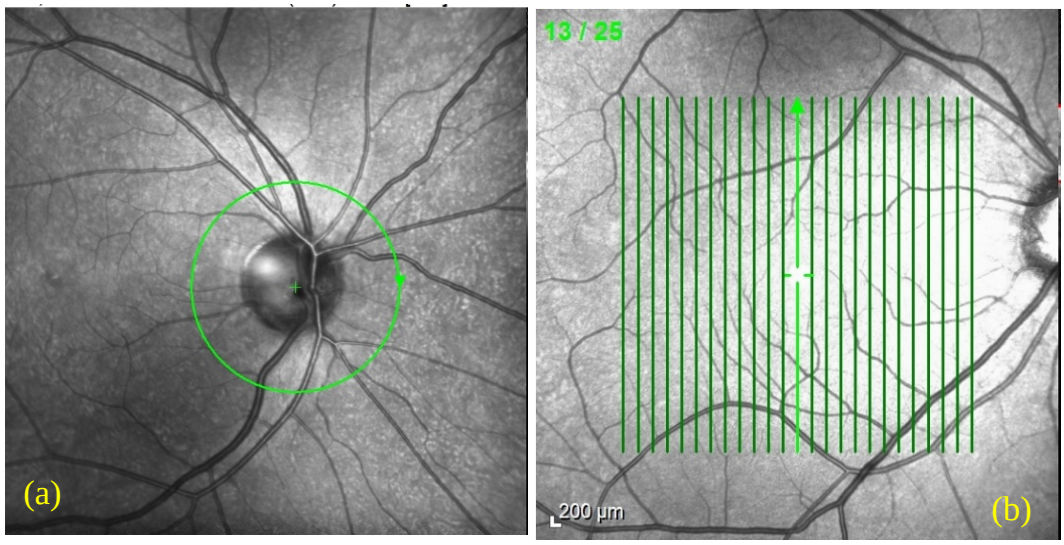

Figure 6-7 The areas of measurement in images of the fundus: (a) RNFL, measured in a circular scan centered on the optic disc; (b) macular thickness.

The RNFL scans were particularly difficult to acquire because the 100 frames needed in a single sequence requires subjects to keep their eye very still for a

longer period. By comparison, the macular scans are automatically paused between sections if there is too much eye movements. This does not completely solve the problem as some scans had missing data for some sections, but it makes the acquisition much more straightforward than it was for the RNFL. There, the combination of difficulties in keeping the eye still with problems linked to partial or near total sight loss (which made it difficult for patients to see the fixation point) meant that data was only acquired for a limited number of patients (9 NMOSD out of 19). The curvature of the retina in subjects who are either very longsighted or very short-sighted is also an issue and made it impossible to acquire RNFL scans for 3 healthy controls.

Further scans had to be excluded as they did not meet the quality control requirements, as stated in OSCAR-IB Consensus[17]: either the signal strength was below 25dB or there were technical issues such as poor focus or the scan was not properly centred.

6.2.8 Statistics

Multiple linear regressions adjusted for age and gender were used to compare the MTR, OCT and visual assessment values between the different groups.

For MTR data comparisons:

- Affected optic nerve in NMOSD and MS patients vs. optic nerve in HC
- Affected optic nerve in NMOSD patients vs affected optic nerve in MS patients.
- In both NMOSD and MS patients: unaffected vs affected optic nerve.

Additional tests were made to assess whether residuals were normally distributed, and some slight heteroscedasticity linked to age was found. To correct for this, a heteroscedastically-robust test (robust standard error estimates) was used. Heteroscedasticity refers to a spread that is uneven and irregular, and finding it for some of the values meant that variances differ substantially either between subject groups or across values of a regression variable. The reason why it needed to be corrected for is because one of the crucial outputs of linear regressions is the residual, that is the difference

between the observed value of the dependent variable and the predicted value. Linear regression models assume that residuals will be scattered with similar variability across the range of predicted values, therefore the presence of heteroscedasticity can seriously affect both significance tests and confidence interval estimations.

Moreover, further tests were made to assess the hypothesis that 4 subjects were unduly influential, and showed that they did indeed have a conservative effect, reducing both the size and significance of the differences between NMOSD patients and both MS patients and healthy controls (i.e. the reduction of MTR in NMOSD is larger when compared to MS and healthy controls when these influential subjects are excluded). Concretely, this means that the detected difference between NMOSD and MS patients is robust even if it failed to reach significance.

For OCT data, each comparison was made for both the macula and RNFL:

- Affected eye in NMOSD and MS patients vs. eye of HC.
- Affected eye in NMOSD patients vs affected eye in MS patients.
- In both NMOSD and MS patients: unaffected eye vs affected eye.

For the visual assessments:

- In NMOSD and MS patients affected eyes, correlation with MTR.

Results associated with $p<0.05$ and 95%CI were considered significant.

6.3 Results

Table 6.3 and 6.4 give the full results for the MS and NMOSD patients respectively, including the visual assessments and OCT measurements for both the macula and the RNFL. **Table 6.5** contains the MTR data and OCT measurements for the healthy controls.

Unless patients had unilateral ON, an average of the values from both nerves was used for the analysis, as the two nerves from the same subject cannot be considered as independent. The absence of independence is further supported by the fact that changes were also found in unaffected nerves of NMOSD patients with unilateral ON.

Age	Gender	EDSS	Dis. Dur. (y)	VA L	VA R	1.25% Sloan Chart L	1.25% Sloan Chart R	2.5% Sloan Chart L	2.5% Sloan Chart R	100 hue test L	100 hue test R	ON L	ON R	No sl. L	No sl. R	MTR L (SD)	MTR R (SD)	RNFL Ave L	RNFL Ave R	Macula (mm^3)L	Macula (mm^3)R
21	F	2.5	2.5	0.14	0	0	0	0	0	12.17	15.87	Y	Y	6	6	26.77 (4.63)	31.74 (8.89)	72	86	8.23	7.97
50	M	3	10	0.14	-0.12	2	25	7	34	18.22	12.33	Y	N	7	8	22.83 (8.08)	30.92 (6.42)	54	90	7.81	8.56
53	F	6	3	-0.1	-0.12	32	31	38	37	8.94	8.25	N	N	4	5	33.96 (6.45)	30.12 (7.13)	77	85	8.67	8.82
69	*F*	*6.5*	*2*	*0*	*0.1*	*0*	*0*	*0*	*6*	*15.1*	*15.23*	*N*	*N*	*10*	*6*	*29.67 (7.09)*	*32.42 (6.28)*	*N/A*	*N/A*	*N/A*	*N/A*
53	F	6	3	0.2	0.1	0	8	0	3	7.48	6.63	N	N	9	8	34.05 (7.50)	30.80 (5.53)	N/A	N/A	N/A	N/A
52	F	4	6	1.14	1.7	0	0	0	0	N/A	29.39	Y	Y	12	11	26.13 (8.40)	22.84 (4.62)	N/A	N/A	N/A	N/A
37	F	4	3	1.52	0.92	0	0	0	0	24.49	22.09	Y	Y	10	8	25.74 (6.02)	25.71 (6.67)	N/A	N/A	7.33	7.37
56	F	6	2	0.02	0.12	19	19	18	17	8.49	11.31	N	N	8	8	35.59 (7.18)	31.27 (6.28)	102	108	9.27	9.33
63	F	6.5	14	0.1	0	0	0	0	0	12.00	14.83	N	N	9	10	31.29 (6.85)	29.22 (6.45)	N/A	53	N/A	7.04
41	F	3	4.5	0	0	0	0	0	0	N/A	11.49	Y	Y	12	9	22.26 (5.18)	25.60 (6.78)	104	97	8.71	8.5
66	M	3.5	15	0.04	0.02	13	17	19	23	6.63	4.47	N	Y	9	9	34.19 (6.94)	29.67 (6.82)	N/A	N/A	8.71	8.72
51	F	6	6	0.2	0.14	10	14	18	19	10	9.38	N	Y	7	3	31.54 (7.22)	26.31 (9.66)	N/A	N/A	N/A	8.16
51	F	2	17	1.7	0.14	19	0	34	0	N/A	8.25	Y	Y	6	7	23.70 (3.13)	30.58 (6.04)	97	95	8.87	8.83
48	M	2	7.5	-0.1	-0.12	22	15	29	20	4.47	6.00	N	N	5	7	31.89 (5.61)	33.07 (8.77)	46	33	7.43	N/A
57	F	5.5	4	0.02	0.52	10	0	17	0	16.00	21.82	Y	Y	10	9	25.92 (5.08)	26.37 (7.09)	N/A	85	N/A	8.29
54	F	2	4.5	1.7	-0.1	16	0	37	0	N/A	4.00	Y	N	8	10	25.18 (3.91)	27.09 (4.92)	74	N/A	7.53	7.75
70	F	4.5	10.5	0.14	0.14	10	5	23	21	15.23	14.42	Y	N	5	6	26.67 (5.52)	33.88 (6.72)	88	N/A	7.69	N/A
57	F	5.5	29	0.12	1.7	15	N/A	32	N/A	9.59	N/A	N	Y	8	4	32.162 (4.98)	22.85 (5.29)	N/A	N/A	8.06	7.93

Table 6-3 Full results for NMOSD patients, with the data for the affected eyes and nerves highlighted.
The patients in blue are the two AQP4-, the one in italic is MOG+. Abbreviations: Dis. dur.: disease duration; VA: visual acuity; ON: optic neuritis; No sl.: number of slices; RNFL: retinal nerve fibre layers ; Y: Yes; N: No; L: left; R: right

Age	Gender	EDSS	Dis. Dur. (y)	VA L	VA R	1.25% Sloan Chart L	1.25% Sloan Chart R	2.5% Sloan Chart L	2.5% Sloan Chart R	100 hue test L	100 hue test R	ON L	ON R	No sl. L	No sl. R	MTR L (SD)	MTR R (SD)	RNFL Ave L	RNFL Ave R	Macula (mm^3)L	Macula (mm^3)R
36	F	4	13	0	-0.14	24	28	22	28	13.42	11.31	Y	N	5	3	24.56 (7.61)	30.01 (9.81)	73	104	8.51	8.99
24	M	4.5	4	N/A	N/A	0	0	4	0	10.77	11.14	Y	Y	5	5	23.18 (7.10)	27.44 (5.99)	63	61	8.18	7.99
50	F	2.5	26	-0.1	0.12	11	14	21	25	N/A	N/A	N	N	8	7	32.60 (6.60)	35.44 (10.57)	N/A	N/A	8.58	8.30
30	F	1.5	6	0	0.12	7	6	23	15	7.75	8.00	N	Y	6	5	31.16 (6.06)	36.36 (6.74)	102	98	8.75	8.71
55	M	7	15	-0.11	0	4	4	3	4	10.20	10.58	N	N	5	5	36.88 (5.57)	33.43 (5.75)	101	N/A	7.45	8.11
35	F	1	5	-0.12	-0.14	19	16	23	29	12.65	12.65	N	N	7	6	31.18 (3.69)	33.23 (4.26)	106	104	9.97	9.81
48	F	1.5	10	-0.2	0.12	0	10	0	34	N/A	9.38	Y	N	7	6	31.59 (6.20)	32.31 (8.26)	46	68	7.15	7.62
43	F	3	15	0	0	35	35	38	38	15.49	12.81	Y	N	5	5	23.20 (6.72)	29.74 (6.86)	88	91	8.63	8.74
54	M	7.5	9	0	0.04	N/A	36	N/A	38	31.81	9.80	Y	N	9	9	28.74 (4.79)	35.17 (10.48)	93	97	N/A	9.17
54	F	1.5	5	-0.14	0	24	27	25	28	12.49	12.96	N	N	6	8	30.20 (9.18)	35.80 (8.88)	85	97	8.42	8.54
34	M	4	14	0.12	0.12	17	19	30	34	11.83	10.58	U	U	6	6	28.57 (5.17)	33.44 (7.54)	87	87	8,35	8.39
38	F	1.5	6	-0.12	-0.16	31	19	37	32	5.29	6.63	Y	N	7	9	32.36 (4.44)	32.31 (5.50)	83	59	9.16	8.50
31	F	3.5	2	0.04	0.1	27	27	35	34	9.59	9.80	N	N	5	7	34.26 (4.89)	29.45 (4.27)	108	108	N/A	N/A
42	F	1	5	-0.2	-0.1	22	24	24	34	8.72	9.80	N	Y	7	9	34.19 (6.89)	33.28 (4.94)	96	102	8.35	8.39
48	F	1.5	5	-0.04	-0.16	5	0	17	13	9.59	8.72	N	N	6	5	32.21 (3.78)	26.04 (6.09)	91	95	8.22	8.32
48	F	2.5	13	-0.1	0.04	0	0	9	11	12.33	13.56	Y	N	7	8	34.70 (4.38)	31.86 (7.50)	85	89	8.57	8.71
47	F	4	5	-0.1	0	29	29	39	30	8.00	8.25	N	N	7	0	33.01 (4.33)	N/A	100	106	8.36	8.45
26	F	1.5	1	0	-0.1	23	34	29	29	7.75	7.21	U	U	8	8	30.28 (6.94)	31.47 (6.41)	N/A	N/A	8.06	7.88

Table 6-4 Full results for MS patients, with the data for the affected eyes and nerves highlighted.
Abbreviations: Dis. dur.: disease duration; VA: visual acuity; ON: optic neuritis; No sl.: number of slices; RNFL: retinal nerve fibre layers; L: left; R: right; U: ON status uncertain.

Age	Gender	No sl. L	No sl. R	MTR L (SD)	MTR R (SD)	RNFL Ave L	RNFL Ave R	Macula (mm^3) L	Macula (mm^3) R
32	M	7	8	30.30 (5.60)	35.12 (7.34)	98	92	8.72	8.65
38	F	7	7	33.12 (6.69)	31.52 (6.20)	80	85	8.24	8.25
29	F	8	8	36.69 (4.79)	33.27 (6.22)	N/A	N/A	N/A	N/A
29	M	8	8	33.62 (8.26)	32.66 (7.80)	112	108	8.9	9.06
42	F	6	8	31.87 (8.20)	34.37 (6.98)	106	105	8.75	8.75
28	M	7	8	32.44 (6.53)	32.80 (10.76)	104	105	8.79	8.62
27	F	6	8	33.56 (4.20)	31.36(6.55)	100	100	8.96	8.97
27	M	6	9	35.63 (7.57)	34.59 (7.59)	128	124	8.71	8.75
27	F	6	7	30.71 (6.17)	33.74 (5.70)	91	94	8.03	7.95
52	F	5	7	34.95 (5.46)	35.01 (6.74)	98	101	9.34	9.46
36	M	9	9	34.49 (5.12)	35.87 (7.56)	111	115	9.10	9.18
23	F	8	7	32.62 (4.20)	32.74 (5.74)	114	112	9.15	9.17
28	F	N/A	8	N/A	33.46 (7.37)	N/A	N/A	8.33	8.29
24	F	5	5	32.94 (6.67)	30.30 (7.54)	103	104	8.46	8.47
23	M	9	8	33.07 (8.70)	30.95 (7.33)	N/A	N/A	N/A	N/A
50	F	4	4	30.97 (6.54)	31.10 (5.00)	81	86	8.94	8.89
27	M	9	9	31.17 (5.82)	32.11 (6.35)	95	92	8.55	8.58
27	M	7	8	34.87 (5.30)	31.68 (5.93)	100	100	8.69	8.79
32	F	7	8	34.45 (4.42)	36.41 (8.54)	96	N/A	N/A	7.14
62	M	6	7	34.95 (6.75)	33.69 (8.02)	N/A	N/A	7.86	7.77
68	F	7	8	34.23 (5.12)	33.72 (4.36)	N/A	N/A	N/A	N/A
57	F	7	7	35.31 (5.01)	32.19 (5.68)	N/A	N/A	N/A	N/A
60	F	3	4	36.53 (7.57)	33.72 (4.36)	107	106	8.88	8.90

Table 6-5 Full results for healthy controls. Abbreviations: No sl.: number of slices; RNFL: retinal nerve fibre layers; L: left; R: right

6.3.1 MTR data between group comparisons

Table 6.6 and **Figure 6-8** shows the results for the MTR data comparison between the various groups. As expected, the differences between the MTR of affected nerves in both MS and NMOSD patients when compared with healthy controls was highly significant (-4.92, $p<0.001$, 95% CI -7.19, -2.66 for MS vs controls and -7.77, $p<0.001$, 95% CI -10.02, -5.52 for NMOSD vs controls).

Healthy controls	NMOSD		MS	
(n=45)	Affected nerves (n=18)	Unaffected nerves (n=18)	Affected nerves (n=10)	Unaffected nerves (n=25)
33.33±2.27	25.94±2.64	31.80±2.20	28.37±3.65	32.64±2.55

Table 6-6 Average MTR values and standard deviations for each group. The *n* corresponds to the number of optic nerves included in each group.

When the initial comparison between the MTR of affected nerves in MS and NMOSD patients was made, it also came out as significant (-2.85, $p=0.032$, 95% CI -5.44, -0.26). After the application of the heteroscedastically-robust

test, the difference between MS and NMOSD was downgraded to borderline significant (-2.85, p=0.08, 95% CI -6.07, 0.37).

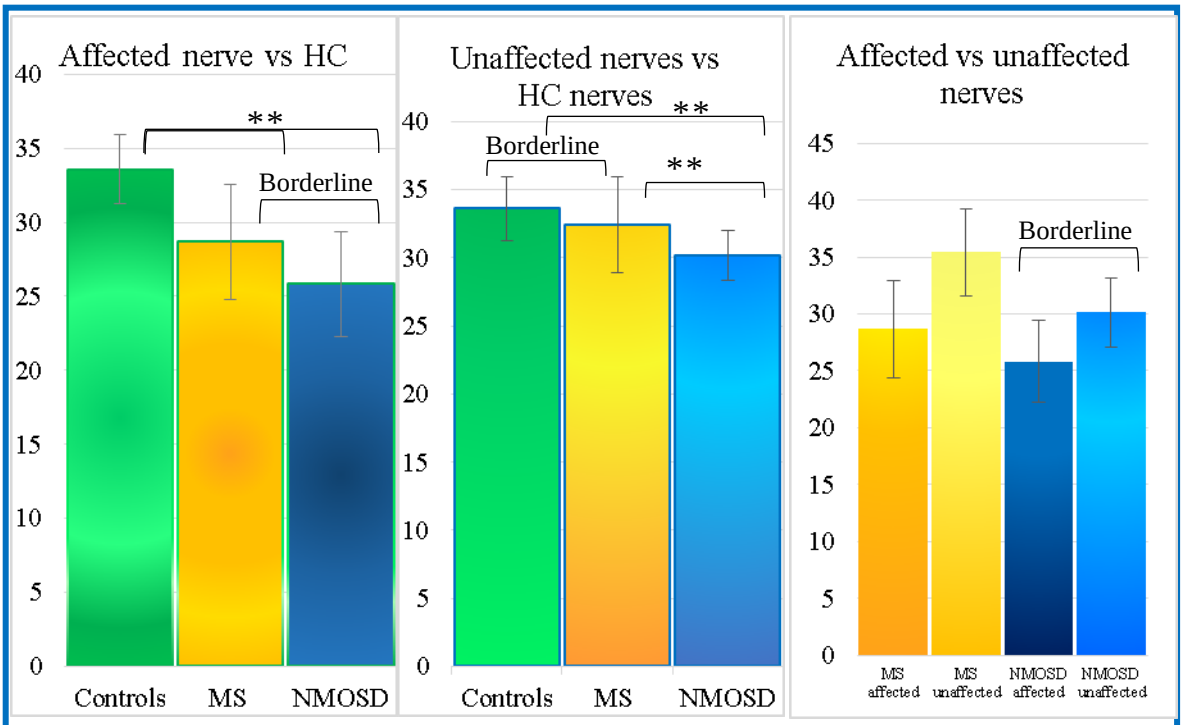

Figure 6-8 Graphs showing the group comparisons for the MTR data. Except for patients with unilateral ON, values for both nerves were averaged. ** p<0.001, except for NMOSD vs. MS unaffected nerves, p=0.007, * p=0.05 HC: healthy controls

The comparison of unaffected nerves in NMOSD and MS patients with healthy controls was straightforward and required no further adjustment. Interestingly, the difference found between the MTR of MS patients unaffected nerves and those of healthy controls was borderline significant (-1.33, p=0.058, 95% CI -2.70, 0.48), and became highly significant when the unaffected nerves of NMOSD patients were compared to those of both healthy controls (-3.59, p<0.001, 95% CI -5.24, -1.93) and MS patients (-2.26, p=0.007, 95% CI -3.87, -0.66).

The last comparison for the MTR was between the affected and unaffected nerves in patients with unilateral optic neuritis. There were only 15 patients contributing to this analysis, 6 NMOSD patients and 9 MS ones. While comparing all affected nerves with all unaffected nerves without separating NMOSD and MS patients gave a statistically significant lower MTR value in the affected nerve (-3.15, p=0.018, 95% CI -5.66, -0.63), once the test was run

on each group of patients separately, the statistical power became insufficient and the difference fell below the significance level. However, lower MTR value in the affected nerves of NMOSD patients remained borderline significant when compared to the values for the unaffected nerves (-3.59, *p*=0.064, 95% CI -7.42, -0.25).

6.3.2 RNFL and macula between group comparisons

The RNFL thickness of affected eyes in both patients groups was significantly lower when compared to healthy controls eyes, with the adjusted values as follow: for NMOSD patients -29.4 (*p*=0.009, 95% CI -50.3 to -7.9) and for MS ones -22.2 (p=0.012, 95% CI -39.1 to -5.3).

No significant difference was found between healthy controls eyes and affected eyes for macular volumes.

When comparisons were made between affected eyes RNFL thickness of the two patient groups, no significant differences were found either. However, as far as the RNFL thickness of NMOSD patients is concerned, the very limited data acquired is likely to have played a part in this lack of difference.

6.3.3 Visual assessments: between group comparisons and correlations with MTR

Visual acuity was significantly lower in NMOSD patients when compared to MS ones: -0.82, *p*=0.009, 95% CI -1.40, -0.24. On the other hand, none of the results of other tests (Sloan 1.25%, Sloan 2.5% and the Farnsworth-Munsell 100-hue test) were significantly different when the two groups were compared.

Correlations were also made between the data for the visual assessments and the MTR data without group subdivision by patient types. Highly significant correlations between the MTR results ($p < 0.001$) and visual acuity measured as well as the different visual assessments were found. The full details for each test are given in **Table 6-7.**

Test	Regression coefficient	95%CI
Visual acuity	-0.071	-0.087 to -0.055
Sloan 1.25%	1.153	0.918 to 1.389
Sloan 2.5%	1.338	1.0135 to 1.662
Farnsworth-Munsell 100-hue test	-0.755	-0.934 to -0.576

Table 6-7 Correlations between MTR data and the different visual assessments in the affected eye/nerve of all patients without sub-group division. p <0.001 for all correlations.

6.4 Discussion

6.4.1 MTR

The results for the optic nerve MTR are the most interesting part of this study. While the loss of significance in the comparison between affected nerves of MS and NMOSD patients after the correction for heteroscedasticity linked to age has to be acknowledged, it is also not entirely surprising if the small size of the groups is taken into account. There were only 10 MS and 12 NMOSD patients with optic neuritis to contribute to this analysis. However, as mentioned above the fact that a subgroup of 4 patients had a particularly high impact on the outcome suggests that the difference is nevertheless valid and could potentially become significant with larger groups of patients and the subsequent increase in statistical power.

It should also be stressed that the ROIs were always very conservative, as those in which lower values could potentially be linked to quality issues were discarded.

From a methodological point of view, matching MS and NMOSD patients for age would solve the heteroscedasticity issue, especially since it appeared that MTR values in WM and GM may be affected by ageing[18]. However finding enough RRMS patients who are in their late forties to early sixties may prove difficult since, due to the earlier onset of the disease, most patients in that age group are likely to be in the secondary progressive phase of the disease.

The differences in the affected optic nerve MTR between healthy controls and patient groups were as expected. While there had not been any previous study using MTR to look at changes in the intra-orbital optic nerve of NMOSD patients, there have been studies done in MS[5,19-23], the earliest one, from Thorpe and colleagues[24] dating back to 1995. Most of them found decreases in the affected optic nerves when compared to healthy controls. Only one study, by Frohman and colleagues[25], did not detect any differences between affected optic nerves in MS patients and healthy controls, and that could be due to methodological issues, as unlike the other studies, they did not use a ROIs approach.

The fact that MTR measurements were highly correlated with decreased visual acuity and other visual tests further validate them by demonstrating a clear link between pathological changes in the optic nerve measured with magnetisation transfer and loss of visual acuity caused by optic neuritis. These correlations, which are also in line with previous studies findings[20,22,23], demonstrate that the changes measured in the optic nerve using MTR are clinically relevant.

Finally, it is worth noting that at individual patients level, 5 affected optic nerves (out of 11) in the MS group had MTR values that are within the healthy nerve range (from 31.59 to 36.36), as can be seen in **Table 6-4**. This too is in line with the findings of longitudinal studies which show progressive recovery 12 months after the acute phase scans[22,26]. One more interesting observation at individual patients level is that such recovery appears to be less common in NMO patients (see **Table 6-3)** as only two out of 17 affected optic nerves had MTR values falling within the healthy range (31.74 and 30.58). This chimes with the fact that optic neuritis is more severe in NMOSD patients than in MS ones and a full recovery rarer[2,27,28].

Possibly the most interesting finding of this study is the significant differences found between unaffected optic nerves in MS and NMOSD patients and the optic nerves of healthy controls, as well as the significant difference between the unaffected nerves of the two patients groups. This suggests that undetected

subclinical changes are occurring in those patients, something which could potentially be clinically useful and was previously observed in MS patients' optic nerves by Trip and colleagues[23]. The possibility of subclinical changes occurring in the optic nerve of non-ON NMOSD patients was also suggested by studies looking at non-affected eyes using OCT in patients with LETM[29,30], in a study comparing RNFL and fovea of NMOSD patients (with and without ON) to healthy controls[31] and in one combining double inversion recovery (DIR) of the optic nerve with OCT measurements of NMOSD patients with mostly unilateral ON[32].

Nevertheless, while the fact that the existence of such sub-clinical pathology had been found with other techniques is promising for the validity of our data, these results would need to be further investigated, both by scanning a larger group of patients and by investigating the mechanisms underlying these abnormalities. The latter could be done in a post-mortem study combining MRI with histology: since it is established that lower MTR values occur in areas where there is a reduction in the proportion of water bound molecules relative to the number of macromolecules, it can be assumed that the underlying cause would be a loss of tissue microstructure integrity[21] which should be detectable at microscopic level.

Another way to take this further would be to include the optic chiasma, the optic tract and optic radiation in the study, as it had been suggested that they are commonly affected in NMOSD patients[33-36]. Furthermore, to be clinically useful, a benchmark would need to be established, and for this a lower measurement error is likely to be needed, as well as automated image processing pipelines to make the analysis less time consuming. Even taking into account the above mentioned requirements, these findings could well become useful both to distinguish between MS and NMOSD and to help diagnose NMOSD following an attack of optic neuritis sometime in the future.

6.4.2 OCT

Based on previous studies results, RNFL thickness was expected to be thinner in the affected eyes of NMOSD patients than in those of MS patients[7-11,37-41]. However, as mentioned above, the amount of data acquired for NMOSD patients was very limited due either to their inability to keep their eyes still or vision that was too poor for OCT scans to be performed.

The fact that so many studies managed to acquire data on NMO patients raised questions about our acquisition protocol. Comparing how the RNFL scans were acquired across studies is highly complex due to the variety of OCT systems available, which all appears to have very different settings. So the only comparisons possible were with studies which also used an OCT-Spectralis system, and even there, the number of frames used for the acquisition was not always specified. For the three studies that give this information, Martinez-Lapiscina and colleagues[40] used 100 frames as we did, however Outteryck and colleagues[42] and Hadhoum and colleagues[32] used at least 50 frames, suggesting that they had to lower the number of frames acquired for some patients. Such a reduction in the number of frames would significantly decrease the amount of time needed for the scan and may therefore have made a difference for some of the patients who had difficulties keeping their eyes still for a long period of time (the acquisition of 100 frames can be quite long as the system automatically pauses if there is too much movement).

There is also the possibility that changes in the RNFL are not as clear cut as the above mentioned studies would suggest. A longitudinal study by Manogaran and colleagues[43], looking at the RNFL thickness of NMOSD patients with ON over four years did not find any changes over that period, while a study comparing OCT with pattern electroretinogram (PERG) in NMOSD, LETM and MS patients did not find a significant difference in RNFL thickness between NMOSD and MS affected nerves[44]. Similarly, a study by Fernandes and colleagues[29] did not find any significant difference in RNFL thickness in affected eyes of MS and NMOSD patients, except when comparing patients

with a single episode of ON, though in a study by Lang and colleagues the difference for the same comparison did not reach significance[45]. Then there is also a study by Martinez-Lapiscina and colleagues[40] that found significant differences only for AQP4-IgG patients with ON or a study done by Outteryck and colleagues where the difference in the average RNFL ceased to be significant once it was adjusted.

Interestingly, two groups found differences when looking at the inner nuclear layer (INL) or RNFL quadrants: Fernandes and colleagues[29] show that INL was thicker in NMOSD patients than in MS ones, while Outteryck and colleagues[38] found significant differences in both RNFL quadrants and macular layers between NMO and MS. This suggests that it could be worthwhile to do further analysis on the acquired data, using segmentation to collect new data from individual macular layers and examining the data available from the RNFL quadrants. The latter have been successfully used in some studies already[7,9,10,13], often uncovering more significant differences between MS and NMOSD than when looking at RNFL thickness as a whole. If segmentation is done, the retinal ganglion cell layer (RGCL), sometimes grouped with the INL as RGCL+, is likely to be of particular interest since significant differences between affected eyes of NMOSD and MS patients were found there too[13,46].

6.5 Conclusion

The retina and visual pathway are structures that can provide useful information on NMOSD, both with and without ON. They may also offer useful ways to differentiate between the NMOSD and MS in the future. However, as the discussion of OCT findings clearly shows, such differentiation remains highly complex and proper validation of novel techniques is crucial before developing clinical applications.

A further reminder of the intricacies involved in most studies looking for markers that could differentiate between NMOSD and MS. The potential usefulness of the findings presented in this thesis, together with a general

evaluation of the suitability of the different MR approaches for clinical use, will be the focus of the following chapter.

Chapter 7

Conclusion

7.1 Overview

This thesis applied different MRI techniques or analysis methods to data from both MS and NMOSD patients in order to look for markers that could be helpful to differentiate between the two diseases. As noted in the introductory chapter on NMOSD, radiological characteristics detected on MRI scans have become a fundamental part of the criteria used in the new diagnosis developed by an International Panel for NMO Diagnosis (IPND) and published in 2015[1]. The inclusion of these criteria highlights the role played by MR techniques in furthering our understanding of both MS and NMOSD, as well as in detecting new markers. However, the limitations of MR techniques should also be acknowledged, especially the importance of using the correct method when looking for something specific, like cortical lesions in NMOSD for example, which were not detected on 7T scanners[2,3], but were found using phase sensitive inversion recovery (PSIR) for this thesis. The other important caveat when using MR scans is image processing, in particular procedures like registration, normalisation and segmentation, which will be discussed further below. Nevertheless, this thesis shows that new approaches can bring useful further insights with potential clinical applications.

7.2 NODDI

Neurite Orientation Dispersion and Density Imaging (NODDI) is a novel diffusion MRI technique devised to analyse the microstructure of dendrites and axons, which provides more specific metrics than standard indices from diffusion tensor imaging, such as fractional anisotropy (FA) or mean diffusivity (MD). As such, it could provide new markers to differentiate between MS and NMOSD, since as mentioned in **Chapter 1**, there should be much less change in the NAWM of NMOSD patients than in MS ones. The work done for this

thesis was an exploratory study, applying NODDI to a dataset of RRMS patients. The aims were to assess whether NODDI could provide additional information about changes occurring in grey matter and normal-appearing white matter (NAWM) of RRMS patients when compared to what is detected in FA maps, as well as the performance of NODDI on single HARDI-shell data since the technique requires at least two shells for optimal results. Two approaches were used, regions of interest (ROIs) and voxel based morphometry (VBM). The key findings were as follow:

7.2.1 ROIS

- Increased FA in the left internal capsule
- Decreased ODI in left and right internal capsules
- Decreased ODI and NDI in the genu of the corpus callosum
- Decreased NDI in the left and right occipital lobes

No correlations were found between EDSS scores, clinical scores and all the above parameters, except for the lower NDI values in the right occipital cortex, which correlated with longer disease duration.

7.2.2 VBM

FA: three clusters were found:

i. Body of the corpus callosum
ii. Left anterior corona radiata and left inferior fronto-occipital fasciculus
iii. Right posterior thalamic radiation.

All three clusters correlated with the Symbol Digit Modalities Test (SDMT). The first also correlated with the delayed story recall and the last with disease duration.

ODI: Five clusters were found:

i. Left optic radiation
ii. Right forceps major, right inferior longitudinal fasciculus and right inferior fronto-occipital fasciculus
iii. Body of the corpus callosum

iv. Right inferior longitudinal fasciculus

v. Right posterior thalamic radiation, right inferior fronto-occipital fasciculus, right inferior longitudinal fasciculus, right superior longitudinal fasciculus and right forceps major.

Clusters ii, iii and iv correlated with SDMT, while correlations with the delayed story recalled and EDSS were also found in clusters i and iv, with the Paced Auditory Serial Addition Test (PASAT) in cluster i and with age in cluster v.

NDI: Two clusters were found:

i. Splenium, left forceps major, body of the corpus callosum

ii. Left hippocampus

No correlation found for the white matter cluster, but the hippocampal one also correlated with SDMT as well as the delayed story recalled.

The results from both approaches show that the application of NODDI to single HARDI shell data is feasible and that ODI and NDI detected regions of diffusion abnormalities in RRMS patients not visible in FA maps. The areas affected by MS detected in the NODDI maps with VBM also correlated with both cognitive and clinical measurements, suggesting that they too are clinically relevant. Still, the usefulness of NDI maps when applied to single shell data is more limited when compared to the optimised multi-shells protocol, due to the impossibility to fit the CSF. This particularly affects NDI estimates of neurite density as they are based on the intracellular volume, estimated as a fraction of the non-CSF compartment[4].

These findings show that while there are some limitations, the application of NODDI to single HARDI shell data can provide new and relevant data when compared to FA. This means that it can be retrospectively applied to existing dataset for new analyses, thus a similar exploratory study to assess whether it could detect additional differences between NMOSD and MS could be performed. If this proved successful, further studies using multiple HARDI shells protocols should be conducted as the application of NODDI with a fully optimised protocol may potentially detect subtle changes in NAWM, especially in the early stages of both diseases, as well as more changes in normal appearing

GM since the fitting of the CSF compartment will provide more sensitive NDI maps.

7.3 Phase-sensitive inversion recovery (PSIR)

PSIR has been shown to be more sensitive than double-inversion recovery (DIR) when used to detect cortical lesions[5,6]. The aim of this study was to assess whether this increased sensitivity would lead to the detection of cortical lesions in NMOSD patients, as well as assessing potential differences in juxtacortical, deep grey matter and cerebellar lesions in MS and NMOSD. Cortical lesions were divided in two categories: intracortical for those lesions found entirely in the cortex and leucocortical for those comprising a combination of cortical grey matter and white matter. Juxtacortical lesions were exclusively white matter but abutting to the cortex.

This approach was particularly relevant in the context of this thesis since there is an ongoing argument about whether or not NMOSD causes abnormalities in cortical grey matter. This question became even more relevant after the publication of the new diagnosis criteria for NMOSD in 2015, as cortical lesions are listed as a one of the 'red flag' characteristics that are unlikely to be found in NMOSD[1].

For the cortical lesions, both intracortical (IC) and leucocortical (LC) were much more common in MS patients than NMOSD ones, but they were nevertheless found in both groups. 16 out of 18 MS patients had IC lesions compared to 6 out of 16 NMOSD ones. LC lesions were found in slightly fewer patients in both groups: 12 MS ones and just 4 NMOSD ones.

White matter lesions are very common in MS and indeed such lesions were detected in all patients using the PD/T2 scans. And while they were also found in most NMOSD patients (89.5%), the actual lesion load was much lower when compared to MS. It is therefore not surprising that the number of NMOSD patients with juxtacortical (JC) lesions was much smaller than the MS one (77.8% of MS patients vs 37.5% of NMOSD ones).

Lesions were also found in the deep grey matter (DGM) and cerebellum, but were rare in both groups since only 22.2% of MS patients had DGM lesions and 33.3% had cerebellar ones, compared to 6.3% NMOSD patient with DGM lesions and 18.8% with cerebellar ones.

Lesion loads and lesion numbers for each type of lesions were also analysed and their usefulness as potential markers assessed. Both loads and numbers of IC, LC and JC lesions were significantly higher in MS patients when compared to NMOSD ones. The differences between the two groups when looking at DGM and cerebellar lesions did not reach significance, quite possibly due to the very small numbers of patients with these types of lesions.

The average size of each type of lesions in MS and NMOSD patients was also calculated. IC lesions were smaller in NMOSD patients than MS ones, but this too did not reach significance level, again potentially due to the small numbers of NMOSD patients with such lesions. The average volume of LC lesions was similar in both groups, but the NMOSD average was greatly influenced by a single patient with particularly large lesions. If excluded from the analysis, the average LC lesion size for the NMOSD groups is also much lower than the MS average. The average juxtacortical lesion size, on the other hand, was very similar in both groups.

When looking at the lesion load and lesion numbers as potential markers that could be used to differentiate between MS and NMOSD, the most accurate results were attained using the JC lesions, with the lesion load as the one with both the greatest sensitivity and greatest specificity: 88% and 72% respectively, incorrectly classifying only 5 patients out of 34, a 79% correct score. When adjusted for age, which was shown to have a strong influence, the results were even better: specificity reached 94% and sensitivity 89%, giving a rate of correctly classified patients of 91%.

While those results are very interesting and potentially useful to differentiate between NMOSD and MS, there is a big caveat: the huge variations between individual patients. This means that while the data is useful for group analysis,

and could be applied in contexts such as clinical trials, it would be much more difficult to find benchmarks that could be used at the level individual patients for diagnosis purposes, especially since this variability appears to be independent of disease duration.

Furthermore, these findings need to be assessed on a much larger cohort of NMOSD patients to determine how common cortical lesions are in NMOSD, something that cannot be done with such a small group of patients.

7.4 Magnetisation transfer ratio (MTR) on the optic nerve

In order to assess the existence of measurable differences in abnormalities resulting from attacks of optic neuritis in NMOSD and MS patients, two different approaches were used: optical coherence tomography (OCT) to measure changes in retinal thickness (both in the retinal nerve fibre layers (RNFL) and the macula) and MTR to look at alterations in the optic nerve myelin. This was completed by a series of visual acuity tests.

The RNFL thickness of affected eyes was found to be significantly lower in both patients groups when compared to healthy controls eyes, but no significant difference was found between the two patient groups. The latter is likely to have been affected by the fact that only very limited data was acquired from NMOSD patients. The reason for this was partly due to the more severe vision loss recorded in NMOSD patients, particularly those with bilateral optic neuritis, which made the acquisition of images especially difficult. Less affected patients also often had problems keeping their eyes sufficiently still to allow the acquisition of images of the required quality. These two issues severely limit the usefulness of RNFL measurements when high quality images are needed to make comparisons between patients possible.

For the macula, no significant difference was found between affected eyes and healthy controls eyes.

Of the visual assessments made (visual acuity, Sloan 1.25%, Sloan 2.5% and the Farnsworth-Munsell 100-hue test), only visual acuity was significantly

different between NNOSD and MS patients. There was also a highly significant correlation between the MTR results without group subdivision by patient types and visual acuity as well as the different visual assessments.

The MTR results, on the other hand, were more promising as not only a highly significant difference was found between the MTR of affected nerves of both MS and NMO patients when compared with healthy controls, but when the initial comparison between the MTR of affected nerves of MS and NMOSD patients was made, it too came out as significant. However, when a necessary correction for age was made, the difference became only borderline significant. Matching NMOSD and MS patients could have avoided this issue, although this is something that is difficult to achieve due to earlier age of onset in MS and the evolution of the disease towards a secondary progressive course that is no longer similar to NMOSD.

Still, the most interesting MTR result is the fact that the difference between the MTR values of the unaffected nerves of NMOSD patients and those of both MS patients and healthy controls was highly significant. This suggests the existence of undetected subclinical changes are occurring in those patients, something which could potentially be clinically useful, but not necessarily for diagnosis purposes as it was previously observed in MS patients' optic nerves by Trip and colleagues[7].

Like the PSIR results, these findings need to be investigated further on a larger cohort. This validation, combined with scanning patients during the acute phase of optic neuritis, could potentially result in the establishment of a benchmark MTR value below which, when combined with one or more other supporting criteria, NMOSD rather than MS would be the most probable diagnosis. The possibility of subclinical changes in unaffected nerves of NMOSD patients, if confirmed, could offer new insights in disease mechanisms and would clearly warrant further investigations.

7.5 Clinical application

Beyond the issues of validation, could these techniques be used in a clinical context? The question of image processing has been briefly mentioned in the introduction of this chapter. This is a potentially a major concern when translating these techniques to the clinic. As was made clear in both the NODDI and MTR chapters, image registrations were necessary for both the VBM part of the NODDI study and to obtain MTR values. Both were particularly challenging to achieve and required the development of a substantial amount of pipelines, together with time consuming quality assessments, before the most suitable processing was found. This kind of work is possible in an interdisciplinary research group like the Queen Square MS group, where computer scientists specialized in image processing can solve the kind of complex problems encountered in the context of this thesis, but would not be achievable in a clinical context. Therefore, for these techniques to be useful for diagnosis or other assessments, further automation of the processing will be necessary. Automated pipelines are currently being developed within the Queen Square MS group, so maybe in a not too distant future, it may indeed become possible to use some of these techniques in a clinical context, provided of course that the findings presented in this thesis are validated by larger cohort studies.

7.6 Future Studies

7.6.1 Changes in normal appearing white matter

It has been repeatedly shown that there is a larger WM lesion load in MS patients than in NMOSD ones, as confirmed by the studies included in this thesis. Pathological changes occurring in the normal-appearing white matter (NAWM), on the other hand, have been less scrutinized and it would therefore be of particular interest to investigate those using emerging MR techniques. One of them would be NODDI, with an optimised multiple HARDI shells protocol, as suggested in Section 7.2, but there is also a new technique, multi-compartment microscopic diffusion imaging[8], introduced by Kaden and colleagues in 2016, which has not yet been used in a clinical context. The key

difference between this technique and NODDI is that this new method uses Spherical Mean Technique (SMT). SMT is based on the fact that, for a given b-value, the spherical mean of the diffusion signal over the gradient directions is not dependent on the microdomain orientation distribution (it is important to note that a voxel will contain a large population of microdomains). This should result in maps of the neurite density and compartment-specific microscopic diffusivities that are not affected by crossing fibres and orientation dispersion. This is a problem that is not fully solved by NODDI, which uses a single and fixed intrinsic diffusivity for nervous tissues and measures axon orientation distribution with a single Watson distribution. Consequently, the maps obtained using SMT should provide more accurate descriptions of tissues microstructure than those obtained from NODDI and therefore have the potentials to detect further subtle changes in normal-appearing brain tissues.

The SMT model requires at least two *b*-shells and like NODDI uses a multi-compartment approach, with both an intra-neurite and an extra-neurite domains. No myelin compartment is included because the T2-relaxation time of the water found between the myelin layers is so short (much shorter than the echo time of standard clinical scans) that it does not contribute to the measured signal[8]. As mentioned above, this technique has not yet been applied in a clinical context, therefore a pilot study based on previously acquired data with a multi *b*-shells protocol optimised for NODDI in MS patients could be used to assess its worth before applying it to a new cohort of MS and NMOSD patients. Such a study would also allow adjustments/optimisations of the acquisition protocol in order to obtain the optimal results from SMT.

Another emerging technique that could provide interesting information about changes occurring in NAWM is quantitative susceptibility mapping (QSM), which is based on the phase of susceptibility weighting imaging (SWI) and provides quantitative measurements[9]. It gives a measure of the average magnetic susceptibility distribution in each voxel[10] and can therefore be used to gain information about microstructural changes. It should be added that QSM

can also supply information about the nature of WM lesions in MS patients[9], and could therefore be used to compare WM lesions in both MS and NMOSD patients to see whether there are differences in the magnetic susceptibility distribution in the lesional tissue between these two disorders.

Different imaging techniques could also be combined, together with techniques such as MTR or MR spectroscopy, in order to get a broader representation of microstructural changes in NAWM caused by both MS and NMOSD.

7.6.2 Changes in cortical and deep grey matter

It would worthwhile to assess whether multi-compartment microscopic diffusion imaging can provide additional information about changes occurring in both cortical and deep grey matter. This could be combined with PSIR to measure cortical thickness, as the greater contrast should provide better segmentation than what can be achieved with T1 images.

QSM has also been shown to detect changes in iron content in deep grey matter[9] and could therefore potentially identify subclinical changes in these regions. Similarly, it has been shown that it can be used to measure susceptibility values of cortical veins, which again could potentially uncover subclinical changes[11].

7.6.3 Visual pathway: from optic chiasma to primary visual cortex

Changes have been observed in both the optic chiasma and optic tracts of NMOSD patients, but rarely in MS[12,13], while a study by Zhao and colleagues found higher MD in the optic radiations of NMOSD patients when compared to healthy controls[14]. This suggests that it could be worthwhile to apply MTR to the whole optic pathway rather than just the optic nerves, to see whether the posterior sections could offer a more accurate way to distinguish between the two diseases. This should be completed by an investigation of whether the changes measured in patients who had no clinically diagnosed episode of ON also occur in the optic chiasma and beyond.

In this context too, multi-compartment microscopic diffusion imaging could be used to see if changes can be detected in the optic chiasma and beyond in both

NMOSD and MS patients who had at least one episode of optic neuritis as well as those who did not. This could complement the MTR approach when assessing whether such changes occur in both types of patients, or whether they are specific to NMOSD.

The field of new MR techniques is evolving rapidly. It is highly likely that more new techniques will emerge in the near future that will allow further explorations of subtle changes caused by neurological diseases, including MS and NMOSD.

Reference

Chapter 1: Introduction: the NMOSD vs MS study

1. Jarius S, Ruprecht K, Wildemann B, et al. Contrasting disease patterns in seropositive and seronegative neuromyelitis optica: A multicentre study of 175 patients. Journal of Neuroinflammation 2012; 9.
2. Neuromyelitis Optica Spectrum Disorder (NMOSD) - Center for Multiple Sclerosis and CNS Demyelinating Diseases - Mayo Clinic Research. http://www.mayo.edu/research/centers-programs/center-multiple-sclerosis-cns-demyelinating-diseases/neuromyelitis-optica-nmo-variant-multiple-sclerosis (accessed 9/12/2016).
3. Papadopoulos MC, Bennett JL, Verkman AS. Treatment of neuromyelitis optica: state-of-the-art and emerging therapies. Nature reviews Neurology 2014; 10(9): 493-506.
4. Jarius S, Ruprecht K, Kleiter I, et al. MOG-IgG in NMO and related disorders: a multicenter study of 50 patients. Part 2: Epidemiology, clinical presentation, radiological and laboratory features, treatment responses, and long-term outcome. Journal of neuroinflammation 2016; 13(1): 280.
5. Cortese R, Magnollay L, De Angelis F, et al. The Central Vein Sign on SWI at 3T MRI Differentiates Multiple Sclerosis from Neuromyelitis Optica (P4.147). Neurology 2016; 86(16 Supplement).
6. Cortese R, Magnollay L, De Angelis F, et al. No Differences in Spinal Cord White and Grey Matter Diffusion Abnormalities between Neuromyelitis Optica Spectrum Disorder and Multiple Sclerosis (P4.151). Neurology 2016; 86(16 Supplement).
7. R. Cortese, L. Magnollay, F. De Angelis, C. Tur, F. Prados, S. Ourselin, M. Yiannakas, D. Miller, T. Yousry, O. Ciccarelli. Perivenular white matter lesions on SWI at 3-T MRI as a potential biomarker to differentiate multiple sclerosis from neuromyelitis optica. ECTRIMS 2015 - Barcelona (Catalonia)
8. Zhang H, Schneider T, Wheeler-Kingshott CA, Alexander DC. NODDI: practical in vivo neurite orientation dispersion and density imaging of the human brain. Neuroimage 2012; 61(4): 1000-16.
9. Muhlert N, Sethi V, Schneider T, et al. Diffusion MRI-based cortical complexity alterations associated with executive function in multiple sclerosis. J Magn Reson Imaging 2013; 38(1): 54-63.

Chapter 2: From Devic's disease to neuromyelitis optica spectrum disorders (NMOSD

1. Jarius S, Ruprecht K, Wildemann B, et al. Contrasting disease patterns in seropositive and seronegative neuromyelitis optica: A multicentre study of 175 patients. Journal of Neuroinflammation 2012; 9.
2. Wingerchuk DM, Hogancamp WF, O'Brien PC, Weinshenker BG. The clinical course of neuromyelitis optica (Devic's syndrome). Neurology 1999; 53: 1107-14.
3. Mata S, Lolli F. Neuromyelitis optica: An update. Journal of the Neurological Sciences 2011; 303: 13-21.
4. Wingerchuk DM. Neuromyelitis optica spectrum disorders. Continuum (Minneap Minn) 2010; 16(5 Multiple Sclerosis): 105-21.
5. Etemadifar M, Hekmatnia A, Tayari N, et al. Features of Virchow-Robin spaces in newly diagnosed multiple sclerosis patients. Eur J Radiol 2011; 80(2): E104-E8.

6. Marrie RA, Gryba C. The incidence and prevalence of neuromyelitis optica: a systematic review. Int J MS Care 2013; 15(3): 113-8.
7. Bennett JL. Finding NMO: The Evolving Diagnostic Criteria of Neuromyelitis Optica. J Neuroophthalmol 2016; 36(3): 238-45.
8. Multiple Sclerosis International Federation : Atlas of MS 2013. 2013. https://www.msif.org/about-us/advocacy/atlas/ (accessed 3.12.2016.
9. Levin MH, Bennett JL, Verkman AS. Optic neuritis in neuromyelitis optica. Prog Retin Eye Res 2013; 36: 159-71.
10. Pittock SJ, Lucchinetti CF. Neuromyelitis optica and the evolving spectrum of autoimmune aquaporin-4 channelopathies: a decade later. Ann N Y Acad Sci 2016; 1366(1): 20-39.
11. Wingerchuk DM, Hogancamp WF, O'Brien PC, Weinshenker BG. The clinical course of neuromyelitis optica (Devic's syndrome). Neurology 1999; 53(5): 1107-14.
12. Jiao YJ, Fryer JP, Lennon VA, et al. Updated estimate of AQP4-IgG serostatus and disability outcome in neuromyelitis optica. Neurology 2013; 81(14): 1197-204.
13. Papadopoulos MC, Bennett JL, Verkman AS. Treatment of neuromyelitis optica: state-of-the-art and emerging therapies. Nature reviews Neurology 2014; 10(9): 493-506.
14. Jarius S, Ruprecht K, Kleiter I, et al. MOG-IgG in NMO and related disorders: a multicenter study of 50 patients. Part 2: Epidemiology, clinical presentation, radiological and laboratory features, treatment responses, and long-term outcome. Journal of neuroinflammation 2016; 13(1): 280.
15. Kitley J, Leite MI, Nakashima I, et al. Prognostic factors and disease course in aquaporin-4 antibody-positive patients with neuromyelitis optica spectrum disorder from the United Kingdom and Japan. Brain 2012; 135: 1834-49.
16. Wingerchuk DM, Lennon VA, Lucchinetti CF, Pittock SJ, Weinshenker BG. The spectrum of neuromyelitis optica. Lancet Neurol 2007; 6(9): 805-15.
17. Etemadifar M, Nasr Z, Khalili B, Taherioun M, Vosoughi R. Epidemiology of neuromyelitis optica in the world: a systematic review and meta-analysis. Mult Scler Int 2015; 2015: 174720.
18. Jarius S, Wildemann B. The history of neuromyelitis optica. J Neuroinflammation 2013; 10: 8.
19. Jarius S, Wildemann B. The case of the Marquis de Causan (1804): an early account of visual loss associated with spinal cord inflammation. J Neurol 2012; 259(7): 1354-7.
20. Jarius S, Wildemann B. An early case of neuromyelitis optica: on a forgotten report by Jacob Lockhart Clarke, FRS. Mult Scler J 2011; 17(11): 1384-6.
21. Allbutt TC. On the ophthalmoscopic signs of spinal disease. The Lancet; 95(2420): 76-8.
22. Pearce JMS. Neuromyelitis optica. Spinal Cord 2005; 43(11): 631-4.
23. O'Riordan JI, Gallagher HL, Thompson AJ, et al. Clinical, CSF, and MRI findings in Devic's neuromyelitis optica. J Neurol Neurosurg Psychiatry 1996; 60(4): 382-7.
24. Lennon V, Wingerchuk D, Kryzer T, et al. A serum autoantibody marker of neuromyelitis optica: distinction from multiple sclerosis. Lancet 2004; 364: 2106-12.
25. Marignier R, Giraudon P, Vukusic S, Confavreux C, Honnorat J. Anti-aquaporin-4 antibodies in Devic's neuromyelitis optica: therapeutic implications. Ther Adv Neurol Disord 2010; 3: 311-21.
26. Costa C, Arrambide G, Tintore M, et al. Value of NMO-IgG determination at the time of presentation as CIS. Neurology 2012; 78(20): 1608-11.

27. Ramanathan S, Reddel SW, Henderson A, et al. Antibodies to myelin oligodendrocyte glycoprotein in bilateral and recurrent optic neuritis. Neurol Neuroimmunol Neuroinflamm 2014; 1(4): e40.
28. Kitley J, Woodhall M, Waters P, et al. Myelin-oligodendrocyte glycoprotein antibodies in adults with a neuromyelitis optica phenotype. Neurology 2012; 79(12): 1273-7.
29. Kitley J, Leite MI, Nakashima I, et al. Prognostic factors and disease course in aquaporin-4 antibody-positive patients with neuromyelitis optica spectrum disorder from the United Kingdom and Japan. Brain: a journal of neurology 2012; 135: 1834-49.
30. Zamvil SS, Slavin AJ. Does MOG Ig-positive AQP4-seronegative opticospinal inflammatory disease justify a diagnosis of NMO spectrum disorder? Neurol Neuroimmunol Neuroinflamm 2015; 2(1): e62.
31. Pittock SJ. Demyelinating disease: NMO spectrum disorders: clinical or molecular classification? Nat Rev Neurol 2016; 12(3): 129-30.
32. Kiyat-Atamer A, Ekizoglu E, Tuzun E, et al. Long-term MRI findings in neuromyelitis optica: seropositive versus seronegative patients. Eur J Neurol 2013; 20: 781-7.
33. Bernard-Valnet R, Liblau RS, Vukusic S, Marignier R. Neuromyelitis optica: a positive appraisal of seronegative cases. Eur J Neurol 2015; 22(12): 1511-8, e82-3.
34. Wingerchuk DM, Banwell B, Bennett JL, et al. International consensus diagnostic criteria for neuromyelitis optica spectrum disorders. Neurology 2015; 85(2): 177-89.
35. Wingerchuk DM, Lennon VA, Pittock SJ, Lucchinetti CF, Weinshenker BG. Revised diagnostic criteria for neuromyelitis optica. Neurology 2006; 66(10): 1485-9.
36. Calabrese M, Oh MS, Favaretto A, et al. No MRI evidence of cortical lesions in neuromyelitis optica. Neurology 2012; 79(16): 1671-6.
37. Downer JJ, Leite MI, Carter R, Palace J, Kuker W, Quaghebeur G. Diagnosis of neuromyelitis optica (NMO) spectrum disorders: is MRI obsolete? Neuroradiology 2012; 54: 279-85.
38. Wang F, Liu Y, Duan Y, Li K. Brain MRI abnormalities in neuromyelitis optica. Eur J Radiol 2011; 80(2): 445-9.
39. Filippi M, Rocca MA, Moiola L, et al. MRI and magnetization transfer imaging changes in the brain and cervical cord of patients with Devic's neuromyelitis optica. Neurology 1999; 53: 1705-10.
40. Rivero RL, Oliveira EM, Bichuetti DB, Gabbai AA, Nogueira RG, Abdala N. Diffusion tensor imaging of the cervical spinal cord of patients with Neuromyelitis Optica. Magn Reson Imaging 2014; 32(5): 457-63.
41. Cabrera-Gomez JA, Quevedo-Sotolongo L, Gonzalez-Quevedo A, et al. Brain magnetic resonance imaging findings in relapsing neuromyelitis optica. Mult Scler 2007; 13(2): 186-92.
42. Wang Y, Wu A, Chen X, et al. Comparison of clinical characteristics between neuromyelitis optica spectrum disorders with and without spinal cord atrophy. BMC Neurol 2014; 14: 246.
43. Benedetti B, Valsasina P, Judica E, et al. Grading cervical cord damage in neuromyelitis optica and MS by diffusion tensor MRI. Neurology 2006; 67: 161-3.
44. Wang Y, Wu A, Chen X, et al. Comparison of clinical characteristics between neuromyelitis optica spectrum disorders with and without spinal cord atrophy. BMC neurology 2014; 14: 246.

45. Qian W, Chan Q, Mak H, et al. Quantitative assessment of the cervical spinal cord damage in neuromyelitis optica using diffusion tensor imaging at 3 Tesla. Journal of magnetic resonance imaging: JMRI 2011; 33: 1312-20.
46. Klawiter EC, Xu J, Naismith RT, et al. Increased radial diffusivity in spinal cord lesions in neuromyelitis optica compared with multiple sclerosis. Mult Scler 2012; 18: 1259-68.
47. Pessoa FM, Lopes FC, Costa JV, Leon SV, Domingues RC, Gasparetto EL. The cervical spinal cord in neuromyelitis optica patients: a comparative study with multiple sclerosis using diffusion tensor imaging. Eur J Radiol 2012; 81(10): 2697-701.
48. Zalewski NL, Morris PP, Weinshenker BG, et al. Ring-enhancing spinal cord lesions in neuromyelitis optica spectrum disorders. J Neurol Neurosurg Psychiatry 2016.
49. Makino T, Ito S, Mori M, Yonezu T, Ogawa Y, Kuwabara S. Diffuse and heterogeneous T2-hyperintense lesions in the splenium are characteristic of neuromyelitis optica. Multiple sclerosis (Houndmills, Basingstoke, England) 2013; 19: 308-15.
50. Khanna S, Sharma A, Huecker J, Gordon M, Naismith RT, Van Stavern GP. Magnetic resonance imaging of optic neuritis in patients with neuromyelitis optica versus multiple sclerosis. J Neuroophthalmol 2012; 32(3): 216-20.
51. Lim Y-M, Pyun SY, Lim HT, Jeong IH, Kim K-K. First-ever optic neuritis: distinguishing subsequent neuromyelitis optica from multiple sclerosis. Neurological Sciences: Official Journal of the Italian Neurological Society and of the Italian Society of Clinical Neurophysiology 2014; 35: 781-3.
52. Mealy MA, Whetstone A, Orman G, Izbudak I, Calabresi PA, Levy M. Longitudinally extensive optic neuritis as an MRI biomarker distinguishes neuromyelitis optica from multiple sclerosis. J Neurol Sci 2015; 355(1-2): 59-63.
53. Storoni M, Davagnanam I, Radon M, Siddiqui A, Plant GT. Distinguishing optic neuritis in neuromyelitis optica spectrum disease from multiple sclerosis: a novel magnetic resonance imaging scoring system. J Neuroophthalmol 2013; 33(2): 123-7.
54. Zhao DD, Zhou HY, Wu QZ, et al. Diffusion tensor imaging characterization of occult brain damage in relapsing neuromyelitis optica using 3.0T magnetic resonance imaging techniques. Neuroimage 2012; 59(4): 3173-7.
55. Liu Y, Duan Y, He Y, et al. A tract-based diffusion study of cerebral white matter in neuromyelitis optica reveals widespread pathological alterations. Mult Scler 2012; 18(7): 1013-21.
56. Rueda Lopes FC, Doring T, Martins C, et al. The role of demyelination in neuromyelitis optica damage: diffusion-tensor MR imaging study. Radiology 2012; 263(1): 235-42.
57. Kim W, Park MS, Lee SH, et al. Characteristic brain magnetic resonance imaging abnormalities in central nervous system aquaporin-4 autoimmunity. Mult Scler J 2010; 16: 1229-36.
58. Yu CS, Lin FC, Li KC, et al. Diffusion tensor imaging in the assessment of normal-appearing brain tissue damage in relapsing neuromyelitis optica. Am J Neuroradiol 2006; 27(5): 1009-15.
59. Liu Y, Duan YY, He Y, et al. A tract-based diffusion study of cerebral white matter in neuromyelitis optica reveals widespread pathological alterations. Mult Scler J 2012; 18: 1013-21.

60. Cabrera-Gómez J, Saiz-Hinarejos A, Graus F, et al. Brain magnetic resonance imaging findings in acute relapses of neuromyelitis optica spectrum disorders. Multiple Sclerosis (Houndmills, Basingstoke, England) 2008; 14: 248-51.
61. Yu CS, Lin FC, Li KC, et al. Diffusion tensor imaging in the assessment of normal-appearing brain tissue damage in relapsing neuromyelitis optica. AJNR Am J Neuroradiol 2006; 27(5): 1009-15.
62. Nakashima I, Fujihara K, Miyazawa I, et al. Clinical and MRI features of Japanese patients with multiple sclerosis positive for NMO-IgG. J Neurol Neurosurg Psychiatry 2006; 77: 1073-5.
63. Sinnecker T, Dorr J, Pfueller CF, et al. Distinct lesion morphology at 7-T MRI differentiates neuromyelitis optica from multiple sclerosis. Neurology 2012; 79(7): 708-14.
64. Cortese R, Magnollay L, De Angelis F, et al. The Central Vein Sign on SWI at 3T MRI Differentiates Multiple Sclerosis from Neuromyelitis Optica (P4.147). Neurology 2016; 86(16 Supplement).
65. Lu ZQ, Zhang BJ, Qiu W, et al. Comparative Brain Stem Lesions on MRI of Acute Disseminated Encephalomyelitis, Neuromyelitis Optica, and Multiple Sclerosis. Plos One 2011; 6.
66. Matsushita T, Isobe N, Piao H, et al. Reappraisal of brain MRI features in patients with multiple sclerosis and neuromyelitis optica according to anti-aquaporin-4 antibody status. Journal of the Neurological Sciences 2010; 291: 37-43.
67. Lim YM, Pyun SY, Lim HT, Jeong IH, Kim KK. First-ever optic neuritis: distinguishing subsequent neuromyelitis optica from multiple sclerosis. Neurol Sci 2014; 35(5): 781-3.
68. Wang F, Liu Y, Duan Y, Li K. Brain MRI abnormalities in neuromyelitis optica. Eur J Radiol 2011; 80: 445-9.
69. Zhang L, Wu A, Zhang B, et al. Comparison of deep gray matter lesions on magnetic resonance imaging among adults with acute disseminated encephalomyelitis, multiple sclerosis, and neuromyelitis optica. Mult Scler 2014; 20(4): 418-23.
70. Duan Y, Liu Y, Liang P, et al. Comparison of grey matter atrophy between patients with neuromyelitis optica and multiple sclerosis: a voxel-based morphometry study. Eur J Radiol 2012; 81: e110-4.
71. de Seze J, Blanc F, Kremer S, et al. Magnetic resonance spectroscopy evaluation in patients with neuromyelitis optica. J Neurol Neurosur Ps 2010; 81(4): 409-11.
72. Kister I, Herbert J, Zhou Y, Ge Y. Ultrahigh-Field MR (7 T) Imaging of Brain Lesions in Neuromyelitis Optica. Mult Scler Int 2013; 2013: 398259.
73. Popescu B, Parisi J, Cabrera-Gomez J, et al. Absence of cortical demyelination in neuromyelitis optica. Neurology 2010; 75: 2103-9.
74. Rocca MA, Agosta F, Mezzapesa DM, et al. Magnetization transfer and diffusion tensor MRI show gray matter damage in neuromyelitis optica. Neurology 2004; 62(3): 476-8.
75. Kim W, Lee JE, Kim SH, et al. Cerebral Cortex Involvement in Neuromyelitis Optica Spectrum Disorder. J Clin Neurol 2016; 12(2): 188-93.
76. Saji E, Arakawa M, Yanagawa K, et al. Cognitive impairment and cortical degeneration in neuromyelitis optica. Ann Neurol 2013; 73(1): 65-76.
77. Liu Y, Duan Y, He Y, et al. Altered topological organization of white matter structural networks in patients with neuromyelitis optica. PloS one 2012; 7: e48846.

78. Pichiecchio A, Tavazzi E, Poloni G, et al. Advanced magnetic resonance imaging of neuromyelitis optica: a multiparametric approach. Multiple Sclerosis (Houndmills, Basingstoke, England) 2012; 18: 817-24.
79. Filippi M, Rocca MA, Moiola L, et al. MRI and magnetization transfer imaging changes in the brain and cervical cord of patients with Devic's neuromyelitis optica. Neurology 1999; 53(8): 1705-10.
80. Aboul-Enein F, Krssak M, Hoftberger R, Prayer D, Kristoferitsch W. Diffuse White Matter Damage Is Absent in Neuromyelitis Optica. Am J Neuroradiol 2010; 31: 76-9.
81. Bichuetti DB, Rivero RL, de Oliveira EM, et al. White matter spectroscopy in neuromyelitis optica: a case control study. J Neurol 2008; 255(12): 1895-9.
82. Aradi M, Koszegi E, Orsi G, et al. Quantitative MRI analysis of the brain after twenty-two years of neuromyelitis optica indicates focal tissue damage. European neurology 2013; 69: 221-5.
83. Meng H, Xu J, Pan C, et al. Cognitive dysfunction in adult patients with neuromyelitis optica: a systematic review and meta-analysis. J Neurol 2016.
84. Liu Y, Fu Y, Schoonheim MM, et al. Structural MRI substrates of cognitive impairment in neuromyelitis optica. Neurology 2015; 85(17): 1491-9.
85. Blanc F, Noblet V, Jung B, et al. White Matter Atrophy and Cognitive Dysfunctions in Neuromyelitis Optica. Plos One 2012; 7.
86. He D, Wu Q, Chen X, Zhao D, Gong Q, Zhou H. Cognitive impairment and whole brain diffusion in patients with neuromyelitis optica after acute relapse. Brain and Cognition 2011; 77: 80-8.
87. Wang Q, Zhang N, Qin W, et al. Gray Matter Volume Reduction Is Associated with Cognitive Impairment in Neuromyelitis Optica. AJNR Am J Neuroradiol 2015; 36(10): 1822-9.
88 Flanagan EP, Weinshenker BG, Krecke KN, et al. Short myelitis lesions in aquaporin-4-IgG-positive neuromyelitis optica spectrum disorders. JAMA Neurol 2015;72:81-87.

Chapter 3: A short introduction to magnetic resonance imaging (MRI) and to the techniques used

1. Elster AD. Questions and Answers in MRI. http://mriquestions.com/index.html (accessed 13/05 2016).
2. NessAiver M. All you really need to know about MRI physics. Baltimore: University of Maryland Medical Center; 1997.
3. Blink EJ. mri: Physics : For anyone who does not have a degree in physics. MRI-physics. net; 2004.
4. Kantzas A, Bryan J, Taheri S. Diffusion Coefficient: Measurement Techniques NMR Method: Principles of NMR and Processing. Fundamentals of Fluid Flow in Porous Media: PERM Inc.
5. Gerard T. NMR proton: principles. 3/2/2016. 2016. http://brussels-scientific.com/?p=6273 (accessed 21/9/2016 2016).
6. Fonseca MGa. Spin Echo Magnetic Resonance Imaging. In: Kharfi F, editor. Imaging and Radioanalytical Techniques in Interdisciplinary Research InTech (Open Access); 2013.
7. Dimmock M. The science of medical imaging: magnetic resonance imaging (MRI). http://theconversation.com/the-science-of-medical-imaging-magnetic-resonance-imaging-mri-15030.

8. Kantzas A, Bryan J, Taheri S. Fundamentals of Fluid Flow in Porous Media. http://perminc.com/resources/fundamentals-of-fluid-flow-in-porous-media/chapter-3-molecular-diffusion/diffusion-coefficient/measurement-techniques/nmr-method/principles-nmr-processing/t2-transverse-relaxation-time/ (accessed 22-08-2016.
9. MRImaster.com. https://mrimaster.com/physics%20intro.html (accessed 23.08.2016.
10. Ridgway JP. Cardiovascular magnetic resonance physics for clinicians: part I. J Cardiovasc Magn Reson 2010; 12: 71.
11. Flögel UJ, Christoph Magnetic Resonance at the Department of Molecular Cardiology. http://www.nmr.hhu.de/sets/theory3.html (accessed 29/08/2016.
12. MRI Shark : Phase Encoding. 2015. http://www.mrishark.com/phase-encoding.html (accessed 30/08/2016.
13. Adair D, Walton M. MRI Signal Generation - imaging. http://199.116.233.101/index.php/MRI_Signal_Generation (accessed 30/08/2016.
14. Gallagher TA, Nemeth AJ, Hacein-Bey L. An introduction to the Fourier transform: relationship to MRI. AJR Am J Roentgenol 2008; 190(5): 1396-405.
15. Hagmann P, Jonasson L, Maeder P, Thiran J-P, Wedeen VJ, Meuli R. Understanding Diffusion MR Imaging Techniques: From Scalar Diffusion-weighted Imaging to Diffusion Tensor Imaging and Beyond. RadioGraphics 2006; 26(suppl_1): S205-S23.
16. Winston GP. The physical and biological basis of quantitative parameters derived from diffusion MRI. Quant Imaging Med Surg 2012; 2(4): 254-65.
17. McRobbie DW. MRI from picture to proton. 2nd ed. Cambridge, UK ; New York: Cambridge University Press; 2007.
18. Beaulieu C. The basis of anisotropic water diffusion in the nervous system - a technical review. NMR Biomed 2002; 15(7-8): 435-55.
19. Oishi K. MRI atlas of human white matter. 2nd ed. Amsterdam: Elsevier/Academic Press; 2011.
20. Alexander AL, Lee JE, Lazar M, Field AS. Diffusion tensor imaging of the brain. Neurotherapeutics 2007; 4(3): 316-29.
21. Tromp D, Perea R, Hurley S. Diffusion Imaging ; The diffusion tensor, and its relation to FA, MD, AD and RD. 2015. http://www.diffusion-imaging.com/2015/10/what-is-diffusion-tensor.html (accessed 15.09.2016 2016).
22. Alexander AL, Hurley SA, Samsonov AA, et al. Characterization of cerebral white matter properties using quantitative magnetic resonance imaging stains. Brain Connect 2011; 1(6): 423-46.
23. Zhang H, Schneider T, Wheeler-Kingshott CA, Alexander DC. NODDI: practical in vivo neurite orientation dispersion and density imaging of the human brain. Neuroimage 2012; 61(4): 1000-16.
24. Tariq M, Schneider T, Alexander DC, Gandini Wheeler-Kingshott CA, Zhang H. Bingham-NODDI: Mapping anisotropic orientation dispersion of neurites using diffusion MRI. Neuroimage 2016; 133: 207-23.
25. Billiet T, Vandenbulcke M, Madler B, et al. Age-related microstructural differences quantified using myelin water imaging and advanced diffusion MRI. Neurobiol Aging 2015; 36(6): 2107-21.
26. Jeurissen B, Leemans A, Tournier JD, Jones DK, Sijbers J. Investigating the prevalence of complex fiber configurations in white matter tissue with diffusion magnetic resonance imaging. Hum Brain Mapp 2013; 34(11): 2747-66.

27. Alba-Ferrara L, De Erausquin GA. Schizophrenia, connectivity, tractography, Anisotropy, MRI imaging. Frontiers in Integrative Neuroscience 2013; (11 March 2013).
28. de Boer RW. Magnetization transfer contrast. Part 1: MR Physics. Philips Medical System MedicaMundi, 1995. http://mri-q.com/uploads/3/4/5/7/34572113/de_boer1.pdf (accessed 19/09/2016).
29. Grossman RI, Gomori JM, Ramer KN, Lexa FJ, Schnall MD. Magnetization transfer: theory and clinical applications in neuroradiology. RadioGraphics 1994; 14(2): 279-90.
30. Mehta RC, Pike GB, Enzmann DR. Magnetization transfer magnetic resonance imaging: a clinical review. Top Magn Reson Imaging 1996; 8(4): 214-30.
31. Schmierer K, Scaravilli F, Altmann DR, Barker GJ, Miller DH. Magnetization transfer ratio and myelin in postmortem multiple sclerosis brain. Ann Neurol 2004; 56(3): 407-15.

Chapter 4: Application of single-shell Neurite Orientation Dispersion and Density Imaging (NODDI) to MS

1. Horsfield MA, Jones DK. Applications of diffusion-weighted and diffusion tensor MRI to white matter diseases - a review. NMR Biomed 2002; 15(7-8): 570-7.
2. Anderson B, Rutledge V. Age and hemisphere effects on dendritic structure. *Brain* 1996; 119 (Pt 6): 1983-90.
3. Jacobs B, Driscoll L, Schall M. Life-span dendritic and spine changes in areas 10 and 18 of human cortex: a quantitative Golgi study. *J Comp Neurol* 1997; 386(4): 661-80.
4. Zhang H, Schneider T, Wheeler-Kingshott CA, Alexander DC. NODDI: practical in vivo neurite orientation dispersion and density imaging of the human brain. *Neuroimage* 2012; 61(4): 1000-16.
5. Muhlert N, Sethi V, Schneider T, et al. Diffusion MRI-based cortical complexity alterations associated with executive function in multiple sclerosis. *J Magn Reson Imaging* 2013; **38**(1): 54-63.
6. Colgan N, Siowa B, O'Callaghan JM, et al. Application of neurite orientation dispersion and density imaging (NODDI) to a tau pathology model of Alzheimer's disease. *Neuroimage* 2016; **125**: 739-44.
7. Tariq M, Schneider T, Alexander DC, GandiniWheeler-Kingshott CA, Zhang H. Bingham-NODDI: Mapping anisotropic orientation dispersion of neurites using diffusion MRI. *Neuroimage* 2016; **133**: 207-23.
8. Lemkaddem A, Daducci A, Kunz N, et al. Connectivity and tissue microstructural alterations in right and left temporal lobe epilepsy revealed by diffusion spectrum imaging. *NeuroImage Clinical* 2014; **5**: 349-58.
9. Winston GP. The physical and biological basis of quantitative parameters derived from diffusion MRI. *Quant Imaging Med Surg* 2012; **2**(4): 254-65.
10. Kamagata K, Hatano T, Okuzumi A, et al. Neurite orientation dispersion and density imaging in the substantia nigra in idiopathic Parkinson disease. *European radiology* 2016; **26**(8): 2567-77.
11. Kamagata K, Hatano T, Aoki S. What is NODDI and what is its role in Parkinson's assessment? *Expert Rev Neurother* 2016; **16**(3): 241-3.
12. Adluru G, Gur Y, Anderson JS, Richards LG, Adluru N, DiBella EV. Assessment of white matter microstructure in stroke patients using NODDI. *Conference proceedings : Annual International Conference of the IEEE Engineering in Medicine*

and Biology Society IEEE Engineering in Medicine and Biology Society Annual Conference 2014; **2014**: 742-5.
13. Wen Q, Kelley DA, Banerjee S, et al. Clinically feasible NODDI characterization of glioma using multiband EPI at 7 T. *NeuroImage Clinical* 2015; **9**: 291-9.
14. Brownlee W, Alves Da Mota P, Prados F, et al. Neurite Orientation Dispersion and Density Imaging (NODDI) Is Sensitive to Microstructural Damage Related to Disability in Relapse-Onset MS (S41.003). *Neurology* 2016; **86**(16 Supplement).
15. Smith A. Symbol-digit modalities test: manual: Western Psychological Services; 1982.
16. Paced Auditory Serial Addition Test (PASAT) http://www.nationalmssociety.org/For-Professionals/Researchers/Resources-for-Researchers/Clinical-Study-Measures/Paced-Auditory-Serial-Addition-Test-(PASAT) (accessed 29/09/2016 2016).
17. Pardini M. Personal communication. 2015.
18. Hickman SI, Barker GJ, Molyneux PD, Miller DH. Technical note: the comparison of hypointense lesions from 'pseudo-T1' and T1-weighted images in secondary progressive multiple sclerosis. *Mult Scler* 2002; **8**(5): 433-5.
19. Prados F, Cardoso MJ, MacManus D, Wheeler-Kingshott CA, Ourselin S. A modality-agnostic patch-based technique for lesion filling in multiple sclerosis. *Med Image Comput Comput Assist Interv* 2014; **17**(Pt 2): 781-8.
20. Modat M, Cash DM, Daga P, Winston GP, Duncan JS, Ourselin S. Global image registration using a symmetric block-matching approach. *J Med Imaging (Bellingham)* 2014; **1**(2): 024003.
21. Ourselin S, Roche A, Subsol G, Pennec X, Ayache N. Reconstructing a 3D structure from serial histological sections. *Image Vision Comput* 2001; **19**(1-2): 25-31.
22. Modat M, Ridgway GR, Taylor ZA, et al. Fast free-form deformation using graphics processing units. *Comput Meth Prog Bio* 2010; **98**(3): 278-84.
23. Cardoso MJ, Modat M, Wolz R, et al. Geodesic Information Flows: Spatially-Variant Graphs and Their Application to Segmentation and Fusion. *IEEE Trans Med Imaging* 2015; **34**(9): 1976-88.
24. Prados F CM, Burgos N, Wheeler-Kingshott CAM, Ourselin S. . NiftyWeb: web based platform for image processing on the cloud. International Society for Magnetic Resonance in Medicine (ISMRM) 24th Scientific Meeting and Exhibition 2016; Singapore; 2016.
25. Ashburner J. A fast diffeomorphic image registration algorithm. *Neuroimage* 2007; **38**(1): 95-113.
26. Ashburner J. VBM Tutorial. London: Wellcome Trust Centre for Neuroimaging; 2010.
27. Werring DJ, Clark CA, Barker GJ, Thompson AJ, Miller DH. Diffusion tensor imaging of lesions and normal-appearing white matter in multiple sclerosis. *Neurology* 1999; **52**(8): 1626-32.
28. Sbardella E, Tona F, Petsas N, Pantano P. DTI Measurements in Multiple Sclerosis: Evaluation of Brain Damage and Clinical Implications. *Mult Scler Int* 2013; **2013**: 671730.
29. Boretius S, Escher A, Dallenga T, et al. Assessment of lesion pathology in a new animal model of MS by multiparametric MRI and DTI. *Neuroimage* 2012; **59**(3): 2678-88.

30. Giorgio A, Palace J, Johansen-Berg H, et al. Relationships of brain white matter microstructure with clinical and MR measures in relapsing-remitting multiple sclerosis. *J Magn Reson Imaging* 2010; **31**(2): 309-16.
31. Miller DH, Thompson AJ, Filippi M. Magnetic resonance studies of abnormalities in the normal appearing white matter and grey matter in multiple sclerosis. *J Neurol* 2003; **250**(12): 1407-19.
32. Alexander AL, Hurley SA, Samsonov AA, et al. Characterization of cerebral white matter properties using quantitative magnetic resonance imaging stains. *Brain Connect* 2011; **1**(6): 423-46.
33. Alba-Ferrara LM, de Erausquin GA. What does anisotropy measure? Insights from increased and decreased anisotropy in selective fiber tracts in schizophrenia. *Front Integr Neurosci* 2013; **7**: 9.
34. Jeurissen B, Leemans A, Tournier JD, Jones DK, Sijbers J. Investigating the prevalence of complex fiber configurations in white matter tissue with diffusion magnetic resonance imaging. *Hum Brain Mapp* 2013; **34**(11): 2747-66.
35. Sepehrband F, Clark KA, Ullmann JFP, et al. Brain tissue compartment density estimated using diffusion-weighted MRI yields tissue parameters consistent with histology. *Human Brain Mapping* 2015; **36**(9): 3687-702.
36. Billiet T, Vandenbulcke M, Madler B, et al. Age-related microstructural differences quantified using myelin water imaging and advanced diffusion MRI. *Neurobiol Aging* 2015; **36**(6): 2107-21.
37. Lin F, Yu C, Jiang T, Li K, Chan P. Diffusion tensor tractography-based group mapping of the pyramidal tract in relapsing-remitting multiple sclerosis patients. *AJNR Am J Neuroradiol* 2007; **28**(2): 278-82.
38. Roosendaal SD, Geurts JJ, Vrenken H, et al. Regional DTI differences in multiple sclerosis patients. *Neuroimage* 2009; **44**(4): 1397-403.
39. Gabilondo I, Martinez-Lapiscina EH, Martinez-Heras E, et al. Trans-synaptic axonal degeneration in the visual pathway in multiple sclerosis. *Ann Neurol* 2014; **75**(1): 98-107.
40. Audoin B, Fernando KT, Swanton JK, Thompson AJ, Plant GT, Miller DH. Selective magnetization transfer ratio decrease in the visual cortex following optic neuritis. *Brain* 2006; **129**(Pt 4): 1031-9.
41. Papadopoulos D, Dukes S, Patel R, Nicholas R, Vora A, Reynolds R. Substantial archaeocortical atrophy and neuronal loss in multiple sclerosis. *Brain Pathol* 2009; **19**(2): 238-53.
42. Geurts JJ, Bo L, Roosendaal SD, et al. Extensive hippocampal demyelination in multiple sclerosis. *J Neuropathol Exp Neurol* 2007; **66**(9): 819-27.
43. Honce JM. Gray Matter Pathology in MS: Neuroimaging and Clinical Correlations. *Mult Scler Int* 2013; **2013**: 627870.
44. Benedict RH, Amato MP, Boringa J, et al. Brief International Cognitive Assessment for MS (BICAMS): international standards for validation. *BMC Neurol* 2012; **12**: 55.
45. Granberg T, Bergendal G, Shams S, et al. MRI-Defined Corpus Callosal Atrophy in Multiple Sclerosis: A Comparison of Volumetric Measurements, Corpus Callosum Area and Index. *J Neuroimaging* 2015; **25**(6): 996-1001.
46. Granberg T, Martola J, Bergendal G, et al. Corpus callosum atrophy is strongly associated with cognitive impairment in multiple sclerosis: Results of a 17-year longitudinal study. *Mult Scler* 2015; **21**(9): 1151-8.

47. Yaldizli O, Penner IK, Frontzek K, et al. The relationship between total and regional corpus callosum atrophy, cognitive impairment and fatigue in multiple sclerosis patients. *Mult Scler* 2014; **20**(3): 356-64.
48. Bergendal G, Martola J, Stawiarz L, Kristoffersen-Wiberg M, Fredrikson S, Almkvist O. Callosal atrophy in multiple sclerosis is related to cognitive speed. *Acta Neurol Scand* 2013; **127**(4): 281-9.
49. Meijer KA, Muhlert N, Cercignani M, et al. White matter tract abnormalities are associated with cognitive dysfunction in secondary progressive multiple sclerosis. *Mult Scler* 2016.
50. Yu HJ, Christodoulou C, Bhise V, et al. Multiple white matter tract abnormalities underlie cognitive impairment in RRMS. *Neuroimage* 2012; **59**(4): 3713-22.
51. Tobin WO, Popescu BF, Lowe V, et al. Multiple sclerosis masquerading as Alzheimer-type dementia: Clinical, radiological and pathological findings. *Mult Scler* 2016; **22**(5): 698-704.
52. Kodiweera C, Alexander AL, Harezlak J, McAllister TW, Wu YC. Age effects and sex differences in human brain white matter of young to middle-aged adults: A DTI, NODDI, and q-space study. *Neuroimage* 2016; **128**: 180-92.
53. Grussu F, Schneider T, Zhang H, Alexander DC, Wheeler-Kingshott CAM. Single-shell diffusion MRI NODDI with in vivo cervical cord data. Joint Annual Meeting ISMRM-ESMRMB 2014; 2014; Milan; 2014

Chapter 5: Can phase-inversion recovery (PSIR) detect cortical lesions in NMOSD patients or are they specific to MS?

1. Absinta M, Sati P, Reich DS. Advanced MRI and staging of multiple sclerosis lesions. *Nat Rev Neurol* 2016; **12**(6): 358-68.
2. Kilsdonk ID, Jonkman LE, Klaver R, et al. Increased cortical grey matter lesion detection in multiple sclerosis with 7 T MRI: a post-mortem verification study. *Brain* 2016; **139**(Pt 5): 1472-81.
3. Nelson F, Poonawalla AH, Hou P, Huang F, Wolinsky JS, Narayana PA. Improved identification of intracortical lesions in multiple sclerosis with phase-sensitive inversion recovery in combination with fast double inversion recovery MR imaging. *AJNR Am J Neuroradiol* 2007; **28**(9): 1645-9.
4. Sethi V, Yousry TA, Muhlert N, et al. Improved detection of cortical MS lesions with phase-sensitive inversion recovery MRI. *J Neurol Neurosur Ps* 2012; **83**(9): 877-82.
5. Favaretto A, Poggiali D, Lazzarotto A, Rolma G, Causin F, Gallo P. The Parallel Analysis of Phase Sensitive Inversion Recovery (PSIR) and Double Inversion Recovery (DIR) Images Significantly Improves the Detection of Cortical Lesions in Multiple Sclerosis (MS) since Clinical Onset. *PLoS One* 2015; **10**(5): e0127805.
6. Calabrese M, Oh MS, Favaretto A, et al. No MRI evidence of cortical lesions in neuromyelitis optica. *Neurology* 2012; **79**(16): 1671-6.
7. Duan YY, Liu Y, Liang PP, et al. Comparison of grey matter atrophy between patients with neuromyelitis optica and multiple sclerosis: A voxel-based morphometry study. *Eur J Radiol* 2012; **81**(2): E110-E4.
8. de Seze J, Blanc F, Kremer S, et al. Magnetic resonance spectroscopy evaluation in patients with neuromyelitis optica. *J Neurol Neurosur Ps* 2010; **81**(4): 409-11.
9. Kister I, Herbert J, Zhou Y, Ge Y. Ultrahigh-Field MR (7 T) Imaging of Brain Lesions in Neuromyelitis Optica. *Mult Scler Int* 2013; **2013**: 398259.

10. Sinnecker T, Dorr J, Pfueller CF, et al. Distinct lesion morphology at 7-T MRI differentiates neuromyelitis optica from multiple sclerosis. *Neurology* 2012; **79**(7): 708-14.
11. Kim W, Lee JE, Kim SH, et al. Cerebral Cortex Involvement in Neuromyelitis Optica Spectrum Disorder. *J Clin Neurol* 2016; **12**(2): 188-93.
12. Popescu BFG, Parisi JE, Cabrera-Gomez JA, et al. Absence of cortical demyelination in neuromyelitis optica. *Neurology* 2010; **75**(23): 2103-9.
13. Yu CS, Lin FC, Li KC, et al. Diffusion tensor imaging in the assessment of normal-appearing brain tissue damage in relapsing neuromyelitis optica. *Am J Neuroradiol* 2006; **27**(5): 1009-15.
14. Rocca MA, Agosta F, Mezzapesa DM, et al. A functional MRI study of movement-associated cortical changes in patients with Devic's neuromyelitis optica. *Neuroimage* 2004; **21**(3): 1061-8.
15. Rocca MA, Agosta F, Mezzapesa DM, et al. Magnetization transfer and diffusion tensor MRI show gray matter damage in neuromyelitis optica. *Neurology* 2004; **62**(3): 476-8.
16. Saji E, Arakawa M, Yanagawa K, et al. Cognitive impairment and cortical degeneration in neuromyelitis optica. *Ann Neurol* 2013; **73**(1): 65-76.
17. Polman CH, Reingold SC, Banwell B, et al. Diagnostic criteria for multiple sclerosis: 2010 revisions to the McDonald criteria. *Ann Neurol* 2011; **69**(2): 292-302.
18. Wingerchuk DM, Lennon VA, Pittock SJ, Lucchinetti CF, Weinshenker BG. Revised diagnostic criteria for neuromyelitis optica. *Neurology* 2006; **66**(10): 1485-9.
19. Etemadifar M, Hekmatnia A, Tayari N, et al. Features of Virchow-Robin spaces in newly diagnosed multiple sclerosis patients. *Eur J Radiol* 2011; **80**(2): E104-E8.
20. Kwee RM, Kwee TC. Virchow-Robin spaces at MR imaging. *Radiographics* 2007; **27**(4): 1071-U37.
21. Muhlert N, Sethi V, Schneider T, et al. Diffusion MRI-based cortical complexity alterations associated with executive function in multiple sclerosis. *J Magn Reson Imaging* 2013; **38**(1): 54-63.
22. Huh SY, Min JH, Kim W, et al. The usefulness of brain MRI at onset in the differentiation of multiple sclerosis and seropositive neuromyelitis optica spectrum disorders. *Mult Scler* 2014; **20**(6): 695-704.
23. Wingerchuk DM. Neuromyelitis optica spectrum disorders. *Continuum (Minneap Minn)* 2010; **16**(5 Multiple Sclerosis): 105-21.
24. Wingerchuk DM, Banwell B, Bennett JL, et al. International consensus diagnostic criteria for neuromyelitis optica spectrum disorders. *Neurology* 2015; **85**(2): 177-89.
25. Yiannakas MC. Personal communication.
26. Kawachi I, Nishizawa M. Significance of gray matter brain lesions in multiple sclerosis and neuromyelitis optica. *Neuropathology* 2015; **35**(5): 481-6.
27. Matthews L, Marasco R, Jenkinson M, et al. Distinction of seropositive NMO spectrum disorder and MS brain lesion distribution. *Neurology* 2013; **80**(14): 1330-7.
28. Kim J-E, Kim S-M, Ahn S-W, et al. Brain abnormalities in neuromyelitis optica. *Journal of the Neurological Sciences* 2011; **302**(1–2): 43-8.
29. Zhang L, Wu A, Zhang B, et al. Comparison of deep gray matter lesions on magnetic resonance imaging among adults with acute disseminated encephalomyelitis, multiple sclerosis, and neuromyelitis optica. *Mult Scler* 2014; **20**(4): 418-23.

Chapter 6: Optic neuritis in MS and NMOSD: looking for differences between diseases using MTR of the optic nerve and optic coherence tomography (OCT)

1. Bennett JL, de Seze J, Lana-Peixoto M, et al. Neuromyelitis optica and multiple sclerosis: Seeing differences through optical coherence tomography. Mult Scler 2015; 21(6): 678-88.

2. Levin MH, Bennett JL, Verkman AS. Optic neuritis in neuromyelitis optica. Prog Retin Eye Res 2013; 36: 159-71.

3. Schimming R, Gellrich N-C, Schön R, Schmelzeisen R. Recovery of optic nerve function following unilateral posttraumatic blindness. International Poster Journal of Dentistry and Oral Medicine 2001; 3(4): Poster 99. http://ipj.quintessenz.de/index.php?doc=html&abstractID=20785&new_language=en (accessed 9/12/2016).

4. Mallik S, Samson RS, Wheeler-Kingshott CA, Miller DH. Imaging outcomes for trials of remyelination in multiple sclerosis. J Neurol Neurosurg Psychiatry 2014; 85(12): 1396-404.

5. Klistorner A, Chaganti J, Garrick R, Moffat K, Yiannikas C. Magnetisation transfer ratio in optic neuritis is associated with axonal loss, but not with demyelination. Neuroimage 2011; 56(1): 21-6.

6. Levin LA. Physiology of the Optic Nerve. In: Tasman W, Jaeger EA, eds. Duane's Foundations of Clinical Ophthalmology. Philadelphia: Lippincott Williams & Wilkins; 2006.

7. Monteiro ML, Fernandes DB, Apostolos-Pereira SL, Callegaro D. Quantification of retinal neural loss in patients with neuromyelitis optica and multiple sclerosis with or without optic neuritis using Fourier-domain optical coherence tomography. Invest Ophthalmol Vis Sci 2012; 53(7): 3959-66.

8. Green AJ, Cree BA. Distinctive retinal nerve fibre layer and vascular changes in neuromyelitis optica following optic neuritis. J Neurol Neurosurg Psychiatry 2009; 80(9): 1002-5.

9. Naismith RT, Tutlam NT, Xu J, et al. Optical coherence tomography differs in neuromyelitis optica compared with multiple sclerosis. Neurology 2009; 72(12): 1077-82.

10. Nakamura M, Nakazawa T, Doi H, et al. Early high-dose intravenous methylprednisolone is effective in preserving retinal nerve fiber layer thickness in patients with neuromyelitis optica. Graefe's archive for clinical and experimental ophthalmology = Albrecht von Graefes Archiv fur klinische und experimentelle Ophthalmologie 2010; 248(12): 1777-85.

11. Ratchford JN, Quigg ME, Conger A, et al. Optical coherence tomography helps differentiate neuromyelitis optica and MS optic neuropathies. Neurology 2009; 73(4): 302-8.

12. Petzold A, de Boer JF, Schippling S, et al. Optical coherence tomography in multiple sclerosis: a systematic review and meta-analysis. Lancet Neurol 2010; 9(9): 921-32.

13. Park KA, Kim J, Oh SY. Analysis of spectral domain optical coherence tomography measurements in optic neuritis: differences in neuromyelitis optica, multiple sclerosis, isolated optic neuritis and normal healthy controls. Acta Ophthalmol 2014; 92(1): e57-65.

14. Polman CH, Reingold SC, Banwell B, et al. Diagnostic criteria for multiple sclerosis: 2010 revisions to the McDonald criteria. Ann Neurol 2011; 69(2): 292-302.

15. Wingerchuk DM, Lennon VA, Pittock SJ, Lucchinetti CF, Weinshenker BG. Revised diagnostic criteria for neuromyelitis optica. Neurology 2006; 66(10): 1485-9.

16. Yiannakas MC, Kearney H, Samson RS, et al. Feasibility of grey matter and white matter segmentation of the upper cervical cord in vivo: a pilot study with application to magnetisation transfer measurements. Neuroimage 2012; 63(3): 1054-9.

17. Tewarie P, Balk L, Costello F, et al. The OSCAR-IB consensus criteria for retinal OCT quality assessment. PLoS One 2012; 7(4): e34823.

18. Altmann-Schneider I, de Craen AJ, van den Berg-Huysmans AA, et al. An in vivo study on brain microstructure in biological and chronological ageing. PLoS One 2015; 10(3): e0120778.

19. Boorstein JM, Moonis G, Boorstein SM, Patel YP, Culler AS. Optic neuritis: imaging with magnetization transfer. AJR Am J Roentgenol 1997; 169(6): 1709-12.

20. Hickman SJ, Toosy AT, Jones SJ, et al. Serial magnetization transfer imaging in acute optic neuritis. Brain 2004; 127(Pt 3): 692-700.

21. Inglese M, Ghezzi A, Bianchi S, et al. Irreversible disability and tissue loss in multiple sclerosis: a conventional and magnetization transfer magnetic resonance imaging study of the optic nerves. Arch Neurol 2002; 59(2): 250-5.

22. Wang Y, van der Walt A, Paine M, et al. Optic nerve magnetisation transfer ratio after acute optic neuritis predicts axonal and visual outcomes. PLoS One 2012; 7(12): e52291.

23. Trip SA, Schlottmann PG, Jones SJ, et al. Optic nerve magnetization transfer imaging and measures of axonal loss and demyelination in optic neuritis. Mult Scler 2007; 13(7): 875-9.

24. Thorpe JW, Barker GJ, Jones SJ, et al. Magnetisation transfer ratios and transverse magnetisation decay curves in optic neuritis: correlation with clinical findings and electrophysiology. J Neurol Neurosurg Psychiatry 1995; 59(5): 487-92.

25. Frohman EM, Dwyer MG, Frohman T, et al. Relationship of optic nerve and brain conventional and non-conventional MRI measures and retinal nerve fiber layer thickness, as assessed by OCT and GDx: a pilot study. J Neurol Sci 2009; 282(1-2): 96-105.

26. Dalton CM, Brex PA, Miszkiel KA, et al. Application of the new McDonald criteria to patients with clinically isolated syndromes suggestive of multiple sclerosis. Ann Neurol 2002; 52(1): 47-53.

27. Peng C, Wang W, Xu Q, et al. Thickness of macular inner retinal layers and peripapillary retinal nerve fibre layer in neuromyelitis optica spectrum optic neuritis and isolated optic neuritis with one episode. Acta Ophthalmol 2016.

28. Masuda H, Mori M, Uzawa A, et al. Recovery from optic neuritis attack in neuromyelitis optica spectrum disorder and multiple sclerosis. J Neurol Sci 2016; 367: 375-9.

29. Fernandes DB, Raza AS, Nogueira RG, et al. Evaluation of inner retinal layers in patients with multiple sclerosis or neuromyelitis optica using optical coherence tomography. Ophthalmology 2013; 120(2): 387-94.

30. Sotirchos ES, Saidha S, Byraiah G, et al. In vivo identification of morphologic retinal abnormalities in neuromyelitis optica. Neurology 2013; 80(15): 1406-14.

31. Jeong IH, Kim HJ, Kim NH, Jeong KS, Park CY. Subclinical primary retinal pathology in neuromyelitis optica spectrum disorder. J Neurol 2016; 263(7): 1343-8.

32. Hadhoum N, Hodel J, Defoort-Dhellemmes S, et al. Length of optic nerve double inversion recovery hypersignal is associated with retinal axonal loss. Multiple sclerosis (Houndmills, Basingstoke, England) 2016; 22(5): 649-58.

33. Khanna S, Sharma A, Huecker J, Gordon M, Naismith RT, Van Stavern GP. Magnetic resonance imaging of optic neuritis in patients with neuromyelitis optica versus multiple sclerosis. J Neuroophthalmol 2012; 32(3): 216-20.

34. Buch D, Savatovsky J, Gout O, Vignal C, Deschamps R. Combined brain and anterior visual pathways' MRIs assist in early identification of neuromyelitis optica spectrum disorder at onset of optic neuritis. Acta Neurol Belg 2016.

35. Yu C, Lin F, Li K, et al. Pathogenesis of normal-appearing white matter damage in neuromyelitis optica: diffusion-tensor MR imaging. Radiology 2008; 246(1): 222-8.

36. Mealy MA, Whetstone A, Orman G, Izbudak I, Calabresi PA, Levy M. Longitudinally extensive optic neuritis as an MRI biomarker distinguishes neuromyelitis optica from multiple sclerosis. J Neurol Sci 2015; 355(1-2): 59-63.

37. Tian GH, Li ZX, Zhao GX, et al. Evaluation of Retinal Nerve Fiber Layer and Ganglion Cell Complex in Patients with Optic Neuritis or Neuromyelitis Optica Spectrum Disorders Using Optical Coherence Tomography in a Chinese Cohort. J Ophthalmol 2015.

38. Outteryck O, Majed B, Defoort-Dhellemmes S, Vermersch P, Zephir H. A comparative optical coherence tomography study in neuromyelitis optica spectrum disorder and multiple sclerosis. Mult Scler 2015; 21(14): 1781-93.

39. Manogaran P, Vavasour IM, Lange AP, et al. Quantifying visual pathway axonal and myelin loss in multiple sclerosis and neuromyelitis optica. NeuroImage Clinical 2016; 11: 743-50.

40. Martinez-Lapiscina EH, Sepulveda M, Torres-Torres R, et al. Usefulness of optical coherence tomography to distinguish optic neuritis associated with AQP4 or MOG in neuromyelitis optica spectrum disorders. Ther Adv Neurol Disord 2016; 9(5): 436-40.

41. Merle H, Olindo S, Donnio A, Richer R, Smadja D, Cabre P. Retinal peripapillary nerve fiber layer thickness in neuromyelitis optica. Investigative ophthalmology & visual science 2008; 49(10): 4412-7.

42. Gabilondo I, Martinez-Lapiscina EH, Martinez-Heras E, et al. Trans-synaptic axonal degeneration in the visual pathway in multiple sclerosis. Ann Neurol 2014; 75(1): 98-107.

43. Manogaran P, Traboulsee AL, Lange AP. Longitudinal Study of Retinal Nerve Fiber Layer Thickness and Macular Volume in Patients With Neuromyelitis Optica Spectrum Disorder. J Neuroophthalmol 2016.

44. Hokazono K, Raza AS, Oyamada MK, Hood DC, Monteiro MLR. Pattern electroretinogram in neuromyelitis optica and multiple sclerosis with or without optic neuritis and its correlation with FD-OCT and perimetry. Doc Ophthalmol 2013; 127(3): 201-15.

45. Lange AP, Sadjadi R, Zhu F, Alkabie S, Costello F, Traboulsee AL. Spectral-domain optical coherence tomography of retinal nerve fiber layer thickness in NMO patients. Journal of neuro-ophthalmology : the official journal of the North American Neuro-Ophthalmology Society 2013; 33(3): 213-9.

46. Schneider E, Zimmermann H, Oberwahrenbrock T, et al. Optical Coherence Tomography Reveals Distinct Patterns of Retinal Damage in Neuromyelitis Optica and Multiple Sclerosis. PloS one 2013; 8(6): e66151.

Chapter 7: Conclusion

1. Wingerchuk DM, Banwell B, Bennett JL, et al. International consensus diagnostic criteria for neuromyelitis optica spectrum disorders. Neurology 2015; 85(2): 177-89.
2. Sinnecker T, Dorr J, Pfueller CF, et al. Distinct lesion morphology at 7-T MRI differentiates neuromyelitis optica from multiple sclerosis. Neurology 2012; 79(7): 708-14.
3. Kister I, Herbert J, Zhou Y, Ge Y. Ultrahigh-Field MR (7 T) Imaging of Brain Lesions in Neuromyelitis Optica. Mult Scler Int 2013; 2013: 398259.
4. Zhang H, Schneider T, Wheeler-Kingshott CA, Alexander DC. NODDI: practical in vivo neurite orientation dispersion and density imaging of the human brain. Neuroimage 2012; 61(4): 1000-16.
5. Favaretto A, Poggiali D, Lazzarotto A, Rolma G, Causin F, Gallo P. The Parallel Analysis of Phase Sensitive Inversion Recovery (PSIR) and Double Inversion Recovery (DIR) Images Significantly Improves the Detection of Cortical Lesions in Multiple Sclerosis (MS) since Clinical Onset. PLoS One 2015; 10(5): e0127805.
6. Sethi V, Yousry TA, Muhlert N, et al. Improved detection of cortical MS lesions with phase-sensitive inversion recovery MRI. J Neurol Neurosur Ps 2012; 83(9): 877-82.
7. Trip SA, Schlottmann PG, Jones SJ, et al. Optic nerve magnetization transfer imaging and measures of axonal loss and demyelination in optic neuritis. Mult Scler 2007; 13(7): 875-9.
8. Kaden E, Kelm ND, Carson RP, Does MD, Alexander DC. Multi-compartment microscopic diffusion imaging. *Neuroimage* 2016; **139**: 346-59.
9. Haacke EM, Liu S, Buch S, Zheng W, Wu D, Ye Y. Quantitative susceptibility mapping: current status and future directions. *Magn Reson Imaging* 2015; **33**(1): 1-25.
10. Groeschel S, Hagberg GE, Schultz T, et al. Assessing White Matter Microstructure in Brain Regions with Different Myelin Architecture Using MRI. *PLoS One* 2016; **11**(11): e0167274.
11. Liu S, Buch S, Chen Y, et al. Susceptibility-weighted imaging: current status and future directions. *NMR Biomed* 2017; **30**(4).
12. Mealy MA, Whetstone A, Orman G, Izbudak I, Calabresi PA, Levy M. Longitudinally extensive optic neuritis as an MRI biomarker distinguishes neuromyelitis optica from multiple sclerosis. *J Neurol Sci* 2015; **355**(1-2): 59-63.
13. Storoni M, Davagnanam I, Radon M, Siddiqui A, Plant GT. Distinguishing optic neuritis in neuromyelitis optica spectrum disease from multiple sclerosis: a novel magnetic resonance imaging scoring system. *J Neuroophthalmol* 2013; **33**(2): 123-7.

14. Zhao D-D, Zhou H-Y, Wu Q-Z, et al. Diffusion tensor imaging characterization of occult brain damage in relapsing neuromyelitis optica using 3.0T magnetic resonance imaging techniques. *NeuroImage* 2012; **59**: 3173-7.